Extremely Shaped Plasmas to Improve the Tokamak Concept

THÈSE N^{O} 5015 (2011)

PRÉSENTÉE LE 1ER AVRIL 2011
À LA FACULTÉ SCIENCES DE BASE
CRPP - PHYSIQUE DU TOKAMAK TCV
PROGRAMME DOCTORAL EN PHYSIQUE

ÉCOLE POLYTECHNIQUE FÉDÉRALE DE LAUSANNE

POUR L'OBTENTION DU GRADE DE DOCTEUR ÈS SCIENCES

PAR

Francesco PIRAS

acceptée sur proposition du jury:

Prof. R. Schaller, président du jury
Dr J.-M. Moret, Dr Y. Martin, directeurs de thèse
Dr R. Pitts, rapporteur
Dr D. Ryutov, rapporteur
Prof. L. Villard, rapporteur

ÉCOLE POLYTECHNIQUE
FÉDÉRALE DE LAUSANNE
Suisse
2011

Some figures in this dissertation are in color only in the electronic version.

An electronic version is available for download from either
http://library.epfl.ch/theses/?nr=5015
or
http://dx.doi.org/10.5075/epfl-thesis-5015

This document was last revised on Thursday 17th March, 2011 and has been compiled using pdfLaTeXwith a template developed by Dr. Christian Schlatter. The official version is the printed version as registered for copyright.

Please cite this publication as:
Francesco Piras, **Extremely Shaped Plasmas to Improve the Tokamak Concept**, Ph.D. thesis, no. 5015, Ecole polytechnique fédérale de Lausanne (EFPL), CH-1015 Lausanne, Switzerland, March 2011.

Abstract

Energy is essential for human existence and our future depends on plentiful and accessible sources of energy. The world population is fast growing and the average energy used per capita increases. One of the greatest challenges for human beings is that of meeting the growing demand for energy in a responsible, equitable and sustainable way.

The possibility to obtain energy by “fusing” light atoms addresses these needs. Nuclear fusion reactions are clean, safe and the amount of fuel present on Earth (hydrogen isotopes) is practically inexhaustible and well distributed. Nuclear fusion is a natural process that occurs in all active stars like our Sun. Since the first demonstration of a deuterium fusion reaction (*Rutherford 1933*), researchers worldwide have tried to replicate this process on Earth by building a thermonuclear fusion reactor. Nevertheless, the challenge posed by the construction of a nuclear fusion reactor is greater than the one presented earlier by the development of a fission reactor. During the IAEA Conference in Geneva in the early 1958, L.A.Artsimovich declared: “Plasma physics is very difficult. Worldwide collaboration is needed for progress” and E.Teller, at the same conference: “Fusion technology is very complex. It is almost impossible to build a fusion reactor in this century”. They were right. The extremely high temperature and density necessary to fuse hydrogen isotopes makes it difficult indeed to create a successful fusion reactor. Even though the physics of the fusion reaction appears clear, we are still facing problems on the road towards bulding the “box” that can efficiently confine the hot gas in the state of plasma.

The best results so far have been obtained confining a plasma with strong magnetic fields in a toroidal configuration (“tokamak”). The *Centre de Recherches en Physique des Plasmas* in Switzerland actively studies this promising configuration towards the development of a nuclear fusion reactor. The experimental activity of the *Tokamak à Configuration Variable* (TCV) mainly focuses on the research of optimized plasma shapes capable of improving the global performance and solve the technological challenges of a tokamak reactor. Several theoretical and experimental results show the importance of the plasma shape in tokamaks. The maximum value of β (an indicator of the confinement efficiency) is for example related to the ratio between the height and the width of the plasma. The plasma shape can also affect the power necessary to access improved confinement regimes, as well as the plasma stability.

This thesis reports on a contribution towards the optimization of the tokamak plasma shape. In particular, it describes the theoretical and experimental studies carried out in the TCV tokamak on two innovative plasma shapes: the **doublet shaped** plasma and the **snowflake divertor**.

Doublet shaped plasmas have been studied in the past by the *General Atomics* group. Since then, the development of new plasma diagnostics and the discovery of new confinement regimes have given new reasons for interest in this unusual configuration. TCV is the only tokamak worldwide theoretically able to establish and control this configuration. This thesis illustrates new motivations for creating doublet plasmas. The vertical stability of the configuration is studied using a rigid model and the results are compared with those obtained with the KINX MHD stability code. The best strategy for controlling a doublet on TCV is also investigated, and a possible setup of the TCV control system is suggested for the doublet configuration. Analyzing the possible scenarios for doublet creation, the most promising scenario consists of the creation of two independent plasmas, which are subsequently merged to establish a doublet. For this reason, particular attention needs to be devoted to the problem of the plasma start-up. In this thesis, a general analysis of the TCV ohmic and assisted with ECH plasma start-up is presented, and recent attempts to create a doublet plasma are reported. Since the magnetic field reconstruction at the breakdown time is important to better diagnose these plasmas, the entire magnetic system of TCV has been calibrated with an original technique, also described in the manuscript.

The last part of this thesis is devoted to the snowflake divertor configuration. This innovative plasma shape has been proposed and theoretically studied by Dr. D.D.Ryutov from the Lawrence Livermore National Laboratory. In Ryutov's articles, this configuration was proposed to alleviate the problems of the plasma-wall interaction and possibly affect the plasma edge stability. The TCV tokamak was the first to report the creation and control of a snowflake configuration, and the candidate was the principal investigator of this work. These results are accordingly discussed in this thesis. Details are provided in particular on the strategy used to establish the configuration. An edge-localized mode (ELM) H-mode regime, supported by electron cyclotron heating, has been successfully established in a snowflake. This regime exhibits 2 to 3 times lower ELM frequency but only a 20%-30% increase in normalized ELM energy ($\Delta W_{\mathrm{ELM}}/W_P$) compared to an identically-shaped, conventional, single-null, diverted H-mode. Enhanced stability of mid- to high-toroidal-mode-number ideal modes is consistent with the different snowflake ELM phenomenology. Finally, the capability of the snowflake to redistribute the edge power on the additional strike points has been confirmed experimentally and is also reported in this thesis.

keywords: plasma physics, nuclear fusion, tokamak, TCV, doublet, breakdown, snowflake, magnetic diagnostics, calibration, error field, edge physics, control, ELM, H-mode.

Sinossi

L'energia è essenziale per l'esistenza dell'uomo. Il nostro futuro dipende dalla presenza di risorse energetiche facilmente accessibili ed illimitate. La popolazione mondiale cresce costantemente ed il consumo pro-capite di energia è in continuo aumento. La necessità di soddisfare il continuo aumento del fabbisogno energetico mondiale in modo responsabile, equo e sostenibile rappresenta una delle più grandi sfide per l'uomo del ventunesimo secolo.
La possibilità di ottenere energia tramite la "fusione" di atomi leggeri soddisfa le queste esigenze. L'energia prodotta dalle reazioni a fusione nucleare è pulita, sicura e la quantità di combustibile presente sulla terra (isotopi dell'idrogeno) è praticamente illimitata e uniformemente distribuita. La fusione nucleare è un processo naturale presente in tutte le stelle attive, compreso il sole. In seguito alla prova sperimentale della possiblità di fondere degli atomi di deuterio (*Rutherford 1933*), molti ricercatori in diverse parti del mondo hanno cercato di ripetere questo processo sulla terra, attraverso la costruzione di un reattore a fusione termonucleare. Tuttavia, le difficoltà legate alla costruzione di un reattore a fusione sono maggiori di quelle precedentemente incontrare durante la costruzione dei primi reattori a fissione. Durante la conferenza IAEA a Ginevra nel lontano 1958, L.A.Artsimovich dichiarò: "La fusione nucleare è molto difficile. Una collaborazioni internazionale è necessaria per progredire", mentre E.Teller affermò, durante la stessa conferenza: "La tecnologia della fusione nucleare è molto complessa. È praticamente impossibile riuscire a costruire un reattore a fusione nucleare durante questo secolo". Entrambi avevano ragione. Le temperature e le densità estreme necessarie per innescare il processo di fusione degli atomi di idrogeno rendono estremamente complessa la concezione di un reattore a fusione. Nonostante la fisica della fusione nucleare sia sufficientemente chiara, rimane da comprendere come costruire la "scatola" che può confinare in modo efficiente il gas allo stato di plasma.
Sinora i migliori risultati sono stati ottenuti confinando un plasma con forti campi magnetici, in una configurazione toroidale detta "tokamak". Il *Centre de Recherches en Physique des Plasmas* in Svizzera si occupa dello studio di questa configurazione verso la costruzione di un reattore a fusione nucleare. L'attività sperimentale del *Tokamak à Configuration Variable* (TCV) è principalmente orientata verso l'ottimizzazione della forma del plasma, allo scopo di migliorare le prestazioni globali e risolvere le differenti problematiche tecnologiche di un reattore tokamak. Diversi risultati, teorici e sperimentali, dimostrano l'importanza della forma del plasma in un tokamak. Un esempio è dato dal valore massimo di β, un indicatore dell'efficienza del confinamento. Questo parametro dipende dal rapporto tra l'altezza e la larghezza del plasma. La forma del plasma può anche cambiare la potenza necessaria per accedere a dei regimi caratterizzati da un confinamento superiore, e può inoltre modificare la stabilità globale e/o della periferia del plasma.
Questa tesi rappresenta un contributo verso l'ottimizzazione della forma del plasma nei tokamak. In particolare, vengono descritti degli studi teorici e sperimentali, condotti nel tokamak TCV, di due forme innovative: la forma **doublet** e la forma **snowflake** (fiocco di neve).
La forma doublet è stata precedentemente studiata dal gruppo *General Atomics*. Attualmente, lo sviluppo nel campo delle diagnostiche per il plasma e la scoperta di nuovi regimi di confinamento conferiscono un rinnovato interesse a questa forma inusuale. TCV è il solo tokamak al mondo capace di creare e controllare una forma doublet. In questa tesi vengono prima discusse le motivazioni che rendono interessante lo studio di questa forma. In seguito, la stabilità verticale della configurazione è analizzata attraverso un modello rigido del plasma, confrontando i risultati ottenuti con quelli forniti dal programma KINX. Viene inoltre individuata la miglior strategia per creare un doublet in TCV, suggerendo una possibile configurazione del sistema di controllo del plasma. Tra i vari scenari possibili, quello più promettente consiste nella creazione di due

plasmi indipendenti, che vengono in seguito uniti per creare un doublet. Per questo motivo, particolare attenzione è dedicata allo studio della ionizzazione del gas. Nella tesi si analizza in modo generale la ionizzazione, ohmica o assistita, del gas in TCV, descrivendo in modo particolare i primi esperimenti di creazione della forma doublet. Essendo la ricostruzione del campo magnetico al tempo della ionizzazione del gas importante per la comprensione del fenomeno, l'insieme dei sensori magnetici di TCV è stato calibrato con una tecnica originale, anch'essa descritta in questo manoscritto.

L'ultima parte di questa tesi è dedicata alla configurazione snowflake. Questa forma innovativa è stata proposta e studiata sul piano teorico dal Dr. D.D.Ryutov del Lawrence Livermore National Laboratory. Nei suoi articoli, Ryutov propone questa configurazione come una possibilità per ridurre il problema delle interazioni tra il plasma e le pareti del reattore. Inoltre lo snowflake avrebbe la potenzialità di influenzare la stabilità del bordo del plasma. La creazione ed il controllo di una forma snowlflake è stata documentata, per la prima volta, da TCV. Questi risultati sono discussi in questa tesi, dove particolare attenzione è dedicata alle strategie impiegate per creare la configurazione. Un regime a confinamento migliorato (modo H), caratterizzato da modi localizzati al bordo (ELMs) e sostenuto da onde a riscaldamento degli elettroni (ECH) è stato ottenuto con successo nella configurazione snowflake. Questo regime presenta una frequenza degli ELMs 2-3 volte inferiore ed un'energia normalizzata degli ELMs ($\Delta W_{\mathrm{ELM}}/W_P$) superiore del $20\% - 30\%$ rispetto ad una configurazione modo H convenzionale. L'aumento della stabilità dei modi a media/alta frequenza toroidale è consistente con le differenti caratteristiche degli ELM nella configurazione snowflake. Infine, la capacità dello snowflake di ridistribuire la potenza al bordo plasma sui punti aggiuntivi di contatto con la parete del reattore è stata confermata sperimentalmente e descritta in questa tesi.

Parole chiave: fisica del plasma, fusione nucleare, tokamak, TCV, doublet, ionizzazione, snowflake, sensori magnetici, calibrazione, errore di campo, fisica del bordo, controllo, ELM, modo H.

Contents

List of Figures

List of Tables

Chapter 1

Introduction

One of the greatest challenges for human beings is that of meeting the growing demand for energy in a responsible, equitable and sustainable way. The possibility to obtain energy "fusing" light atoms is an especially attractive response to these needs. This exothermic process, known as nuclear fusion, is one of the most promising sources of energy. Nuclear fusion reactions, the fuel for most of the stars in the Universe, occur at extremely high temperature and/or density. The challenge of nuclear fusion research is to find the scientific and technological solution to reproduce these conditions on Earth.

1.1 Why nuclear fusion?

Life on Earth is driven by energy. Human beings use far more energy than any other living being that has ever evolved. The control of fire and the exploitation of fossil fuels have made it possible to release, in a relatively short time, vast amounts of energy that accumulated long before the species appeared.

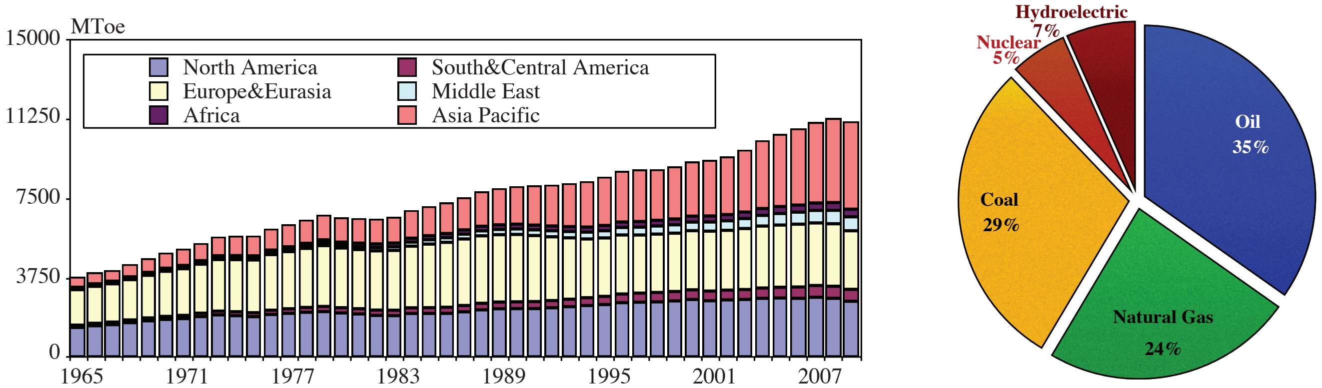

(a) (b)

Figure 1.1.1: (a) Primary energy consumption in million tons oil equivalent (MToe) per region; (b) world primary energy consumption by fuel in 2009 [1].

Figure 1.1.1(a) shows the evolution of the primary energy consumption in the last 55 years. The constant growth of the energy consumption is driven by the increase of the world population and the energy use per capita. Historically, most of the energy consumption has been geographically located in North America and Europe. In the last ∼ 15 years, a strong increase of energy consumption has come from the Asia Pacific region, due to the fast economic growth of the People's Republic of China.

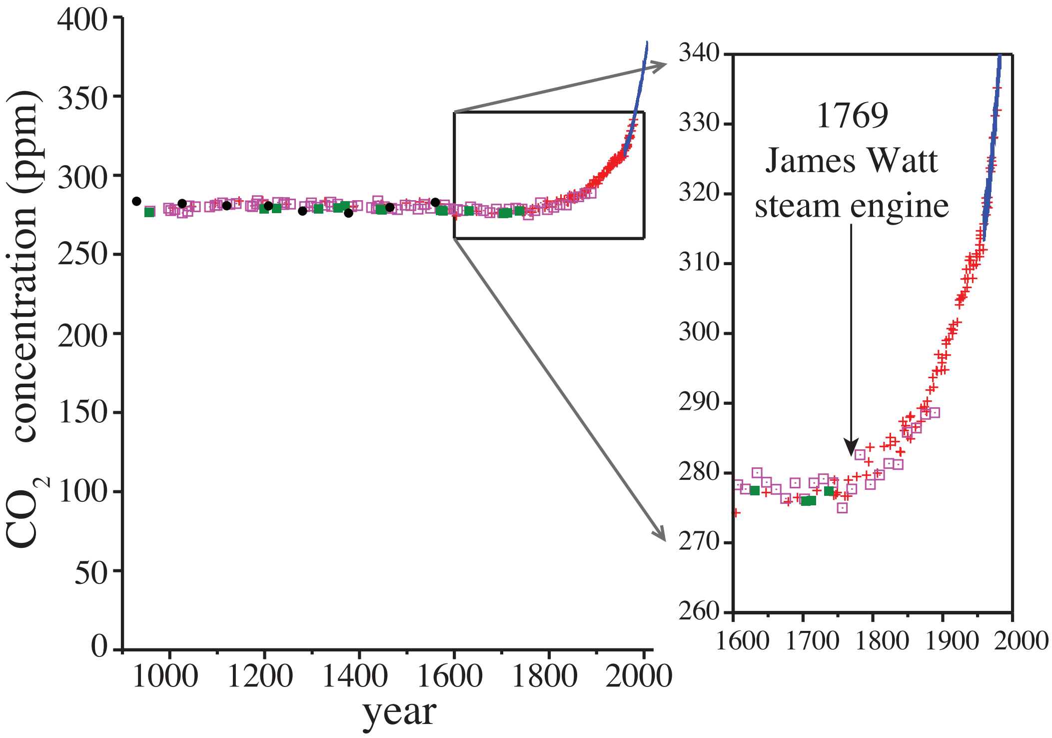

Figure 1.1.2: Carbon dioxide (CO_2) concentration (in parts per million) in the last 1100 years, measured from air trapped in ice cores (up to 1977) and directly in Hawaii (from 1958 onwards) [2].

Most of the energy consumed today is produced from fossil fuels (Fig. 1.1.1(b)). There are several consequences of the combustion of fossil fuels:

1. Fossil fuels are a finite resource. There is the possibility that cheap oil and gas will run out in our lifetime. The peak of oil production is already passed and suppliers already cannot meet the oil demand. Moreover, since fossil fuels are a valuable resource because of their use in the manufacture of plastics and other materials, a reserve should be kept for future needs.

2. Even if fossil fuels are still available somewhere in the world, the energy needs and, consequently, the economy of a country, should not be vulnerably dependent on other countries. The international geopolitical equilibria are strongly influenced by the energy market.

3. Burning fossil fuels has environmental implications. Examples are greenhouse gas accumulation (see Fig. 1.1.2), acidification, air pollution, water pollution, damage to land surface and ground-level ozone. These environmental problems are caused by the release of pollutants that are naturally present in fossil fuel structures, such as sulphur and nitrogen. Currently, oil burning is responsible for about 30% of all carbon dioxide emissions in the air. Natural gas does not release as much carbon dioxide because of its methane structure. The largest emissions are caused by coal combustion.

It appears clear that something must be done urgently, replacing the fossil fuels with alternative energy sources.
Lot of progress has been made in the renewable energies, like solar, wind, geothermal, hydropower and biomass (see Fig. 1.1.3). In spite of all this, skepticism surrounds renewable energies and the possibility that they will reach a high enough share to realistically replace fossil fuels. This is mainly due to the high investments necessary to build renewable power plants and their distribution grid. Concerning hydropower, unfortunately most of the resources in Europe have been

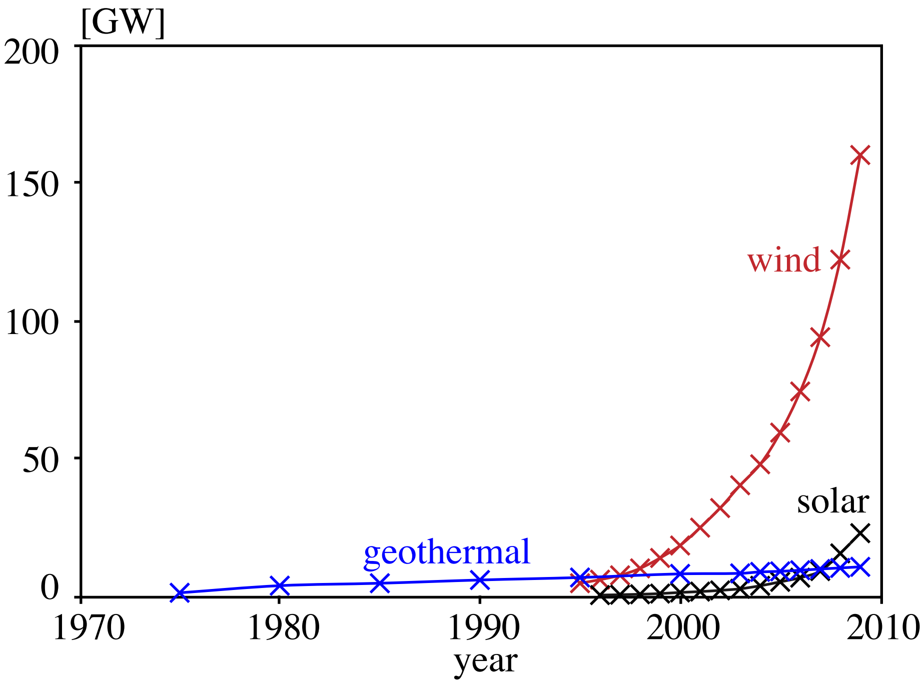

Figure 1.1.3: Cumulative installed geothermal, wind and solar power.

exploited and the number of new hydropower plants in future will be small. More details on renewable energies can be found in [2].

About 5% of world's total primary energy supply is today produced by nuclear fission power plants (see Fig. 1.1.1(b)). More plants are planned to be built to satisfy the increasing electricity demand. The risk of accidents and terrorist attacks and the fact that solutions for the long term storage of highly radioactive waste are still missing makes the established nuclear fission industry not very attractive.

Another potential source of energy comes from nuclear fusion reactions. Fusion is the exothermic process at the core of stars like our sun. Light nuclei collide and fuse into heavier elements releasing a large amount of energy.

The idea of using human-initiated fusion reactions was first made practical for military purposes in nuclear weapons. The first fission-fusion-fission-based weapons released some 500 times more energy than early fission weapons. Attempts at controlling fusion had already started by this point. Registration of the first patent related to a fusion reactor by the United Kingdom Atomic Energy Authority dates back to 1946 [4]. Research in this field has been accompanied by extreme scientific and technological difficulties, but has resulted in progress. Today, the largest nuclear fusion experiment is the Joint European Torus (JET). In 1997, JET produced a peak of 16.1 MW of fusion power (65% of input power) [5]. In June 2005, the construction of the International Thermonuclear Experimental Reactor (ITER), designed to produce ten times more fusion power than the power put into the plasma over many minutes, was announced. The production of net electrical power from fusion is planned for DEMO (DEMOnstration Power Plant), the next generation experiment after ITER. Additionally, the world's largest and highest-energy laser, the National Ignition Facility (NIF), will attempt to produce more fusion power than the input power.

1.2 The nuclear fusion reactor

Large-scale thermonuclear fusion processes, involving many nuclei fusing at once, must occur in matter at very high densities and/or temperatures. The fusion of two nuclei with lower masses than iron (which, along with nickel, has the largest binding energy per nucleon) generally releases energy while the fusion of nuclei heavier than iron absorbs energy. The opposite is true for the reverse process, nuclear fission (see Fig. 1.2.1).

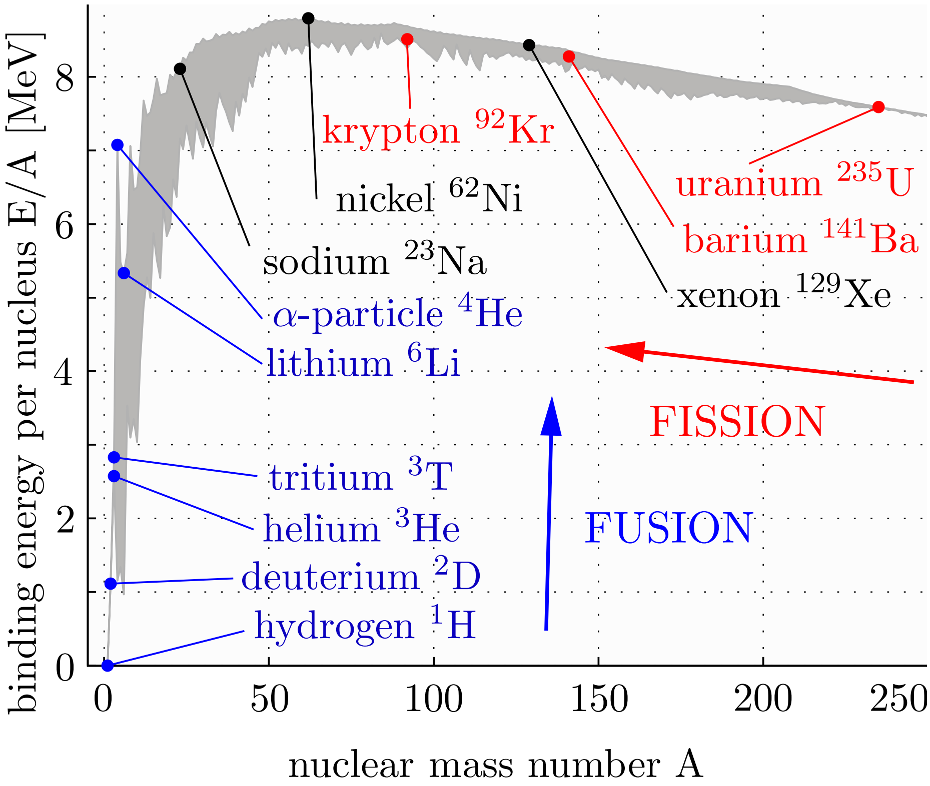

Figure 1.2.1: For light elements the binding energy per nucleon increases, stabilizes in the sequence through xenon and finally decreases with the heavier elements.

It takes considerable energy to force nuclei to fuse, even those of the lightest element, hydrogen. This is because all nuclei have a positive charge (due to their protons), and as like charges repel, nuclei strongly resist being placed close together. Accelerated to high speeds (that is, heated to thermonuclear temperatures), they can, however, overcome this electromagnetic repulsion and get close enough for the attractive nuclear force to be sufficiently strong to achieve fusion. The fusion of lighter nuclei, which creates a heavier nucleus, generally releases more energy than it takes to force the nuclei together; this is an exothermic process that can produce self-sustaining reactions. To be a useful energy source, a fusion reaction must satisfy several criteria. It must:

- Be exothermic: this may seem obvious, but it limits the reactants to the low Z side of the curve of binding energy (see Fig. 1.2.1). It also makes helium ^{4}He the most common product because of its extraordinarily tight binding.

- Involve low Z nuclei: this is because the electrostatic repulsion must be overcome before the nuclei are close enough to fuse.

- Have two reactants: at anything less than stellar densities, three body collisions are too improbable.

- Have two or more products: this allows simultaneous conservation of energy and momentum without relying on the electromagnetic force.
- Conserve both protons and neutrons: the cross sections for the weak interaction are too small.

Few reactions meet these criteria. The following are those with the largest cross sections:

$$
\begin{aligned}
{}^2_1\mathrm{D} + {}^3_1\mathrm{T} &\rightarrow {}^4_2\mathrm{He}\ (3.5\ \mathrm{Mev}) + \mathrm{n}^0\ (14.1\ \mathrm{MeV}) && (1.2.1)\\
{}^2_1\mathrm{D} + {}^2_1\mathrm{D} &\rightarrow {}^3_1\mathrm{T}\ (1.01\ \mathrm{Mev}) + \mathrm{p}^+\ (3.02\ \mathrm{MeV}) && (1.2.2)\\
&\rightarrow {}^3_2\mathrm{He}\ (0.82\ \mathrm{Mev}) + \mathrm{n}^0\ (2.45\ \mathrm{MeV}) && (1.2.3)\\
{}^2_1\mathrm{D} + {}^3_2\mathrm{He} &\rightarrow {}^4_2\mathrm{He}\ (3.6\ \mathrm{Mev}) + \mathrm{p}^+\ (14.7\ \mathrm{MeV}) && (1.2.4)\\
{}^3_1\mathrm{T} + {}^3_1\mathrm{T} &\rightarrow {}^4_2\mathrm{He} + 2\mathrm{n}^0 + 11.3\ \mathrm{MeV} && (1.2.5)\\
{}^3_2\mathrm{He} + {}^3_2\mathrm{He} &\rightarrow {}^4_2\mathrm{He} + 2\mathrm{p}^+ + 12.9\ \mathrm{MeV} && (1.2.6)\\
{}^3_2\mathrm{He} + {}^3_1\mathrm{T} &\rightarrow {}^4_2\mathrm{He} + \mathrm{p}^+ + \mathrm{n}^0 + 12.1\ \mathrm{MeV} && (1.2.7)\\
&\rightarrow {}^4_2\mathrm{He}\ (4.8\ \mathrm{MeV}) + {}^2_1\mathrm{D}\ (9.5\ \mathrm{MeV}) && (1.2.8)\\
&\rightarrow {}^4_2\mathrm{He}\ (0.5\ \mathrm{MeV}) + \mathrm{n}^0\ (1.9\ \mathrm{MeV}) + \mathrm{p}^+\ (11.9\ \mathrm{MeV}) && (1.2.9)\\
{}^2_1\mathrm{D} + {}^6_3\mathrm{Li} &\rightarrow 2{}^4_2\mathrm{He} + 22.4\ \mathrm{MeV} && (1.2.10)\\
&\rightarrow {}^3_2\mathrm{He} + {}^4_2\mathrm{He} + \mathrm{n}^0 + 2.56\ \mathrm{MeV} && (1.2.11)\\
&\rightarrow {}^7_3\mathrm{Li} + \mathrm{p}^+ + 5.0\ \mathrm{MeV} && (1.2.12)\\
&\rightarrow {}^7_4\mathrm{Be} + \mathrm{n}^0 + 3.4\ \mathrm{MeV} && (1.2.13)\\
\mathrm{p}^+ + {}^6_3\mathrm{Li} &\rightarrow {}^4_2\mathrm{He}\ (1.7\ \mathrm{MeV}) + {}^3_2\mathrm{He}\ (2.3\ \mathrm{MeV}) && (1.2.14)\\
{}^3_2\mathrm{He} + {}^6_3\mathrm{Li} &\rightarrow 2{}^4_2\mathrm{He} + \mathrm{p}^+ + 16.9\ \mathrm{MeV} && (1.2.15)\\
\mathrm{p}^+ + {}^{11}_5\mathrm{B} &\rightarrow 3{}^4_2\mathrm{He} + 8.7\ \mathrm{MeV} && (1.2.16)
\end{aligned}
$$

The fusion cross-section of few reactions is represented in Fig. 1.2.2 as a function of the particles energy.
The Deuterium-Tritium (D-T) reaction is the one with the highest cross-section, i.e. the highest probability of resulting in a fusion reaction. Moreover, the maximum cross-section is obtained with a smaller projectile energy compared to the other reactions. It is, therefore, the more promising for a fusion reactor. Deuterium can be obtained from seawater; tritium, a heavier isotope of hydrogen, is not found in large quantities naturally (because it has a half-life of only 12.6 years) but it can be manufactured from lithium. Its production in a fusion reaction is envisaged by breeding from lithium using neutrons from the fusion reactions themselves:

$$
\begin{aligned}
{}^7_3\mathrm{Li} + {}^1_0\mathrm{n} &\rightarrow {}^4_2\mathrm{He} + {}^3_1\mathrm{T} + {}^1_0\mathrm{n} - 2.47\ \mathrm{MeV} && (1.2.17)\\
{}^6_3\mathrm{Li} + {}^1_0\mathrm{n} &\rightarrow {}^4_2\mathrm{He}\ (2.05\ \mathrm{MeV}) + {}^3_1\mathrm{T}\ (2.73\ \mathrm{MeV}) && (1.2.18)
\end{aligned}
$$

There is enough fusion fuel to produce energy for a million years [2].
Other advantages of nuclear fusion reactions as source of energy are:

- Few radioactive particles are produced by fusion reactions;
- As fossil fuels are not used, there is no possibility of release of chemical combustion products;

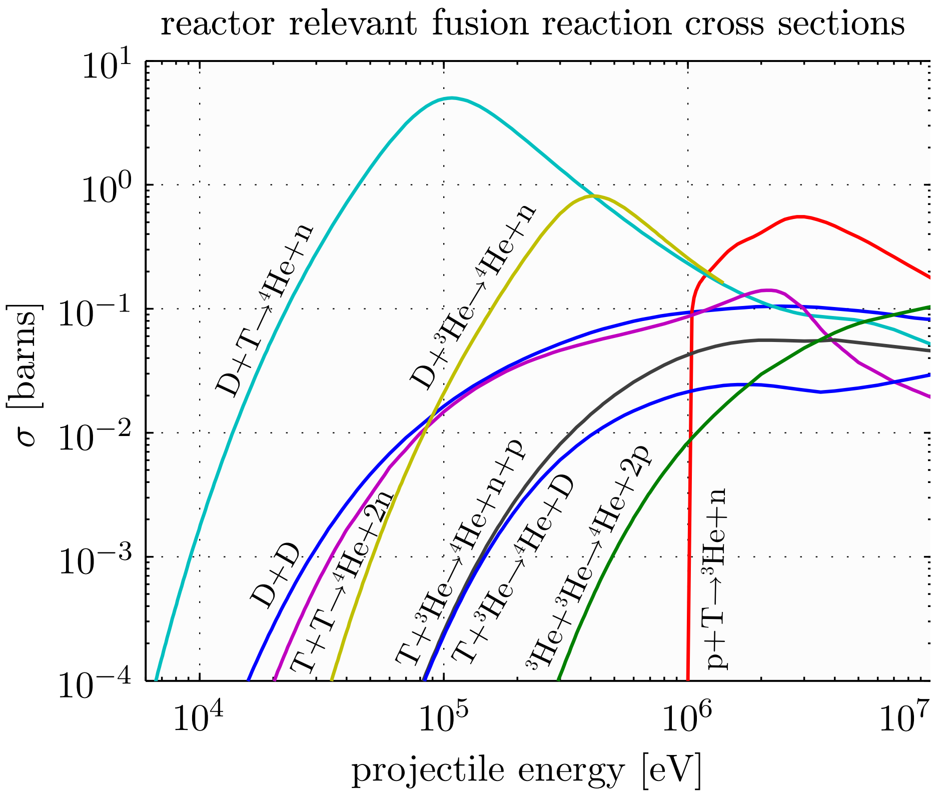

Figure 1.2.2: Fusion cross-section of a few reactions as a function of the projectile energy.

- The fusion reaction is intrinsically safe. Even if the control of the reactor is lost, there is no risk of avalanche phenomena as in nuclear fission reactions.

In order to make a fusion reaction, particles need to have a high enough kinetic energy high enough to contrast the electrostatic repulsive force between nuclei (see Fig. 1.2.2). The optimum temperature to burn a D-T mixture is 10 keV (100 millions °C , to be compared e.g. with the maximum temperature of the sun, 15 millions °C). At this temperature, all the matter is in the state of **plasma**, the most common phase in the visible universe. Plasma is an ensemble of free charged particles, which is globally neutral and exhibits collective behavior. The challenge of nuclear fusion research is how to obtain the high plasma temperature and/or density necessary to maximize the probability to have nuclear fusion reactions. These conditions must be maintained long enough to extract energy from the fusing plasma.

Technologically, several strategies have been investigated in the last 60 years to “confine” the hot plasma. One force capable of confining the fuel well enough is gravity. The mass needed, however, is so great that gravitational confinement is only found in stars. Another technique is inertial confinement. The idea is to apply a rapid pulse of energy to a large part of the surface of a pellet of fusion fuel, causing it to simultaneously implode, creating very high pressures and temperatures. If the fuel is dense enough and hot enough, the fusion reaction rate will be high enough to burn a significant fraction of the fuel before it has dissipated. To achieve these extreme conditions, the initially cold fuel must be explosively compressed with lasers. In this thesis I will focus my attention on a different technique: magnetic confinement.

1.3 Magnetic confinement

Electrically charged particles (such as fuel ions) follow magnetic field lines. The fusion fuel can therefore be trapped using a strong magnetic field. The contact between the hot plasma and the solid surfaces of the reactor should be avoided because the plasma would melt it or cool down.
The simplest magnetic configuration is a solenoid, a long cylinder wound with magnetic coils producing a field with the lines of force running parallel to the axis of the cylinder. Such a field would prevent ions and electrons from being lost radially, but not from being lost at the ends of the solenoid. There are two approaches to solving this problem. One is to try to “plug” the ends with a magnetic mirror, the other is to eliminate the ends altogether by bending the field lines around to close on themselves. A simple toroidal field, however, provides poor confinement because the radial gradient of the field strength results a orbital drift and outward particle losses.

1.3.0.1 Magnetic mirrors

A major area of research in the early years of fusion energy research was the magnetic mirror. A magnetic mirror is a magnetic field configuration where the field strength changes when moving along a field line. The mirror effect results in a tendency for charged particles to bounce back from the high field region. The concept was largely abandoned due to the low performance compared to the tokamak configuration (see Fig. 1.3.1(a)).

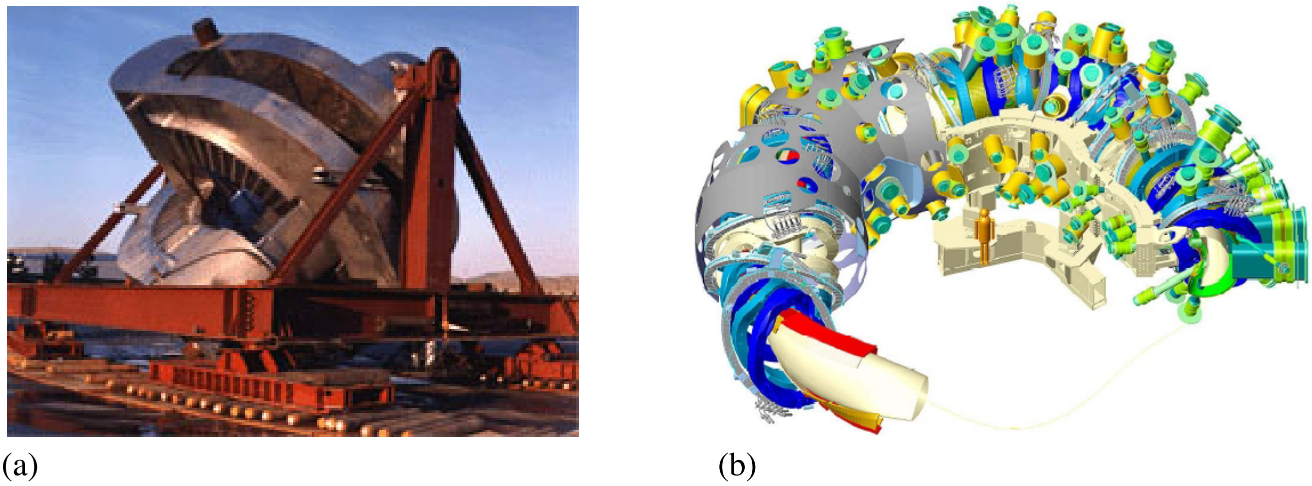

(a) (b)

Figure 1.3.1: (a) One of the magnets for the Mirror Fusion Test Facility-B (MFTF-B) in the Lawrence Livermore National Laboratory (LLNL)-USA, the Lab’s most ambitious magnetic mirror fusion experiment. The facility was mothballed in 1986 when funding sources dried up after the decision was made to devote resources exclusively to tokamaks. (b) Wendelstein 7-X, the large stellerator under construction at the Greifswald branch of IPP in Germany. The plasma performances are expected to be comparable to that of a tokamak, however, avoiding the disadvantages of a large plasma current and therefore enabling steady state operation.

1.3.0.2 Toroidal machines

An early attempt to build a magnetic confinement system was the stellarator, introduced by Lyman Spitzer in 1951. Essentially the stellarator consists of a torus that has been cut in half and then attached back together with straight "crossover" sections to form a figure-8. This has the effect of propagating the particles from the inside to the outside as they orbit the device, thereby canceling out the drift across the axis, at least if the particles travel sufficiently fast. Newer

versions of the stellarator design have replaced the "mechanical" drift cancellation with additional magnets that "wind" the field lines into a helix to cause the same effect (see Fig. 1.3.1(b)).
In the 1960s the Soviet physicists Igor Yevgenyevich Tamm and Andrei Sakharov presented the toroidal tokamak in public, with results that far outstripped existing efforts from any competing design, magnetic or not. Since then the majority of effort in magnetic confinement has been based on the tokamak principle.
In 1991, START was built at Culham, UK, as the first purpose built spherical tokamak. This was essentially a spheromak with an inserted central rod. START produced impressive results, with β values at approximately 40% - three times that produced by standard tokamaks at the time. The concept has been scaled up to higher plasma currents and larger sizes, with the experiments NSTX (US), MAST (UK) and Globus-M (Russia) currently running.
Other configurations produced in toroidal machines are the Reversed Field Pinch (RFP) and the Levitated Dipole Experiment (LDX).

1.4 The tokamak reactor

Tokamak is a Russian acronym meaning toroidal chamber with magnetic coils.

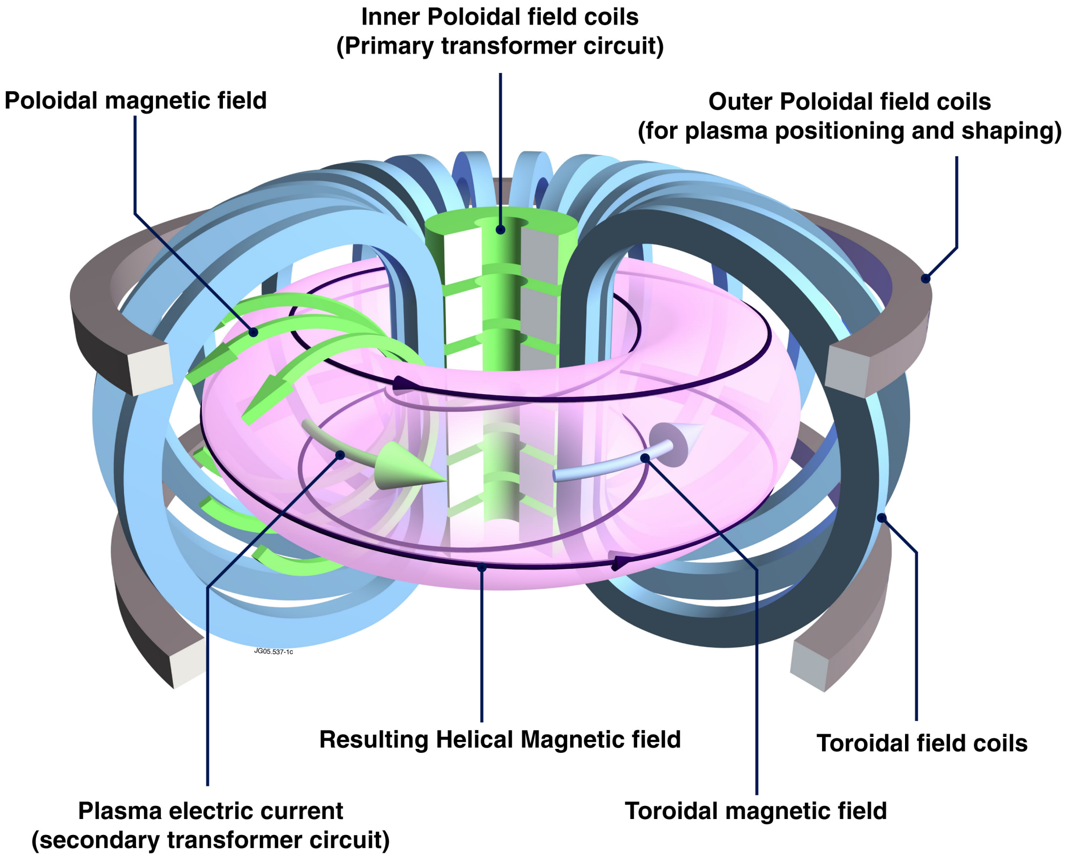

Figure 1.4.1: The tokamak device. The toroidal field is produced by a set of toroidal field coils. The poloidal field necessary to twist the magnetic field lines is given by the plasma current, induced by the inner poloidal field coils. The plasma shape and position are controlled with the poloidal field coils.

A tokamak is a type of machine that uses a magnetic field to confine a plasma in the shape of a torus (see Fig. 1.4.1). Achieving a stable plasma equilibrium requires magnetic field lines that move around the torus in a helical shape. Such a helical field can be generated by adding a toroidal field (traveling around the torus in circles) and a poloidal field (traveling in circles orthogonal to

the toroidal field). In a tokamak, the toroidal field is produced by electromagnets that surround the torus, and the poloidal field is the result of a toroidal electric current that flows inside the plasma. This current is induced inside the plasma with a second set of electromagnets.
The main components that are present in a tokamak device are:

- **Vacuum Vessel** (**VV**) : it has a toroidal shape and contains the fusing plasma. It needs to isolate the low pressure plasma from the atmosphere. Especially in large tokamaks, a strong mechanical stress is induced by the high current flowing in the VV, which complicates the design. The inner wall is covered with protection tiles capable of tolerating the thermal stress caused by the direct contact with the plasma edge.

- **Toroidal Field** (**TF**) **coils** : located around the torus they generate the toroidal field (B_ϕ) necessary to confine the plasma (see Fig. 1.4.1). Since the TF is stronger near the tokamak central column ($B_\phi \propto 1/R$, with R the tokamak major radius), the inner part of the tokamak is referred to as High Field Side (HFS) and the outer part Low Field Side (LFS).

- **Poloidal Field** (**PF**) **coils** : they are mainly used to create the PF necessary to impose the plasma equilibrium (see Fig. 1.4.1). Plasma shape and plasma position are controlled by the PF coils.

- **Ohmic** (**OH**) **coils** : located inside the torus in the central column (see Fig. 1.4.1), they produce a variable poloidal field that induces a toroidal electric field in the plasma region and, therefore, the plasma current necessary to create the main PF. The plasma pulse length is mainly limited by the maximum current in the OH coils.

The fuel mixture inside the VV is heated to reach the fusion conditions using several heating schemes:

1.4.0.3 Ohmic heating

Plasma is a conductor and like all conductors is characterized by a non-zero resistivity η. The ohmic input power per unit volume is given by:

$$P_{OH} = \eta j^2 \tag{1.4.1}$$

where j is the plasma current density. Since $\eta \propto T_e^{-3/2}$, the plasma resistivity decreases drastically with temperature. For hot plasmas, the plasma resistivity is similar to that of super-conductors, therefore the efficiency of the ohmic heating is lower at high temperature. Furthermore, the plasma current density is limited upwards by magnetohydrodynamic (MHD) stability limits.

1.4.0.4 Neutral beam heating

Energetic neutral particles can be injected to heat the plasma further. Neutral particles are not sensitive to the magnetic field and can therefore penetrate and reach the plasma core. In the plasma region these energetic particles are ionized and confined by the magnetic field lines. Through Coulomb collisions, they slow down, transferring their energy to the electrons and the ions.

1.4.0.5 Heating by electromagnetic waves

Electromagnetic waves can be efficiently absorbed by the plasma in a tokamak. Depending on their properties, either the electrons or the ions can be heated. Electron Cyclotron Heating (ECH) waves have a frequency that is a multiple of the electron cyclotron frequency. They can be used to heat the electrons in a particular location, given by the intersection of the wave with resonance layer, which depends on the magnetic field.

1.5 A tokamak power plant

The tokamak reactor described in the previous section should be integrated in a more complex structure to produce electricity. Most of these elements are not present in today's tokamak facilities. DEMO will have all the necessary equipment to extract the thermal energy from the plasma and convert it to electricity.

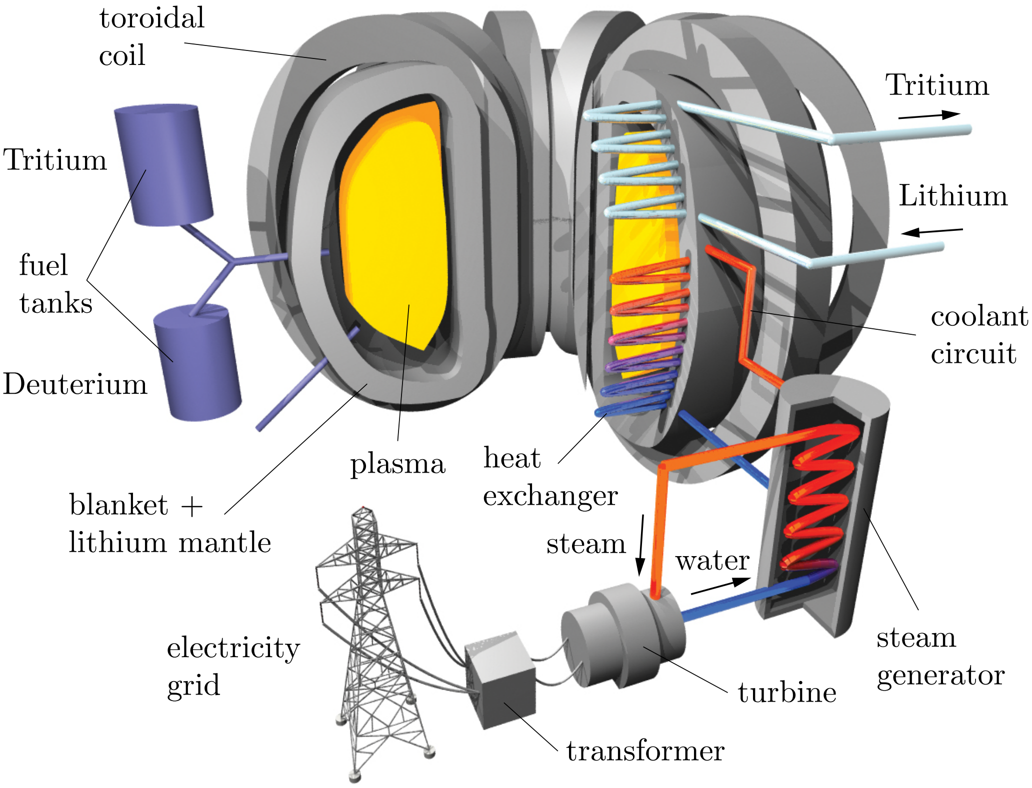

Figure 1.5.1: Main components of a tokamak power plant.

Figure 1.5.1 shows a schematic of a nuclear fusion power plant based on the tokamak concept. The hot plasma is confined with the coil system described in the previous section. Energetic neutrons generated by the fusion reactions in Eq. 1.2.1 are not magnetically confined and are therefore lost towards the first wall. Here, a lithium mantle is present and the tritium is produced by the reactions 1.2.17. The neutrons are slowed down in the blanket, where their kinetic energy is converted to thermal energy. A heat exchanger is then used to transfer the thermal energy to a steam generator and to produce electricity through a turbine in the normal way.

1.6 Motivation and outline of this thesis

This thesis makes a contribution to the understanding of the physics of tokamaks. Several physics questions are experimentally investigated and modeled with a view to a better understanding of the magnetic confinement technique, and in particular of the role of plasma shaping. The shape of a plasma in a tokamak device depends on the geometry of the VV and of the external poloidal magnetic field produced by the PF coils. The performance of a reactor depends strongly on the plasma shape. For example, the maximum value of β, the ratio between the kinetic and magnetic pressures, depends on the plasma elongation [6,7] (ratio between the height and the width of the plasma). The value of β is an indicator of the efficiency of the magnetic confinement technique. The plasma shape also strongly influences the plasma confinement [8]. In high confinement (H-mode) plasmas, variation of the plasma shape can change the pedestal pressure [9] and therefore the confinement time and the pedestal stability. In diverted configurations, the minimum input power to access to a H-mode regime depends on the position of the X-point, i.e. a point where the poloidal magnetic field vanishes.

The aim of the Tokamak à Configuration Variable (TCV) in the Centre de Recherches en Physique des Plasmas (CRPP) is to study the impact of plasma shaping on several aspects of tokamak operation. The flexibility of the machine allows the creation of a wide and unique range of plasma shapes, not achievable in more conventional tokamaks. After more than 15 years of TCV operation, several questions still remain to be answered concerning plasma shaping. This thesis reports on the study of two unconventional and innovative plasma shapes: the doublet plasma and the snowflake divertor. Both configurations have been experimentally studied in the TCV tokamak.

Doublet plasmas are characterized by two plasma currents flowing in the same toroidal direction. As a result of this magnetic equilibrium, a poloidal X-point is present with an internal separatrix. Having an intrinsic zone of negative magnetic shear which does not depend on a hollow current profile, doublets may have an internal transport barrier, equivalent to the H-mode edge barrier. Doublets can therefore add significant new knowledge concerning transport barriers and H-mode physics, and can permit the testing of present models of the L-H mode transition. Doublet plasmas may also provide means of reducing the plasma-wall interaction. If a transport barrier is established at the location of the internal separatrix, a layer of cold plasma (mantle) may be present between the internal separatrix and the Scape-Off Layer (SOL), which is characterized by a high fraction of volumetric losses. The effective power reaching the solid surfaces of the reactor would thus decrease, increasing the lifetime of the tokamak Plasma-Facing Components (PFCs). Moreover, kink/ballooning instabilities, possibly present in the plasma pedestal created at the internal separatrix, may be less problematic since their pulsed ejected power should not directly reach the PFCs due to the attenuation effect given by the volumetric losses in the doublet mantle. Some current could be driven at the internal separatrix ohmically or with ECH. This may simplify the access to the second stability region for high-n ballooning modes. Moreover, the variation of the current density and pressure profiles in a relatively thin plasma layer outside the separatrix may influence the global external kink mode stability and change the β limit. Another advantage of doublet plasmas is given by the smaller vertical growth rate, that is close to a single axis equilibrium equivalent to one half of the doublet both in term of marginal wall position and resistive wall growth rates. Finally, doublet experiments may help in understanding the magnetic reconnection physics, since the process that leads to a creation of an internal separatrix may be the result of a magnetic reconnection phenomenon.

Doublet shaped plasmas were studied at General Atomics for many years. Research in this field was stopped in 1984, when Doublet III was converted to DIII-D. All the properties of the doublet configuration listed above provide a strong motivation to create and study it in the TCV tokamak, the only tokamak worldwide capable of establishing this configuration.

The **snowflake divertor** plasma configuration, also studied in this thesis, is a possible solution to reduce the plasma-wall interaction by acting on the magnetic field topology. The strong potential impact of this configuration is a consequence of the absolute need to find a solution to reduce the overheating of the tokamak walls. Especially in large reactors like ITER, the high localized heat flux can damage the tokamak first wall. Therefore, the necessity to reduce the plasma-wall interaction is considered one of the greatest challenges of tokamak research. The snowflake divertor has been proposed and theoretically studied by Dr. Dmitri Ryutov from the Lawrence Livermore National Laboratory (LLNL). Snowflake plasmas are characterized by a second-order null, where both the poloidal magnetic field and its first spatial derivatives vanish. The second-order null modifies the magnetic topology near the plasma boundary and is therefore expected to affect the edge plasma properties. In particular, the flux expansion around the null point is 2-3 times larger than in the conventional single-null configuration and the connection length in that region increases, reducing the local heat load to the divertor plates. Additionally, the magnetic shear in the edge where an H-mode pedestal would lie is modified, providing a possible way to influence the pedestal stability. Squeezing the flux tubes near the null point may also decouple the turbulence in the divertor legs and in the SOL and affect any radial blob displacement. Moreover, the large flux expansion around the null point should change the prompt losses of ions having turning points in the vicinity of the poloidal field null. The interesting theoretical properties of the snowflake configuration represent a strong motivation for an experimental investigation. The feasibility of this configuration was demonstrated for the *first* time in the TCV tokamak. Dedicated experiments have been carried out to study the properties of this configuration in the H-mode regime. A review of these experimental results is given in this thesis.

This manuscript is organized as follows. Having introduced the magnetic confinement of plasmas and the tokamak concept in this chapter, a more detailed description of TCV is given in **Chapter 2**. TCV is part of the CRPP laboratory, located in Lausanne, Switzerland. The main mission of CRPP is to contribute to the controlled fusion research program towards the development of a fusion reactor. In particular, CRPP is actively involved in the construction of ITER and the design of DEMO.

The bulk of the thesis is then organized in two parts. The first part (**Part I**) of the thesis is devoted to the doublet shaped configuration. To create a doublet plasma, the problem of the double breakdown has to be solved first, developing a good and precise observer of the magnetic configuration inside the VV during ionization. A dedicated chapter is therefore reserved for the magnetic system of TCV (**Chapter 3**). This diagnostic has been calibrated with an original technique, to better reconstruct the magnetic field inside the VV. Moreover, a new set of flux loops have been installed to measure the asymmetric magnetic field. The hardware specifications, the modeling technique and the consequences of the experimental measurements are discussed in Chapter 3. These results have been published in the following peer-reviewed journal article:

> F.Piras, J.-M.Moret and J.X.Rossel, **Measurement of the magnetic field errors on TCV**, *Fusion Eng. Des.*, vol. 85, p. 739, 2010.

Chapter 4 is devoted to the plasma start-up problem. After a general overview of the technique used to create a plasma on TCV, a simple model for the inductive plasma start-up is described. In particular, using the calibration results of Chapter 3, a model to reconstruct the magnetic configuration at the breakdown time has been developed. The last sections of the chapter focus on the assisted plasma start-up with ECH at the second harmonic (X2). Some interesting experimental results are obtained, extremely useful for the double breakdown experiments presented in chapter 5 and for the development of the ITER plasma start-up. These results will be published in the following journal:

> F.Piras et al, **Plasma Start-up on TCV**, *Plasma Phys. Control. Fusion*, to be published

Chapter 5 finally reports the study of the doublet shaped plasma. This chapter theoretically investigates the possibility to create and control a doublet shaped plasma on TCV. Since TCV has not been designed to create this configuration, the establishment of this shape pushes the machine towards its limits, making the creation of a doublet a real challenge. In the last section of the chapter, attempts to create a doublet are illustrated. The study of the doublet configuration will be published as:

> F.Piras et al, **On the Possibility to Create and Control a Doublet Shaped Plasma on TCV**, *Plasma Phys. Control. Fusion*, to be published

The second part of this thesis (**Part II**) deals with the snowflake divertor configuration. **Chapter 6** reports the challenges faced in establishing the configuration. The general properties of a snowflake divertor are described, based on experimental measurements. A dedicated experimental campaign has been conducted to study the properties of a snowflake divertor in the H-mode regime. The results clearly showed a variation of the edge properties compared to a conventional single-null diverted plasma. The results obtained have been published in several peer-reviewed journals and presented in various conferences. In particular:

> F.Piras, S.Coda, I.Furno, J.-M.Moret, R.A.Pitts, O.Sauter, B.Tal, G.Turri, A.Bencze, B.P.Duval, F.Felici, A.Pochelon and C.Zucca, **Snowflake divertor plasmas on TCV**, *Plasma Phys. Control. Fusion*, vol. 51, p. 055009, 2009.

> F.Piras, S.Coda, B.P.Duval, B.Labit, J.Marki, S.Yu.Medvedev, J.-M.Moret, A.Pitzschke and O.Sauter, **"Snowflake" H-mode in a tokamak plasma**, *Phys. Rev. Lett.*, vol. 105, p. 155003, 2010.

> F.Piras, S.Coda, B.P.Duval, B.Labit, J.Marki, S.Yu.Medvedev, J.-M.Moret, A.Pitzschke and O.Sauter, **"Snowflake" Divertor Experiments on TCV**, *Plasma Phys. Control. Fusion*, vol. 52, p. 124010, 2010.

> F.Piras, S.Coda, B.P.Duval, B.Labit, J.Marki, S.Yu.Medvedev, J.-M.Moret, A.Pitzschke and O.Sauter, **"Snowflake" Divertor Experiments on TCV**, *37th EPS Conference, Dublin*, vol. 15, p. 115, 2010 (INVITED TALK).

The specific contributions given by this thesis work are finally summarized in **Chapter 7**, along with conclusions.

Chapter 2

The TCV tokamak

2.1 Introduction

The Tokamak à Configuration Variable (TCV) is a compact, highly elongated tokamak, capable of producing limited or diverted plasmas with currents up to 1 MA [10]. The main aim of TCV is to investigate the effects of plasma shape on tokamak physics and performance.

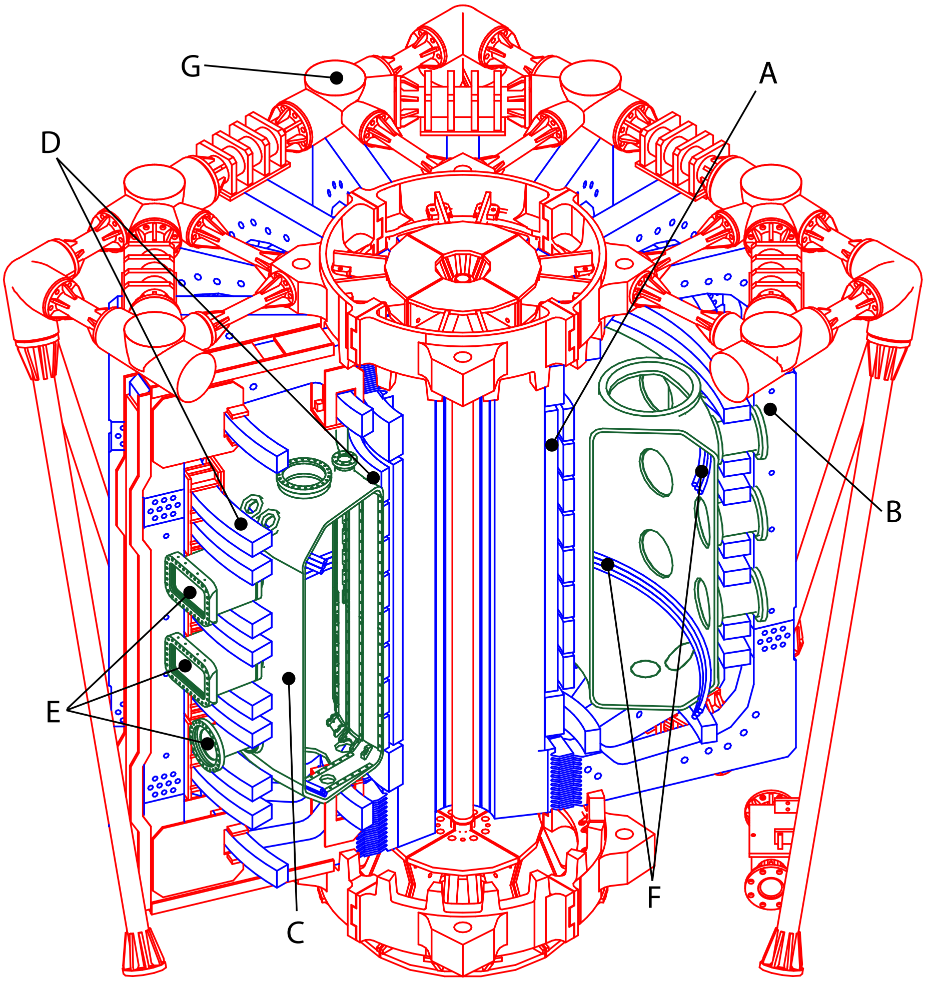

Figure 2.1.1: The TCV tokamak: (A) primary transformer circuit, OH coil; (B) TF coils; (C) the VV; (D) PF coils; (E) diagnostic port; (F) internal coils for plasma vertical stabilization; (G) mechanical support structure.

Parameter	**Symbol**	**Value**
Major radius	R_0	0.88 m
Maximum minor radius	a_0	0.255 m
Internal height of vessel	h	1.5 m
Aspect ratio	$\epsilon = R_0/a$	$2.9 \div 3.6$
Toroidal magnetic field on axis	$B_{\phi 0} = B_\phi(R_0)$	≤ 1.54 T
Plasma current	I_P	≤ 1 MA
Transformer flux	Φ_T	3.4 Vs
Loop voltage	V_{loop}	≤ 10 V
Toroidal vessel resistance	Ω_{VV}	45 mΩ
Vessel time constant	τ_{VV}	6.7 ms
Vessel elongation	κ_{VV}	3
Vessel base vacuum	p_0	$\leq 10^{-7}$ mbar
Pulse duration	T_S	≤ 4 s
Intershot delay	T_D	≥ 400 s
OH heating power	P_{OH}	≤ 1 MW
ECH-X2 heating power	$P_{\mathrm{ECH-X2}}$	≤ 3 MW
ECH-X3 heating power	$P_{\mathrm{ECH-X3}}$	≤ 1.5 MW
Helium cleaning glow discharge	t_G	300 s
Vessel temperature	T_{VV}	≤ 300 °C

Table 2.1: Main parameters of TCV.

Parameter	**Symbol**	**Value**
Plasma width	a_P	≤ 0.48 m
Plasma height	h_P	≤ 1.44 m
Electron density on axis	n_{e0}	$\leq 20 \times 10^{19}$ m^{-3}
Electron temperature (OH) on axis	T_{e0}	≤ 1 keV
Electron temperature (ECH) on axis	T_{e0}	≤ 15 keV
Ion temperature on axis	T_{i0}	≤ 1 keV
Electron plasma frequency	f_{Pe}	$28 \div 120$ GHz
Electron cyclotron frequency	f_{ce}	41 GHz
Ion cyclotron frequency	f_{ci}	11 MHz
Electron Larmor radius	ρ_e	$70 \div 250$ μm
Ion Larmor radius	ρ_i	$2.5 \div 4$ mm
Edge plasma elongation	κ_e	$0.9 \div 2.8$
Edge plasma triangularity	δ_e	$-0.8 \div 1$

Table 2.2: Main plasma parameters.

A sketch of TCV is shown in Fig. 2.1.1. The machine has been designed such that it can produce diverse plasma shapes without requiring hardware modifications. This versatility can easily be achieved for plasmas with moderate elongation, but for highly elongated plasmas a close fitting passive shell becomes necessary, which is clearly in conflict with the idea of variable shape. The design of TCV can be considered as a compromise between maximum shape variability and a good passive vertical stability. The machine appears like a rectangular, strongly elongated torus, with a VV three times higher than wide. TCV produced its first plasma in November 1992, with full

tokamak operation starting in June 1993. Since then, various plasma shapes have been created and controlled, contributing significantly to plasma physics research.
The main TCV and plasma parameters are listed respectively in Tables 2.1 and 2.2.
This chapter describes the main components of the TCV tokamak, reporting on the TCV actuators, diagnostics and shaping capabilities. Sec. 2.4 describes the TCV VV and its electromagnetic model.

2.2 TCV coil system

Figure 2.2.1 represents the TCV poloidal cross-section. Two OH coil circuits are used to create the desired toroidal electric field inside the VV. The first circuit (O1) powers the coil A1; the second circuit (O2) powers the coils B, C and D connected in series. The extreme shaping flexibility of TCV, as discussed in Sec. 2.4.1, is given by the 16 independently powered PF coils (E-F). Each coil is connected to a separate power supply to impose the desired current/voltage. The TF in TCV is created by 16 TF coils connected in series. Each coil is connected through a bus, modeled with the two PF coils T1 and T2. T3 represents the return loop of the connection.

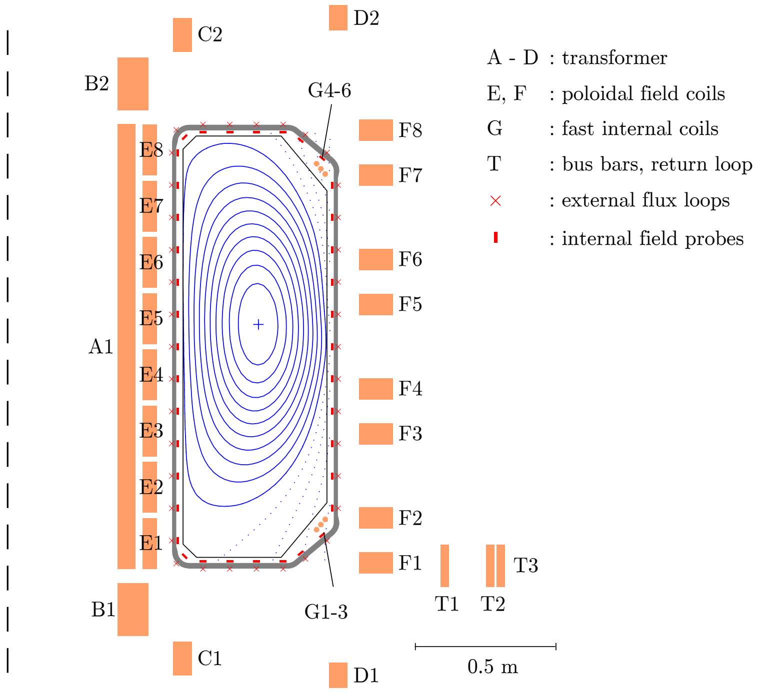

Figure 2.2.1: Poloidal cross-section of TCV. The ohmic coils (A-D), the poloidal field coils (E-F), the fast internal coils (G) and the toroidal field coil connections (T) are represented.

Coils	U [V]	I [kA]
1 x TOR	626	78
2 x OH	1400	31
8 x E	651	7.7
8 x F	1250	7.7

Table 2.3: Characteristics of the 12-phase power rectifiers.

All toroidal and poloidal power supplies on TCV are based on thyristor semiconductors. 12-pulse rectifiers are used to minimize the dead time of the rectifiers. Each thyristor is assembled in a compact six-pulse bridge, 3900A/1800V [11]. The characteristics of the 12-phase power rectifiers are summarized in Table 2.3 for each TCV coil.
The rectifiers are powered by a motor generator with nominal power of 220 MVA, nominal voltage of 10 kV and electric frequency of $96 \div 120$ Hz [12].
Each rectifier can be controlled in three different ways:

- **Current feedback:** The current is controlled by the internal controller and limited at the same time. This mode is used for the control of the TF coils current and also during maintenance tests.

- **Open loop voltage drive:** This is the usual method of driving the PF coils. In this regulation mode there is no preprogrammed current value, but the plasma control system provides voltage reference signals for each power supply. There is a current limitation to avoid over-current.

- **Hybrid mode:** The hybrid mode is a combination of the other two methods. It allows us to preprogram a current reference signal and to override this preprogrammed current with an externally driven voltage.

The vertical stabilization of the most highly elongated TCV plasmas is not possible with the main poloidal power supply system and the external PF coils because of the relatively slow switching time of the thyristors and the shielding effect of the VV. Consequently, a fast power supply is used to supply a low-impedance fast internal coil (G coils in Fig. 2.1.1 and 2.2.1). A pulsed 2000A/560V insulated-gate bipolar transistor (IGBT) power supply is used for this purpose. The switching frequency is typically 10 kHz [13]. A more detailed description of the TCV coil system and their control is given in [14].

2.3 The first wall

Various modifications have been made to the TCV first wall protection elements as experiments have progressed from the start of operations in 1992 to the present time (see Fig. 2.3.1).
In **1992** no tiles were present at the top of the VV. Poloidal bands were present to protect the in-vessel poloidal magnetic field probes. Additionally, a toroidal belt limiter was located in the lower half of the VV. The floor was fully covered with graphite tiles to protect the stainless steel, leading to a first wall carbon coverage of about 50%.
In **1994**, a new set of floor and roof tiles was installed, providing target surfaces for diverted discharges. The first wall carbon coverage reached 65% of the total internal surface area.
The current TCV first wall was installed in **1998** [15]. The outer wall is now almost fully covered with graphite tiles to reduce plasma contamination and increase the flexibility in plasma shaping. The central column tiles were completely redesigned to improve the power handling. The TCV first wall today has 1692 high purity, isotropic, polycrystalline graphite tiles installed, reaching a first wall carbon coverage of about 90% of the total internal surface. To further reduce the plasma contamination, the vessel is sporadically baked out at 250 °C and coated with boron to cover impurities and getter oxygen. The boronisation with a mixture of helium and B_2D_6 creates a 100 nm thick layer by chemical vapor deposition. Between plasma pulses, the chamber is conditioned by glow discharges with helium.

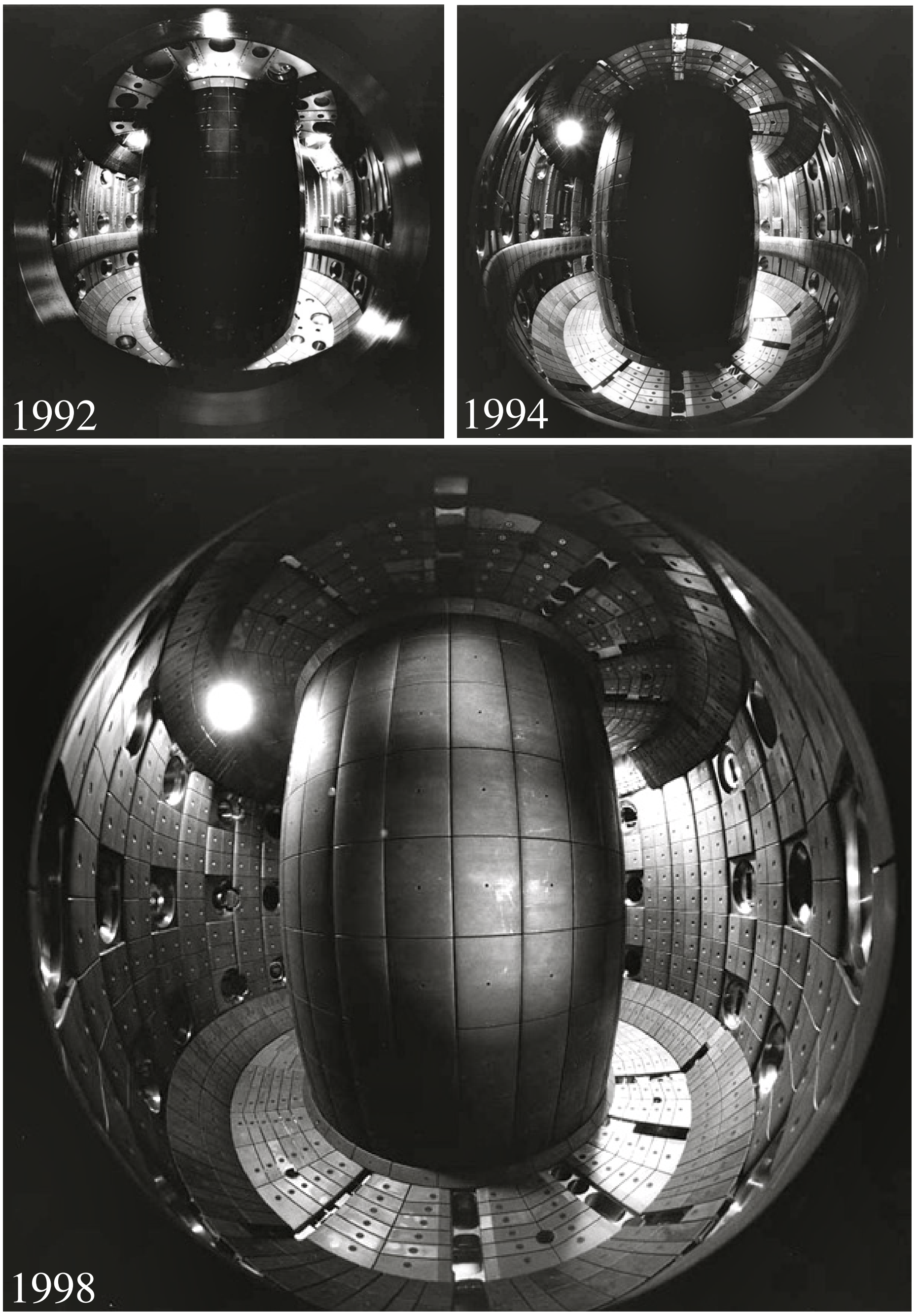

Figure 2.3.1: Fisheye views of the TCV first wall in 1992, 1994 and 1998.

2.4 The vacuum vessel

The TCV VV is continuously welded (no insulating breaks) and has a low toroidal resistance (45 mΩ) for passive stabilization of the plasma vertical motion. Consequently, large vessel currents, up to 200 kA, are induced by the loop voltage which creates a vertical magnetic field inside the VV. A precise model of the electromagnetic properties of the VV is therefore necessary to quantify this magnetic field perturbation. The importance of this passive current estimation is manifold:

- Plasma start-up: breakdown conditions are established by compensating the magnetic field produced by the VV eddy currents acting on the PF coil currents, such that the poloidal field vanishes at the desired breakdown position.

- Magnetic diagnostic interpretation: passive currents flowing in the VV influence the magnetic measurements and the derived plasma parameters.
- Plasma control system: passive currents have also a beneficial stabilizing effect on the vertical plasma position, which is unstable for elongated plasmas. The electromagnetic characterization of the VV is necessary to design effective active plasma position controllers.

The TCV VV is made of stainless steel, 15 mm thick on the side walls and 20 mm thick on the top and bottom. Portholes in the vessel make its electromagnetic modeling difficult. Instead of a complicated 3D representation, a toroidally symmetric model with an experimentally determined spatial distribution of the effective resistivity was chosen [16]. The VV is divided in current filaments $\mathbf{I_v}$ whose circuit equation is:

$$0 = \underline{\underline{R}}_{vv}\mathbf{I_v} + \underline{\underline{M}}_{vv}\dot{\mathbf{I}}_\mathbf{v} + \underline{\underline{M}}_{va}\dot{\mathbf{I}}_\mathbf{a} \tag{2.4.1}$$

where $\underline{\underline{R}}_{vv}$ is the diagonal matrix of the VV filament resistances, based on an experimental estimation [17]. $\underline{\underline{M}}_{vv}$ is the matrix of the mutual inductances between the VV filaments, $\underline{\underline{M}}_{va}$ is the matrix of the Green's functions between the VV filaments and the PF coils, $\mathbf{I_v}$ is the vector of the currents in the the vessel filaments and $\mathbf{I_a}$ is the vector of the currents in the PF coils.
In Appendix B, the filamentary model is used to describe the ITER VV.

2.4.1 Plasma shaping

The 16 independently powered PF coils, the extremely elongated VV fully covered with graphite tiles and the fast internal coils (G coils) provide TCV with a unique plasma shaping flexibility. Figure 2.4.1 gives an example of the multitude of shapes that can be established on TCV. Note in particular the configurations (i) and (n), which will be extensively described in Chapters 5 and 6 respectively.
The plasma shape can be parametrized through the elongation (κ), the triangularity (δ) and the squareness (λ). These parameters are defined from the analytical representation of the Last Closed Flux Surface (LCFS):

$$R = R_0 + a\cos\left[\theta + \delta\sin\theta - \lambda\sin 2\theta\right] \tag{2.4.2}$$
$$z = z_0 + \kappa a\sin\theta \tag{2.4.3}$$

where R is the machine major radius, z the vertical coordinate, θ the poloidal angle, a the plasma minor radius and $[R_0; z_0]$ the coordinate of the plasma magnetic axis.
Plasma shaping is an important parameter that has to be considered to maximize the confinement time and the global plasma performance. Plasma elongation, for example, is very important since the MHD ideal stability limits depend on this parameter. High values of κ allow higher plasma current and therefore higher values of β and confinement [18]. The limit is given by the plasma vertical growth rate, which rises as the elongation is increased. Plasma triangularity can change the plasma radial transport [19, 8] and the pedestal stability in H-mode plasmas.
Even though TCV does not include a dedicated divertor, a strike point can be located more or less everywhere inside the VV and each PF coil can play the role of a divertor coil. Diverted configurations have been successfully established in TCV [20] (see Fig. 2.4.1). The geometry of the divertor modifies the plasma-wall interaction [21], the access to the H-mode and the pedestal stability.

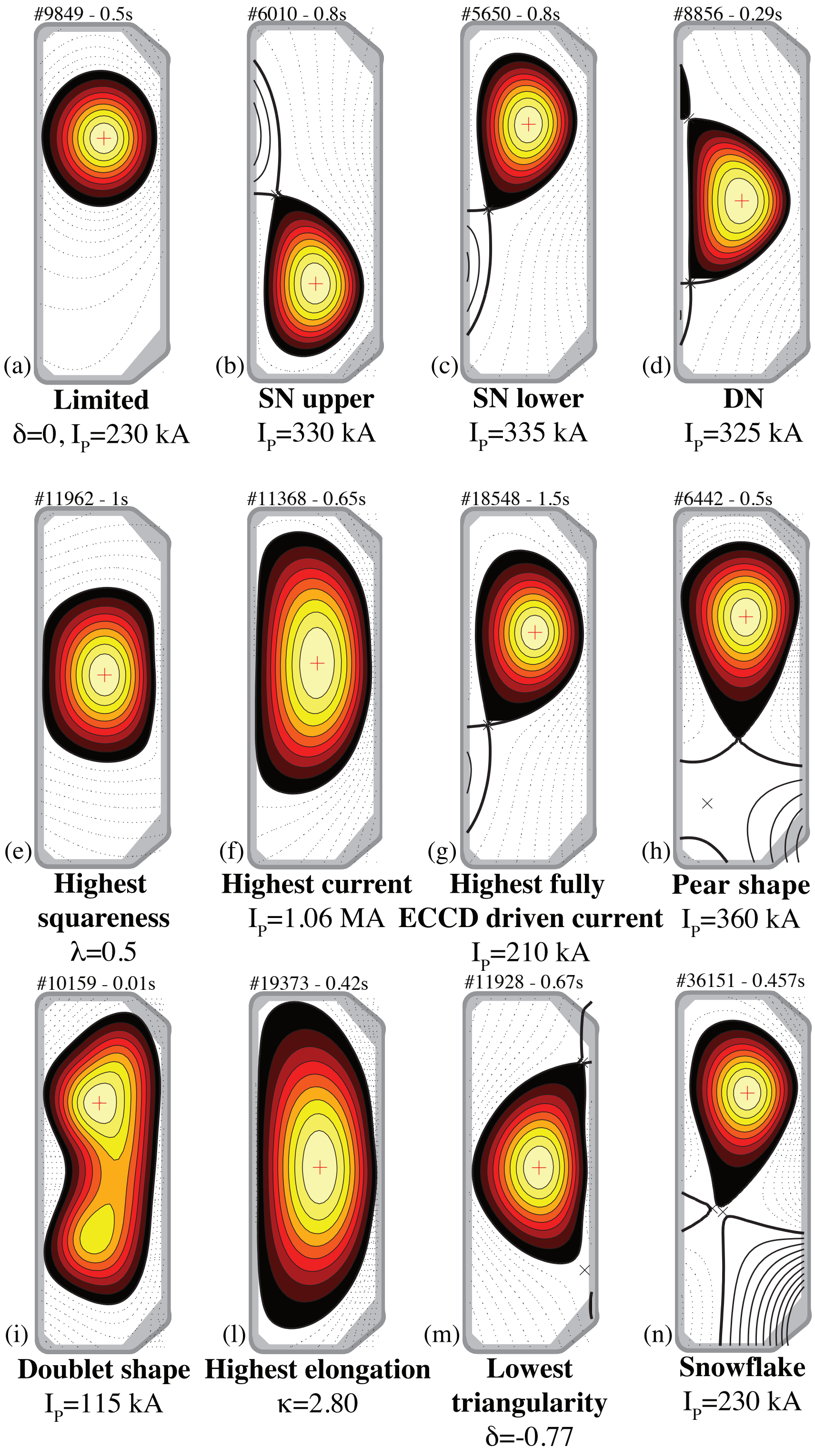

Figure 2.4.1: Plasma shapes achieved on TCV: (a) standard limited configuration, (b) diverted upper single-null, (c) diverted lower single-null, (d) diverted double-null, (e) highest squareness, (f) highest plasma current, (g) highest fully ECCD driven plasma current, (h) pear shaped plasma, (i) doublet shaped configuration (see Chapter 5), (l) highest plasma elongation, (m) lowest plasma triangularity and (n) snowflake divertor configuration (see Chapter 6).

2.4.2 The Electron Cyclotron Heating system

ECH constitutes the only available auxiliary heating system on TCV. 9 gyrotrons are currently installed to inject in the plasma a total power of 4.5 MW. 6 gyrotrons operate at a frequency of 82.7 GHz (ECH-X2), to match the second electron cyclotron harmonic frequency on the plasma axis [22]. 3 further gyrotrons operate at the third electron cyclotron harmonic frequency (118 GHz, ECH-X3). Each gyrotron can be programmed for variable output power during a plasma pulse. The power is injected through 7 launchers located at the top and on the LFS of the VV (see Fig. 2.4.2).

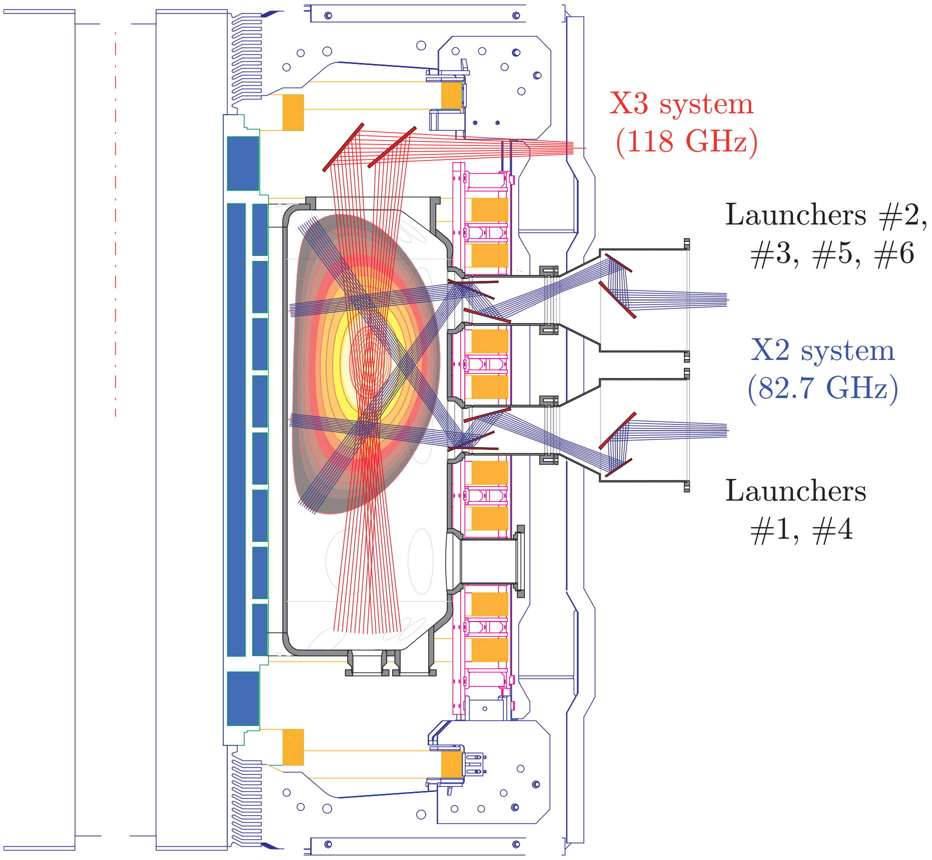

Figure 2.4.2: Poloidal cross-section of TCV and location of the launchers for the second and third harmonic ECH.

Each launcher is steerable in real time in both toroidal and poloidal directions (see Fig. 2.4.3). This allows one to heat plasmas in different poloidal locations during the same discharge. Moreover, changing the toroidal direction of the launchers, the current driven by the ECH-X2 can be changed in real time.

2.4.3 TCV diagnostics

Several diagnostics are installed on TCV to measure the main plasma parameters. A short list of these diagnostics is given in this section:

2.4.3.1 Electron diagnostics

- **DMPX:** The Duplex Multiwire Proportional soft X-ray counter (DMPX) is a 64-channel soft X-ray detector. The detector is made up of two superimposed wire-chambers sensitive to soft X-ray emission with energy between 3 and 30 keV. The lower energy limit can be

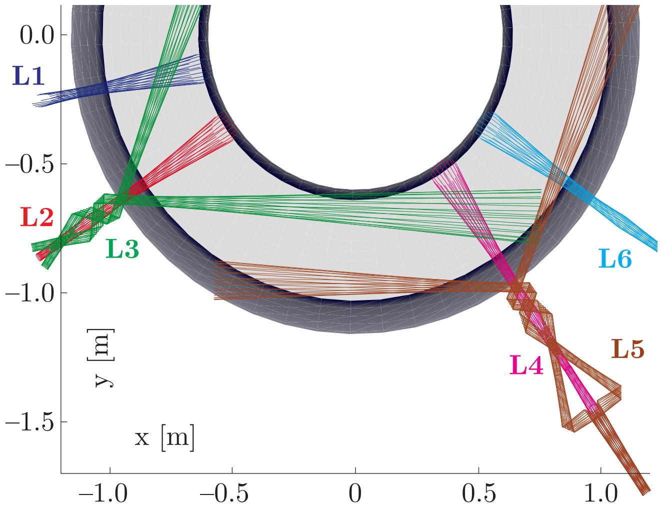

Figure 2.4.3: Toroidal cross-section of TCV and location of the launchers for the second harmonic ECH.

changed by changing the absorber in front of the chambers in between shots. The DMPX has high time and space resolution: the acquisition is performed at 200 kHz and, at the equatorial plane of the TCV VV, the mean distance separating two lines-of-sight is 7.9 mm at the top chamber and 16.3 mm at the bottom. The wirechambers operate in the proportional regime; the measured signal, integrated along the lines-of-sight, is proportional to the mean incident soft X-ray power flux.

- **ECE:** The ECE radiometer is a diagnostic that analyses the Electron Cyclotron Emission generated by the plasma. Its goal is to obtain the radial electron temperature profile on both the HFS and LFS of TCV. Each system (LFS & HFS) has 24 channels. Two horizontal lines-of-sight are installed inside the chamber on the central column at $z = 0$ and $z = 21$ cm. The frequency bandwidth analyzed by the ECE radiometers corresponds to $78 \div 114$ GHz for the HFS and $65 \div 100$ GHz for the LFS systems. Each channel of the ECE radiometers has a width of 750 MHz corresponding to 1 cm spatial resolution in the direction of major radius in the plasma center.

- **FIR:** A 14-channel Mach-Zehnder type interferometer is used to measure the line-integrated density along parallel chords in the vertical direction. The system comprises a FIR (FarInfraRed) laser, pumped by a CO_2 laser, and emitting a continuous wave at 214 μm, and a multi-element detector unit (InSb hot-electron bolometer). The system is fully automated and part of the basic and essential diagnostic set in operation for each TCV shot. The measurement along the central chord is used for real time control of the plasma density.

- **TS:** The Thomson Scattering (TS) system is the main diagnostic for the measurement of the spatial profiles of the electron temperature and density on TCV. The profiles are measured along the line of sight of a laser beam passing through the plasma in the vertical direction at $R = 0.9$ m (mid-radius of the TCV VV). Wide-angle camera lenses collect the scattered light from the observation volumes in the plasma and focus it onto sets of fiber bundles. At present, there are 35 observation positions covering the region from $z = -17$ cm to $z = +66$ cm with a spatial integration length that depends on the channel location. Special channels with higher spatial resolution (integration length 12 mm) are positioned near the top (TS-edge) for observation of the pedestal in H-mode plasmas.

- **XTOMO:** The TCV soft X-ray tomographic system (XTOMO) consists of 10 pinhole cameras at a single toroidal location. Each camera is equipped with a linear array of 20 p-n junction silicon photodiodes resulting in 200 lines of sight covering the whole plasma cross section. Each camera has a 47 micron thick Be filter, allowing the detection of photons with energies between 1 keV and 10 keV, covering the thermal spectrum of most TCV plasmas.

2.4.3.2 Ion diagnostics

- **CXRS:** The Charge eXchange Recombination Spectroscopy (CXRS) diagnostic provides local measurements of ion temperature and impurity density, as well as toroidal and poloidal rotation, through the analysis of spectral moments of impurity line radiation, typically $\mathrm{CVI} - 529.1$ nm. The line is populated by charge exchange (CX) reactions between intrinsic impurity (carbon) and a diagnostic neutral beam (DNB), which is weak enough not to perturb the plasma significantly.

2.4.3.3 Visible and near-visible radiation

- **AXUV:** The AXUV (Absolute eXtreme UltraViolet bolometer cameras) diagnostic consists of two sets of 7 pinhole cameras. Each camera has 20 lines-of-sight, so that 2×140 channels are available in all. The two camera sets have identical geometries, i.e. the corresponding channels in each camera view essentially the same plasma volume. The distribution of the lines-of-sight in a single poloidal cross section is such that tomographic reconstruction of the 2D emission profile is possible.

- **BOLO:** The foil bolometer (BOLO) system consists of 8 pinhole cameras (one top, one bottom and six lateral) each with 8 channels - gold foils which heat up due to the impact plasma radiation and neutral particles. 2D tomographic reconstruction of the total radiated power is possible.

- **FastCam:** A Fast Visible Camera (FastCam) is installed on a TCV equatorial port to tangentially detect the plasma radiation in the visible spectrum. The camera has a very high temporal resolution (up to 250000 fps for a 128×16 pixel array).

- **MultiCam:** MultiCam is a multi-camera system composed of four PCO Pixelfly visible cameras. The light coming from the plasma through relay optics is distributed to the cameras by a series of beam splitters. A filter can be placed in front of each camera. This way each camera observes a specific part of the visible spectrum in the very same volume of the plasma. The imaging frequency of these cameras is 50 fps at full (640×480) resolution.

- **PD:** A set of 18 photodiodes (PDs) are installed on TCV. The signals are amplified onboard to improve the robustness of the transmission. A set of filters is installed in front of the diodes to acquire different lines of the spectrum. 9 PDs have an H_α filter and are installed on the lateral ports. They have a small hole to reduce the view angle. 9 PDs are installed on the top of TCV and they can detect all plasma radiation. They are combined with different filters.

2.4.3.4 Edge diagnostics

- **LP:** A total of 72 Langmuir probes (LP) have been installed on TCV. The system is robust and precise in terms of the stability of the probes to vibrations during operation and has a spatial resolution of 11 mm on the bottom of the chamber and 14 mm on the central column. The TCV Langmuir probes are machined in graphite and are of the domed design with a diameter of 4 mm. The probe head protrudes nominally by only 1 mm beyond the tile surface.

- **TC:** 15 Thermocouples (TCs) are installed in the vessel floor and 4 in the central column. As heat propagation is a slow process, the temperature rise on each thermocouple only starts to be visible several seconds after the shot(s) - hence the information gathered from them is mostly related to the cooling-down of the tile's graphite material (partly radiative, partly by conduction towards the screw at the bottom of the tile).
- **VIR:** The Vertical InfraRed (VIR) diagnostic is a fast infrared camera installed on top of the tokamak. The task of the diagnostic is to observe the heat deposition at the bottom of TCV on a fast time-scale (up to 25 kHz). This is accomplished by analyzing the time evolution of recorded tile surface temperature profiles using knowledge of the physical properties of the tile material in order to infer the heat fluxes that caused those temperatures. The core of the diagnostic is the Thermosensorik CMT256M HS, a camera using a 256 × 256 pixel semiconductor detector with CMT (Cadmium Mercury Telluride) technology. Passing through relay optics consisting of a folding mirror and a number of lenses, the photons emitted from the tile surfaces in the short- to medium wavelength infrared range are detected by the chip, amplified and subsequently digitized on 14 bits.

2.4.3.5 Magnetic diagnostics

The TCV magnetic system is based on 4 arrays of 38 magnetic field probes, 61 flux loops, 24 saddle flux loops and a diamagnetic flux loop. More details concerning the TCV magnetic system and its calibration are given in the next chapter.

Part I

Doublet plasma configuration

Chapter 3

Measurement of the magnetic field errors on TCV

3.1 Introduction

In tokamak devices plasma is confined with a magnetic field. The spatial distribution of the field defines the plasma position, the plasma shape and, in diverted plasmas, the topology of the X-point and the position of the strike points [10, 23, 24]. During the plasma creation, the magnetic structure is a key pre-requisite to obtain a stable and reproducible breakdown [16].

To control the magnetic field distribution, it is important to know precisely the position and the electric current in each coil. Moreover, the real-time control system of the plasma parameters and the magnetic equilibrium reconstruction are mainly based on the magnetic measurements. The quality of the observers used as input for the control system and of the offline magnetic analysis therefore imposes important constraints on the required precision of the magnetic system in a tokamak.

Axisymmetric magnetic field errors, i.e. having a toroidal mode number $n = 0$, lead to a deformation of the plasma shape, incorrect plasma position and degradation of the null point at breakdown. They are due to errors in the radius and vertical position of the PF coils and their measured currents.

Misalignments and deformations of the PF coils cause non-axisymmetric error fields ($n > 0$) [25, 26, 27]. These toroidal asymmetries are often responsible for the creation of magnetic islands inside the plasma and locked modes [28, 29, 30, 31, 32, 33] and therefore reduction of the plasma confinement. During the breakdown, breaking of the toroidal symmetry leads to a reduction of the connection length of the magnetic field lines and the probability to obtain a stable and reproducible breakdown is therefore decreased.

The axisymmetric error field on TCV [10] has been described in detail in [17]. The whole magnetic system has been calibrated and the errors on the radial and vertical position of the PF coils and of the measured currents computed.

A set of 24 saddle flux loops (SLs) is now used on TCV to measure the radial magnetic flux at different toroidal and vertical positions. This new magnetic diagnostic has been implemented in the calibration process described in [17] and is used to obtain the $n = 1$ error field on TCV [34]. The misalignments or tilts of the PF coils are then estimated from the computed error field.

This chapter is organized as follows. The TCV magnetic system, including the SLs, is described in Sec. 3.2. The calibration method is summarized in Sec. 3.3 and the results are discussed in Sec. 3.4. In the last section, the magnetic field inside the VV is computed for a typical TCV discharge.

3.2 The TCV magnetic system

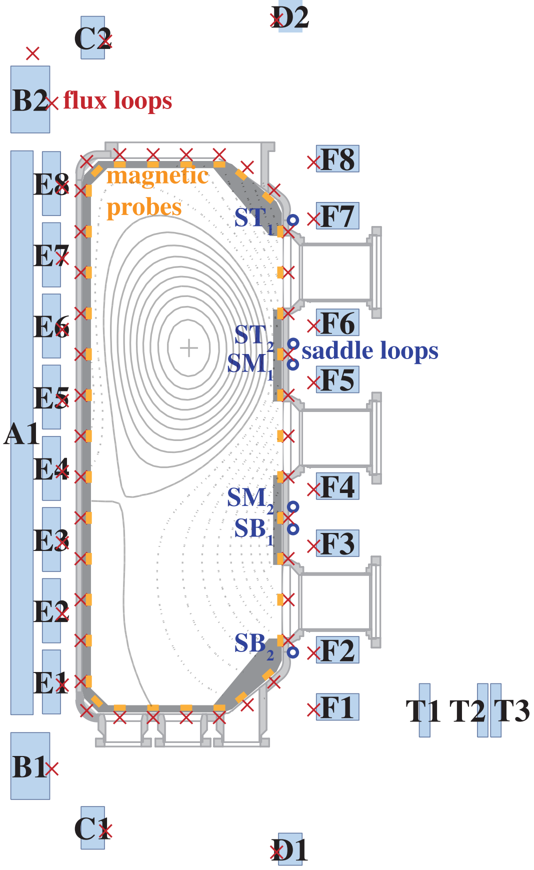

Figure 3.2.1: TCV poloidal cross section with a typical plasma equilibrium showing the ohmic transformer coils A, B, C and D, the shaping coils E and F, the toroidal field coil connections T, the poloidal flux loops (red crosses), the magnetic field probes (orange rectangles) and the saddle flux loops (blue circles).

In Fig. 3.2.1 the cross-section of TCV is shown together with the magnetic sensors. The set of coils used to create and control the plasma has been already described in Sec. 2.2.

The standard magnetic system on TCV is based on 4 poloidal arrays of 38 magnetic field probes measuring the poloidal magnetic field tangential to the VV. These arrays are toroidally separated by 90^o. The signals from two opposite arrays are averaged to cancel the toroidal asymmetries. The poloidal flux is measured on TCV with 61 flux loops placed around the VV and close to the PF coils. Because of the presence of the ports, not all the vessel flux loops have a constant radius. Only a selection of 48 flux loops that do not bypass any port are considered.

The SL system (also shown in Fig. 3.2.1) is comprised of 24 SLs located at three different vertical levels denoted TOP, MIDDLE and BOTTOM, as shown in Fig. 3.2.2. Their vertical extension is given by 6 virtual poloidal flux loops ($\mathrm{ST}_{1,2}$, $\mathrm{SM}_{1,2}$ and $\mathrm{SB}_{1,2}$ in Fig. 3.2.2). Each of them cover a toroidal angle of 45°, corresponding to an extension of two TCV sectors. They are made of one turn of 1 mm diameter mineral insulated coaxial wire (THERMOCOAX®) and they are fixed to the outer surface of the VV. On each SL, the induced voltage is proportional to the first time-derivative of the radial magnetic flux enclosed by the SL surface:

$$v_{SL} = -\frac{\mathrm{d}\psi_{SL}}{\mathrm{d}t} = -\int_{\Omega_{SL}} \dot{\mathbf{b}}\,\mathrm{d}\mathbf{\Omega} \tag{3.2.1}$$

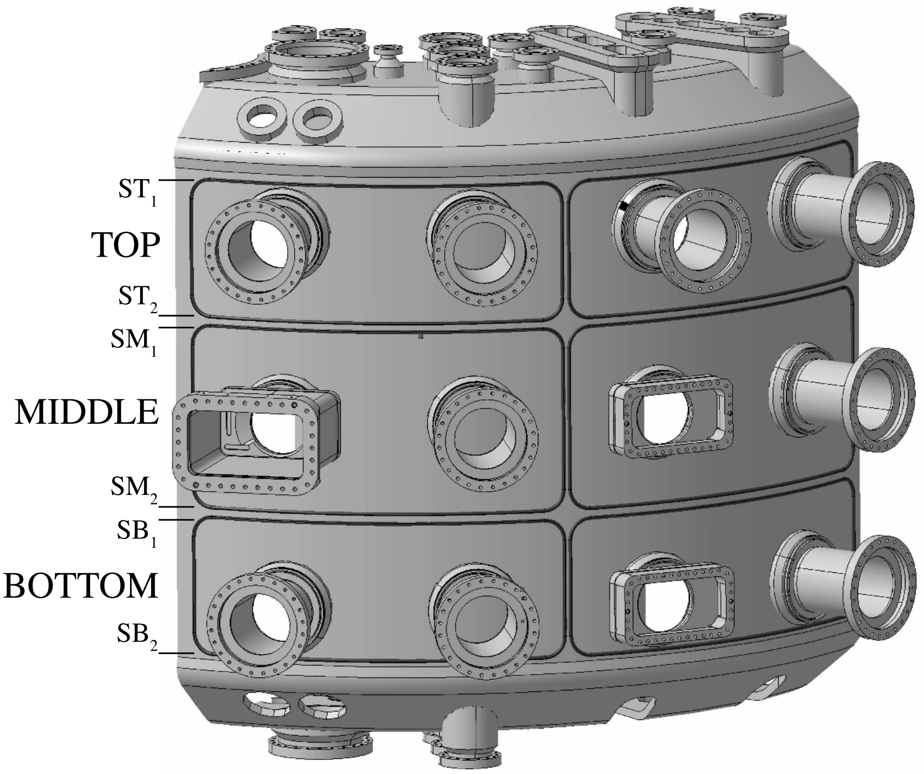

Figure 3.2.2: SLs location around the TCV VV. Each SL covers two sectors toroidally and is vertically delimited by the virtual poloidal flux loops $\mathrm{ST}_{1,2}$, $\mathrm{SM}_{1,2}$ and $\mathrm{SB}_{1,2}$. They are located at three vertical positions (TOP, MIDDLE and BOTTOM).

where ψ_{SL} is the flux in the SL, $\dot{\mathbf{b}}$ is the first time-derivative of the magnetic field and Ω_{SL} is the SL surface.

Each SL signal is pre-amplified near the machine to limit the impact of the long transmission line. They are then either amplified to be used as time derivatives of the magnetic flux or integrated to obtain the flux itself. An over-voltage protection is inserted between the pre-amplifiers and the amplifiers to protect the circuits against spikes induced by the plasma dynamics. The resulting signals are then filtered and acquired or used by the real time control system. A different filter is used by the real time shape and position control with a higher cut-off frequency to avoid a too large phase lag that would impair fast instability feedback.

The block diagram of the signal processing is shown in Fig. 3.2.3. All the electronic devices have been calibrated offline using the method previously described in [17].

3.3 The calibration method

The magnetic field error in TCV is evaluated using an extension of the procedure explained in [17]. In this section, the method is summarized emphasizing the new features introduced by the SL signals.

Each PF coil is separately powered with a given current. The typical wave form used has a flattop of 20 kA for the ohmic coils (O1 and O2) and the TF coils and 4 kA for the other coils (E and F). During the flattop phase, the current is controlled within 10 A for 1 s. The stationary phase is longer than the VV time constant (∼ 13.4 ms) to ensure that the eddy currents in the VV and in the mechanical structures vanish. For each powered coil, all the magnetic signals are acquired and time averaged on the flattop phase to reduce the noise and the statistical error.

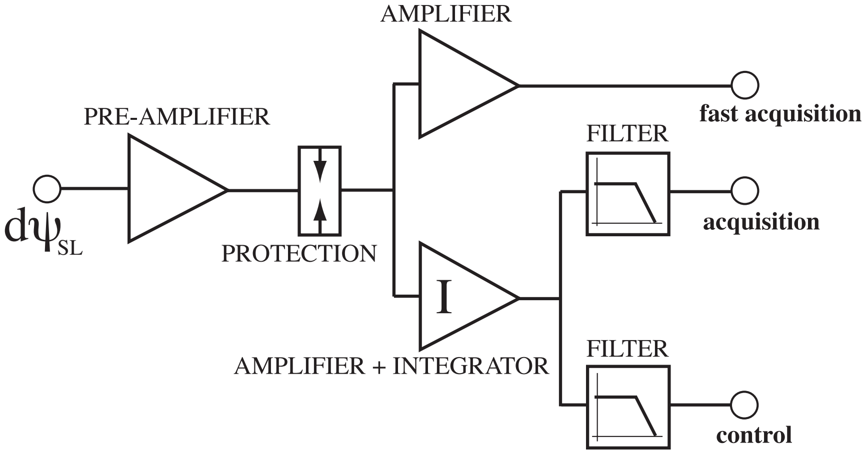

Figure 3.2.3: Block diagram of the electronic circuit used to acquire the SL signals.

The measured quantities are then compared with the expected values, yielding the vector of the differences between the experimental values and the theoretical predictions:

$$\mathbf{\Delta\Psi}_f = \mathbf{\Psi}_f - \underline{\underline{\mathbf{M}}}_{fc}\mathbf{I_c} \tag{3.3.1}$$

$$\mathbf{\Delta b}_m = \mathbf{b}_m - \underline{\underline{\mathbf{B}}}_{mc}\mathbf{I_c} \tag{3.3.2}$$

$$\mathbf{\Delta\Psi}_s = \mathbf{\Psi}_s - \underline{\underline{\mathbf{M}}}_{sc}\mathbf{I_c} \tag{3.3.3}$$

$\mathbf{\Psi}_f$, $\mathbf{b}_m$ and $\mathbf{\Psi}_s$ are the vectors of the measured quantities in the flux loops, magnetic probes and SLs respectively; $\underline{\underline{\mathbf{M}}}_{fc}$, $\underline{\underline{\mathbf{B}}}_{mc}$ and $\underline{\underline{\mathbf{M}}}_{sc}$ are the matrices of the Green's functions between the coils and the considered sensors and $\mathbf{I_c}$ is the vector of the coil currents. Notice that $\mathbf{I}_c = \underline{\underline{\mathbf{T}}}_{ca}\mathbf{I}_a$, where $\mathbf{I}_a$ is the current in the combined PF circuits and $\underline{\underline{\mathbf{T}}}_{ca}$ is the transfer matrix used to obtain the current in each coil from the current in each circuit. In the same manner $\underline{\underline{\mathbf{M}}}_{fa} = \underline{\underline{\mathbf{M}}}_{fc}\underline{\underline{\mathbf{T}}}_{ca}$, where $\underline{\underline{\mathbf{M}}}_{fa}$ is the matrix of the Green's functions between the PF coil systems and the flux loops. Similarly $\underline{\underline{\mathbf{B}}}_{ma} = \underline{\underline{\mathbf{B}}}_{mc}\underline{\underline{\mathbf{T}}}_{ca}$ and $\underline{\underline{\mathbf{M}}}_{sa} = \underline{\underline{\mathbf{M}}}_{sc}\underline{\underline{\mathbf{T}}}_{ca}$.
The difference between the measured quantities and the expected values in Eqs. 3.3.1-3.3.3 is due to the errors in the geometrical characteristics of the PF coils, in the magnetic sensors and in the electronic devices used to acquire the signals.
Mathematically, this discrepancy can be expressed by a first order Taylor expansion as follow:

$$\begin{aligned}\mathbf{\Delta\Psi}_f = &\Big(\underline{\underline{\mathbf{M}}}_{fa}\mathbf{\Delta G_a} + \frac{\partial\underline{\underline{\mathbf{M}}}_{fc}}{\partial R_c}\mathbf{\Delta R_c}\underline{\underline{\mathbf{T}}}_{ca} + \frac{\partial\underline{\underline{\mathbf{M}}}_{fc}}{\partial Z_c}\mathbf{\Delta Z_c}\underline{\underline{\mathbf{T}}}_{ca}\\ &+\underline{\underline{\mathbf{M}}}_{fc}\frac{\partial\underline{\underline{\mathbf{T}}}_{ca}}{\partial\beta_T}\mathbf{\Delta}\beta_\mathbf{T} + \mathbf{\Delta G_f}\underline{\underline{\mathbf{M}}}_{fa}\\ &+\mathbf{\Delta R_f}\frac{\partial\underline{\underline{\mathbf{M}}}_{fa}}{\partial R_f} + \mathbf{\Delta Z_f}\frac{\partial\underline{\underline{\mathbf{M}}}_{fa}}{\partial Z_f}\Big)\mathbf{I}_a\end{aligned} \tag{3.3.4}$$

$$\begin{aligned}\mathbf{\Delta b}_m = &\Big(\underline{\underline{\mathbf{B}}}_{ma}\mathbf{\Delta G_a} + \frac{\partial\underline{\underline{\mathbf{B}}}_{mc}}{\partial R_c}\mathbf{\Delta R_c}\underline{\underline{\mathbf{T}}}_{ca} + \frac{\partial\underline{\underline{\mathbf{B}}}_{mc}}{\partial Z_c}\mathbf{\Delta Z_c}\underline{\underline{\mathbf{T}}}_{ca}\\ &+\underline{\underline{\mathbf{B}}}_{mc}\frac{\partial\underline{\underline{\mathbf{T}}}_{ca}}{\partial\beta_T}\mathbf{\Delta}\beta_\mathbf{T} + \mathbf{\Delta G_m}\underline{\underline{\mathbf{B}}}_{ma} + \mathbf{\Delta R_m}\frac{\partial\underline{\underline{\mathbf{B}}}_{ma}}{\partial R_m}\\ &+\mathbf{\Delta Z_m}\frac{\partial\underline{\underline{\mathbf{B}}}_{ma}}{\partial Z_m} + \mathbf{\Delta}\alpha_\mathbf{m}\frac{\partial\underline{\underline{\mathbf{B}}}_{ma}}{\partial\alpha_m}\Big)\mathbf{I}_a\end{aligned} \tag{3.3.5}$$

$$\begin{aligned}\boldsymbol{\Delta\Psi}_s \quad = & \Big(\underline{\underline{\underline{\mathbf{M}}}}_{sa}\mathbf{\Delta G_a} + \frac{\partial \underline{\underline{\underline{\mathbf{M}}}}_{sc}}{\partial R_c}\mathbf{\Delta R_c}\underline{\underline{\underline{\mathbf{T}}}}_{ca} + \frac{\partial \underline{\underline{\underline{\mathbf{M}}}}_{sc}}{\partial Z_c}\mathbf{\Delta Z_c}\underline{\underline{\underline{\mathbf{T}}}}_{ca} \\ & + \frac{\partial \underline{\underline{\underline{\mathbf{M}}}}_{sc}}{\partial X_c}\mathbf{\Delta X_c}\underline{\underline{\underline{\mathbf{T}}}}_{ca} + \frac{\partial \underline{\underline{\underline{\mathbf{M}}}}_{sc}}{\partial Y_c}\mathbf{\Delta Y_c}\underline{\underline{\underline{\mathbf{T}}}}_{ca} \\ & + \frac{\partial \underline{\underline{\underline{\mathbf{M}}}}_{sc}}{\partial \alpha_{cx}}\mathbf{\Delta}\alpha_{\mathbf{cx}}\underline{\underline{\underline{\mathbf{T}}}}_{ca} + \frac{\partial \underline{\underline{\underline{\mathbf{M}}}}_{sc}}{\partial \alpha_{cy}}\mathbf{\Delta}\alpha_{\mathbf{cy}}\underline{\underline{\underline{\mathbf{T}}}}_{ca} \\ & + \underline{\underline{\underline{\mathbf{M}}}}_{sc}\frac{\partial \underline{\underline{\underline{\mathbf{T}}}}_{ca}}{\partial \beta_T}\mathbf{\Delta}\beta_{\mathbf{T}} + \mathbf{\Delta G_s}\underline{\underline{\underline{\mathbf{M}}}}_{sa} + \mathbf{\Delta R_s}\frac{\partial \underline{\underline{\underline{\mathbf{M}}}}_{sa}}{\partial R_s} \\ & + \mathbf{\Delta Z_s}\frac{\partial \underline{\underline{\underline{\mathbf{M}}}}_{sa}}{\partial Z_f}\Big)\mathbf{I}_a\end{aligned} \qquad (3.3.6)$$

In the Eqs. 3.3.4-3.3.6, $\mathbf{\Delta G_a}$, $\mathbf{\Delta G_f}$, $\mathbf{\Delta G_m}$ and $\mathbf{\Delta G_s}$ are calibration errors in the PF circuit currents, the flux loops, the magnetic field probes and the SLs; $\mathbf{\Delta}\beta_{\mathbf{T}}$ is the variation of the current distribution in the T coils; $\mathbf{\Delta R_c}$ and $\mathbf{\Delta Z_c}$ are the errors in the radius and in the vertical position of the PF coils; $\mathbf{\Delta R_f}$, $\mathbf{\Delta Z_f}$, $\mathbf{\Delta R_m}$, $\mathbf{\Delta Z_m}$, $\mathbf{\Delta R_s}$ and $\mathbf{\Delta Z_s}$ are the errors in the position of the flux loops, magnetic probes and the virtual flux loops used to characterize the SLs (see Fig. 3.2.1 - 3.2.2); $\mathbf{\Delta}\alpha_{\mathbf{m}}$ is the error in the orientation of the magnetic probes; $\mathbf{\Delta X_c}$ and $\mathbf{\Delta Y_c}$ are the shifts of the PF coils along the X axis and the Y axis and $\mathbf{\Delta}\alpha_{\mathbf{cx}}$ and $\mathbf{\Delta}\alpha_{\mathbf{cy}}$ the tilts around the same axis (see Appendix A).

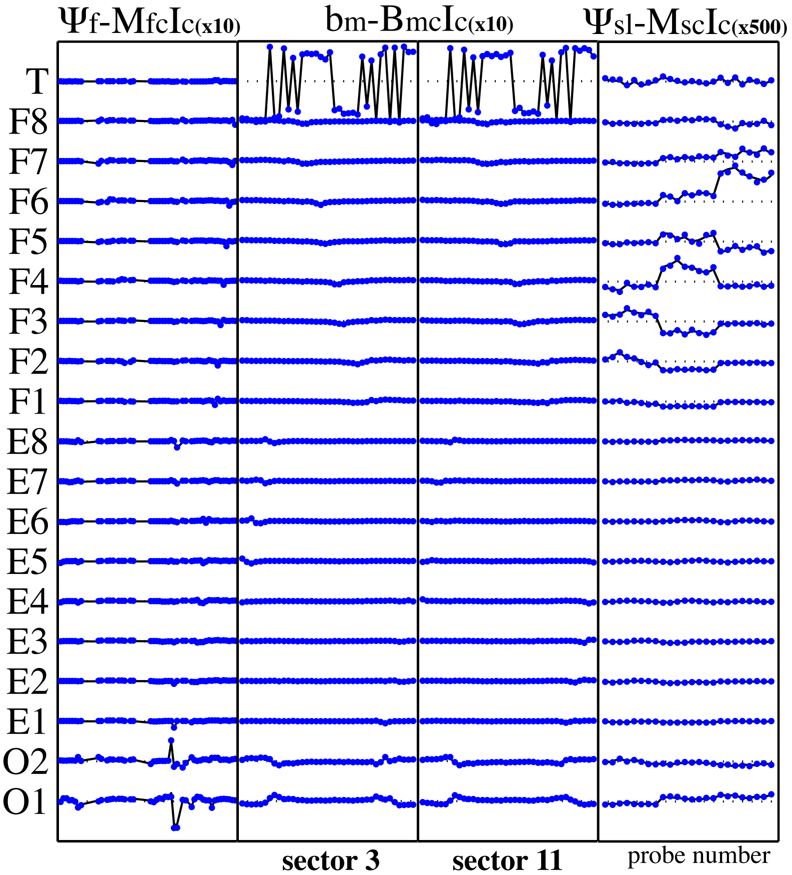

Figure 3.3.1: Differences between the measured magnetic quantities and the theoretical predictions for each coil as a function of the considered sensor. The blue dots show the differences with the measurements as defined in Eqs. 3.3.1-3.3.3, the solid lines are the differences computed from the derived errors on the calibration and the location of the magnetic signals, as in Eqs. 3.3.4-3.3.6 (black line).

Each of the error parameters produce a difference between the measured quantities and the expected values that is estimated as a first-order expansion of the related Green's function with respect to the considered parameter.

The discrepancies found in Eqs. 3.3.1-3.3.3 are used as an input for the system of Eqs. 3.3.4-3.3.6. The error parameters are then estimated by inverting the system. This estimation can then be used as a set of correction factors for the geometrical and calibration parameters. Even if they represent a large number of parameters, ($\mathbf{\Delta G_a}^{1\times19}$, $\mathbf{\Delta R_c}^{1\times26}$, $\mathbf{\Delta Z_c}^{1\times26}$, $\mathbf{\Delta X_c}^{1\times26}$, $\mathbf{\Delta Y_c}^{1\times26}$, $\boldsymbol{\Delta\alpha}_{\mathbf{cx}}{}^{1\times26}$, $\boldsymbol{\Delta\alpha}_{\mathbf{cy}}{}^{1\times26}$, $\mathbf{\Delta G_m}^{1\times76}$, $\mathbf{\Delta R_m}^{1\times76}$, $\mathbf{\Delta Z_m}^{1\times76}$, $\boldsymbol{\Delta\alpha}_{\mathbf{m}}{}^{1\times76}$, $\mathbf{\Delta G_f}^{1\times48}$, $\mathbf{\Delta R_f}^{1\times48}$, $\mathbf{\Delta Z_f}^{1\times48}$, $\mathbf{\Delta G_s}^{1\times24}$, $\mathbf{\Delta R_s}^{1\times6}$, $\mathbf{\Delta Z_s}^{1\times6}$, $\boldsymbol{\Delta\beta}_{\mathbf{T}}{}^{1\times1}$: 660 parameters in total), the inversion of the system is feasible since typically each signal must be corrected for 3 or 4 parameters but provides 19 independent measurements, one from each powered PF circuit, giving a total number of 3173 measurements ($\mathbf{\Psi}_f^{48\times19}$, $\mathbf{b}_m^{76\times19}$, $\mathbf{\Psi}_s^{24\times19}$ and $\mathbf{I}_c^{19\times19}$).

The correction parameters are determined in the least square sense by minimizing a cost function combining the residual errors:

$$\begin{aligned}\chi^2 &= \textstyle\sum_{f,k} w_{\Psi_f}^2 \Delta\Psi_{fk}^2 + \sum_{m,k} w_{b_m}^2 \Delta b_{mk}^2 \\ &+ \textstyle\sum_{s,k} w_{\Psi_s}^2 \Delta\Psi_{mk}^2 + \sum_p w_p^2 \Delta P_p^2\end{aligned} \tag{3.3.7}$$

where k is the data point index and $w_{\Psi_f}^2$, $w_{b_m}^2$ and $w_{\Psi_s}^2$ are weights, set to the inverse of the uncertainty of the considered measurement. To obtain a solution compatible with the expected values of the corrections, the results of the off-line calibration and the known position of the coils and sensors have to be added to the minimization process. This is done with the last term in Eq. 3.3.7, where P_p is the considered parameter and w_p^2 is the corresponding weight, chosen to be the inverse of the expected error.

The results of this minimization process are shown in Fig. 3.3.1, where the differences between the measured quantities and the expected values computed from Eqs. 3.3.1-3.3.3 (blue dots) are compared to the differences computed from the Eqs. 3.3.4-3.3.6, using the derived corrections in the calibration and the location of the magnetic signals (black line). The good agreement between the two traces verifies the corrections of the parameters obtained from the minimization process. The only source of non-axisymmetric errors in Eq. 3.3.6 is the wrong alignment of the PF coils. Therefore, the computed asymmetric error is only due to the misalignment between the PF coils and the VV where the SLs are mounted. This corresponds to the real non-axisymmetric error only if the VV is aligned with the TF produced by the TF coils. Unfortunately, since the TF around the VV is not measured, it is not possible to verify this assumption. Nevertheless, the mechanical uncertainty on the position of the TF coils with respect to the VV is of the order of a millimeter.

3.4 Poloidal field coil irregularities

The solution of Eq. 3.3.7 described above and its consequences are detailed in this section.

In Fig. 3.3.2, the axisymmetric $n = 0$ errors in the PF coils (ΔG_a, ΔR_c and ΔZ_c) are plotted together with the $n = 1$ position errors (ΔX_c, ΔY_c, $\Delta E_c = \sqrt{\Delta X_c^2 + \Delta Y_c^2}$, $\Delta\alpha_{cx}$ and $\Delta\alpha_{cy}$). The error on the position of the PF coils is a few millimeters. Only coils C and D have a larger error ($\sim$ 2 cm). The position of the central column, where the A and E coils are located, seems to be shifted by 5 mm with respect to the VV. The E coils are also all shifted relative to the VV, suggesting the possibility of a tilt between the central column and the VV of 0.25^o.

The error bars of the estimated errors are different for each parameter and each PF coil. This is due to the non-uniform coupling between the PF coils and the magnetic sensors and the different sensitivity of the considered parameter.

The variation of flux on the SLs due to a shift of a PF coil in the X direction or a tilt around the X axis is plotted for each coil in Fig. 3.4.1. The flux variation due to a tilt of a coil is smaller than the one created by a rigid movement in one direction, consequently the error bars for the parameters

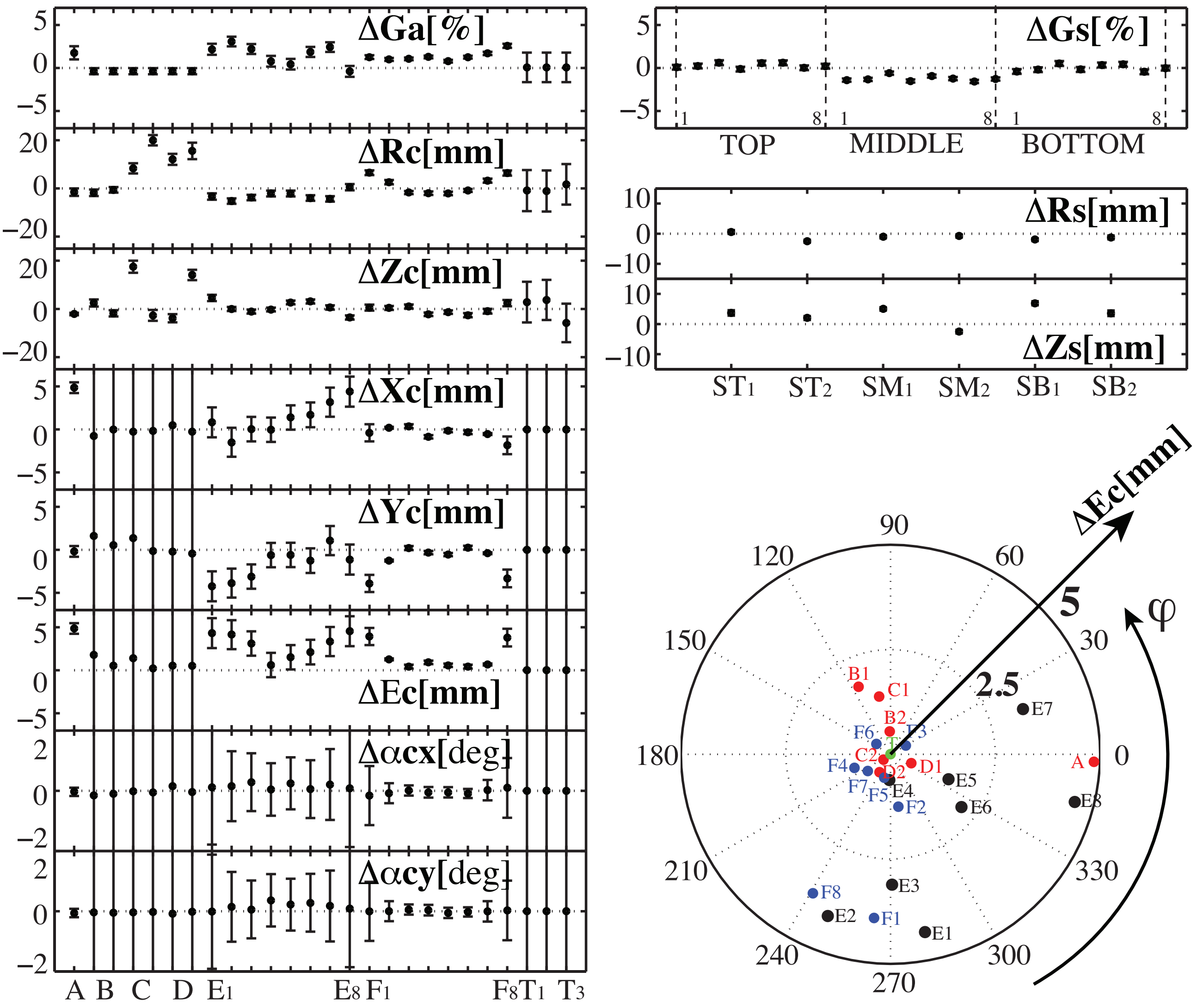

Figure 3.3.2: Corrections for the coil current calibration, the coil location, the SL calibration and their location.

$\Delta\alpha_{cx}$ and $\Delta\alpha_{cy}$ in Fig. 3.3.2 are larger. The different order of magnitude between the flux induced by the E coils and the F coils (note that the data for the F coils has been scaled by a factor 0.1 to fit on the plot) justifies the larger error bars of the E coils. The F coils are closer to the SLs and therefore are better coupled with them. The error bars for the O2 and the TF coil systems are even larger because besides the small coupling with the SLs, it is not possible to measure the effect of each single coil but only the magnetic field produced by the current distribution in the considered coil system. Notice that due to the large distance between the O2, the TF coils and the plasma region, the $n = 1$ error field induced by their misalignment is relatively small (see Fig. 3.4.2).

On the right side of Fig. 3.3.2, the error on the SLs is plotted. The first plot is the error on the gain of each loop (ΔG_s). This is due to the calibration error of the amplifiers and to a wrong estimation of the toroidal extension of the SLs. The error of the radial and vertical position of the virtual poloidal flux loops (ΔR_s and ΔZ_s) is also shown in Fig. 3.3.2.

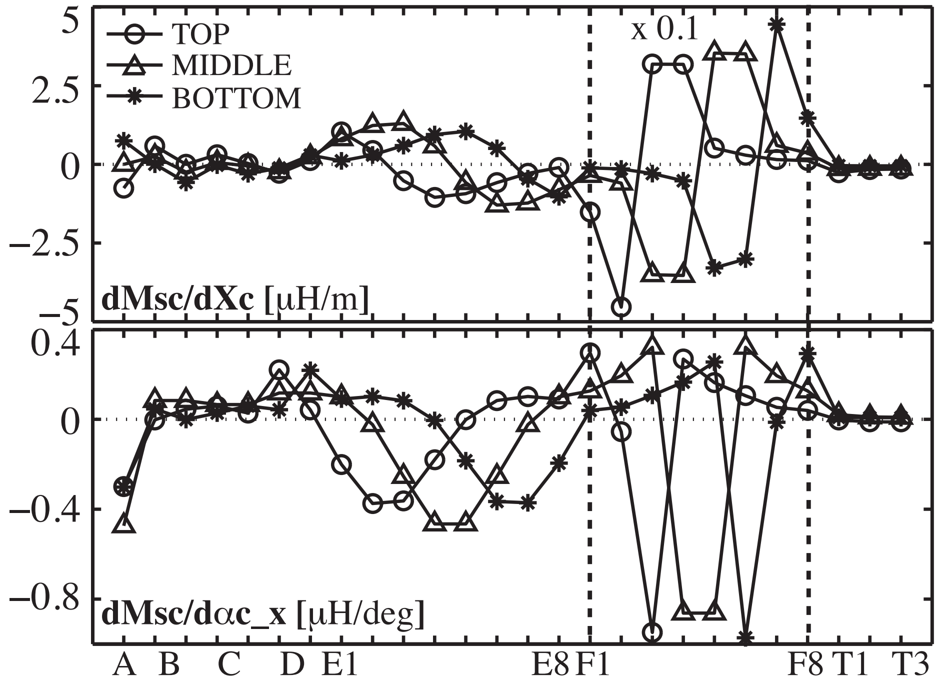

Figure 3.4.1: Variation of flux in the SLs due to a shift of a coil in the X direction or a tilt around the X axis (note that the data for the F coils has been scaled by a factor 0.1 to fit on the plot).

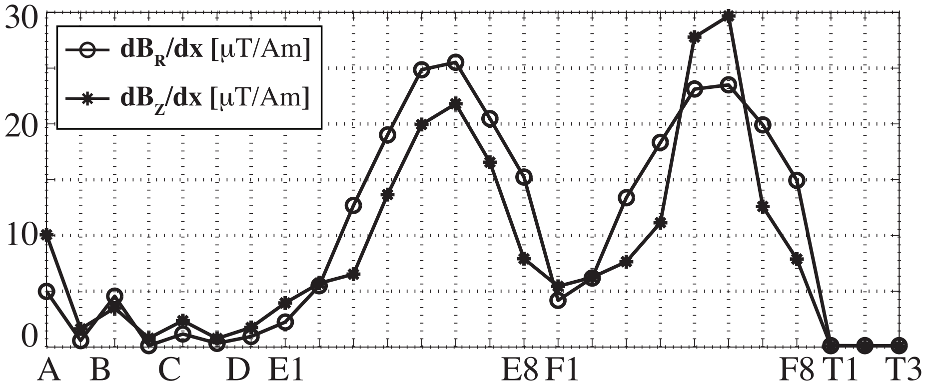

Figure 3.4.2: Absolute value of the radial and vertical $n = 1$ error field per unit current and displacement of the PF coils averaged on the plasma region.

3.5 Magnetic field error

The errors on the PF coils current calibration (ΔG_a in Fig. 3.3.2) and on their radial and vertical position (ΔR_c and ΔZ_c in Fig. 3.3.2) lead to an aximmetric $n = 0$ error field inside the VV. Its spatial distribution depends on the currents in the PF coils. In Fig. 3.5.1 (left), the radial and vertical $n = 0$ error field is plotted for a typical TCV discharge. In Fig. 3.5.2 (left) the same error field distribution is shown at the breakdown time.

The non-aximmetric $n = 1$ error field is computed from the shift and tilt irregularities of the PF coils (ΔX_c, ΔY_c, $\Delta\alpha_{cx}$ and $\Delta\alpha_{cy}$ in Fig. 3.3.2). In Fig. 3.5.1 (right) and in Fig. 3.5.2 (right), the distribution of the $n = 1$ error field is represented for a TCV discharge and at the breakdown time.

Both the $n = 0$ and the $n = 1$ error fields are of the order of few mT and they are stronger in the proximity of the PF coils. At the breakdown time, the $n = 0$ error field is responsible for a variation of the magnetic configuration and the $n = 1$ error field may reduce the connection

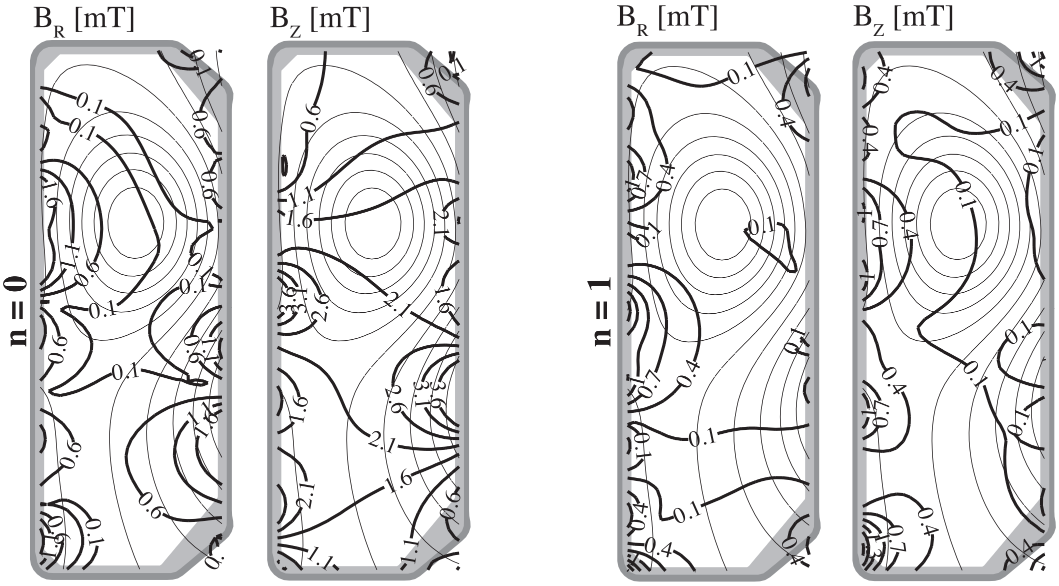

Figure 3.5.1: Radial and vertical $n = 0$ (left) and $n = 1$ (right) error field distribution inside the VV for a typical TCV discharge (shot #39109, 0.6 s).

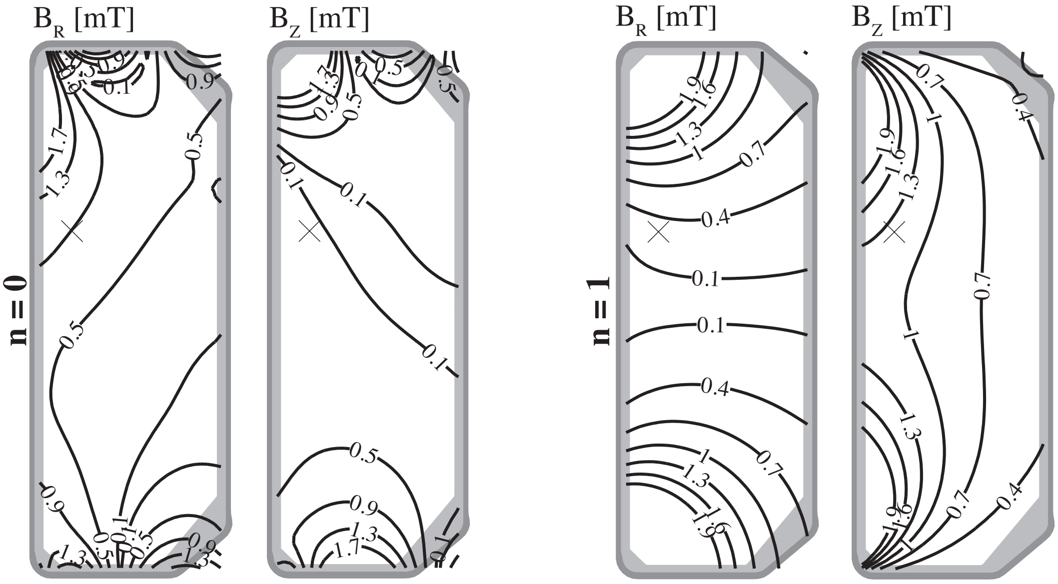

Figure 3.5.2: Radial and vertical $n = 0$ (left) and $n = 1$ (right) error field distribution inside the VV for a typical TCV breakdown (shot #39109, 0 s). The point marked with a cross is the breakdown position.

length in the null point region, where the magnetic field is smaller than 1 mT. However, at the breakdown time the magnetic field is strongly perturbed by the eddy currents induced in the VV and in the magnetic structure ($\sim$ 20 mT). The distribution of the error field at the breakdown time in Fig. 3.5.2 is only representative of the PF coils contribution.

In order to estimate the topological effect of the error field on the magnetic equilibrium, the $n = 1$ vacuum error field distribution inside the VV is added to the equilibrium magnetic field. The resulting magnetic field configuration is illustrated by a Poincaré plot obtained by following a set of field lines and tracing their position after each toroidal turn (Fig. 3.5.3). An $n = 1, m = 1$ magnetic island is created at the normalized radius $\rho \sim 0.65$ (m being the poloidal mode number). The other $n = 1, m > 1$ modes are also present, but they have a smaller amplitude. Ergodization due to islands overlapping is present only at the very edge.

The main components of the $n = 1$ magnetic field error can be corrected by applying an asymmetric

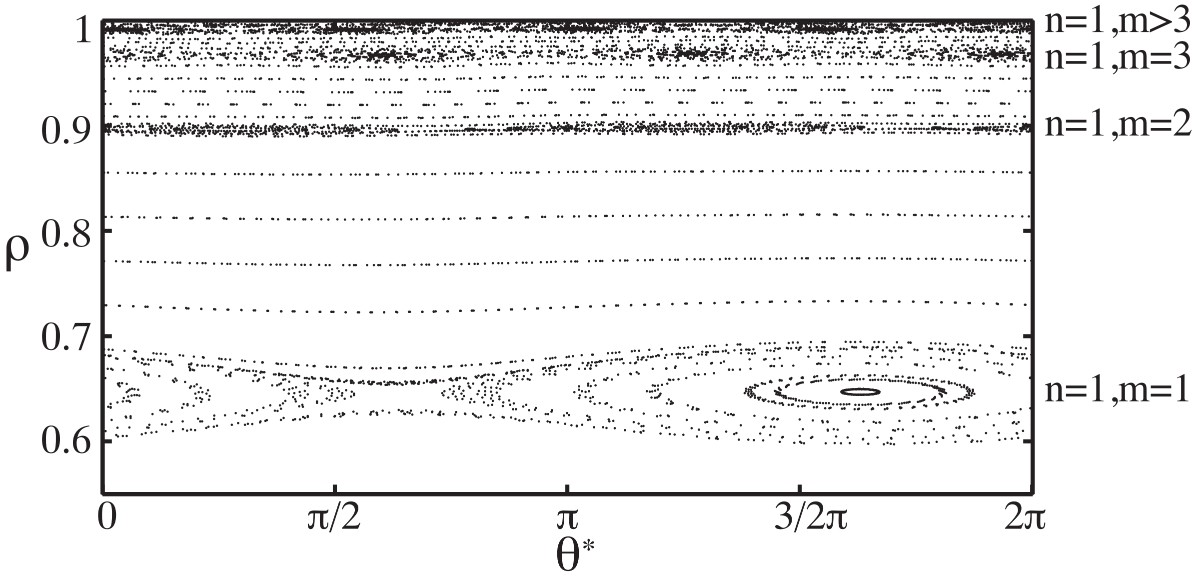

Figure 3.5.3: Poincaré plot of the vacuum error field added to the equilibrium magnetic field of a typical TCV discharge (shot # 39109, 0.6s). $\rho = \sqrt{1 - \psi/\psi_0}$ is the normalized plasma minor radius (ψ is the poloidal flux) and $\theta^\star$ is the poloidal angle in straight field line coordinates.

field of opposite sign. Based on the results of the presented magnetic calibration, a saddle coil system for the TCV tokamak has been proposed [35].

3.6 Conclusion

The magnetic system on TCV has been extended with a set of saddle loops used to measure the radial magnetic flux at different toroidal and vertical positions. From the calibration of the magnetic system, the errors on the position of the PF coils and on the measured current have been computed and the associated error field, inside the VV, has been estimated for a typical TCV discharge.

The sources of the $n = 0$ error field have been identified and the geometrical and calibration parameters corrected to minimize it. The typical $n = 0$ error field inside the VV is of the order of 1 mT.

The $n = 1$ perturbation, introduced by the misalignment of the poloidal field coils, produces an error field inside the VV smaller than 1 mT. This error field as been added to the equilibrium field of a typical TCV discharge. It creates an $n = 1, m = 1$ magnetic island at $\rho \sim 0.65$. Islands with higher mode number have a smaller size and the consequent ergodization due to the island overlapping is small.

Chapter 4

Inductive and assisted plasma start-up

4.1 Introduction

During tokamak operation, the gas used is strongly ionized and thus in the state of plasma. Gas breakdown is the process that leads to the creation to this plasma. In an inductive plasma start-up scenario, free electrons are accelerated by an electric field and ionize neutral atoms and molecules present in the VV (impact ionization). Since the number of free electrons rises with ionization, the breakdown has an unstable nature (avalanche) well described by Townsend's theory. For ECH assisted plasma start-up, electrons are predominately accelerated by electromagnetic waves resonating with their cyclotron motion. As the gas in the breakdown becomes partially ionized, the plasma current rises as a consequence of the applied toroidal electric field, and the plasma volume grows to the designed equilibrium (flattop phase).

Although the physical mechanisms behind the inductive plasma start-up are clear, it is possible, and often necessary, to optimize the early phase of the plasma discharge. An important complication is given by the limited number of measurements available during the plasma start-up. Most of the signals designed to record the flattop phase cannot be used during the start-up due to the fast dynamic of the observed phenomena and the low (or saturated) signal intensities, as expected for cold, small and low density plasmas. Another complication is given by the rapid variation of the magnetic topology during the start-up phase. Before any plasma current is established, the magnetic field lines are open and particles are lost rapidly to solid surfaces. Later, some magnetic field lines close and radial transport becomes the most important loss mechanism.

In large tokamaks, limits on the electric current in the mechanical structures and in the VV reduce the maximum value of the toroidal electric field. The space of parameters that allows a successful start-up can be drastically reduced. Most of these parameters are often not easily controllable (neutral gas, impurity content, poloidal magnetic field configuration, ...) making the plasma start-up difficult to control and reproduce.

The possibility of assisting the plasma start-up using ECH is being investigated for the next tokamak generation. A lot of research has already been performed on gas ionization using the first ECH harmonic (X1) [36]. Recently, second harmonic ECH assisted plasma start-up is receiving strong interest, especially with regard to a possible use to assist the ITER plasma start-up.

This chapter reports the results of a study of inductive and assisted plasma start-up conducted on TCV. In the first sections the inductive plasma start-up is presented, describing the TCV breakdown scenario, the main physical mechanisms involved during the breakdown phase and discussing the tools developed to set-up and analyze the poloidal magnetic field configuration at the breakdown time. Different magnetic configurations are compared through a statistical analysis of a large number of breakdown events in TCV. In the last sections, ECH-X2 assisted breakdown experiments are described.

4.2 Breakdown scenario

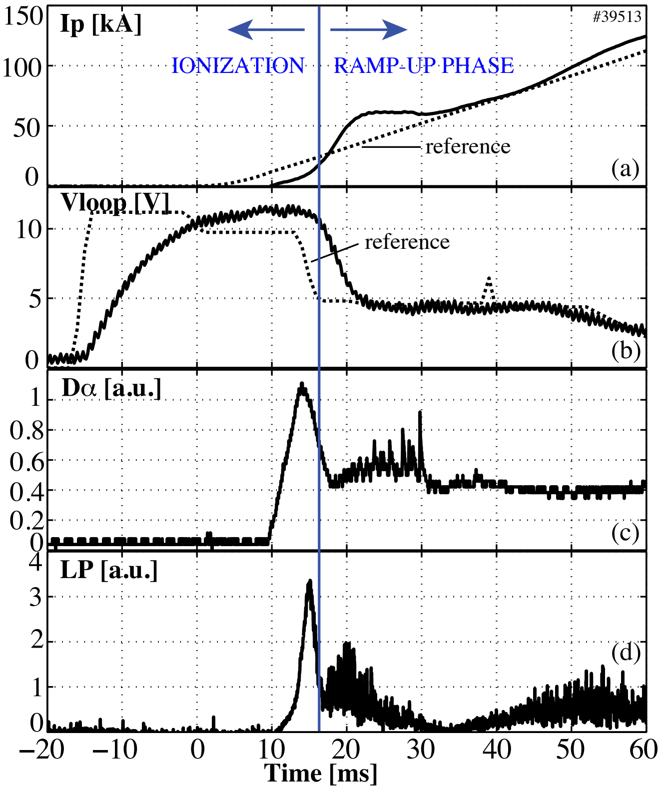

Figure 4.2.1: Plasma start-up scenario of a typical TCV discharge (shot #39513). (a) Pre-programmed plasma current waveform (dashed line) and plasma current; (b) toroidal electric voltage and its reference trace (dashed line); (c) signal from the vertical D_α photodiode; (d) saturation current from a Langmuir probe on the LFS of TCV.

The typical start-up scenario on TCV is shown in Fig. 4.2.1. The breakdown time is programmed at $t = 0$ s. The "pre-fill" gas injection starts at -45 ms until $t = -30$ ms. Two metal filaments, situated at the top and bottom of the VV, are heated before $t = 0$ to increase the number of free electrons for acceleration by the toroidal electric field. Two filaments are necessary to ensure a $\mathbf{B} \times \nabla\mathbf{B}$ electron drift velocity in the direction of the main plasma region with positive and negative toroidal magnetic field. They are 1 mm diameter tungsten wires 32 mm long extended in the toroidal direction to minimize the Lorentz force on them from the toroidal magnetic field. The schematic of the circuit used to power the filaments is shown in Fig. 4.2.2. They are fed with a voltage of $U_{\text{fil}} = 1.5$ V and ohmically heated with an electric power of $U_{\text{fil}} I_{\text{fil}} \sim 40$ W until they reach a temperature of $2000 - 2800$ K. A polarization voltage U_{pol} of -900 V is also applied between the filament and the VV to push the electrons towards the main plasma region.

A toroidal electric field is induced by a magnetic flux variation created by the ohmic coils. The reference waveform, shown in Fig. 4.2.1(b), is such that the toroidal electric voltage reaches approximately 10 V at $t = 0$ s. The exact breakdown time is nevertheless influenced by the machine conditions (neutral gas pressure, magnetic configuration) and may differ from that expected. Since the plasma current control system is already operational at $t = 0$ s, it reacts to a delay in the breakdown time with a toroidal electric field proportional to the plasma current reference. This leads to a resulting electric voltage larger than 10 V when the breakdown is late.

The typical signature of the gas breakdown on the D_α signal is illustrated in Fig. 4.2.1(c). This signal is proportional to the line intensity produced by the excitation $D^{n=3} \rightarrow D^{n=2}$. In the coronal regime, the ratio of ionization rate to line intensity ($D^{3\rightarrow 2}$) is independent of density and

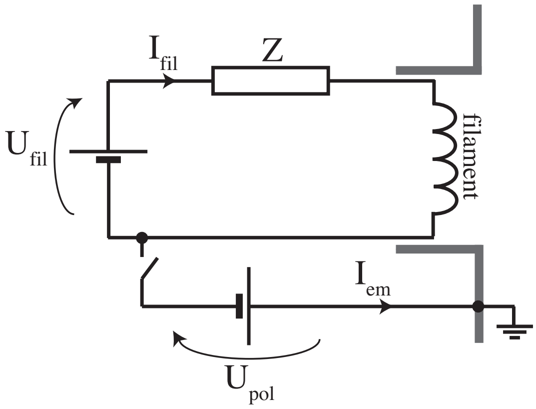

Figure 4.2.2: Schematic of the electric circuit of the tungsten filament used to produce the free-electrons before the breakdown. U_{fil} and I_{fil} are the electric voltage and current of the circuit used to ohmically heat the filament with equivalent impedance Z. U_{pol} is the polarization voltage used to accelerate the electrons from the filament towards the plasma region; I_{em} is the current of the polarization circuit proportional to the emitted electrons per unit time.

temperature [37], therefore:

$$\frac{\#\ \text{ionizations}}{\text{unit time}} = n_D n_e < \sigma_{\text{ion}} v_e > \propto \frac{\#\ D^{3\rightarrow 2}}{\text{unit time}} \tag{4.2.1}$$

where n_D is the neutral gas density, n_e is the electron density, σ_{ion} is the ionization cross-section and v_e is the electron velocity (the neutral particle velocity is supposed negligible). Assuming that the time variation of $< \sigma_{\text{ion}} v_e >$ is small compared to the time variation of n_D and n_e, the maximum of the ionization rate, i.e. the maximum of the D_α signal, is obtained for $n_e \sim n_D$.
Two different phases of the plasma start-up may be distinguished: the ionization phase, and the plasma ramp-up. During the **ionization phase** (see Sec. 4.4), electrons are accelerated along open or partially closed magnetic field lines until they reach the vessel walls. The covered distance (connection length) depends on the properties of the magnetic configuration. Neutral particles are ionized by impact ionization. After each ionization, a new electron is available and is also accelerated by the toroidal electric field. When the ionization rate is greater than the electron loss rate, an avalanche ensues and gas breakdown occurs.
During the **ramp-up phase**, particles are confined on closed magnetic field lines organized to guarantee MHD equilibrium. The plasma current is large enough to create a poloidal magnetic field of the same order of magnitude as that produced by the PF coils and the VV. This condition on the plasma current can be expressed as follows:

$$I_P > \frac{2\pi a B}{\mu_0} \sim 5\ \text{kA} \tag{4.2.2}$$

where I_P is the plasma current, $a \sim 10^{-1}$ m is the plasma minor radius and $B \sim 10$ mT is the stray field produced by the external conductors. Figure 4.2.1(d) shows the evolution of the saturation current on a Langmuir probe (see Sec. 2.4.3.4) located on the LFS of TCV. No plasma reaches these LFS tiles during the plasma start-up except during the ionization phase, when the open magnetic field lines intersect this Langmuir probe. A reduction of the saturation current on the Langmuir probe is thus a clear indication of the beginning of the ramp-up phase. On Fig. 4.2.1, the plasma current during this transition is $\sim$ 10 kA, in a good agreement with the estimation in Eq. 4.2.2.

The reference waveform for the plasma current during the ramp-up phase has a time derivative large enough to ensure a rapid ionization (burn-through) phase without exceeding the maximum toroidal electric field value:

$$j < \frac{E}{\eta} \tag{4.2.3}$$

where η is the plasma resistivity, j is the plasma current density and E is the toroidal electric field. Moreover, the maximum value of the plasma current derivative must be limited to avoid MHD instabilities:

$$j < \frac{2}{q}\frac{B_\phi}{\mu_0 R} \tag{4.2.4}$$

where q is the plasma safety factor and B_ϕ is the toroidal magnetic field. Typical values of the plasma current derivative are of the order of $1.5 - 2$ MA/s.

4.3 Magnetic configuration set-up

The poloidal magnetic field configuration plays a key role during the plasma start-up. During the ionization phase, the currents in the PF coils have to compensate the stray field (~ 20 mT) resulting from currents in the VV (see Sec. 2.4). In the regions with smaller poloidal magnetic field, the connection length is higher and breakdown may occur. On TCV, flexibility, given by the 16 independent powered PF coils, allows the creation of a poloidal field null point at different positions within the VV and with different properties.

During the ramp-up phase, the PF coils generate the magnetic field necessary to guarantee the MHD equilibrium of the plasma channel. Since the plasma elongation/triangularity is negligible during the early ramp-up phase, the PF coils mainly generate a pure vertical field to compensate the plasma outwards force due to the kinetic (tube force) and magnetic (hoop force) plasma pressure. The amplitude of this vertical field affects the plasma radius and, therefore, the current profile.

The technique used to impose the magnetic configuration during the ionization and the ramp-up phases is described in this section. The MGAMS (Matrix Generation Algorithm and Measurement Simulation) [38] code is used to define the breakdown position and the value of the radial and vertical field ($\mathbf{b}_\mathbf{p}^{\mathbf{R},\mathbf{Z}}$) at two points in the poloidal cross section of the breakdown region (typically located at 10 cm towards the LFS and the HFS of the programmed breakdown position). To study the $n = 0$ component of the poloidal magnetic field, a simple toroidally symmetric model for the VV is used (see Sec. 2.4). For the same reason, the $n > 0$ error field produced by the PF coils [34] (see Chapter 3) is neglected. The following set of equations is then solved:

$$0 = \underline{\underline{R}}_{vv}\mathbf{I_v} + \underline{\underline{M}}_{vv}\dot{\mathbf{I}}_\mathbf{v} + \underline{\underline{M}}_{va}\dot{\mathbf{I}}_\mathbf{a} + \underline{\underline{M}}_{vP}\dot{}\mathbf{I}_P \tag{4.3.1}$$

$$\mathbf{b}_\mathbf{p}^{\mathbf{R},\mathbf{Z}} = \underline{\underline{B_{pa}}}\mathbf{I_a} + \underline{\underline{B_{pv}}}\mathbf{I_v} + \underline{\underline{\alpha_{pT}}}B_\phi \tag{4.3.2}$$

Equation 4.3.1 describes the electromagnetic dynamic of the VV (see Sec. 2.4). $\underline{\underline{M}}_{vP}$ is the matrix of the Green's functions between the VV filaments and the plasma current (modeled from the computed MHD equilibria). These terms model the magnetic coupling between the plasma current and the VV. In Eq. 4.3.2 the programmed magnetic field is associated with the current in the PF coils and in the VV by means of the matrices of the Green's functions $\underline{\underline{B_{pa}}}$ and $\underline{\underline{B_{pv}}}$. Since the connections between the TF coils (T coils) also generate a poloidal magnetic field inside the VV (see Sec. 2.2), the coefficient $\underline{\underline{\alpha_{pT}}}$ associates the toroidal magnetic field B_ϕ with this poloidal magnetic field at the breakdown position. During the ramp-up phase, the same set of equations is solved, where the vector $\mathbf{b_p^{R,Z}}$ is computed from the FBTE (Free Boundary Tokamak Equilibrium) [39] code which solves the free-boundary equilibrium problem for a certain number of equilibria through the ramp-up phase. Only a subset of the PF coils, close to the breakdown region, are used to impose the desired magnetic configuration with the current on the other coils being computed from FBTE.

The system of Eqs. 4.3.1-4.3.2 is solved for the breakdown and ramp-up phases. The unknowns are the currents in the vessel filaments and in the subset of the PF coils used to impose the desired magnetic configuration. Further details on the solution of Eqs. 4.3.1-4.3.2 are given in Appendix C.

4.4 Physics of the ionization phase

4.4.1 Ionization rate

The inductive ionization phase is well described by the Townsend model [40], summarized in this section for the TCV case. The evolution of the electron density n_e is proportional to the difference between the ionization frequency ν_{ion} and the loss rate ν_{loss}:

$$\frac{dn_e}{dt} = n_e\left(\nu_{\text{ion}} - \nu_{\text{loss}}\right) \tag{4.4.1}$$

Therefore the ionization phase is the result of an avalanche process:

$$n_e = n_{e0}\exp\left[\left(\nu_{\text{ion}} - \nu_{\text{loss}}\right)t\right] \tag{4.4.2}$$

where n_{e0} is the initial electron density. The ionization frequency may be written as a function of the mean-free-path λ_{ion} for the ionization event:

$$\nu_{\text{ion}} = \frac{v_e}{\lambda_{\text{ion}}} \tag{4.4.3}$$

where the relative velocity between electrons and neutrals $\mathbf{v} = \mathbf{v_e} - \mathbf{v_n}$ has been approximated by the electron velocity v_e. λ_{ion} represents the distance required for electrons to travel between two successive ionizations. This quantity can be expressed as:

$$\lambda_{\text{ion}} = \frac{1}{n_n\sigma_{\text{ion}}} \tag{4.4.4}$$

where n_n is the neutral density and $\sigma_{\text{ion}} = \sigma_{\text{ion}}(v_e)$ is the ionization cross-section.
A generalized form of λ_{ion} is the first Townsend coefficient:

$$\alpha[1/\text{m}] = \lambda_{\text{ion}}^{-1} = Ap[\text{Pa}]\exp\left(-\frac{Bp[\text{Pa}]}{E[\text{V/m}]}\right) \tag{4.4.5}$$

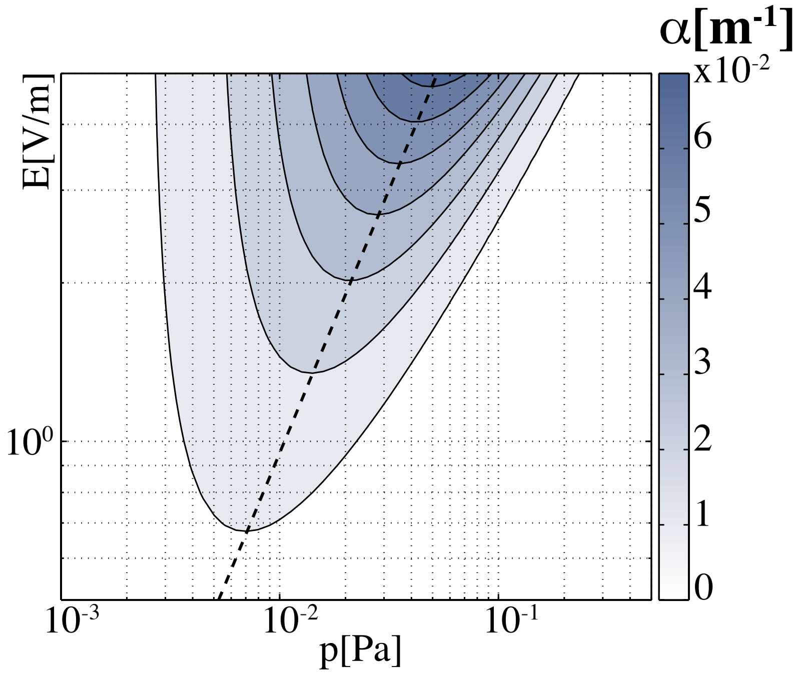

Figure 4.4.1: Townsend's first coefficient as a function of the neutral pressure p and the electric field E in logarithmic scales. The dashed line is the set of points where α is maximum.

where p is the neutral gas pressure, E is the electric field and $A = 3.9$ Pa^{-1}m^{-1} and $B = 96.6$ VPa^{-1}m^{-1} are parameters depending on the gas type and electric field value. Experimental measurements [41] have shown the validity of this relation over a wide range of E/p for Hydrogen and Deuterium plasmas. In Fig. 4.4.1 Townsend's first coefficient is plotted as a function of p and E. For a given value of E, there is an optimal value of the neutral pressure corresponding to a maximum of $\alpha(p)$, i.e. the minimum value of λ_{ion} (dashed line in Fig. 4.4.1):

$$\frac{\mathrm{d}\alpha}{\mathrm{d}p} = 0 \rightarrow p = \frac{E}{B} \tag{4.4.6}$$

To estimate the ionization and loss frequencies, electron transport across and along the toroidal magnetic field must be studied.

4.4.2 Losses along the magnetic field

The average velocity of an electron due to the electric field E is:

$$u_{\parallel} = \mu E \tag{4.4.7}$$

where $\mu = \frac{e}{m_e \nu_{en}}$ is the mobility, ν_{en} is the collision frequency between electrons and neutral particles, e is the electron charge and m_e is the electron mass. Following [42, 43], we approximate the collision frequency as:

$$\nu_{en}[1/\mathrm{s}] = 3.6 \times 10^7 p[\mathrm{Pa}] \tag{4.4.8}$$

Therefore, from Eq. 4.4.7 the average velocity is:

$$u_{\parallel}[\mathrm{m/s}] \sim 48.8 \times 10^2 \frac{E[\mathrm{V/m}]}{p[\mathrm{Pa}]} \tag{4.4.9}$$

This relation has been experimentally verified for both hydrogen [44] and deuterium [45]. Since the magnetic configuration at breakdown is characterized by open magnetic field lines, electrons reach the wall after a certain number of toroidal turns. The direct loss rate of the electrons may thus be estimated as:

$$\nu_{\parallel\mathrm{drift}}[1/\mathrm{s}] = \frac{u_\parallel}{L} \sim 4.88\frac{E[\mathrm{V/m}]}{p[\mathrm{Pa}]L[\mathrm{km}]} \tag{4.4.10}$$

where L is the connection length (length of the considered magnetic field line).
The diffusion loss rate parallel to the magnetic field is associated with the random motion of the electrons due to elastic collisions with the neutral particles. This mechanism can be estimated as:

$$D_\parallel = \lambda^2\nu_{en} \tag{4.4.11}$$

where $D_\parallel$ is the diffusion coefficient and $\lambda = \frac{w}{\nu_{en}}$ is the electron mean free path between collisions. $w[\mathrm{m/s}] = \sqrt{\frac{kT_e}{m_e}} \sim 4.19 \times 10^5 T_e^{1/2}[\mathrm{eV}]$ is the electron thermal velocity.
The electron temperature is a function of the ratio E/p [42] and has similar values for hydrogen and deuterium [45]. We can approximate T_e as:

$$T_e[\mathrm{eV}] \sim 0.13\frac{E[\mathrm{V/m}]}{p[\mathrm{Pa}]} \tag{4.4.12}$$

For large values of E/p, T_e appears to be limited to ∼ 10 eV. Imposing $T_e \sim 10$ eV, the loss rate due to the diffusion parallel to the magnetic field lines is:

$$\nu_{\parallel\mathrm{diff}}[1/\mathrm{s}] \sim \frac{D_\parallel}{L^2} = 4.88 \times 10^{-2}\frac{1}{p[\mathrm{Pa}]L^2[\mathrm{km}]}. \tag{4.4.13}$$

4.4.3 Losses across the magnetic field

Electrons are also lost in the orthogonal plane due to diffusion mechanisms and drift losses.
The diffusion across B_ϕ may be estimated from:

$$D_\perp \sim \rho_{Le}^2\nu_{en} \tag{4.4.14}$$

where $\rho_{Le} = \frac{w}{\Omega_e}$ is the electron gyroradius and $\Omega_e = \frac{eB_\phi}{m_e}$ is the electron gyrofrequency. Imposing $T_e \sim 10$ eV and $B_\phi = 1.43$ T (standard TCV value on axis):

$$D_\perp[\mathrm{m^2/s}] \sim 10^{-3}p[\mathrm{Pa}] \tag{4.4.15}$$

The diffusion loss rate can then be estimated as:

$$\nu_{\perp\mathrm{diff}}[1/\mathrm{s}] \sim \frac{D_\perp}{a_0^2} = 17.4 \times 10^{-3}p[\mathrm{Pa}] \tag{4.4.16}$$

where $a_0 = 0.255$ m is the half width of the TCV VV. The drift velocity of electrons across B_ϕ is:

$$u_\perp = \frac{1}{R_0 \Omega_e} \left(\frac{1}{2} v_\perp^2 + v_\parallel^2 \right) \tag{4.4.17}$$

where $R_0 = 0.88$ m and $v_\perp$ and $v_\parallel$ are the perpendicular and parallel components of the electron velocity. Choosing $v_\perp = w$ and $v_\parallel \sim u_\parallel$, the loss rate due to the perpendicular drift is:

$$\nu_{\perp\text{drift}}[1/\text{s}] \sim \frac{u_\perp}{a_0} = 18.96 \times 10^{-12} \left[8.78 \times 10^{11} + 24.3 \times 10^6 \left(\frac{E[\text{V/m}]}{p[\text{Pa}]} \right)^2 \right] \tag{4.4.18}$$

4.4.4 Summary of the ionization and loss frequencies

The ionization frequency can be estimated as:

$$\nu_{\text{ion}} \sim u_\parallel \alpha \tag{4.4.19}$$

An approximation of the total loss frequency is $\nu_{\text{loss}} \sim \max\left(\nu_{\parallel\text{diff}}, \nu_{\parallel\text{drift}}, \nu_{\perp\text{diff}}, \nu_{\perp\text{drift}}\right)$. The loss frequencies due to recombination and attachment may be neglected [46].

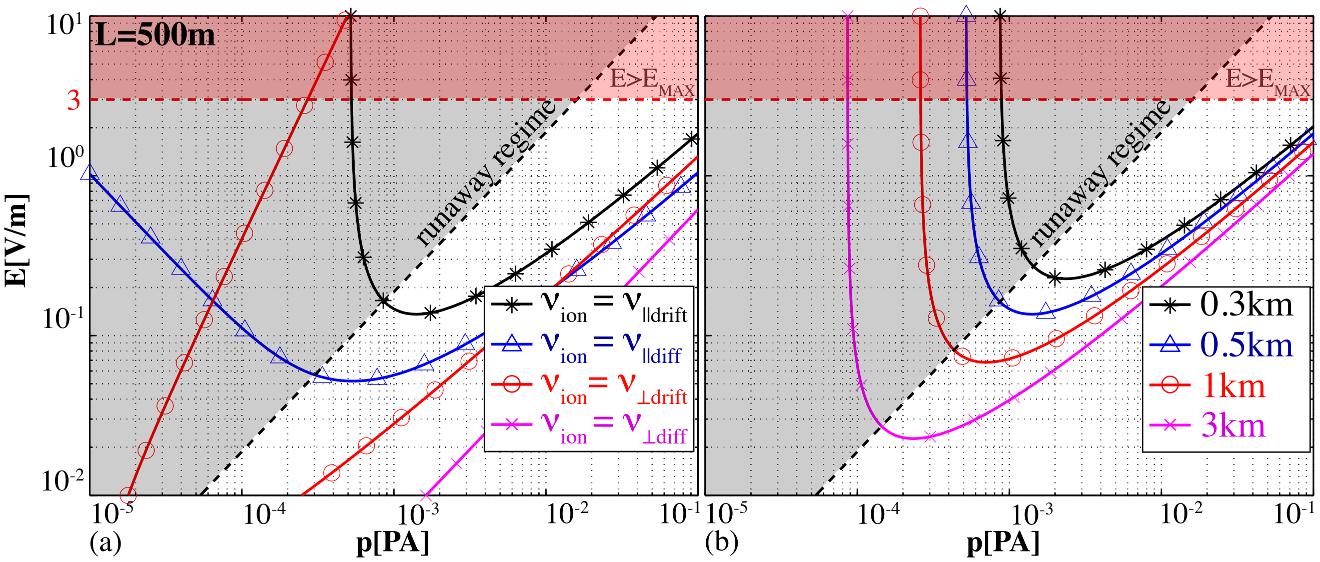

Figure 4.4.2: (a) Graphical representation of the conditions $\nu_{\text{ion}} = \nu_{\parallel\text{drift}}, \nu_{\parallel\text{diff}}, \nu_{\perp\text{drift}}, \nu_{\perp\text{diff}}$ in the $E-p$ cartesian plane for a connection length of 500 m and outside the runaway regime. The region with $E > 3$ V/m is not accessible due to the maximal voltage limit in the ohmic coil (red region). The gray region is the "runaway regime" where the model is not valid. (b) Condition $\nu_{\text{ion}} = \nu_{\parallel\text{drift}}$, that is the curve of the minimum electric field, in the $E-p$ cartesian plane for different values of the connection length and outside the runaway regime.

Figure 4.4.2(a) shows the following four conditions in the $E-p$ cartesian plane:

$$\nu_{\text{ion}} = \nu_{\parallel\text{drift}}, \nu_{\parallel\text{diff}}, \nu_{\perp\text{drift}}, \nu_{\perp\text{diff}} \tag{4.4.20}$$

The parallel drift losses are clearly strongest. In the same plot the operational space of TCV is shown ($E < 3$ V/m).

Since $\nu_{\|\text{drift}}$ the most important loss, in Fig. 4.4.2(b) the condition $\nu_{\text{ion}} = \nu_{\|\text{drift}}$ is shown for different values of the connection length. Note that this condition identifies the curve of the minimum electric field required for breakdown as a function of the neutral pressure. The importance of the connection length is emphasized in this plot. In magnetic configurations with small connection lengths there is only a narrow range of the breakdown parameters (p and E) that allows successful breakdown. Therefore, the reliability of the breakdown increases with the connection length.

4.4.5 The runaway regime

The model used to describe the ionization phase is based on the assumption that the collision frequency is only a function of the pressure p. For high values of E/p this model may not be used as the collision frequency decreases for high electron energies. Therefore, a "runaway regime" may characterize the ionization phase.
Following [47], the runaway regime occurs in a region where:

$$\frac{E}{p} > 180 \ [\mathrm{Vm^{-1}Pa^{-1}}] \tag{4.4.21}$$

This region is shown in Fig. 4.4.2 in grey. The runaway electrons are described supposing that they are accelerated indefinitely along the field lines until they reach the wall. From the equation of motion, the parallel velocity is:

$$u_{\|}(x) = \left(\frac{2eE}{m_e}\right)^{1/2} \sqrt{x} \tag{4.4.22}$$

where x is the distance covered along the field line. The ionization frequency is therefore:

$$\nu_{\text{ion}} = \alpha < u_{\|} >= \alpha(E,p)\left(\frac{eE}{2m_e}L\right)^{1/2} \tag{4.4.23}$$

The direct loss rate is now estimated from the time necessary for an electron to reach the end of a given field line:

$$\nu_{\|\text{drift}} = \tau^{-1}_{\|\text{drift}} = \left(\frac{eE}{2m_e L}\right)^{1/2} \tag{4.4.24}$$

The loss rate due to the drift velocity across the magnetic field are also different in the runaway regime. Since $v_{\|} >> v_{\perp}$, the Eq. 4.4.17 can be rewritten as:

$$u_{\perp}(x) \sim \frac{1}{R_0\Omega_e} v_{\|}^2 \sim \frac{1}{R_0\Omega_e}\left(\frac{eE}{m_e}\right)^2 t^2 \tag{4.4.25}$$

Since $u_{\perp} = \frac{\mathrm{d}x_{\perp}}{\mathrm{d}t}$, integrating Eq. 4.4.25 the loss rate from drifts across the magnetic field is:

$$\nu_{\perp\text{drift}}[1/\mathrm{s}] \sim \frac{u_{\perp}}{a_0} = \frac{1}{(3a_0R_0\Omega_e)^3}\left(\frac{eE}{m_e}\right)^{2/3} \tag{4.4.26}$$

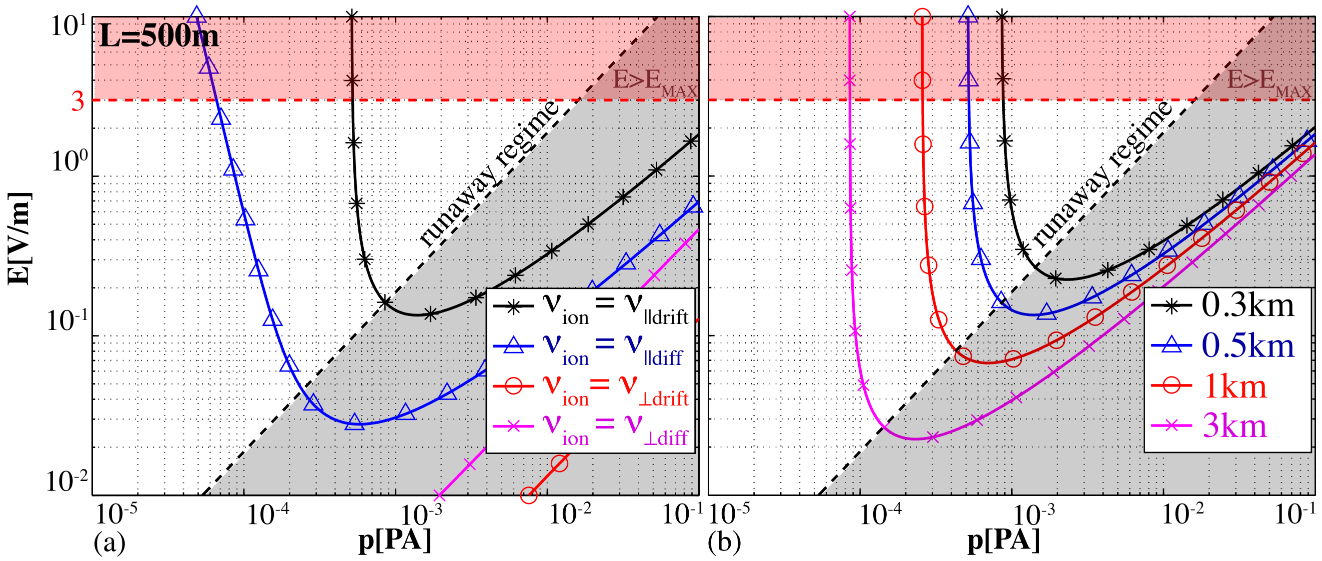

Figure 4.4.3: (a) Graphical representation of the conditions $\nu_{\text{ion}} = \nu_{\|\text{drift}}, \nu_{\|\text{diff}}, \nu_{\perp\text{drift}}, \nu_{\perp\text{diff}}$ in the $E-p$ cartesian plane for a connection length of 500 m and in the runaway regime. The region with $E > 3$ V/m is not accessible due to the maximal voltage limit in the ohmic coil (red region). The gray region is the "non-runaway regime" where the model is not valid. (b) Condition $\nu_{\text{ion}} = \nu_{\|\text{drift}}$, that is the curve of the minimum electric field, in the $E-p$ cartesian plane for different values of the connection length and in the runaway regime.

Figure 4.4.3(a) shows the minimum electric field necessary to have an avalanche process according to the different loss mechanisms. Also in the runaway regime, parallel direct losses are still the most important. In Fig. 4.4.3(b) the minimum electric field is plotted for different values of the connection length for the runaway regime. The advantages associated with a long connection length are also valid in a runaway regime.

4.5 Interpretation of the experimental data

The Townsend model, derived in the previous section, is now used to describe the dynamics of the ionization phase in TCV. In Fig. 4.5.1 three different breakdown scenarios are represented. The evolution of the toroidal electric field E and the connection length L is different for each case and the star symbols in the figure indicate the breakdown times. The green curve represents a shot where ionization was not observed (no D_α radiation measured).
The theoretical condition necessary to trigger the avalanche is $\nu_{\text{ion}} - \nu_{\text{loss}} > 0$. Nevertheless, this condition may be too optimistic due to the large number of favorable approximations used to derive the Townsend model. A more realistic condition may be expressed as $\nu_{\text{ion}} - \nu_{\text{loss}} > TH$, where TH is a threshold necessary for reliable ionization. The value of TH is estimated from a typical TCV breakdown. Fig. 4.5.2 shows the plasma current evolution during the early ramp-up phase. An approximate expression for the plasma current based on the Townsend model is:

$$I_P = n_e u_\| e S_P \propto \exp\left[(\nu_{\text{ion}} - \nu_{\text{loss}})t\right] \tag{4.5.1}$$

where S_P is the poloidal cross section of the plasma current. Fitting the plasma current evolution with an exponential function gives $\nu_{\text{ion}} - \nu_{\text{loss}} \sim 1700\ \text{s}^{-1}$. This condition is shown in Fig. 4.5.3 for several values of the neutral gas pressure (blue curves) in the E-L plane. On the same plot, the breakdown evolutions from Fig. 4.5.1 are represented. The breakdown points (colored stars)

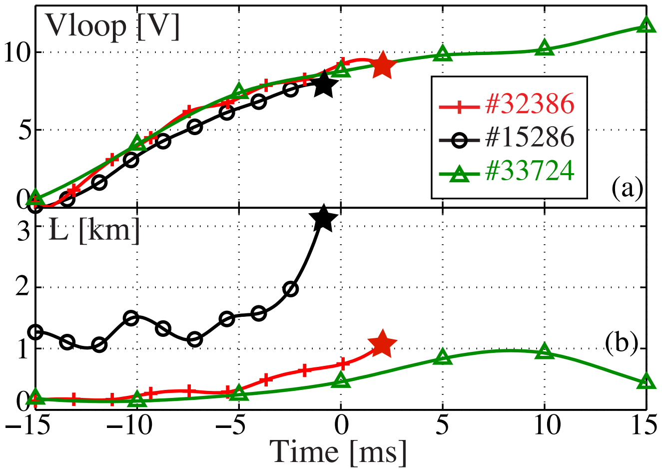

Figure 4.5.1: Evolution of (a) the toroidal electric voltage V_{loop} and (b) the connection length L for three breakdowns. The colored stars represent the breakdown points. Note that for the green curve (shot #33724) there is no breakdown.

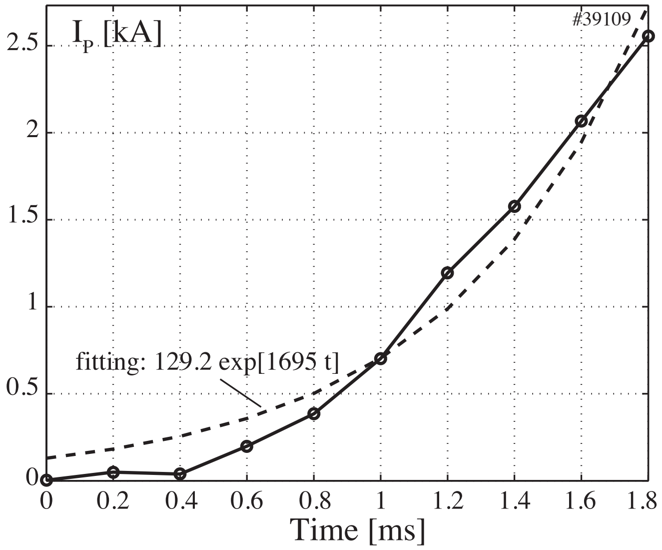

Figure 4.5.2: Evolution of the plasma current during the early ramp-up for a typical TCV breakdown (solid line). The dashed line represents a fitting of the curve using an exponential function.

should be located in the region where the condition $\nu_{\mathrm{ion}} - \nu_{\mathrm{loss}} > 1700\ \mathrm{s}^{-1}$ is verified according to the neutral gas pressure. Unfortunately, since the neutral gas pressure is not measured, the model cannot be verified.

4.6 Physics of the ramp-up phase

During the ramp-up phase, plasma is confined by closed magnetic field lines. The plasma current and the plasma volume rise until a balance between the input ohmic power and the lost power is reached.

This section describes a 0-D model used to model the plasma ramp-up phase. The plasma is considered as uniform and the effect of impurities neglected. Despite the model's simplicity, some general experimental observations are qualitatively reproduced. The following set of equations is solved:

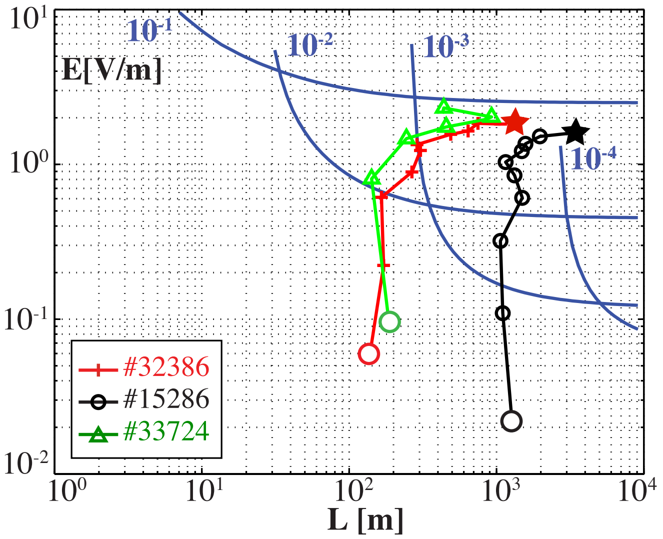

Figure 4.5.3: Representation of the plasma start-up on the $E-L$ plane for three typical TCV breakdowns. In the same plot the curves of the minimum E, L for ionization are plotted as a function of the neutral gas pressure (blue curves). The colored stars represent the breakdown points.

$$\begin{aligned}
\frac{3}{2}\frac{\mathrm{d}}{\mathrm{d}t}(n_e k_B T_e) &= P_{\mathrm{OH}} - P_{\mathrm{ion}} - P_{\mathrm{rad}} - P_{ei} - P_b - \frac{3}{2}\frac{n_e k_B T_e}{\tau_E} && (4.6.1)\\
\frac{3}{2}\frac{\mathrm{d}}{\mathrm{d}t}(n_e k_B T_i) &= P_{ei} - P_{\mathrm{cx}} - \frac{3}{2}\frac{n_e k_B T_i}{\tau_E} && (4.6.2)\\
\frac{\mathrm{d}n_e}{\mathrm{d}t} &= n_0 n_e S_i - \frac{n_e}{\tau_p} && (4.6.3)\\
\frac{\mathrm{d}n_n}{\mathrm{d}t} &= -\frac{V_P}{V_v}\frac{\mathrm{d}n_e}{\mathrm{d}t} + \Gamma && (4.6.4)\\
\frac{\mathrm{d}I_P}{\mathrm{d}t} &= \frac{U}{L_P} - \frac{R_P}{L_P} I_P && (4.6.5)
\end{aligned}$$

Equation 4.6.1 describes the evolution of the electron energy. $P_{\mathrm{OH}} = \frac{R_P I_P^2}{V_P}$ is the ohmic power normalized to the plasma volume V_P, $R_P = \eta\frac{2R}{a^2}$ is the plasma resistance, with R equal to the plasma major radius, $a \sim k_a I_P$ is the plasma minor radius chosen proportional to I_P through the constant k_a and $\eta[\Omega\mathrm{m}] \sim 5.1\cdot 10^{-5}\frac{Z\ln\Lambda}{T_e[\mathrm{eV}]^{3/2}}$ is the Spitzer resistivity with T_e equal to the electron temperature. $P_{\mathrm{ion}} + P_{\mathrm{rad}} \sim n_n n_e S_i(W_{\mathrm{ion}} + W_{\mathrm{rad}})$ is the sum of the ionization and radiation losses, with $S_i[\mathrm{m}^3\mathrm{s}^{-1}] = \frac{2\times 10^{-13}}{6+T_e[\mathrm{eV}]/13.6}\sqrt{\frac{T_e[\mathrm{eV}]}{13.6}}\exp\left(\frac{-13.6}{T_e[\mathrm{eV}]}\right)$ equal to the electron ionization rate and $W_{\mathrm{ion}} + W_{\mathrm{rad}} = 30$ eV to the total energy lost per ionization accounting for multiple excitations occurring before an ionization event. n_n and n_e are respectively the neutral and electron densities. $P_{ei}[\mathrm{W/m^3}] = 7.75\times 10^{-34}(T_e[\mathrm{eV}] - T_i[\mathrm{eV}])\frac{n_e^2\ln\Lambda}{T_e^{3/2}[\mathrm{eV}]}$ is the power transferred from electrons to ions through elastic collisions, with T_i the ion temperature. $P_b[\mathrm{W/m^3}] \sim 1.53\times 10^{-38} n_e^2 T_e^{1/2}[\mathrm{eV}] Z_{eff}$ is the bremsstrahlung radiation and $\tau_E = \tau_{E0} + k_\tau I_P$ is the electron energy confinement time, increasing with the plasma current through the constant k_τ.

Equation 4.6.2 is used to describe the dynamics of the ion energy.

$P_{\mathrm{cx}}[\mathrm{W/m^3}] = \frac{3}{2}e n_e n_0(T_i[\mathrm{eV}] - T_0[\mathrm{eV}])S_{\mathrm{cx}}$ is the charge-exchange power loss, $S_{\mathrm{cx}}[\mathrm{m}^3\mathrm{s}^{-1}] = 1.066\times 10^{-14} T_i^{0.327}[\mathrm{eV}]$ is the rate coefficient for charge exchange and T_0 is the neutral gas temperature.

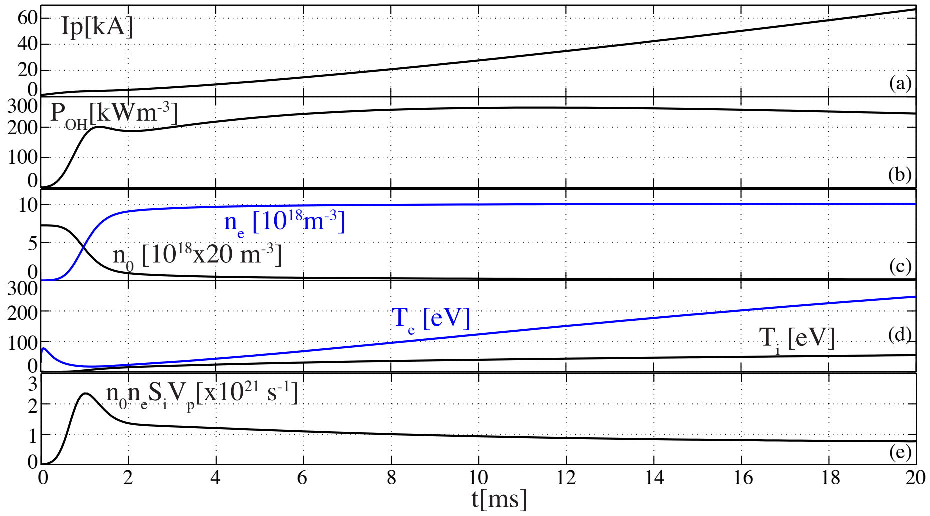

Figure 4.6.1: Temporal evolution of (a) the plasma current, (b) the ohmic power, (c) the electron (blue) and the neutral (black) density, (d) the electron (blue) and ion (black) temperature and (e) the number of ionizations per unit time.

The evolution of the plasma density is given by Eq. 4.6.3, where τ_p is the particle confinement time, assumed equal to τ_E.

Particle conservation is explicitly imposed by Eq. 4.6.4, where V_v is the volume of the VV and Γ is the external neutral gas flux.

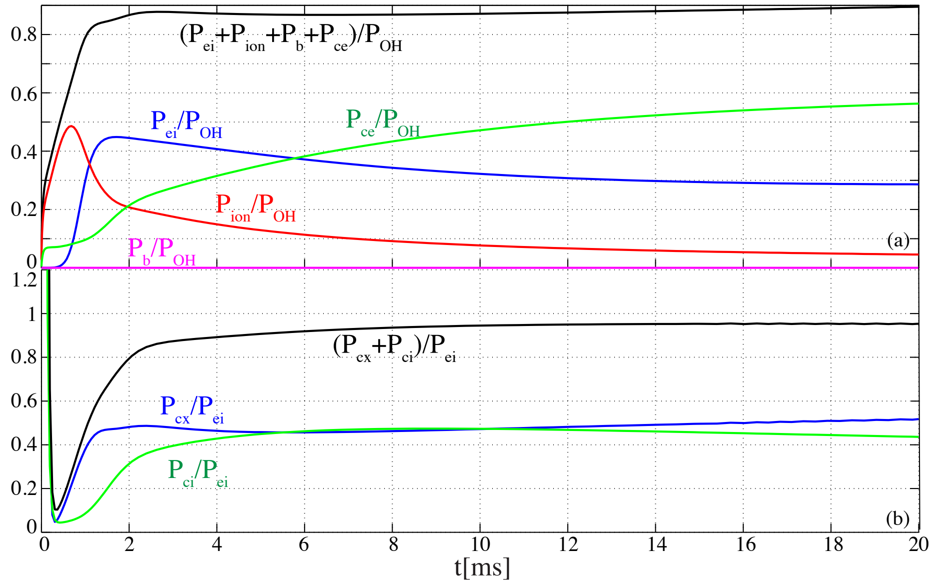

Figure 4.6.2: Temporal evolution of the power for (a) the electrons and (b) the ions.

Equation 4.6.5 is used to describe the plasma current dynamics where U is the toroidal electric voltage and L_P is the plasma inductance, supposed constant.

Figure 4.6.1 shows the solution of the system of Eqs. 4.6.1-4.6.5. The neutral gas pressure is equal to $p_0 = 1.5$ mPa and the toroidal electric voltage is 10 V. At the start of the ramp-up phase, neutral gas is ionized and the electron density rises. The ionization rate $(n_n n_e S_i V_P)$ has a maximum and reproduces qualitatively the D_α signal on Fig. 4.2.1.

Figure 4.6.2 represents the different power terms during the ramp-up phase between the electrons and ions (note that $P_{ce} = \frac{3}{2}\frac{n_e k_B T_e}{\tau_E}$ and $P_{ci} = \frac{3}{2}\frac{n_e k_B T_i}{\tau_E}$). Early in the ramp-up phase, most of the input power is lost to ionize neutral particles (P_{ion}). Later, the most important power loss term for the electrons is energy transferred to the ions (P_{ei}). As the electron temperature rises, the cross-section for elastic collisions between electrons and ions decreases, causing P_{ei} to decrease. Conversely, direct losses due to radial transport increase as they are proportional to the electron temperature and density. Note that the bremsstrahlung loss term P_b is always negligible during the ramp-up phase. For the ions, P_{cx} and radial transport losses (P_{ci}) are of the same order of magnitude.

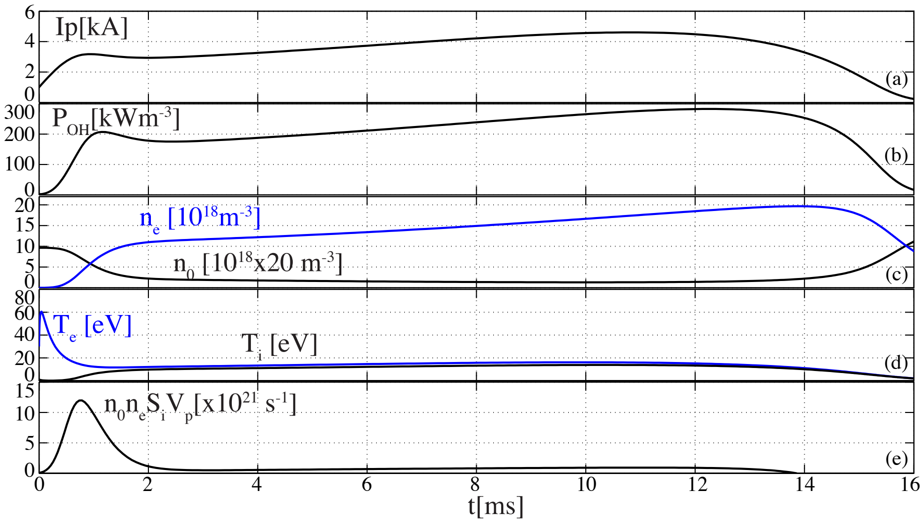

Figure 4.6.3: Temporal evolution of (a) the plasma current, (b) the ohmic power, (c) the electron (blue) and the neutral (black) density, (d) the electron (blue) and ion (black) temperature and (e) the number of ionizations per unit time for a plasma start-up failure.

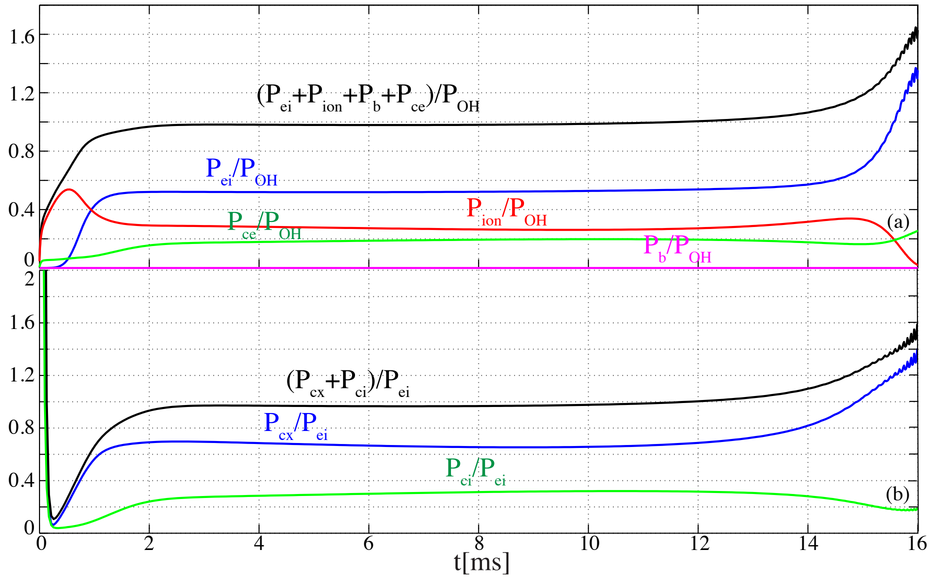

Figure 4.6.4: Temporal evolution of the power for (a) the electrons and (b) the ions for a plasma start-up failure.

The same equations were solved with the addition of a neutral gas flux during the ramp-up phase $\Gamma\ [\text{m}^{-3}\text{s}^{-1}] = 9 \times 10^{22} t\ [\text{s}]$. The results are shown on Fig. 4.6.3. Even if most of the particles are ionized, the plasma current and the plasma temperature stay low and the plasma discharge ends prematurely. Figure 4.6.4 shows the power evolution for electrons and ions. The losses due to the ionization and elastic collisions between electrons and ions stay high during the early ramp-up and are later responsible for the plasma collapse.

4.7 Magnetic properties at the ionization-phase

During the ionization phase, the magnetic field distribution is given by the current in the VV and in the PF coils. The current distribution in the vessel is not directly controllable and is the result of the electromagnetic interaction between the vessel itself and the magnetic field produced by the active coils. The current in the PF coils can, however, be measured directly [17]. The current in the VV is not measured and it can only be estimated from the magnetic measurements. In control theory, the current in the VV represents an observable state variable of the dynamic system.
The current distribution is the VV is described using Eq. 2.4.1. The measured quantities are related to the currents in the system and their derivatives according to the specific properties of the considered sensor:

$$\mathbf{m} = \mathbf{f}\left(\mathbf{I_a}, \mathbf{I_v}, \dot{\mathbf{I}}_\mathbf{a}, \dot{\mathbf{I}}_\mathbf{v}\right) = \underline{\underline{M}}\left[\mathbf{I_a}; \mathbf{I_v}; \dot{\mathbf{I}}_\mathbf{a}; \dot{\mathbf{I}}_\mathbf{v}\right] \tag{4.7.1}$$

where $\mathbf{m}$ is the vector with the measurements and $\underline{\underline{M}}$ the coupling matrix between the currents, the current derivatives and the measurements. Note that in Eqs. 2.4.1 and 4.7.1 the plasma current is not present, so the model is only valid before the breakdown time. It is consequently important to detect accurately the beginning of the gas ionization. When the ionization starts, the D_α signal rises and, simultaneously, the plasma current observer detects a positive time derivative signal (see Fig. 4.2.1). The described model thus determines the breakdown time as the beginning of a sequence of a certain temporal length during which the plasma current derivatives are always positive.
In the system comprising Eqs. 2.4.1 and 4.7.1, the currents and their derivatives are considered as independent variables. The link between these quantities is therefore explicitly added by imposing:

$$\dot{\mathbf{I}}_\mathbf{a/v} = \frac{\mathrm{d}\mathbf{I_{a/v}}}{\mathrm{d}\mathbf{t}} \tag{4.7.2}$$

where $\dot{\mathbf{I}}_\mathbf{a/v}$ is the vector of the fitted current derivatives and $\mathbf{I_{a/v}}$ is the vector of the fitted currents. Equations 2.4.1-4.7.2 are solved using a least square fitting method for each time-step until the breakdown time. The weights for the equations are chosen simply as the inverse of the uncertainties of the considered measured quantities. To obtain consistency between the the fitted current derivatives and the derivatives of the fitted currents (Eq. 4.7.2) an iterative process is used. Figure 4.7.1 shows the flow diagram of the procedure used by the described algorithm. At the first step, the magnetostatic problem is solved (only Eq. 4.7.1 i.e. without the current derivatives). The current derivatives are then computed form Eq. 4.7.2 and a new solution is found using the full system of equations. The iteration process stops when the ratio between the residue of the least square fit χ_{min} and the variance of the measured quantities σ_y is smaller than unity:

$$n_{tot} = \frac{\chi^2_{min}}{\sum_i \omega_i^2 \sigma^2_{m_i}} \tag{4.7.3}$$

where ω_i is the weight of the considered quantity. $\chi^2_{min} = \sum_i \omega_i^2 \left[m_i - (M \cdot I)_i\right]^2$ is computed from the measured quantities m_i and the fitted unknowns I. $n_{tot} < 1$ is an indication of a good fit in the solution.

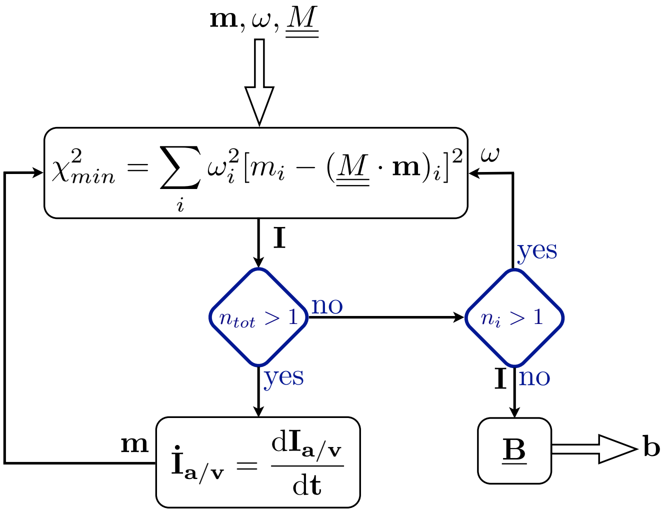

Figure 4.7.1: Flow diagram of breakdown code used to compute the magnetic configuration at the ionization time.

The increase in the robustness of the model and the residue on each measurement is also computed:

$$n_i = \frac{[m_i - (M \cdot I)_i]^2}{\omega_i^2 \sigma_{m_i}^2} \tag{4.7.4}$$

If, for a particular equation, $n_i > 1$, that equation is eliminated and the system of equations is re-solved. Poor signals, or badly calibrated sensors, may therefore be automatically removed. More details on the solution technique are given in Appendix D.

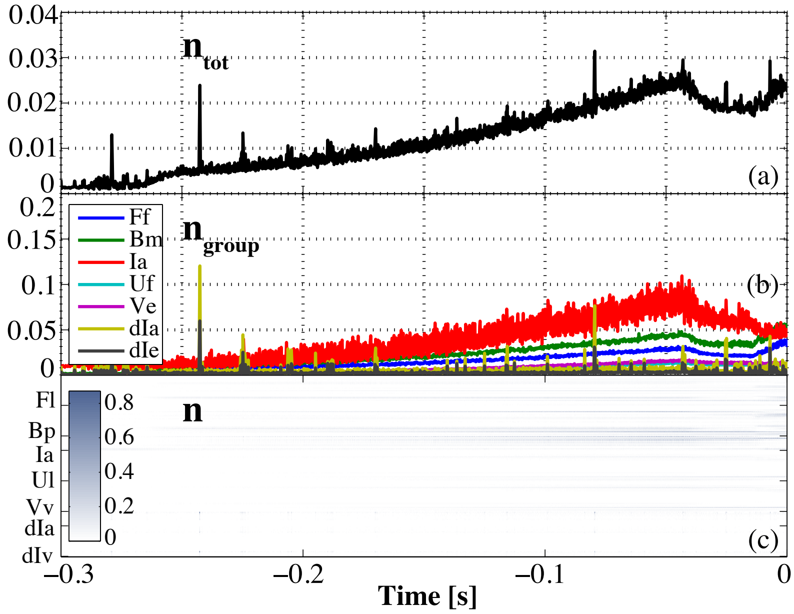

Figure 4.7.2: Residues of the fitting method for a typical TCV breakdown (shot #38071) (a) total residue of the fitting method, (b) residue of the groups of measurements, (c) residue of each measurements.

In Fig. 4.7.2 the residues of the fitting method for a typical TCV breakdown are shown. The n_{tot} parameter (Fig. 4.7.2(a)) previously defined and the individual residues (Fig. 4.7.2(c)) are always smaller than one. Figure 4.7.2(b) shows the residual for each group of equations defined as:

$$n_{\mathrm{group}_j} = \frac{\sum_{i\in j} \left[m_i - (M \cdot I)_i\right]^2}{\sum_{i\in j} \omega_i^2 \sigma_{m_i}^2} \tag{4.7.5}$$

where j is the considered group of equations that is a family of measurements made with the same kind of sensors. For all sets of equations, n_{group} is smaller than unity, indicating good fitting process quality. Moreover, for each group of equations n_{group} has the same order of magnitude. This condition is important to ensure that the equations are of equal weight in the fitting mechanism. The solution of the least square fitting method is a vector with the currents in the PF coils and in the vessel at each time step before breakdown. The precision of the fitting method is taken from the covariance matrix of the fitted quantities:

$$\underline{\underline{\sigma}}^2_{xx} = \mathrm{E}\left[(\mathbf{I} - \bar{\mathbf{I}})(\mathbf{I} - \bar{\mathbf{I}})^T\right] \tag{4.7.6}$$

where E is the expectation value symbol, $\mathbf{I}$ the vector of the fitted quantities considered as a random variable and $\bar{\mathbf{I}}$ its average value. Since the fitted quantities are obtained from:

$$\mathbf{I} = \left(\underline{\underline{M}}^T \underline{\underline{M}}\right)^{-1} \underline{\underline{M}}^T \mathbf{m} \tag{4.7.7}$$

an expression for the covariance matrix is:

$$\underline{\underline{\sigma}}^2_{mm} = \left(\underline{\underline{M}}^T \underline{\underline{M}}\right)^{-1} \underline{\underline{M}}^T \underline{\underline{\sigma}}^2_{mm} \underline{\underline{M}} \left(\underline{\underline{M}}^T \underline{\underline{M}}\right)^{-1} \tag{4.7.8}$$

where $\underline{\underline{\sigma}}^2_{mm}$ is the diagonal covariance matrix of the measured quantities. The correlation coefficients c_{ij} between the fitted parameters are computed from:

$$c_{ij} = \frac{(\sigma^2_{xx})_{ij}}{(\sigma_{xx})_{ii}(\sigma_{xx})_{jj}} \tag{4.7.9}$$

This matrix should be independent of the considered discharge and depend on the geometry of the experiment through $\underline{\underline{M}}$ and on the intrinsic errors of the measurements.
The relative covariance matrix $\underline{\underline{c}}$ is shown in Fig. 4.7.3. The correlation between the fitted parameters (non-diagonal terms in the matrix) is the result of magnetic coupling between the considered circuits and the iterative process that mathematically links the electric currents with their derivatives.
From the computed currents in the PF coils and in the VV at breakdown, the magnetic configuration in the plasma region is deduced from the Green's functions:

$$\mathbf{b} = \underline{\underline{B}} \mathbf{I}(k_{bk}) \tag{4.7.10}$$

where $\mathbf{b}$ is the computed magnetic quantity (poloidal flux and magnetic field) at the breakdown time, $\underline{\underline{B}}$ is the matrix containing the relevant Green's functions and $\mathbf{I}(k_{bk})$ is the vector of the fitted currents and current derivatives at the breakdown time step k_{bk}.

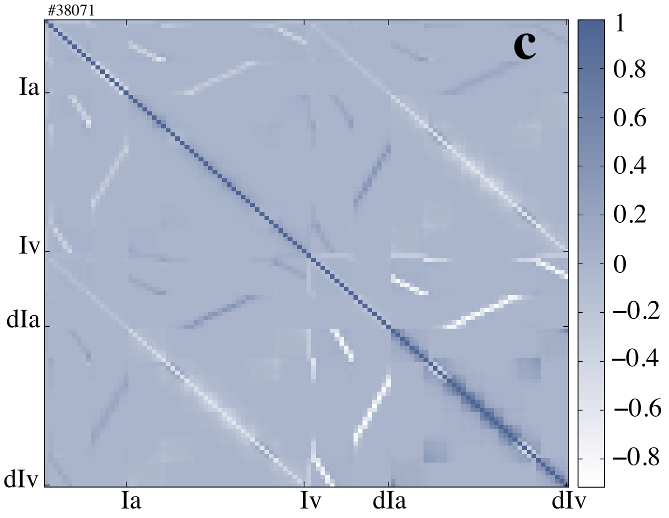

Figure 4.7.3: Relative covariance matrix of the fitted quantities for a typical TCV breakdown (shot #38071).

From the poloidal magnetic flux distribution, the position of the minima in the absolute value of the poloidal magnetic field (X-points) are detected as the set of points defined by:

$$\frac{\mathrm{d}\Psi}{\mathrm{d}R} = 0 \bigcup \frac{\mathrm{d}\Psi}{\mathrm{d}z} = 0 \tag{4.7.11}$$

where Ψ is the poloidal magnetic flux and R and z are the radial and vertical position variables. The precise determination of the null point location is found from the saddle points from the fit of a local quadratic function.

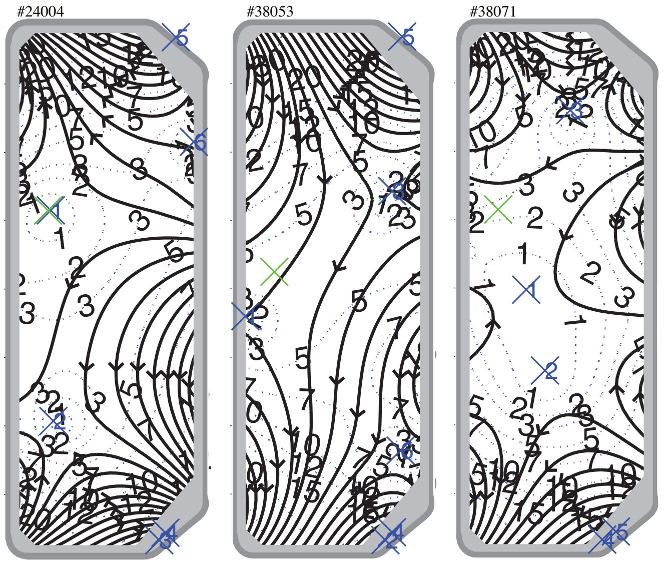

Figure 4.7.4: Reconstruction of the magnetic configuration at the breakdown time for three different discharges. The green cross represents the desired breakdown point imposed from the MGAMS code. The blue crosses indicate the position of the minima of the magnetic field. The solid black lines are a contour plot of the poloidal flux and the dashed blue lines are contour plots of the magnetic field with the corresponding amplitude in mT written in black.

Figure 4.7.4 shows the reconstruction of the magnetic configuration at the breakdown time of three different discharges. The green crosses are the pre-programmed positions of the breakdown

points. Several null points are detected for each configuration (blue crosses) where the magnetic field is smaller than 1 mT and whose location and shape depend on the particular discharge.
The precision of the magnetic reconstruction is computed from the covariance matrix $\underline{\underline{\sigma}}^2_{xx}$ as follows:

$$\underline{\underline{\sigma}}^2_{\mathbf{bb}} = \underline{\underline{B}}_{bx}\underline{\underline{\sigma}}^2_{xx}\underline{\underline{B}}^T_{bx} \tag{4.7.12}$$

where $\underline{\underline{\sigma}}^2_{\mathbf{bb}}$ is the magnetic field covariance matrix, $\underline{\underline{B}}_{bx}$ is the matrix of the Green's functions between the magnetic field and the vector of the fitted currents $\mathbf{x}$.

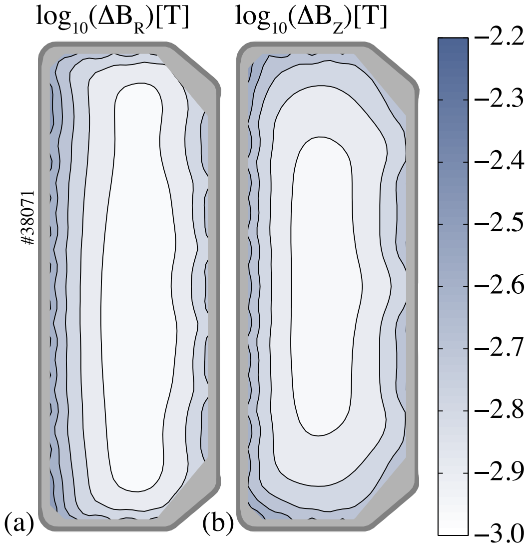

Figure 4.7.5: Absolute error of (a) the reconstructed radial and (b) the vertical magnetic field on a logarithmic scale for a typical TCV breakdown (shot #38071).

In Fig. 4.7.5 the distribution of the error on the radial and vertical magnetic field is plotted. These quantities are computed from the diagonal of the square-root of the covariance matrix $\underline{\underline{\sigma}}^2_{\mathbf{bb}}$. The error in the reconstruction is of the order of mT, and is smaller in the center. This is a result of the least square solution method which tends to interpolate the different measurements. As the central zone of the cross-section is covered by a larger number of probes than in the periphery, more measurements are available.
The minima of the poloidal magnetic field are characterized by a larger connection length. Therefore, the ionization phase should commence close to one of these points. For this reason, it is important to characterize each minimum from the magnetic point of view. For each minimum, the gradient of the radial and vertical poloidal magnetic field ($\nabla b_{R,Z}$), the induced voltage at the breakdown time and the connection length are computed. The last parameter is evaluated using a field line tracing code. Four points separated 1 mm from the considered null point are selected and the length of the magnetic field line passing through the points, terminating on the VV, is estimated. The connection length is taken as the average of the connection length of these four points.
Each null point can also be characterized by its size and its orientation. These quantities are computed from the matrix of the magnetic field derivatives:

$$\nabla \mathbf{b_{R,Z}} = \begin{pmatrix} \partial_R b_R & \partial_z b_R \\ \partial_R b_Z & \partial_z b_Z \end{pmatrix} \tag{4.7.13}$$

Since $\nabla \mathbf{b}_{\mathbf{R},\mathbf{Z}}$ is a symmetric matrix, the eigenvectors are orthogonal. Moreover, the divergence and the curl of the magnetic field are zero before the breakdown (no plasma current), leading to $\epsilon_1 = -\epsilon_2 = \epsilon$, where ϵ_i are the eigenvalues of $\nabla \mathbf{b}_{\mathbf{R},\mathbf{Z}}$.

The size of the magnetic field null is defined as follows:

$$\rho\ [\mathrm{m}] = \frac{10^{-3}}{\epsilon\ [\mathrm{T/m}]} \tag{4.7.14}$$

where ρ is the equivalent radius of the null point defined as the distance from the X-point necessary to increase the poloidal magnetic field by 1 mT (note: only a first order expansion of the magnetic field is used to compute the equivalent radius).

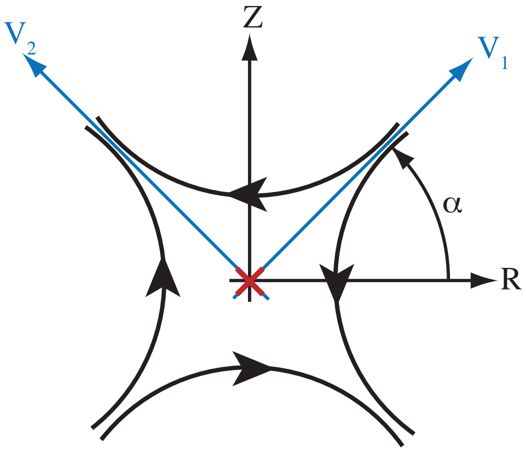

Figure 4.7.6: Representation of a magnetic null point. The red cross is the point with zero poloidal magnetic field (X-point). The radial and vertical directions (R and z) are represented together with the direction of the associated eigenvectors (blue arrows). The orientation of the null point is defined through the angle α.

The orientation of the null point is, on the other hand, defined as the angle in the counterclockwise direction of the first eigenvector (see Fig. 4.7.6).

The magnetic reconstruction has been validated using a fast tangential visible camera (FastCam, see Sec. 2.4.3.3) installed on TCV. The D_α line radiation increases monotonically with the ionization rate. Supposing, as a zero order approximation, that the same neutral pressure and the same induced electric field inside the VV are present, the ionization rate only depends on the connection length.

The connection length distribution for a typical TCV breakdown is plotted in Fig. 4.7.7(b) together with the reconstructed magnetic field map (Fig. 4.7.7(a)). The connection length distribution is considered independent of the toroidal direction. The image on a virtual camera with same position and orientation of the FastCam is computed. The magnitude of the signal on each simulated pixel is calculated by integrating the connection length over the corresponding view line:

$$P_{i,j} = \int \mathrm{L}\left(R_{i,j}(t), z_{i,j}(t)\right) \mathrm{d}t \tag{4.7.15}$$

where $P_{i,j}$ is the signal on the concerned pixel, L is the connection length as a function of the radial and vertical position expressed in terms of the parametric functions $R_{i,j}(t)$ and $z_{i,j}(t)$. Fig. 4.7.8 shows a comparison of the image form the FastCam and the virtual camera based on the connection length distribution. The good agreement between the two images is considered

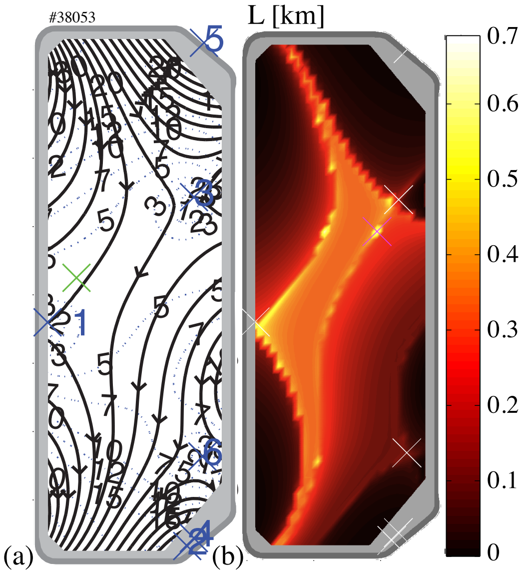

Figure 4.7.7: Magnetic field reconstruction (a) and connection length (b) at the ionization time for a typical TCV breakdown (shot #38053).

as a validation of the magnetic reconstruction code. In addition to the reconstruction errors and optical artifacts, the differences are due to differences in timing. The equilibrium reconstruction code computes the magnetic configuration just before the breakdown (no plasma current) whereas the frame from the FastCam is, evidently, recorded later, close to the maximum of the D_α signal (end of the ionization phase). After few milliseconds, the magnetic configuration may be slightly different due to the evolution of the current in the VV and in the ohmic coils. The differences may also result from an imperfect alignment of the FastCam, since even small errors in the camera position can result in a large error in the camera view angle. Moreover, the radiated light has been considered proportional to the connection length. This is a simplifying assumption since more complex mechanisms, not considered in this comparison, are involved .

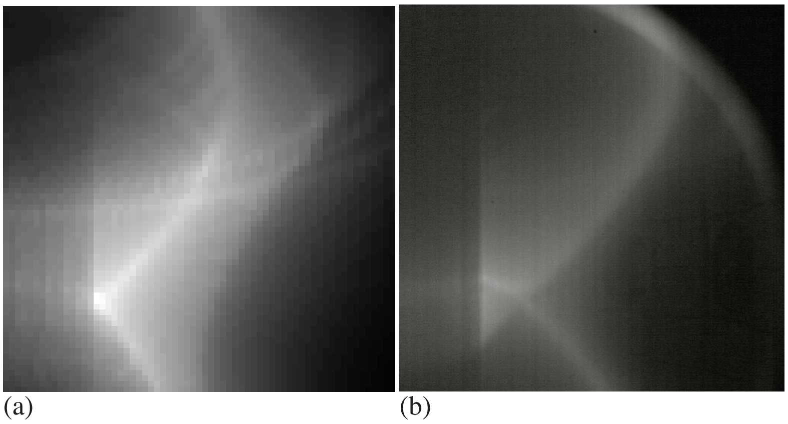
(a) (b)

Figure 4.7.8: (a) 3D visualization of the connection length distribution at the breakdown time ($t = 5.2$ ms); (b) frame from the FastCam at $t = 7$ ms - shot # 38053.

4.8 The ramp-up phase

The analysis of the ramp-up phase differs from the problem of the magnetic reconstruction during the ionization-phase since the plasma current is now a magnetic field source and must be included in the model. Note that in addition to the value of the plasma current, the spatial distribution of the current inside the VV is an unknown of the problem. A single filament model is used to represent the plasma current. The plasma current distribution is therefore characterized by three unknowns: the plasma current and the position of the plasma filament inside the VV (r_P and z_P):

$$\mathbf{m_{ru}} = \mathbf{f_{ru}}\left(\mathbf{I_a}, \mathbf{I_v}, I_P, r_P, z_P\right) = \underline{\underline{M}}_{ru}(r_P, z_P)\left[\mathbf{I_a}; \mathbf{I_v}; I_P\right] \tag{4.8.1}$$

In Eq. 4.8.1, $\mathbf{m_{ru}}$ is the vector containing the measured signals and $\underline{\underline{M}}_{ru}(r_P, z_P)$ is a matrix containing the Green's functions used to couple the sources of the magnetic field with the measured magnetic quantities. $\underline{\underline{M}}_{ru}(r_P, z_P)$ is clearly a function of the plasma filament position.

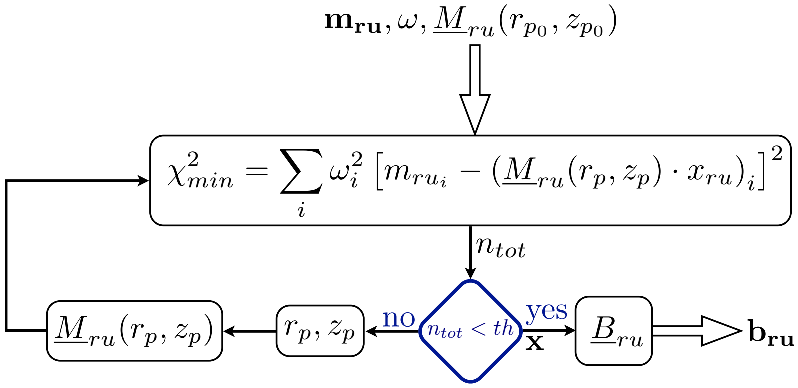

Figure 4.8.1: Flow diagram of the single filament code used to analyze the plasma ramp-up phase.

The flow diagram used to solve Eq. 4.8.1 is shown in Fig. 4.8.1. The problem is reformulated as a nonlinear optimization of the objective scalar multivariable function n^2_{tot} depending on the variables r_P and z_P. The Nelder-Mead algorithm [48] is then used to find a solution, implemented using the fminsearch Matlab function.

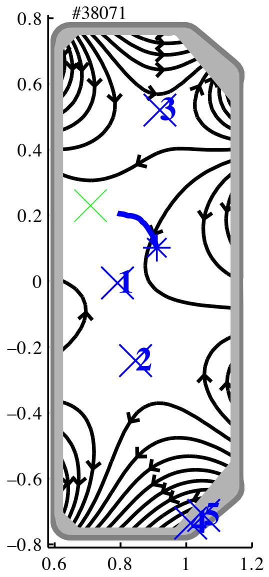

Figure 4.8.2: Magnetic configuration of the breakdown #38071. On the same plot the evolution of the plasma centroid is plotted (blue line). The blue star is the first computed point (I_P = 8 kA); the blue crosses are the positions of the null points during the ionization phase, the green cross is the MGAMS target.

The result of the code is shown in Fig. 4.8.2, where the evolution of the plasma centroid (plasma single filament) is shown for a given TCV shot. The first computed point has a $I_P = 8$ kA. For smaller values of plasma current, the precision of this method is not considered to be sufficient. Moreover, the single filament model may be inappropriate since, for small values of plasma current, no closed magnetic field lines may yet exist. In spite of the limitations of the single filament model, the plasma centroid represented in Fig. 4.8.2 is initially found close to the null point 1 (i.e. the null point with the largest connection length) and later moves towards the programmed plasma position (green cross).

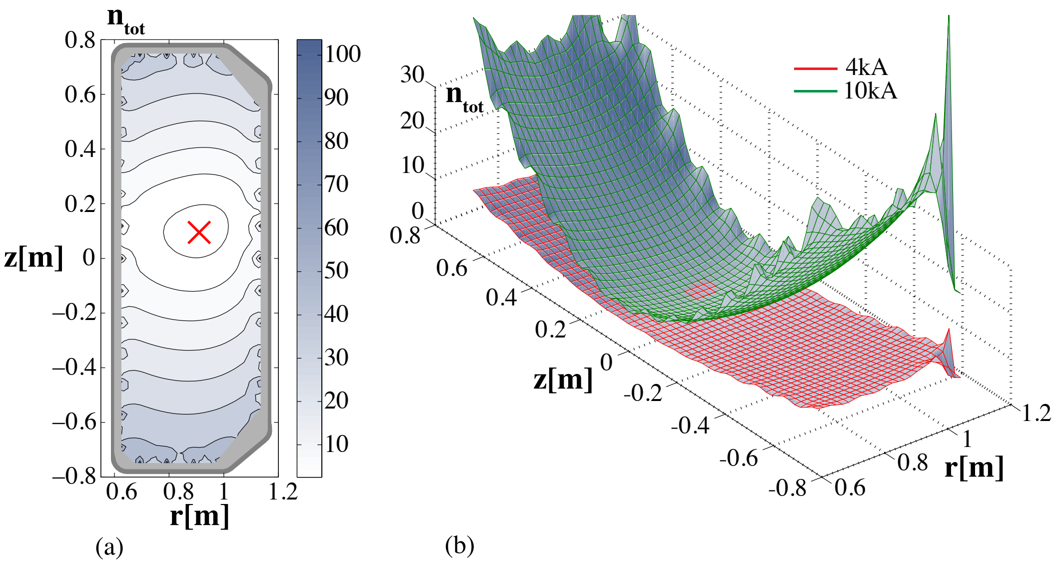

(a) (b)

Figure 4.8.3: (a) Spatial distribution of n_{tot} inside the VV for $I_P = 10$ kA. The position of the plasma current filament corresponds to the minima (red cross). (b) 3D representation of n_{tot} for $I_P = 4$ kA (red) and $I_P = 10$ kA (green)

In Fig. 4.8.3(a), the spatial distribution of the n_{tot} parameter is plotted. The position of the filament corresponds to the position of the minima of n_{tot} (red cross). Since n_{tot} has a single minimum, there is only one solution to the optimization problem. The precision of the reconstruction is better for larger values of plasma current due to the higher values of the measured magnetic quantities. In Fig. 4.8.3(b) a comparison between the case with $I_P = 4$ kA and $I_P = 10$ kA is shown. The value of n_{tot} at the minimum point is the same for the two cases but the depth of the minimum is accentuated for the larger plasma current.

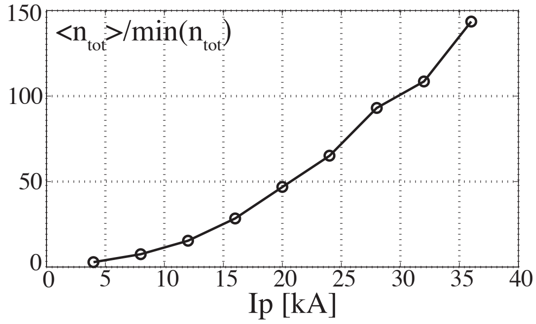

Figure 4.8.4: Ratio between the average value of n_{tot} and its minimum value inside the VV. This parameter is proportional to the depth of the n_{tot} minima.

This aspect is summarized in Fig. 4.8.4, where the ratio between the average value of n_{tot} and its minimum value is plotted as a function of I_P.

4.9 Statistical analysis of the breakdown

The magnetic configuration of ~ 20000 discharges has been analyzed using the code described in the previous sections and the breakdown information stored in a database. Shots are then grouped in 240 clusters characterized by equal MGAMS parameters used to program the breakdown. Within each cluster the same breakdown position, number of null point, null point orientation and topology (quadrupole, sextupole, ...) are present.
The main objective of the statistical analysis is to identify regions of the operational space with higher probability of success on plasma start-up. Different indicators of a plasma failure (blip) have been used. The simplest one is based on the maximum value of the plasma current ($\max(I_P)$). A discharge with $\max(I_P) < I_P^{TH}$ is considered as a blip, where I_P^{TH} is the chosen threshold. Another indicator used to detect a plasma blip is the integral of the plasma current ($\int I_P \mathrm{d}t$). A blip is detected if $\int I_P \mathrm{d}t < TI_P^{TH}$, with TI_P^{TH} equal to an empirical threshold. An advantage this indicator is that discharges with low flat-top plasma currents are not considered as blips.
To identify the role played by the magnetic configuration at the breakdown time, the ionization must be spatially localized for each shot. From observations reported in Section 4.7, the null point with the longest connection length could be considered as the ionization location. However, there are magnetic configurations where the ionization starts at a null point close to the central column, even if the connection length there is not the longest. This is due to the different toroidal electric field inside the VV, which decreases with the radial distance R. The ionization rate is therefore used as a parameter to select the null point where the ionization starts. The ionization rate is a function of the electric field, the connection length and the neutral gas pressure ($\nu_{\mathrm{ion}} = \nu_{\mathrm{ion}}(E, L, p)$). For each null point, the electric field and the connection length are computed. Since the neutral gas pressure is not measured, ν_{ion} is calculated for several values of p between 10^{-4} Pa and 10^{-1} Pa. The null point with the largest value of the mean ionization rate over p is then selected.
In Fig. 4.9.1, each breakdown (grey points) is classified as a function of the toroidal electric voltage (V_{loop}) and the connection length (L) at the selected null point, the breakdown time (t_b) and the plasma current ramp rate ($\mathrm{d}I_P$). The last parameter is defined as:

$$\mathrm{d}I_P = \frac{I_P\left(\max(\mathrm{D}_\alpha)\right)}{t\left(\max(\mathrm{D}_\alpha)\right) - t_b} \tag{4.9.1}$$

where $I_P\left(\max(\mathrm{D}_\alpha)\right)$ and $t\left(\max(\mathrm{D}_\alpha)\right)$ are respectively the plasma current and the time instant at the maximum of the D_α signal. $\mathrm{d}I_P$ is therefore the mean value of the time derivative of I_P during the ionization phase.
Figure 4.9.1(a) shows that V_{loop} increases monotonically with the breakdown time t_b. The highest values of connection length are reached for breakdowns characterized by $V_{\mathrm{loop}} \sim 10$ V (see Fig. 4.9.1(b)). The reason is shown in Fig. 4.5.1, where the evolution of V_{loop} and L is shown for a typical TCV breakdown. V_{loop} rises and reaches ~ 10 V at $5-10$ ms. If no breakdown occurs, V_{loop} is further increased by the plasma control feedback system (see Fig. 4.9.2). The usual behavior of the connection length is shown on Fig. 4.5.1(b); it reaches a maximum around $5-10$ ms and then decreases. This is in agreement with the MGAMS request, i.e. the magnetic configuration optimized for $t \sim 0$. Later, the currents in the VV change together with the current in the ohmic coil and, consequently, the magnetic configuration is modified.
Breakdowns in the $L - V_{\mathrm{loop}}$ plane were divided into four clusters. The first three clusters all have $L < 1.6$ km, and we divided into ranges of toroidal electric voltage: $V_{\mathrm{loop}} < 9$ V, $9 \text{ V} < V_{\mathrm{loop}} < 11$ V and $V_{\mathrm{loop}} > 11$ V. The fourth cluster collects breakdowns with $L > 1.6$ km. The centroids of the clusters are shown in Fig. 4.9.1 with square-markers. The large squares delimit the range that

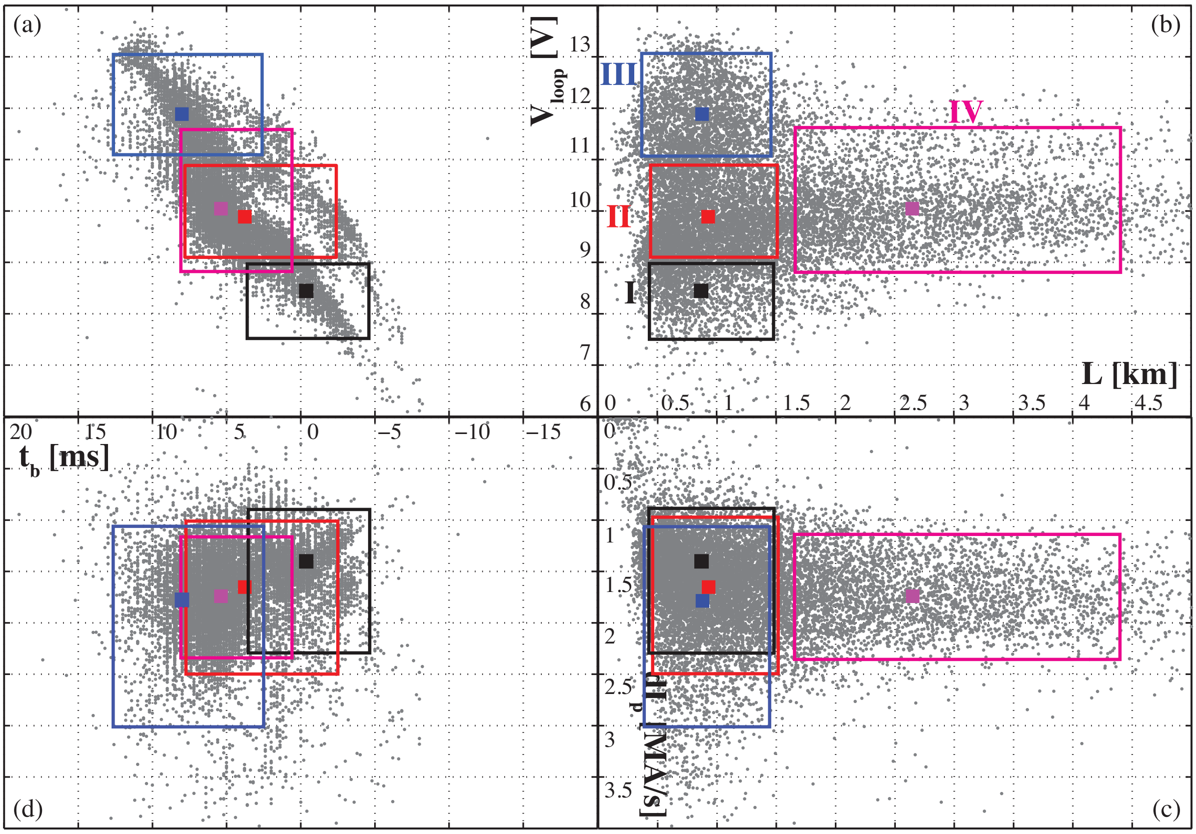

Figure 4.9.1: Breakdown conditions in the $V_{\rm loop} - t_b$ plane (a), $V_{\rm loop} - L$ plane (b), $t_b - dI_P$ plane (c) and $L - dI_P$ plane (d) The squared regions are clusters. Their centroid is represented with a small square.

	I	II	III	IV
$I_P \cdot t < 25$ kAs	12.8%	10.3%	11.2%	6.3%
$I_P < 50$ kA	7.3%	7.5%	8.3%	4.0%
$I_P < 10$ kA	2.3%	3.0%	3.1%	1.1%

Table 4.1: Blip rate computed using different methods for the clusters in Fig. 4.9.1.

incudes 90% of points in the considered cluster. The current derivatives for cluster III are the largest. This is due to the higher value of $V_{\rm loop}$. Moreover, since the breakdowns for cluster III occur later, the plasma current takes more time to reach the plasma current reference and $V_{\rm loop}$ remains high during the first part of the ramp-up phase.

The blip rates for the different clusters are summarized in Table 4.1.

Clusters I, II and III have approximately the same blip rate. Cluster IV has a blip rate that is smaller by a factor two. The main difference between cluster IV and the others is that cluster IV has a longer connection length. Since the end of the ionization phase initiates the ramp-up phase, a large connection length statistically improves the quality of the ionization phase and, consequently, the ramp-up phase.

In Fig. 4.9.3, the size of the null point, expressed as the equivalent radius ρ previously defined, is plotted as a function of L for each breakdown. There is a linear relation between the two quantities, which can be expressed as:

$$\rho[\mathrm{m}] \sim 8 \times 10^{-8} L[\mathrm{km}] \qquad (4.9.2)$$

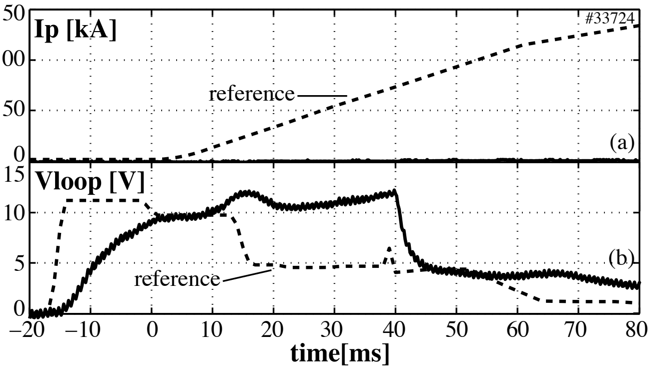

Figure 4.9.2: Plasma breakdown failure: (a) pre-programmed plasma current waveform (dashed line) and plasma current; (b) toroidal electric voltage and its reference trace (dashed line).

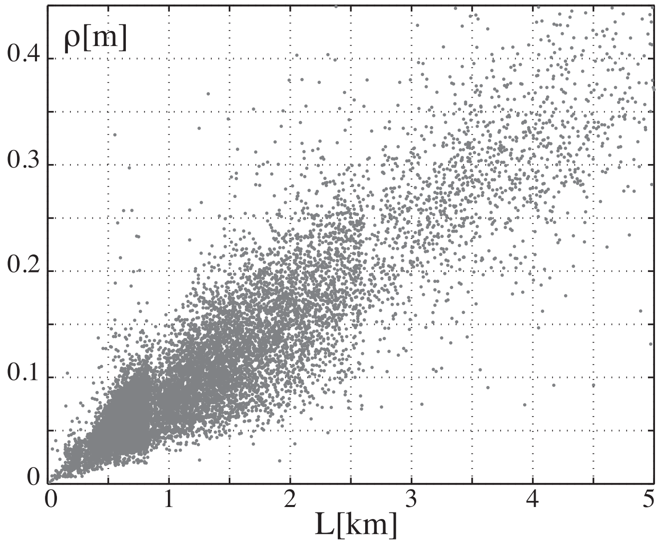

Figure 4.9.3: Size of the null point expressed as the equivalent radius ρ as a function of the connection length L.

The difference between each breakdown point and the fitting curve is due to the specific properties of the specific magnetic configuration. When the null point is very close to the VV wall, even if the null point is large, the magnetic field lines soon intersect the wall such that the connection length is smaller than that predicted from the fit. On the other hand, even for small null points, the connection length can be very long due to the presence of another null point located close to the path of a considered magnetic field line.

In Fig. 4.9.4 each breakdown is represented as a point in the plane $\rho-\alpha$, where α is the null point orientation and ρ is its equivalent radius. Note that for breakdowns with negative plasma current, α has been corrected as follows:

$$\alpha = 180\text{deg} - \alpha \tag{4.9.3}$$

The breakdown points are classified in six clusters, as shown in Fig. 4.9.4. The blip rate for each cluster is summarized in Table 4.2.

The blip rate is slightly reduced for null points with $\alpha > 90$ deg, i.e. $\partial_Z B_R > 0$ (plasma vertically stable).

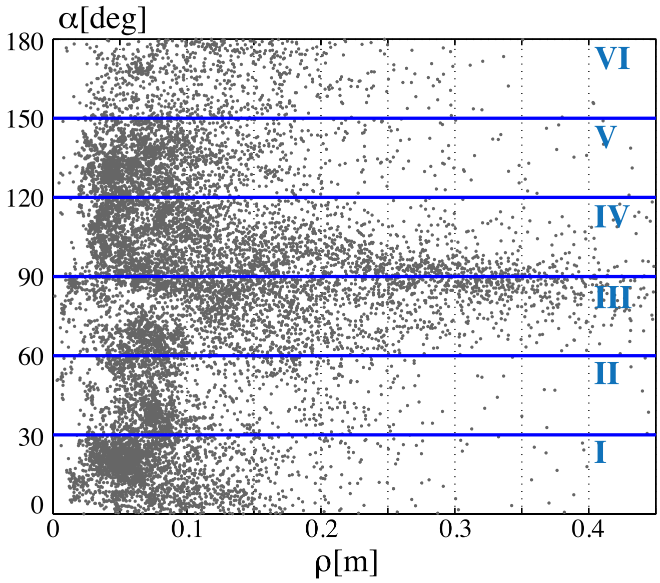

Figure 4.9.4: Orientation, α, of the null point as a function of the equivalent radius ρ. The blue lines delimit six clusters.

	I	II	III	IV	V	VI
$I_P \cdot t < 25$ kAs	11.7%	14.1%	10.5%	5.9%	8.7%	10.5%
ρ [m]	0.07	0.10	0.17	0.14	0.09	0.12

Table 4.2: Blip rate and mean size of the clusters represented on Fig. 4.9.3.

4.10 Assisted plasma start-up with ECH-X2

Understanding the physics of the assisted plasma start-up with ECH-X2 is important for upcoming tokamaks like ITER and KSTAR, where the maximum available electric field is limited by a thick VV and the presence of superconducting coils. The plasma initiation and burn-through with limited toroidal electric field may be problematic (see Sec. 4.5) and some additional power may be required for reliable plasma startup.

Much research has already been reported for assisted plasma start-up with ECH-X1 (first harmonic) [49, 50, 51, 52, 47, 36, 53, 54]. Experiments in the TCA tokamak, at the CRPP, explored assisted breakdown with ECH-X1 and ECH-O1 [36]. More recently, ECH-X2 assisted breakdown has been studied by several authors [54, 55, 56].

Several experiments were performed on TCV to investigate the assisted ECH-X2 plasma start-up. In this section, the physics of the ECH assisted breakdown is summarized (Sec. 4.10.1) and some TCV experiments are presented and discussed in Sec. 4.10.2.

4.10.1 The physics of the ECH assisted plasma start-up

Before ionization commences, a small fraction of the free electrons are distributed uniformly inside the VV. These electrons can interact with a linearly polarized EC wave in the resonant region as follows:

$$\begin{aligned}\frac{\mathrm{d}v_x}{\mathrm{d}t}+\Omega_e v_y &= 0\\ \frac{\mathrm{d}v_y}{\mathrm{d}t}-\Omega_e v_x &= -\frac{e}{m_e}E_0\sin(k_0x-\omega t)\\ v_z &= v_z^{\mathrm{th}}\end{aligned}\tag{4.10.1}$$

Equations 4.10.1 describe the electron motion in Cartesian coordinates, where E_0 is the EC electric field amplitude, ω is the EC frequency, $k_0 = \omega/c$, $B_z = B_\phi$ and v_z^{th} the thermal velocity in the z direction. The condition $v_z = v_z^{\mathrm{th}}$ is valid only if $L_{\mathrm{heat}} << \lambda_{en}$, where L_{heat} is the electron heating length, i.e. the toroidal distance where electrons interact with the EC wave and $\lambda_{en} = 1/\nu_{en}$.
Initially electrons are cold and the heating efficiency is small ($k_0\rho_e << 1$). Nevertheless, the heating rate is positive since the collision mean-free path is long and electrons may therefore be accelerated. Electrons that will leave the resonant region following magnetic field lines may then ionize neutrals. The ionization energy may result either entirely from the EC wave (pre-ionization) or only in combination with acceleration in the ohmic electric field. The EC is often injected a particular toroidal location so that, after one toroidal turn, the same electrons, together with the new created electrons, may again pass through the resonance region. This leads to an electron multiplication phenomena similar to the one described by the Townsend theory. Once a plasma channel is created, the plasma column moves towards the first MHD equilibrium location and the ramp up phase ensues.
Many parameters influence the scenario described above. The wave polarization, the EC injected power, the size of the resonance layer and of the poloidal magnetic field can change the efficiency of the early EC absorption and of the electron multiplication phase. In the next subsection, several experiments conducted on TCV to study the incidence of the listed parameters are presented.

4.10.2 ECH-X2 assisted plasma start-up experiments

The typical TCV assisted EC-X2 plasma start-up scenario is shown schematically in Fig. 4.10.1. The EC power is injected in the VV 15 ms before the expected breakdown time and mantained for 30 ms. The poloidal magnetic configuration is chosen such that no ionization occurs without EC injected power.
The first investigated parameter is the EC-X2 **power**. The same scenario in Fig.4.10.1 was repeated changing the EC-X2 input power. For high injected EC power, the breakdown occurs earlier and for smaller values of toroidal electric field (Fig. 4.10.2). Moreover, the reliability of the breakdown is clearly improved when the breakdown is assisted with EC, with a drastic reduction of the number of breakdown failures. For all these discharges, the poloidal magnetic field configuration is constant and the EC power is injected from the LFS equatorial port (see Fig. 4.10.3). The EC toroidal angle is 104 deg (counter-injection) and the EC poloidal angle, i.e. angle between the EC beam and the horizontal $z = 0$ plane, is 35 deg. Note that no pre-ionization is observed in contrast to experiments reported in [55], probably due to only half the injected EC-X2 power in the TCV experiments.
A variation of the breakdown dynamic is observed when the toroidal angle of the injected beam is changed. The fastest burn through of D_α is obtained with an EC incident angle of 90 deg, even though little variation of the breakdown time is observed (Fig. 4.10.4). During this scan the EC poloidal angle was kept constant at (35 deg) and the EC power equal to 260 kW.
Finally, the effect of the EC polarization on the breakdown was investigated. More prompt ramp-ups are obtained with the X-polarization, as shown in Fig. 4.10.5. The compared discharges are

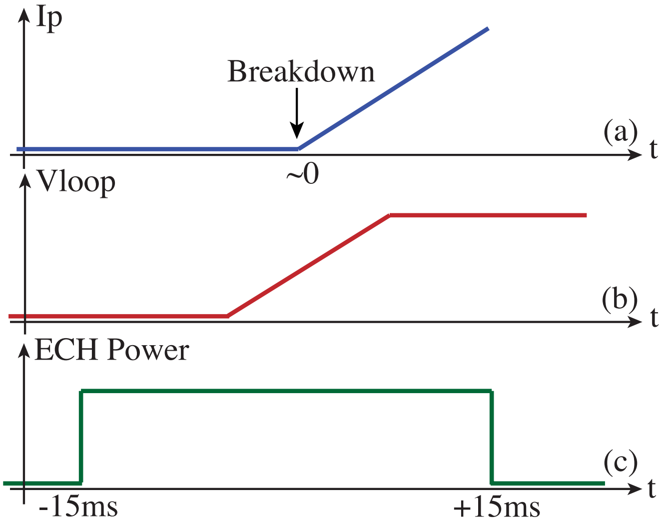

Figure 4.10.1: Assisted plasma start-up with EC scenario: (a) plasma current, (b) toroidal electric voltage and (c) EC-X2 power.

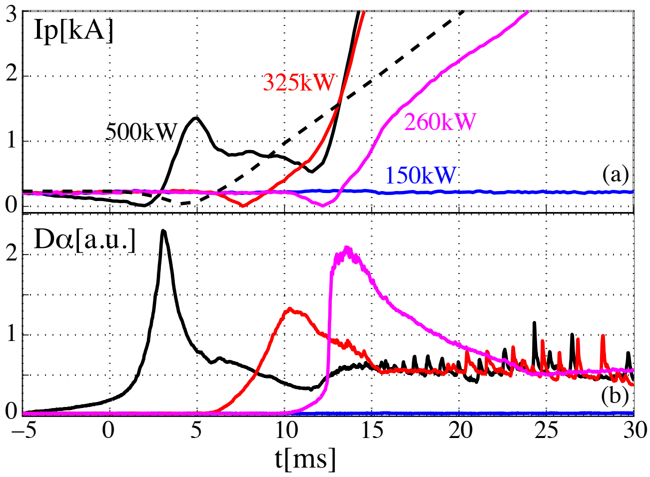

Figure 4.10.2: Assisted plasma start-up with EC scenario: scan of the input power. (a) Plasma current and (b) D_α signal.

characterized by an EC input power of 260 kW, a poloidal EC angle of 35 deg and a toroidal EC angle of 104 deg.

4.10.3 Conclusions

In this chapter inductive and the assisted plasma start-up with ECH-X2 in TCV has been described. For inductive plasma start-up, the tools used to create a plasma have been described. The general theory to describe the ionization phase and the ramp-up phase has been reported and applied to the TCV case. A model to analyze the poloidal magnetic configuration during the plasma start-up has been developed and a statistical analysis based on the results of this model showed the importance of having a magnetic configuration at the breakdown time characterized by a long connection length in the ionization region.
The last part of the chapter was dedicated to the assisted plasma start-up with EC-X2. Starting from a simple qualitative description of the EC-X2 assisted plasma start-up, TCV experiments were reported where some EC parameters have been changed to study their influence on the EC-X2 absorption efficiency. Unfortunately, it has not been possible, due to time restrictions, to

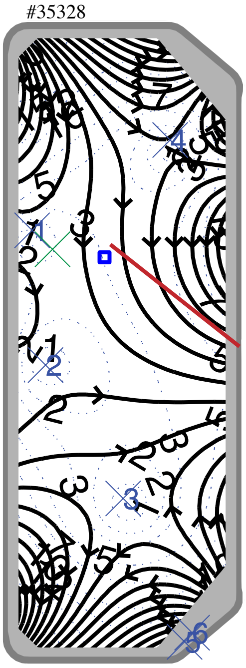

Figure 4.10.3: Magnetic field reconstruction at the breakdown time. The red line represents the EC-X2 beam and the blue square the plasma filament at the beginning of the ramp-up phase as detected with the single filament model.

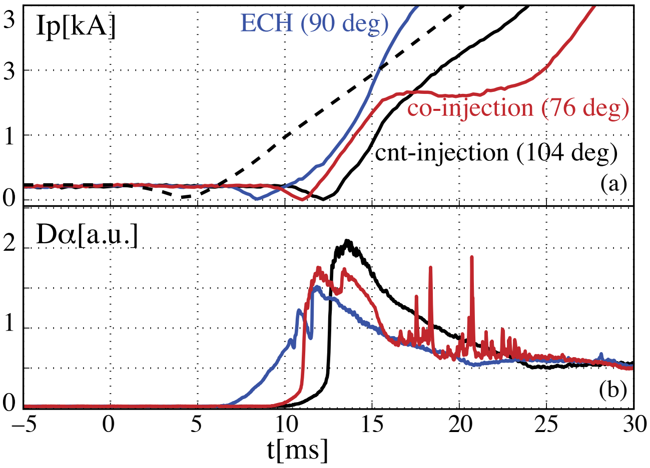

Figure 4.10.4: Assisted plasma start-up with EC scenario: scan of the toroidal angle. (a) Plasma current and (b) D_α signal.

further this work on the assisted plasma start-up with EC-X2. Future activities in this field should include the detection of the conditions necessary to obtain pre-ionization, an analysis of the effect of the variation of the poloidal magnetic field in the resonance region and the development of a model to better describe the experimental observations in the presence of strong EC.

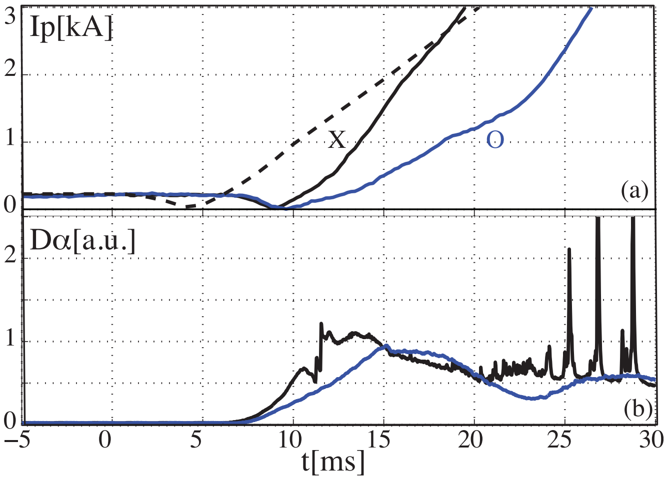

Figure 4.10.5: Assisted plasma start-up with EC scenario: scan of the toroidal angle. (a) Plasma current and (b) D_α signal.

Chapter 5

Doublet shaped plasmas

5.1 Introduction

A doublet shaped plasma is a tokamak MHD equilibrium characterized by two plasma currents confined with nested magnetic flux surfaces (Fig. 5.1.1(b)). Since the two plasma currents have the same toroidal direction, a magnetic X-point is present between the two plasma axes. The magnetic flux surface that contains the X-point is the separatrix.
In a conventional diverted single-axis plasma (Fig. 5.1.1(a)), the X-point defines the position of the separatrix which corresponds to the plasma boundary. Outside the separatrix, the magnetic field lines are open and intersect the divertor plates through the Scrape-Off Layer (SOL). In a doublet shaped plasma, outside the internal separatrix there is a region with closed magnetic field lines (mantle) delimited externally by the plasma boundary and the SOL (Fig. 5.1.1(b)).

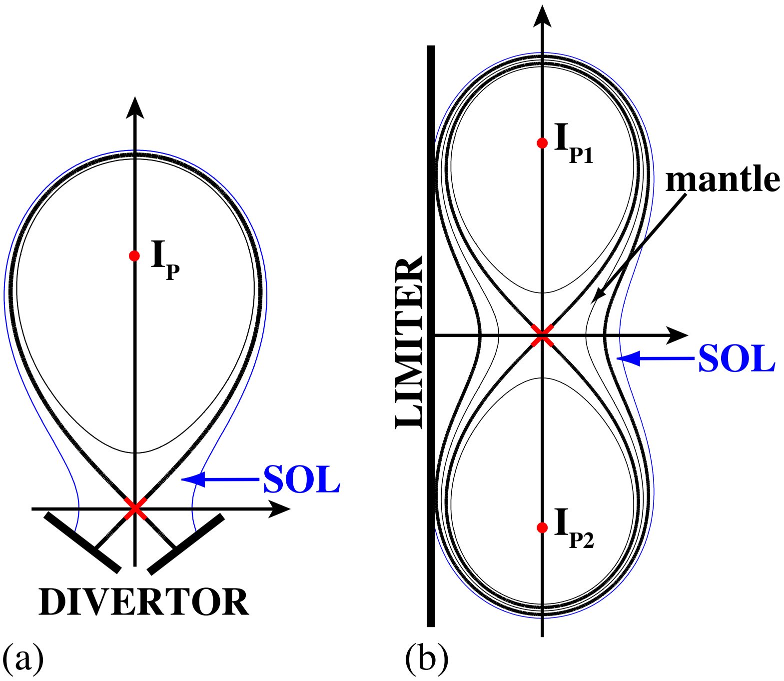

Figure 5.1.1: Conventional single-axis diverted plasma (a) and doublet shaped plasma (b) in a straight filamentary tokamak model. The red circles represent the current filaments and the red crosses the X-points.

Several doublet configurations can be obtained by changing the thickness of the mantle outside the internal separatrix (Fig. 5.1.2). The thickness of the mantle is quantified by the ratio between the poloidal flux at the separatrix Ψ_s and the poloidal flux at the plasma boundary Ψ_b. The general properties of the configuration may be related to this parameter. Doublets without a mantle are characterized by $\Psi_s/\Psi_b \sim 1$.

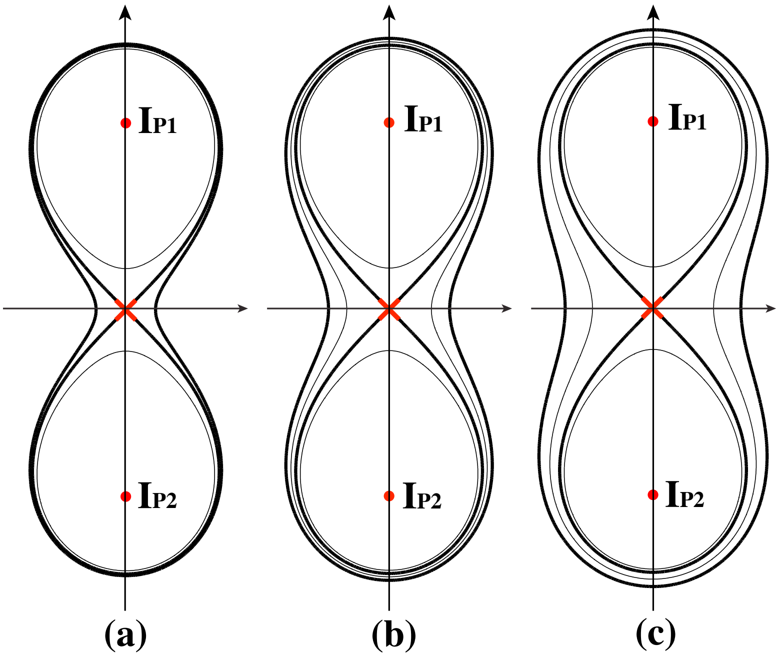

Figure 5.1.2: Doublet configurations in a straight filamentary model with (a) $\Psi_s/\Psi_b = 0.99$, (b) $\Psi_s/\Psi_b = 0.98$ and (c) $\Psi_s/\Psi_b = 0.96$.

If the two lobes have different plasma current and/or plasma shape, the resulting equilibrium is called an asymmetric doublet (Fig. 5.1.3(b)). In this configuration, the smallest plasma (I_{P2} in Fig. 5.1.3(b)) should only be useful for creating the X-point and the plasma mantle around the boundary of the main plasma (I_{P1}), characterized by a better confinement. This configuration may lead to a better use of the magnetized volume in a tokamak.

Figure 5.1.3(c) shows another possible doublet configuration with a divertor system. The divertor coils create a second X-point and an external separatrix. This configuration may have some interesting properties since it should maintain the advantages of diverted configurations, i.e. good management of heat and particle exhaust and core impurity concentration. Moreover the large values of magnetic shear close to the two X-points may give additional interest to this unusual configuration.

Doublet shaped plasmas were studied at General Atomics for many years [57,58,59]. Research in this field was stopped in 1984, when Doublet III was converted into DIII-D [60]. Compared with conventional tokamak circular shaped plasmas, this configuration had the advantage of reducing the plasma turbulence due to the good features of the configuration, i.e. the magnetic well and the magnetic shear [57]. Moreover, since in doublets the aspect ratio is quite different from the circumferential ratio, i.e. the ratio between the poloidal and toroidal circumference of the plasma [61], the upper limit for β was considerably larger than that of circular plasmas [62].

Later results on Doublet III showed that a larger magnetic shear could be obtained by creating an X-point with external coils, i.e. in a diverted plasma configuration. Moreover, the advantage of having a higher β limit was shown to be comparable with that of plasmas with elongation similar to the overall doublet elongation [63]. The current limit against kink modes was found to be lower for doublets, even if the maximum β was obtained at almost the same value of plasma current [63].

More recently, the doublet has received renewed interest [64] because it has an intrinsic zone of negative shear, which is tied to the magnetic configuration and does not depend on a hollow current profile. Negative magnetic shear is generally thought to have beneficial effects on plasma

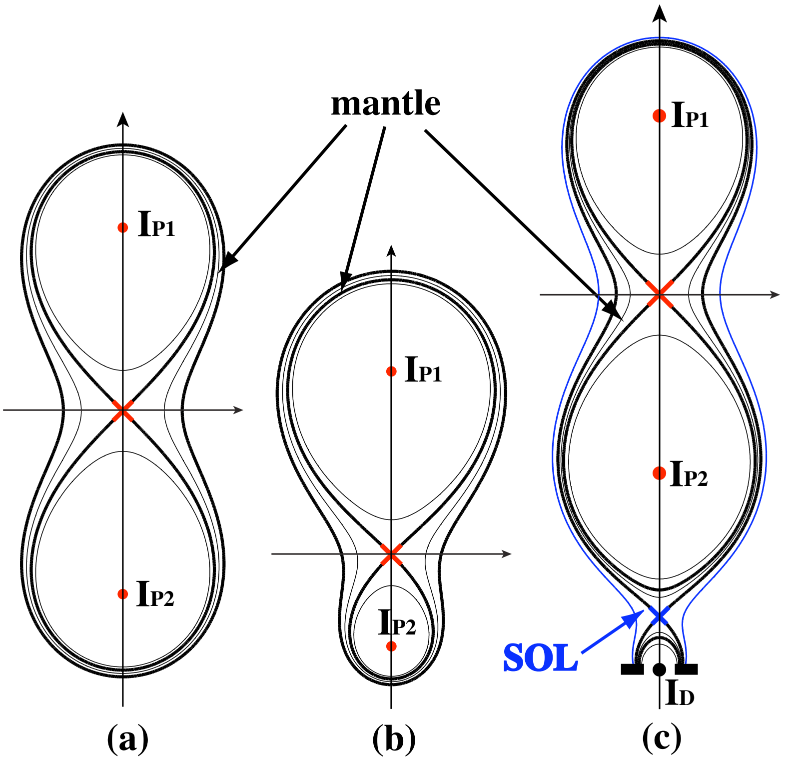

Figure 5.1.3: Doublet configurations in a straight filamentary model. (a) Symmetric doublet, (b) asymmetric doublet and (c) diverted symmetric doublet.

confinement in tokamaks [65]. The hope is to create a plasma barrier, equivalent to an H-mode edge barrier, at the location of the internal separatrix. This configuration should bring several benefits:

1. In single-axis plasmas, outside the separatrix, the magnetic field lines are open (SOL). Power escaping the core region reaches the plasma facing components (PFCs) after a SOL characteristic time $\tau_{SOL} \sim L_x/c_s$, where L_x is the SOL connection length and $c_s \sim [k(T_e + T_i)/m_i]^{1/2}$ is the sound speed. Choosing $T_e = T_i = 25$ eV, $c_s \sim 5 \times 10^4$ ms^{-1} and $L_x = 10$ m (typical of TCV diverted configurations), the SOL characteristic time is $\tau_{SOL} \sim 0.2$ ms.

   In a doublet configuration, particles that cross the internal separatrix reach the mantle, a region with closed magnetic field lines. The mantle characteristic time (τ_{MTL}) is related to the cross-field transport by $\tau_{MTL} \sim \Delta^2_{MTL}/D_\perp$, where Δ_{MTL} is the radial thickness of the doublet mantle and $D_\perp$ is the cross-field diffusion coefficient. Supposing $\Delta_{MTL} = 5 \times 10^{-2}$ m for a hypothetical TCV doublet and $D_\perp = 1$ m^{2}s^{-1} similar to typical SOL cross-field diffusion coefficients [66], the obtained mantle characteristic time is $\tau_{MTL} \sim 2.5$ ms. Therefore, since $\tau_{MTL} > \tau_{SOL}$, the heat flux on doublet PFCs should be reduced. Ideally, a layer of cold plasma should be confined in the doublet mantle, characterized by a high fraction of volumetric losses that should decrease the plasma temperature and reduce the effective power reaching the SOL and the PFCs.

2. Kink/ballooning instabilities, possibly present in the plasma pedestal created at the internal separatrix, may be less problematic since the pulsed ejected power (ELM like) should not directly reach the PFCs due to the attenuation effect given by the volumetric losses in the doublet mantle.

3. Some current could be driven at the internal separatrix ohmically or with ECH. This may simplify the access to the second stability region for high-n ballooning modes.

   Moreover, the variation of the current density and pressure profile in a relatively thin plasma layer outside the separatrix may influence the global external kink mode stability and change the β limit [67,68].

Another important property of doublets is the reduced vertical instability growth rate compared with D-shaped plasmas with the same overall elongation [63]. Higher values of β can be obtained increasing the plasma elongation κ [6]. On the other hand, the vertical instability growth rate increases with κ. The vertical stability of a doublet configuration is close to a single axis equilibrium equivalent to one half of the doublet both in terms of marginal wall position and resistive wall growth rates [69]. Higher values of β can therefore be obtained in a doublet configuration for similar values of vertical instability growth rate.

Doublet plasmas may also provide important knowledge concerning H-mode [70, 71] physics. It is well known that the location of the X-point in single-axis plasmas affects the L-H mode transition [71]. The H-mode power threshold changes with the direction of the ion $B \times \nabla B$ drift with respect to the X-point and it is higher for limited plasmas [71]. Having an unusual internal X-point, the doublet configuration may be a good candidate to verify present models of the L-H mode transition.

It should also be mentioned that these experiments may help in understanding the physics of magnetic reconnection, since the process that leads to the creation of an internal separatrix may be the result of a magnetic reconnection phenomenon [64].

These many interesting properties of the doublet configuration generate a strong motivation to study it. TCV is now the only tokamak worldwide capable of creating a doublet shaped plasma. This is mainly due to the high ratio between the height and the width of the vessel poloidal cross-section (2.6) and the flexibility given by the 16 independently powered shaping coils. In the following sections a preliminary investigation to verify the capability of TCV for doublet creation is presented. The possible scenarios are introduced and compared in Sec. 5.2. The stability of a doublet configuration is then analyzed in Sec. 5.3 and a possible control strategy is presented in Sec. 5.4. Finally, the problem of the double plasma start-up is faced in Sec. 5.5 where some preliminary experimental results are presented.

5.2 Doublet scenario

Only limited, symmetric doublets will be considered in the following sections. Three theoretical scenarios for creating doublets can be considered, as documented in [64]. They will be considered in turn in the following.

5.2.1 Lateral constriction of highly elongated, racetrack-shaped plasma

Figure 5.2.1 shows a sequence of theoretical free-boundary tokamak equilibria computed with FBTE [39] illustrating this scenario. Stability analysis of these equilibria shows that the vertical growth rate first increases as the elongation grows, then goes through a maximum, and finally decreases. The maximum growth rate is reached at the time when the internal separatrix begins to form. Its value depends on the assumed current profile functions. For typical TCV profiles, the intermediate configurations are ideally unstable. For this reason, no experimental work has been devoted to this scenario.

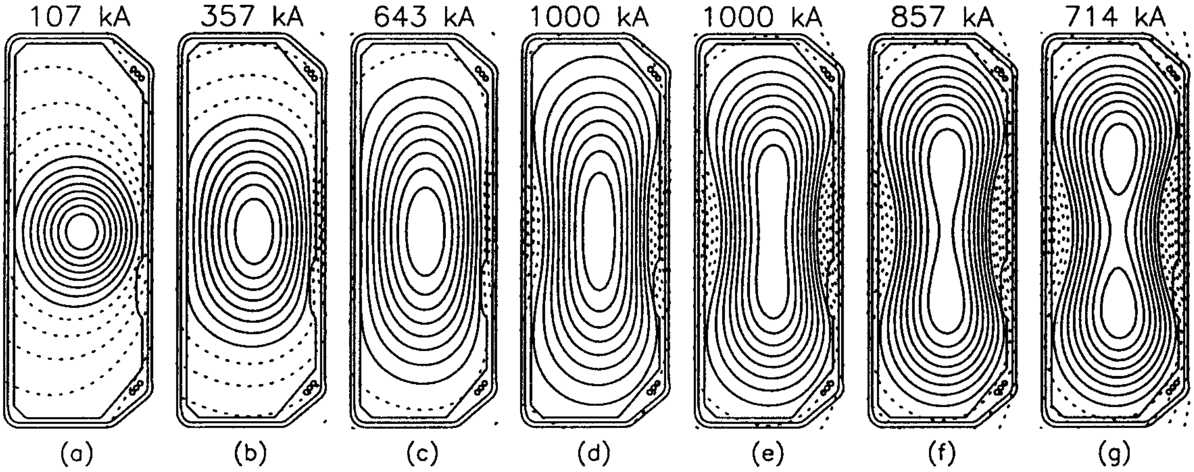

Figure 5.2.1: Theoretical scenario for creating doublets by lateral constriction.

5.2.2 Hour-glass scenario

This scenario (Fig. 5.2.2) begins with a pear-shaped plasma representing the upper lobe of the doublet. The poloidal flux is controlled in such a way that it stays constant on the boundary of the final doublet shape. When the current is gradually increased under these conditions, the plasma spills over into the lower lobe, an internal separatrix appears and finally the currents in the two lobes become equal.

However, the stability of the intermediate equilibria in this scenario depends on the assumed current profile. For broad current profiles, all equilibria exist, as shown in Fig. 5.2.2, whereas for peaked profiles, the highly asymmetric doublet (Fig. 5.2.2(e)) cannot exist in the sense that they cannot be generated with the TCV poloidal field coils. The boundary between existing and non-existing equilibria manifests itself by an extreme sensitivity of the plasma shape to small variations in the coil currents.

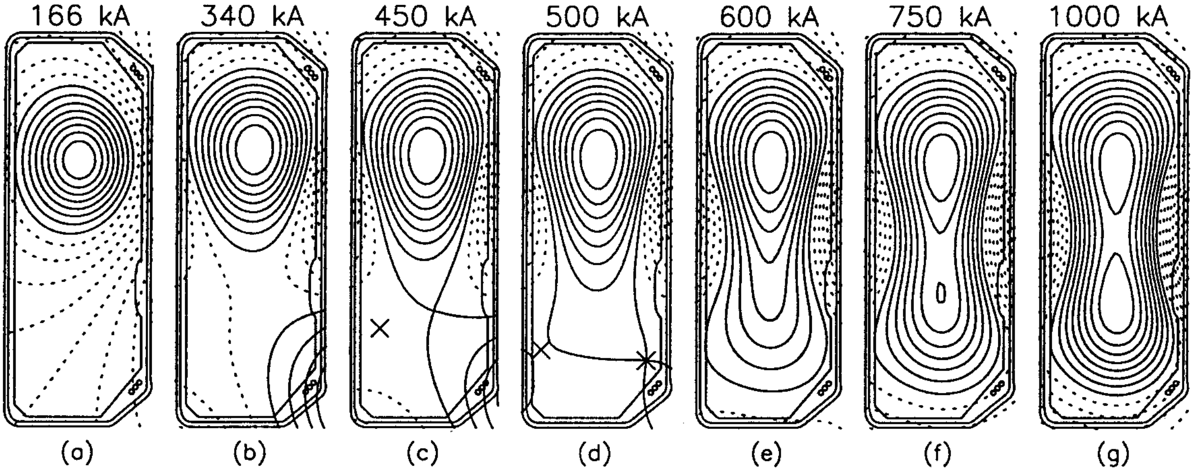

Figure 5.2.2: Theoretical scenario for creating doublets by “spill-over”.

5.2.3 Merging two droplet-shaped plasmas

This was the preferred scenario in the original doublet experiments at GA [59]. A sequence of theoretical equilibria based on the TCV geometry is shown in Fig. 5.2.3.

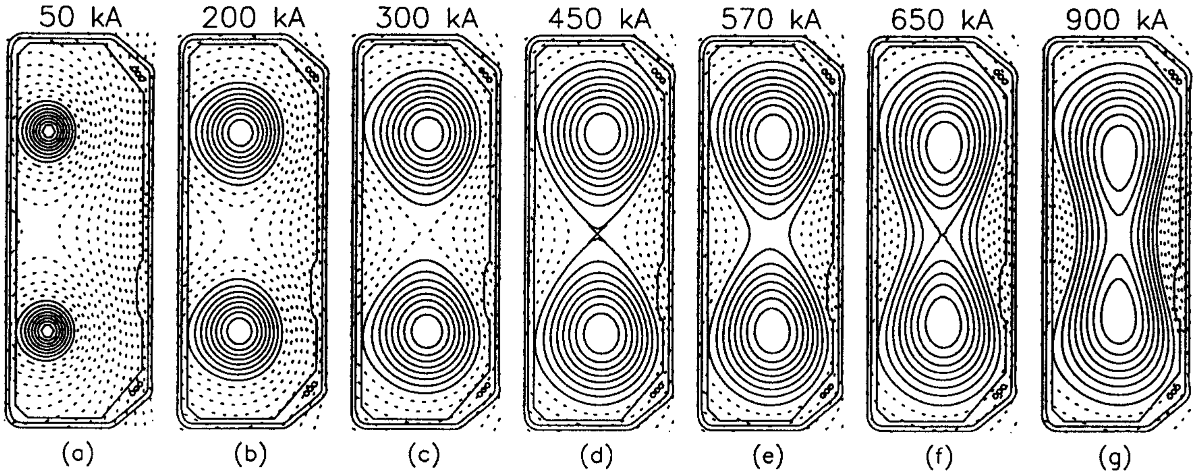

Figure 5.2.3: Theoretical scenario for creating doublets by merging two plasmas.

In order to create two plasmas, the breakdown at the two magnetic nulls must be simultaneous, because if one plasma starts up slightly too early it destroys the field null for the other plasma. If the two currents are roughly equal, they can both grow and finally merge to form a doublet. This is the scenario that has been chosen for attempts at doublet creation on TCV.

5.3 Doublet vertical stability

The vertical stability of symmetric and asymmetric doublets has been previously studied in [63,72] using the equilibrium code CAXE [72] and the stability code KINX [73]. The characteristic feature of the doublet $n = 0$ stability is the presence of two unstable modes. The more unstable mode features a mirror symmetric displacement of the two domains inside the outer separatrix. Conversely, the less unstable mode is characterized by a displacement of the two plasma columns in the same vertical direction. A comparison shows that the $n = 0$ mode growth rate is much lower for doublets than for a single-axis plasmas with the same overall elongation, with a larger difference for asymmetric doublets.

In this section, a simple model to describe the doublet vertical stability is described. The results of the analysis are used to define a possible TCV scenario for doublet creation.

5.3.1 Doublet Rigid Model

The stability is analyzed using a linear electromagnetic model of a system of two plasmas surrounded by the TCV VV. The two plasmas can move inside the VV but no deformation is allowed (Rigid Model). Similarly to what was already described in [74, 75] for single-axis plasmas, the plasma inertia is neglected since it does not play an important role for low growth rates of the unstable modes ($\gamma < 1000\ \mathrm{s}^{-1}$), i.e. rates which are controllable by the feedback control system on TCV [76]. The two plasmas can only rigidly shift vertically inside the VV. To simplify further, current in the PF coils is assumed to be constant and the variation of the plasma current is neglected. The TCV VV is modeled with 38 magnetically coupled filaments (see Sec. 2.4). The interaction between the VV filaments and the plasma currents is given by the following equation:

$$0 = \underline{\underline{R}}_{vv}\mathbf{I}_v + \underline{\underline{M}}_{vv}\delta\mathbf{I}_v + \frac{\mathrm{d}\underline{\underline{M}}_{vP1}}{\mathrm{d}z_1} I_{P1_0}\delta z_1 + \frac{\mathrm{d}\underline{\underline{M}}_{vP2}}{\mathrm{d}z_2} I_{P2_0}\delta z_2 \tag{5.3.1}$$

where z_i is the vertical position of the i-th plasma and $\underline{\underline{M}}_{vPi}$ is the mutual inductance between the VV filaments and the i-th plasma current. All the quantities dependent on the plasma equilibria are obtained by averaging over the plasma current distribution derived from a doublet shaped plasma equilibrium:

$$G_i = \frac{\sum_h g_i(R_h, z_h) j_i(R_h, z_h)}{\sum_h j_i(R_h, z_h)} \tag{5.3.2}$$

where j_i is the current density distribution for the i-th plasma, R and z are the radial and the vertical coordinates and g is the considered quantity.
The vertical force balance equation ($\delta F_{zi} = 0$) for the two plasmas is:

$$0 = -\frac{\partial \underline{\underline{M}}_{vP1}}{\partial z_1} \delta \mathbf{I}_v + (\alpha_{11} + \beta_1) I_{P1_0} \delta z_1 + \alpha_{12} I_{P2_0} \delta z_2 \tag{5.3.3}$$

$$0 = -\frac{\partial \underline{\underline{M}}_{vP2}}{\partial z_2} \delta \mathbf{I}_v + \alpha_{21} I_{P1_0} \delta z_1 + (\alpha_{22} + \beta_2) I_{P2_0} \delta z_2 \tag{5.3.4}$$

with:

$$\alpha_{11} = \frac{2\pi R_{1_0}}{I_{P1_0}} \frac{\partial \mathbf{B}^r_{P1a}}{\partial z_1} \mathbf{I}_{a_0} \tag{5.3.5}$$

$$\beta_1 = \frac{2\pi R_{1_0}}{I_{P1_0}} \frac{\partial B^r_{P1P2}}{\partial z_1} I_{P2_0} \tag{5.3.6}$$

$$\alpha_{12} = 2\pi R_{1_0} \frac{\partial B^r_{P1P2}}{\partial z_2} \tag{5.3.7}$$

where $\mathbf{B}^r_{P1a}$ is the vector of the Green's functions used to compute the radial magnetic field on plasma 1 produced by the PF coil currents. Similar expressions can be written for α_{22}, β_2 and α_{21}.
Introducing the "common-mode" Q and the "differential-mode" S variables:

$$Q = \frac{Z_1 I_{P1_0} + Z_2 I_{P2_0}}{2} \tag{5.3.8}$$

$$S = \frac{Z_1 I_{P1_0} - Z_2 I_{P2_0}}{2} \tag{5.3.9}$$

The following system of equations is obtained:

$$0 = \underline{\underline{R}}_{vv} \mathbf{I}_v + \underline{\underline{M}}_{vv} \delta \mathbf{I}_v + \frac{\partial \underline{\underline{M}}_{vQ}}{\partial Q} \delta Q + \frac{\partial \underline{\underline{M}}_{vS}}{\partial S} \delta S \tag{5.3.10}$$

$$0 = -\frac{\partial \underline{\underline{M}}_{vQ}}{\partial Q} \delta I_v + \Gamma_{QQ} \delta Q + \Gamma_{QS} \delta S \tag{5.3.11}$$

$$0 = -\frac{\partial \underline{\underline{M}}_{vS}}{\partial S} \delta I_v + \Gamma_{SQ} \delta Q + \Gamma_{SS} \delta S \tag{5.3.12}$$

where $\underline{\underline{M}}_{vQ} = \underline{\underline{M}}_{vP1} + \underline{\underline{M}}_{vP2}$ and $\underline{\underline{M}}_{vS} = \underline{\underline{M}}_{vP1} - \underline{\underline{M}}_{vP2}$ are respectively the matrix of the magnetic coupling between the common-mode and the differential-mode with the VV. The following quantities are also defined:

$$
\begin{aligned}
\Gamma_{QQ} &= \alpha_{11}+\beta_1+\alpha_{12}+\alpha_{22}+\beta_2+\alpha_{21} && (5.3.13)\\
\Gamma_{QS} &= \alpha_{11}+\beta_1-\alpha_{12}-\alpha_{22}-\beta_2+\alpha_{21} && (5.3.14)\\
\Gamma_{SQ} &= \alpha_{11}+\beta_1+\alpha_{12}-\alpha_{22}-\beta_2-\alpha_{21} && (5.3.15)\\
\Gamma_{SS} &= \alpha_{11}+\beta_1-\alpha_{12}+\alpha_{22}+\beta_2-\alpha_{21} && (5.3.16)\\
& && (5.3.17)
\end{aligned}
$$

A simple solution is found for the perfectly symmetric doublet, i.e. plasmas with the same current and radial position, namely:

$$
\begin{aligned}
\beta_1 &= \beta_2=-\alpha_{12}=-\alpha_{21} && (5.3.18)\\
\alpha_{11} &= \alpha_{22} && (5.3.19)
\end{aligned}
$$

therefore:

$$\Gamma_{SQ}=\Gamma_{QS}=0 \tag{5.3.20}$$

and

$$
\begin{aligned}
\Gamma_{QQ} &= 2\alpha_{11} && (5.3.21)\\
\Gamma_{SS} &= 2\alpha_{11}+4\beta_1 && (5.3.22)
\end{aligned}
$$

The common-mode and the differential-mode are decoupled and the dynamics of the two instabilities can be studied independently.
The common-mode is described by the following set of equations:

$$
\begin{aligned}
0 &= \underline{\underline{R}}^{Q}_{vv}\mathbf{I}_v+\underline{\underline{M}}^{Q}_{vv}\delta\mathbf{I}_v+\frac{\mathrm{d}\underline{\underline{M}}_{vQ}}{\mathrm{d}Q}\delta Q && (5.3.23)\\
0 &= -\frac{\mathrm{d}\underline{\underline{M}}_{vQ}}{\mathrm{d}Q}\delta\mathbf{I}_v+\Gamma_{QQ}\delta Q && (5.3.24)
\end{aligned}
$$

where $\underline{\underline{R}}^{Q}_{vv}$ and $\underline{\underline{M}}^{Q}_{vv}$ are the matrices of the resistance and the inductances of the orthogonal anti-symmetric eigenmodes used to describe the VV.
On the other hand, the differential-mode is described as follows:

$$
\begin{aligned}
0 &= \underline{\underline{R}}^{S}_{vv}\mathbf{I}_v+\underline{\underline{M}}^{S}_{vv}\delta\mathbf{I}_v+\frac{\mathrm{d}\underline{\underline{M}}_{vS}}{\mathrm{d}S}\delta S && (5.3.25)\\
0 &= -\frac{\mathrm{d}\underline{\underline{M}}_{vS}}{\mathrm{d}S}\delta I_v+\Gamma_{SS}\delta S && (5.3.26)
\end{aligned}
$$

where $\underline{\underline{R}}^{S}_{vv}$ and $\underline{\underline{M}}^{S}_{vv}$ are the matrix of the resistances and the inductances of the orthogonal symmetric eigenmodes used to describe the VV.
The current distribution along the vessel contour of the first three vessel anti-symmetric and symmetric eigenmodes is shown in Fig. 5.3.1. The importance of the vessel eigenmodes in stabilizing

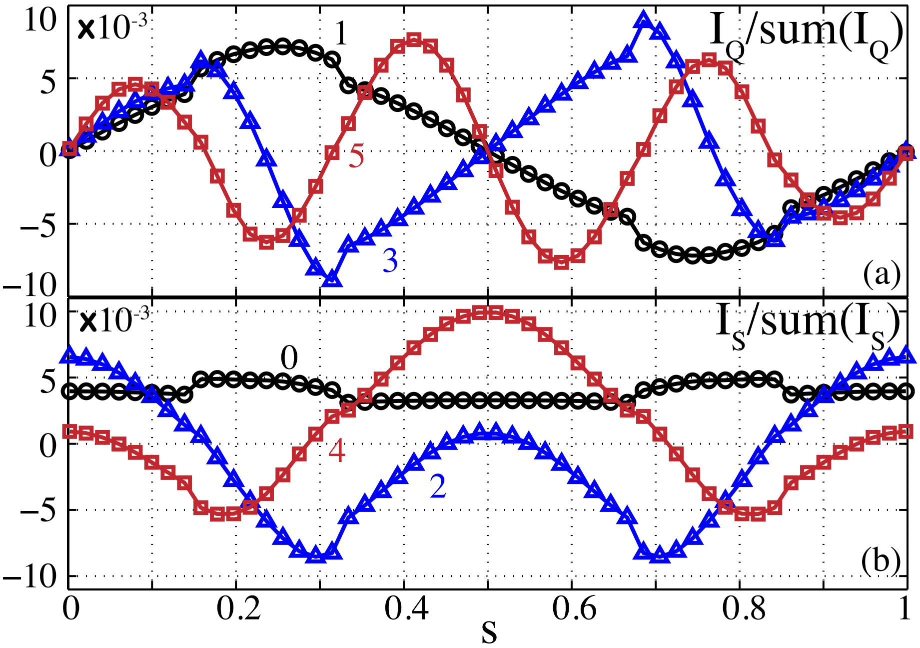

Figure 5.3.1: First three (a) antisymmetric and (b) symmetric eigenmodes of the vessel current vs the normalized vessel contour length.

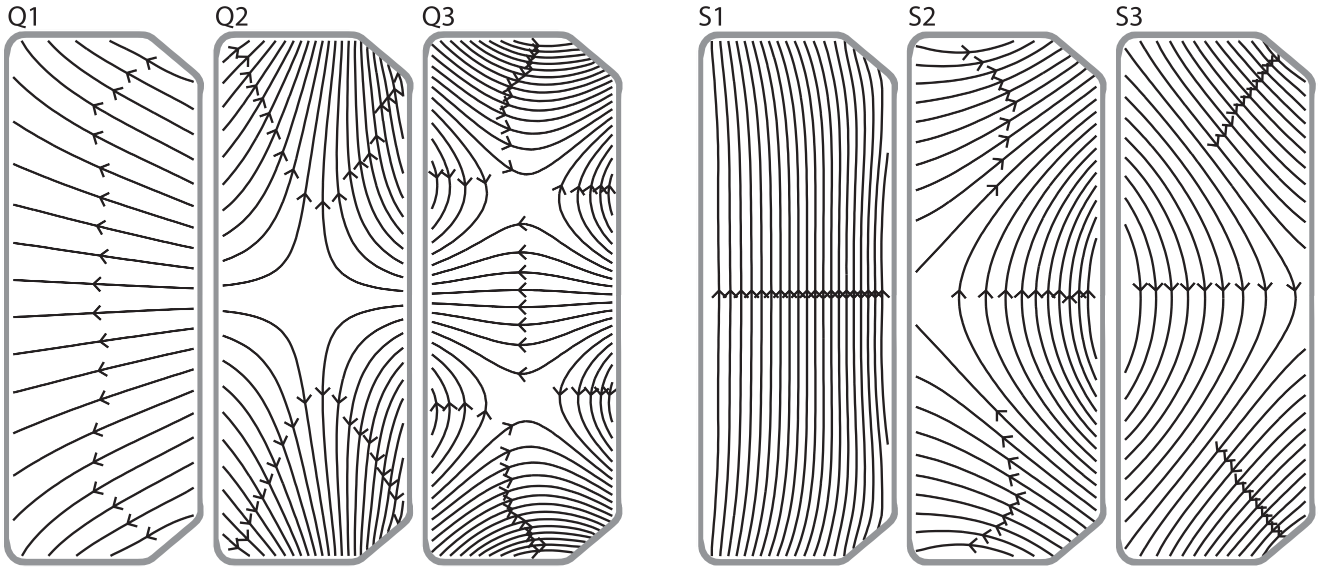

Figure 5.3.2: Magnetic field distribution of the first three anti-symmetric (Q) and symmetric (S) eigenvalues of the vessel current.

Q	M^Q_{vv}/R^Q_{vv} [ms]	M'^2_{vQ}/M^Q_{vv} [N MA^{-1}cm^{-1}]
1	8.1	559
2	3.6	18
3	2.7	171
S	M^S_{vv}/R^S_{vv} [ms]	M'^2_{vS}/M^S_{vv} [N MA^{-1}cm^{-1}]
1	13.4	49×10^{-3}
2	4.6	673
3	4.1	465

Table 5.1: Time constant $(M^{Q/S}_{vv}/R^{Q/S}_{vv})$ and effectiveness in vertical stabilization $(M'^2_{vQ/S}/M^{Q/S}_{vv})$ of the first three anti-symmetric (Q) and symmetric (S) vessel modes.

the vertical plasma displacement is given by the time constant of the mode, $\underline{\underline{M}}^{S/Q}_{vv}/\underline{\underline{R}}^{S/Q}_{vv}$, and the parameter $\underline{\underline{M}}'^2_{vS/Q}/\underline{\underline{M}}^{S/Q}_{vv}$, with $\underline{\underline{M}}'_{vS/Q} = \frac{\mathrm{d}\underline{\underline{M}}_{vS/Q}}{\mathrm{d}S/Q}$. This parameter is proportional to the vertical force on the plasma column given by the vessel eigenmodes when the plasma moves and therefore quantifies the modes' effectiveness in vertical stabilization. The properties of the vessel eigenmodes represented in Fig. 5.3.1 are summarized in Table 5.1 for the doublet equilibrium in Fig. 5.3.3(a). The anti-symmetric modes (Q) are characterized by a dominant eigenmode with a time constant 2.5 times higher than the second mode and a better coupling to the plasma columns. This is due to the low periodicity of the vessel current distribution of this eigenmode, Fig. 5.3.1, which leads to a more uniform distribution of the radial magnetic field inside the VV, as shown in Fig. 5.3.2. The problem can be therefore simplified considering only the most important eigenmode, leading to an analytical expression of the plasma growth rate:

$$\gamma_Q = \frac{\frac{R^Q_{vv}}{M^Q_{vv}}}{1 + \frac{M'^2_{vQ}}{M^Q_{vv}\Gamma_{QQ}}} \tag{5.3.27}$$

The eigenmode is unstable in nature if $\gamma_Q > 0$, that is:

$$-\frac{M'^2_{vQ}}{M^Q_{vv}} < \Gamma_{QQ} < 0 \tag{5.3.28}$$

The condition $\Gamma_{QQ} < 0$ corresponds to $\frac{\mathrm{d}\underline{\underline{B}}^r_{Pia}}{\mathrm{d}z_i}\mathbf{I}_{a0} < 0$, i.e. the curvature of the external magnetic field is negative. Notice that this instability is equivalent to that of a single-axis elongated plasma. If $\Gamma_{QQ} < -\frac{M'^2_{vQ}}{M^Q_{vv}}$, even if $\gamma_Q > 0$, the plasma is ideally unstable. The rigid model cannot describe this unstable state due to the approximation of zero plasma mass.

The solution for the symmetric (S) modes is more complex since it is not possible to isolate a dominant vessel eigenmode. The first eigenmode has the longest vessel time constant (Table 5.1), but a very poor coupling with the plasma columns. This is due to the weakness of the radial field produced by this mode, as shown in Fig. 5.3.2. The other two modes have a smaller time constant but a stronger coupling with the plasma and are therefore the most important.

5.3.2 Rigid Model vs KINX

The growth rate of the unstable vertical modes of a doublet plasma computed using the rigid model (RM) are compared with those evaluated with the KINX code [73]. The reference equilibrium, computed with the CAXE code [72], is shown in Fig. 5.3.3(a). Parabolic profiles for the pressure and current distribution are used for the domains inside the separatrix and a current-less $\beta = 0$ mantle is considered. Starting from this equilibrium, the comparison is made changing the thickness of the mantle (Fig. 5.3.3(b)) and the distance of the two plasmas from the inner wall (Fig. 5.3.3(c)).

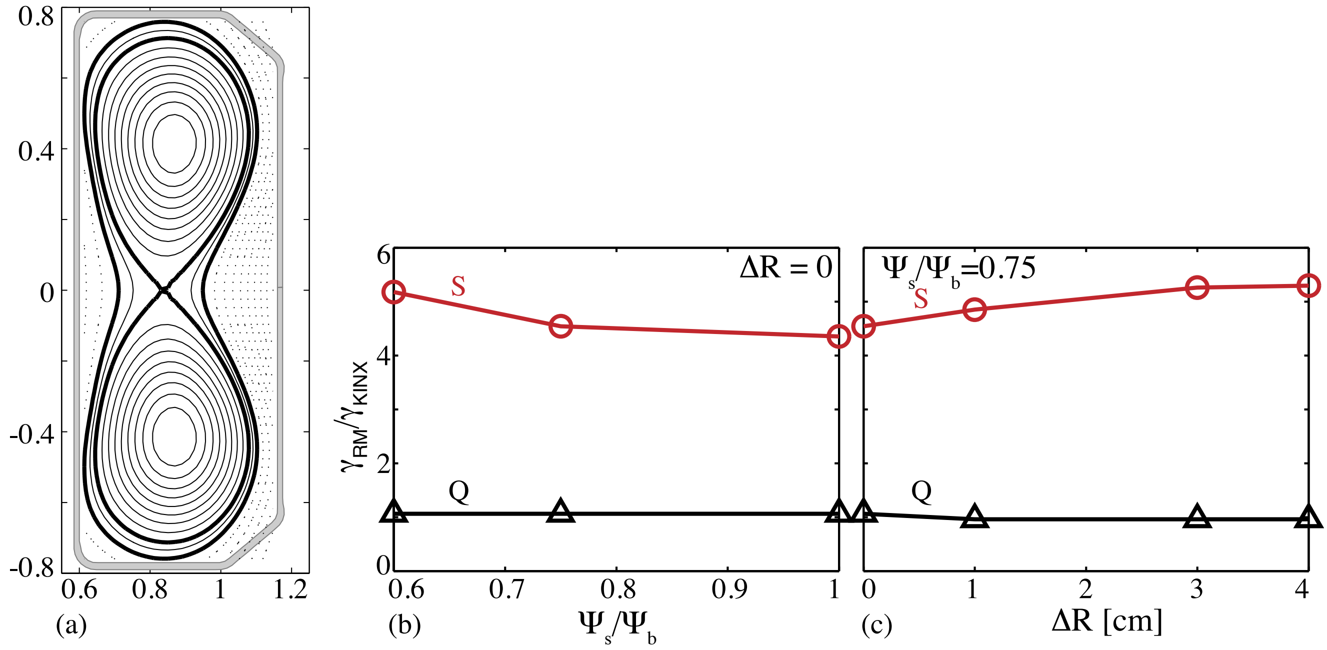

Figure 5.3.3: MHD equilibria of a symmetric doublet computed with the CAXE code (a); ratio of the vertical instability growth rate computed with the rigid model and the KINX code for the symmetric mode (red) and antisymmetric mode (black) as a function of Ψ_s/Ψ_b (b) and ΔR (c).

Independently of the thickness of the doublet mantle, parametrized by the previously defined parameter Ψ_s/Ψ_b, there is a good agreement between the growth rate computed by the RM and the KINX code for the anti-symmetric mode (Q), which is equal to $\gamma^Q_{\mathrm{RM}} \sim \gamma^Q_{\mathrm{KINX}} = 70\ \mathrm{s}^{-1}$. A similar result is obtained when the distance from the from the inner wall ΔR is changed (Fig. 5.3.3(c)). Conversely, there is a large discrepancy between the growth rates of the symmetric mode computed with the two approaches. The RM gives a growth rate approximately 5 times higher than that computed with the KINX code. γ^S_{KINX} goes from 185 s^{-1} to 220 s^{-1} as Ψ_s/Ψ_b increases, showing a stabilizing influence of the doublet mantle. When ΔR increases, γ^S_{KINX} goes from 211 s^{-1} to 238 s^{-1} as expected since the stabilizing effects of the conductive wall tend to vanish. Thus the RM will predict ideal instability for cases for which KINX predicts controllability.

The large difference in the predicted growth rate of the symmetric unstable mode between the two codes is due to the nature of the plasma displacements, that inevitably lead to a plasma shape deformation.

In the KINX code, the equilibrium magnetic field is expressed as:

$$\mathbf{B} = \nabla\psi \times \nabla\phi + F(\psi)\nabla\phi \tag{5.3.29}$$

where $\psi = RA_\phi$ is a streaming function of the poloidal magnetic field and A_ϕ is the toroidal component of the vector potential. ϕ is the toroidal angle in the right-handed cylindrical coordinate system described by R, ϕ and z. The quantity $F(\psi) = RB_\phi$ is a surface quantity related to the poloidal current flowing in the plasma and the TF coils.

In the vacuum region, the flux function ψ_v is introduced such that the plasma surface and the VV are constant ψ_v surfaces, with the condition $\psi_v = \psi$ at the plasma boundary [77].
Let us assume the absence of perturbed TF in vacuum. This condition does not prevent the existence of a surface current at the plasma-vacuum interface. Considering for simplicity the case of a pressure-free and current-free mantle plasma, the perturbed magnetic field can be expressed as follows:

$$\delta \mathbf{B} = \nabla \chi \times \nabla \phi + a_t \nabla \phi \tag{5.3.30}$$

with $\chi = \xi \cdot \nabla \psi$, ξ equal to the perturbation vector and $a_t = \text{const}$. A similar expression can be written for the vacuum region:

$$\delta \mathbf{B}_v = \nabla \chi_v \times \nabla \phi + a_{tv} \nabla \phi \tag{5.3.31}$$

The value of a_{tv} is proportional to the perturbed poloidal current in the conducting wall enclosing the vacuum region ($\mu_0 \delta I_w = 2\pi a_{tv}$), therefore the perturbed vacuum field vanishes when the perturbed poloidal wall current is zero (the poloidal conductivity of the wall is zero).
Conversely, the TF perturbation in the plasma is related to the plasma displacement normal to the magnetic surfaces. Integrating over the $\psi = \text{const}$ plasma cross-section S_p between the equilibrium magnetic surfaces with contours δS_p^{in} and δS_p^{out}, the value of a_t can be expressed in terms of the normal plasma displacement $\xi_n = \mathbf{n}_\psi \cdot \xi$, with $\mathbf{n}_\psi$ normal to the magnetic surfaces:

$$\int_{S_p} \delta \mathbf{B} \mathrm{d}S_p = a_t \int_{S_p} \frac{\mathrm{d}S_p}{R} = \int_{S_p} \nabla \times \mathbf{A} \mathrm{d}S_p = \oint_{\delta S_p} \mathbf{A} \mathrm{d}l \tag{5.3.32}$$

Since $\mathbf{A} = \xi \times \mathbf{B}$:

$$\oint_{\delta S_p} \xi \times \mathbf{B} \mathrm{d}l = \oint_{\delta S_p} \xi_n F \frac{\mathrm{d}l}{R} \tag{5.3.33}$$

The following expression for a_t is therefore obtained:

$$a_t \int_{S_p} \frac{\mathrm{d}S_p}{R} = \int_{\delta S_p^{out}} \xi_n F \frac{\mathrm{d}l}{R} - \int_{\delta S_p^{in}} \xi_n F \frac{\mathrm{d}l}{R} \tag{5.3.34}$$

Equation 5.3.34 links the TF in the mantle to the plasma displacement. This perturbed TF vanishes for an up-down antisymmetric plasma displacement normal to the magnetic surfaces ξ_n, as in the case of the Q mode $n = 0$ vertical instability of symmetric doublets.
In the following it will be shown that in the case of symmetric plasma displacement (mode S), the perturbed TF is associated with a perturbed surface current $\mathbf{j}_s$.
Ampere's law applied at the plasma boundary links the discontinuity on the perturbed magnetic field to the surface current:

$$\mu_0 \mathbf{j}_s = \mathbf{n}_\psi \times (\delta \mathbf{B}_v - \delta \mathbf{B}) \tag{5.3.35}$$

From the linearized magnetic pressure continuity equation at the plasma-vacuum interface:

$$\delta \mathbf{B} \cdot \mathbf{B} = \delta \mathbf{B}_v \cdot \mathbf{B}_v \tag{5.3.36}$$

In the absence of an equilibrium surface current, $\mathbf{B} = \mathbf{B}_v$, therefore the perturbed surface current flows along the equilibrium magnetic field lines ($\mathbf{j}_s \parallel \mathbf{B}$).

Substituting the expressions of $\delta\mathbf{B}$ and $\delta\mathbf{B}_v$ (Eqs. 5.3.30 and 5.3.31) into the Eq. 5.3.35, the following expression for the perturbed surface current is obtained:

$$\mu_0 \mathbf{j}_s = (a_{tv} - a_t)\frac{\mathbf{B}}{\mid \nabla\psi \mid} \tag{5.3.37}$$

From the expression of the perturbed magnetic energy:

$$\delta W \sim \int \delta\mathbf{B}^2 \mathrm{dVol} \tag{5.3.38}$$

if $a_t \neq 0$, i.e. the unstable S mode in symmetric doublets, $\delta\mathbf{B}^2 > 0$, leading to a stabilizing effect of the unstable mode induced by the surface current $\mathbf{j}_s \neq 0$.

The rigid model by definition cannot take this effect into account. Plasma deformation induces a plasma current that flows along the magnetic field lines in the plasma edge. This current has a stabilizing effect, reducing the effective growth rate of the vertically unstable mode. The current is mainly localized in the mantle. A reduction of the mantle thickness therefore leads to an increase of the unstable growth rate and a reduction of the discrepancy between the growth rate computed with the RM and KINX, as shown in Fig. 5.3.3. Even for a mantle-less doublet ($\Delta\psi_{\mathrm{mantle}} = 0$), there is a large difference between the growth rate predicted by the rigid model and KINX. In this configuration the deformation leads to an edge current which flows in the edge of the two plasma columns and contributes to stabilization of the unstable mode.

5.3.3 Rigid Model vs MHD_NX

To create a doublet merging two droplet-shaped plasmas (Sec. 5.2.3), the stability of the droplet configuration needs to be analyzed. The KINX code cannot analyze the stability of a droplet plasma. Conversely, the MHD_NX code [78, 79, 80] computes the ideal MHD stability of plasma equilibrium configurations with arbitrary topology of axisymmetric magnetic surfaces, including doublets and droplets.

A sequence of up-down symmetric droplet equilibria is computed with the free-boundary equilibrium generator MGAMS/FBTE [39, 38]. Each equilibrium consists of two limited plasmas, as illustrated in Fig. 5.3.4(a), with parabolic pressure and current profiles. The relative position of the two plasmas is changed and the stability of each equilibrium is computed.

A direct comparison between the RM and the MHD_NX code is not possible, since the RM computes the resistive growth rate and the MHD_NX code the ideal stability, i.e. with a perfect conductive wall surrounding the plasma. However, a qualitative comparison may be useful to identify general trends and behaviors of droplet plasmas.

Figure 5.3.4(b) shows the contour plot of the vertical growth rate of the symmetric mode computed with the RM as a function of the position of the symmetric droplet plasma. The growth rate increases when the vertical distance between the two plasmas is reduced. The black line in Fig. 5.3.4(b) represents the $n = 0$ MHD stability limit of the droplet computed with the MHD_NX code. Plasmas with a vertical distance smaller than the limit defined by the black curve are ideally unstable. This condition should correspond to the extremely high growth rate computed with the RM (red region in Fig. 5.3.4(b)). A comparison between the stability region computed with the RM and MHD_NX shows a good qualitative agreement (same shape). The RM predicts an ideal instability for higher distance between the two plasmas compared to the MHD_NX code. This is

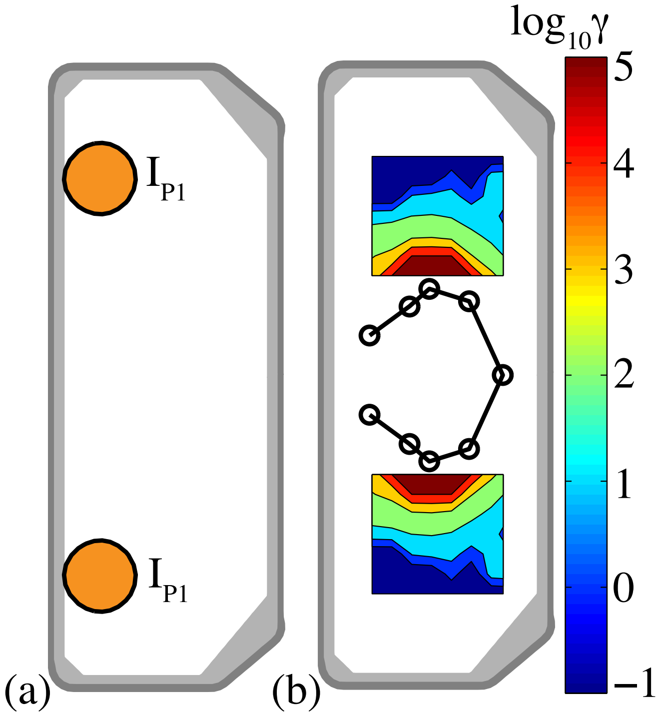

Figure 5.3.4: (a) Droplet configuration and (b) contour plot of the symmetric unstable mode growth rate computed with the RM as a function of the position of the plasma columns in a symmetric droplet. The black curve represents the ideal stability limit computed with the MHD_NX code.

probably due to the effect of the surface currents in the droplet edge configuration, as discussed in the previous section.

The stability diagram in Fig. 5.3.4(b) should be considered when programming the discharge evolution. During the droplet phase, the two plasmas should be kept as far as possible to reduce the vertical growth rate, especially during the early phase, when the active control system is less effective due to the low plasma current in the two lobes. The two plasmas should grow close to the HFS VV, where the conductive wall contributes to stabilization of the two plasmas.

5.4 Doublet control system

In this section a possible control strategy implementable in the TCV control system is proposed to stabilize and control a droplet/doublet configuration. Several quantities must be controlled in real-time. The unstable nature of the vertical position of the two plasmas imposes a careful design of the plasma position control system. Moreover, the plasma current, temperature and density have to be controlled independently in the two plasmas .

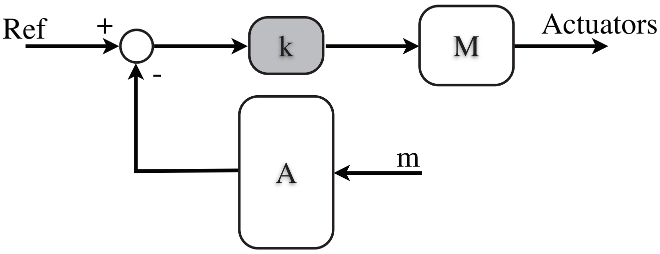

Figure 5.4.1: Block diagram of the TCV control system

Fig. 5.4.1 shows a simplified block diagram of the TCV control system. The block “A” represents the observer, i.e. the link between the measured quantities and the controlled parameters. The functionalities of this block depend on the hardware used. The analog system [14], used to control the G coils (Sec. 2.2), only allows linear operations, i.e. the controlled parameters are a linear combination of the measured quantities. With the more advanced control system based on the D-TACQ [81] hardware, the observed quantities can be the result of a complex combination of the input quantities, giving the possibility to perform non-linear mathematical computations in real-time. The analog system has a faster response and it is therefore more adequate to control quantities rapidly varying. The “k” block is the controller which translates the error on the observed quantities into a parameter change request. This block usually consists of a PID controller, even if more complex control strategies could be implemented in the new digital control system. Finally the “M” block converts the output from the controller into signals to be sent to the actuators. As for the other elements, only linear operations (mainly a matrix multiplication) are allowed with the TCV analog control system.

5.4.1 Plasma position control system

The positions of the two plasma columns of a droplet/doublet configuration must be controlled to ensure stable behavior longer than the vessel resistive time (vertical position) and to compensate the outward radial force of toroidal plasmas. For single-axis conventional elongated plasmas, a radial field is produced by the external active coils to impose the desired vertical plasma position and a vertical field to set the radial position.

In TCV, two independent systems are used to control single-axis plasma positions. The "slow" control system uses the digital D-TACQ hardware [81] and controls a combination of the PF coils to produce the desired magnetic field in the plasma region. The bandwidth is limited by the dynamics of the power supply thyristors [14] (see Sec. 2.2), around 1 kHz. The "fast" control system uses the analog hardware to control the voltage on the internal G coils. They are capable of producing a radial field in the TCV VV with fast response ($\sim$ 10 kHz) limited by the bandwidth of the IGBT modules of the power supplies (see Sec. 2.2). The relatively small radial field produced by these coils, together with its time response make this system capable of following the fast evolution of the plasma vertical position. For most TCV plasmas, the G coils are controlled by the derivative term in the feedback controller.

For doublet plasmas, the position of the two plasma columns must be controlled independently. This aspect imposes some constraints on the TCV control system. In doublet plasmas the S-mode is the most unstable. The G-coils produce a fairly uniform radial field on TCV, therefore the "fast" controller cannot be used for doublet configurations. The "slow" TCV control system is therefore the only available tool that can be used to stabilize and control the doublet position.

In the next sections, a control strategy that can be implemented in the "slow" control system is proposed to control and stabilize the plasma position in a doublet configuration.

5.4.1.1 Plasma vertical position observer

To control independently the position of the two plasma columns of a doublet, two distinct observers are necessary. In this section an observer of the Q-mode and of the S-mode are proposed, even if different solutions are possible to control the two plasmas. The advantage of this solution is that the two controllers are independent, i.e. the Q-mode controller can be designed independently of the S-mode controller.

The linearity is one of the properties that the observer should have. Even if the "slow" TCV control system supports non-linear controllers, linearity will allow us to build an observer that

could be implemented in the "fast" control system. This condition may become useful in the future, when the new RMP coils [35] will be used to replace the G-coils. With the new system the "fast" controller will be able to control independently the two plasma columns with a linear observer, i.e. a linear combination of the magnetic measurements.
To extract plasma position information from the magnetic measurements, the measured quantities are related to the sources of magnetic field in TCV:

$$\mathbf{\Psi}_f - \underline{\underline{M}}_{fc}\cdot\mathbf{I}_c = \underline{\underline{M}}_{fx}\cdot\mathbf{I}_x \qquad (5.4.1)$$

$$\mathbf{b}_m - \underline{\underline{B}}_{mc}\cdot\mathbf{I}_c = \underline{\underline{B}}_{mx}\cdot\mathbf{I}_x \qquad (5.4.2)$$

The quantities in Eqs. 5.4.1 and 5.4.2 have been defined in Sec. 3.3, $\mathbf{I}_x$ is the vector of the currents in the toroidal filaments used to describe the plasma columns and $\underline{\underline{M}}_{fx}$, $\underline{\underline{B}}_{mx}$ are the Green's functions to link the current in the plasma filaments to the measured poloidal flux and magnetic field. Combining the two equations, the following expression is obtained:

$$\mathbf{I}_x = \underline{\underline{A}}^{-1}\cdot\left(\underline{\underline{M}}^T_{fx}\cdot\mathbf{\Psi}_f + \underline{\underline{B}}^T_{mx}\cdot\mathbf{b}_m - \underline{\underline{M}}^T_{fx}\cdot\underline{\underline{M}}_{fc}\cdot\mathbf{I}_c - \underline{\underline{B}}^T_{mx}\cdot\underline{\underline{B}}_{mc}\cdot\mathbf{I}_c\right) = \underline{\underline{M}}_{xm}\cdot\mathbf{m} \qquad (5.4.3)$$

with $\underline{\underline{A}} = \underline{\underline{M}}^T_{fx}\cdot\underline{\underline{M}}_{fx} + \underline{\underline{B}}^T_{mx}\cdot\underline{\underline{B}}_{mx}$. Equation 5.4.3 allows us to find the current in the toroidal filaments used to describe the plasma current from a linear combination ($\underline{\underline{M}}_{xm}$) of the magnetic measurements ($\mathbf{m}$).
For up-down symmetric doublets ($\Psi(R,z) = \Psi(R,-z)$), a subgroup of the plasma filaments is used to model the upper plasma column ($\mathbf{I}^U_x$) and second to describe the lower plasma column ($\mathbf{I}^L_x$):

$$\mathbf{I}_x = \begin{bmatrix}\mathbf{I}^U_x\\ \mathbf{I}^L_x\end{bmatrix} = \begin{bmatrix}\underline{\underline{M}}^U_{xm}\\ \underline{\underline{M}}^L_{xm}\end{bmatrix}\cdot\mathbf{m} \qquad (5.4.4)$$

The observer for the Q-mode is then defined as:

$$zI^Q_P = \mathbf{a}_Q\cdot\mathbf{m} = \frac{(\mathbf{z}^U - z^U_{ax})\cdot\mathbf{I}^U_x + (\mathbf{z}^U - z^L_{ax})\cdot\mathbf{I}^L_x}{2} = \frac{\mathbf{\Delta z^U}\cdot\underline{\underline{M}}^U_{xm} + \mathbf{\Delta z^L}\cdot\underline{\underline{M}}^L_{xm}}{2}\cdot\mathbf{m} \qquad (5.4.5)$$

where $\mathbf{z^{U/L}}$ is the position of the filament of the upper/lower plasma column and $z^{U/L}_{ax}$ is the reference position of the upper/lower plasma axis. Similarly, the observer for the S-mode is:

$$zI^S_P = \mathbf{a}_S\cdot\mathbf{m} = \frac{(\mathbf{z}^U - z^U_{ax})\cdot\mathbf{I}^U_x - (\mathbf{z}^U - z^L_{ax})\cdot\mathbf{I}^L_x}{2} = \frac{\mathbf{\Delta z^U}\cdot\underline{\underline{M}}^U_{xm} - \mathbf{\Delta z^L}\cdot\underline{\underline{M}}^L_{xm}}{2}\cdot\mathbf{m} \qquad (5.4.6)$$

5.4.1.2 Plasma radial position observer

A simple radial position observer can be based on the difference between the poloidal flux on the HFS and on the LFS at the plasma midplane. The flux loops mounted on the TCV vessel (see Sec. 3.2) can be used to obtain this quantity in real-time. A correction for the vessel current can be introduced using the signals from the poloidal magnetic field probes installed inside the TCV VV:

$$rI^i_P \sim \Delta\psi^i = \Psi^i_{f_{IN}} + 2\pi R_{IN}\Delta R b^i_{m_{IN}} - \Psi^i_{f_{OUT}} - 2\pi R_{OUT}\Delta R b^i_{m_{OUT}} \qquad (5.4.7)$$

where, for the $-\mathrm{i}^{\mathrm{th}}$ plasma column, $\Psi^i_{f_{IN/OUT}}$ is the magnetic flux from the flux loop located at inner/outer TCV wall at the plasma midplane, $b^i_{m_{IN/OUT}}$ is the magnetic field measured with the pick-up coil inside the inner/outer TCV wall at the plasma midplane, ΔR is the VV thickness and $R_{IN/OUT}$ is the radial position of the inner/outer pick-up coil.
As for the vertical position observer, the common mode rI_P^Q and the differential mode rI_P^S are defined:

$$
\begin{aligned}
rI_P^Q &= \frac{rI_P^1 + rI_P^2}{2} && (5.4.8)\\
rI_P^S &= \frac{rI_P^1 - rI_P^2}{2} && (5.4.9)
\end{aligned}
$$

These quantities are computed in real-time from the magnetic signals. The advantage of these observers is their simplicity, especially due to their linearity and therefore they can be implemented in a basic hardware control system. The error signals sent to the controller are given by the difference between the observed quantities and the equivalent reference signals, computed from the pre-programmed plasma discharge.

5.4.1.3 The position control system actuators

The actuator of the position control system is a combination of the currents in the PF coils. The chosen combination is such that the coupling with the plasma columns is maximized, i.e. maximum force on the plasma columns. This is especially important for the vertical position controller, due to the unstable nature of the plasma vertical displacement.
Concerning the vertical control system, the quantity which must be maximized is the radial magnetic field on the $-\mathrm{i}^{\mathrm{th}}$ plasma column b^R_{Pi}. For the Q-mode, the restoring vertical force must have the same direction in the two plasma columns, therefore the important quantity is $b_P^{RQ} = b^R_{P1} + b^R_{P2}$. Conversely, the S-mode is characterized by a restoring vertical force with opposite sign between in the two plasma columns, i.e. $b_P^{RS} = b^R_{P1} - b^R_{P2}$. Similarly, for the radial control system the quantities $b_P^{ZQ} = b^Z_{P1} + b^Z_{P2}$ and $b_P^{ZS} = b^Z_{P1} - b^Z_{P2}$ need to be maximized to efficiently control the radial position of the two plasmas.
Several combinations of the current in the PF coils have to be defined to control each of the desired magnetic field distributions independently, to avoid a cross-coupling between the different control loops. Mathematically the problem can be solved as follows:

$$
\begin{bmatrix} 1 & 0 & 0 & 0 \\ 0 & 1 & 0 & 0 \\ 0 & 0 & 1 & 0 \\ 0 & 0 & 0 & 1 \end{bmatrix} = \begin{bmatrix} \underline{\underline{B}}^{RQ}_{Pc} \\ \underline{\underline{B}}^{RS}_{Pc} \\ \underline{\underline{B}}^{ZQ}_{Pc} \\ \underline{\underline{B}}^{ZS}_{Pc} \end{bmatrix} \cdot \mathbf{I}^b_c \qquad (5.4.10)
$$

where $\underline{\underline{B}}^{RQ}_{Pc}$, $\underline{\underline{B}}^{RS}_{Pc}$, $\underline{\underline{B}}^{ZQ}_{Pc}$ and $\underline{\underline{B}}^{ZS}_{Pc}$ are the Green's function between the magnetic field distribution and the current in the PF coils. The solution of the system of Eqs. 5.4.10 is a set of current distributions in the PF coils capable of imposing the desired magnetic distribution inside the VV keeping the magnetic coupling with the other field distributions small. Two different solutions have been computed, using only the E coils and the F coils. The results are summarized in Table 5.2 for the reference doublet equilibrium represented in Fig. 5.3.3(a). Notice that since the vessel current is not included in the model, the solution is only valid in steady-state conditions.

#	F1	F2	F3	F4	F5	F6	F7	F8	b_P^{RQ} [μT/A]	b_P^{RS} [μT/A]	b_P^{ZQ} [μT/A]	b_P^{ZS} [μT/A]
1	0.63	0	0	-1	1	0	0	-0.63	12.9	0	0	0
2	-1	0	0	0.69	0.69	0	0	-1	0	27.2	0	0
3	1	0	0	0.31	0.31	0	0	1	0	0	68.1	0
4	0.03	0	0	-1	1	0	0	-0.03	0	0	0	15.3
	E1	E2	E3	E4	E5	E6	E7	E8	b_P^{RQ} [μT/A]	b_P^{RS} [μT/A]	b_P^{ZQ} [μT/A]	b_P^{ZS} [μT/A]
5	0.65	0	0	-1	1	0	0	-0.65	9.4	0	0	0
6	-1	0	0	0.72	0.72	0	0	-1	0	20.1	0	0
7	-1	0	0	-0.4	-0.4	0	0	-1	0	0	4.9	0
8	0.11	0	0	1	-1	0	0	-0.11	0	0	0	5.2

Table 5.2: Coupling between several PF coil combinations and the plasma radial and vertical modes (Q and S) in steady state conditions ($\omega = 0$).

The F coils have the highest steady-state response. This is mainly due to the stronger magnetic coupling between the F coils and the plasma columns.

To verify the capability of the actuators to dynamically control the plasma positions ($\omega > 0$), the vessel current must be introduced into the analysis.

The same model introduced in Sec. 2.4 is used to describe the VV:

$$0 = \underline{\underline{R}}_{vv}\mathbf{I}_v + \underline{\underline{M}}_{vv}\dot{\mathbf{I}}_v + \underline{\underline{M}}_{vc}\dot{\mathbf{I}}_c \tag{5.4.11}$$

Rewriting Eq. 5.4.11 in Fourier's space, the current in the vessel filaments can be written as:

$$\mathbf{I}_v(\omega) = \frac{\mathrm{i}\omega\underline{\underline{M}}_{vc}}{\underline{\underline{R}}_{vv} + \mathrm{i}\omega\underline{\underline{M}}_{vv}} \cdot \mathbf{I}_c(\omega) \tag{5.4.12}$$

Finally, the total field coupled to the plasma columns is given by:

$$b_P^{R/Z,Q/S}(\omega) = \underline{\underline{B}}_{Pc}^{R/Z,Q/S}\mathbf{I}_c(\omega) + \underline{\underline{B}}_{Pv}^{R/Z,Q/S}\mathbf{I}_v(\omega) \tag{5.4.13}$$

where $\underline{\underline{B}}_{Pv}^{R/Z,Q/S}$ and $\underline{\underline{B}}_{Pc}^{R/Z,Q/S}$ represent the Green's functions between the magnetic field distributions and current in the vessel filaments and in the PF coils respectively.

Figure 5.4.2 shows the evolution of $b_P^{R/Z,Q/S}(\omega)$ for each PF coil current distribution in Table 5.2. The amplitude of the field coupled to the plasma columns decreases as the frequency increases, due to the shielding effect of the VV. The amplitude of the magnetic field depends on the given PF coil current distribution, as already indicated in Table 5.2. Concerning the radial magnetic field, b_P^{RS} is higher than b_P^{RQ} (Fig. 5.4.2(a-b)). As a result, the "S-mode" vertical controller should be faster than the "Q-mode" vertical controller and the problem of the higher growth rate of the vertical common-mode should be somewhat alleviated. For all the PF coil current distributions, the F coils have higher values of magnetic field in the plasma columns due to their stronger coupling with plasma. The difference is extremely high for the b_P^{ZQ} case, where the field produced by the F coil current distribution is one order of magnitude higher than that given by the E coil distribution (Fig. 5.4.2(c)).

To quantify the coupling between the action of the different control loops, the "cross-talk" (ct) parameter is defined as follows:

$$ct(\omega) = \frac{b_P^{RQ}(\omega)}{\max\left[b_P^{RS}(\omega), b_P^{ZQ}(\omega), b_P^{ZS}(\omega)\right]} \tag{5.4.14}$$

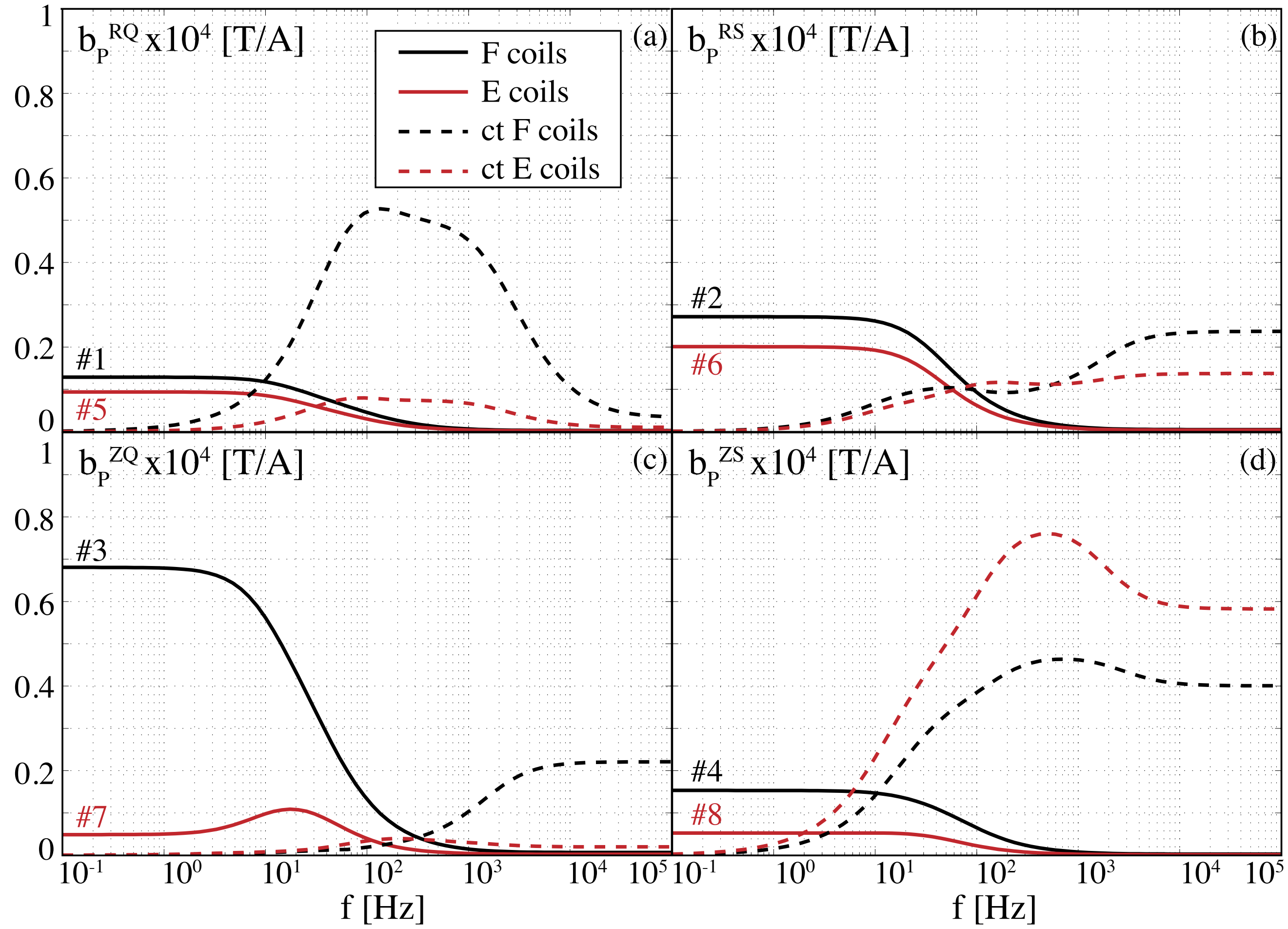

Figure 5.4.2: Solid lines: bode diagram of (a) b_P^{RQ}, (b) b_P^{RS}, (c) b_P^{ZQ} and (d) b_P^{ZS} for the PF current distributions in Table 5.2 together with the respective "cross-talk" (*ct*) parameter (dashed lines).

Equation 5.4.14 defines the *ct* parameter for the b_P^{RQ} field distribution. Similarly, the *ct* parameter can be deduced for the other magnetic field distributions.

Figure 5.4.2 shows the evolution of *ct* for each PF coil current combination. This parameter is zero only for $\omega \rightarrow 0$. When the frequency increases, *ct* rises due to the coupling to the other magnetic field distributions given by the current induced in the VV. Nevertheless, the desired magnetic field is always the dominant one ($ct < 1$) and the highest values of *ct* are obtained at high frequency, close to the maximum bandwidth of the control loop (~ 1 kHz).

5.4.2 Plasma current/temperature control system

In a doublet configuration, we would like to monitor and control the current flowing in each of the two plasma columns. The main problem encountered when a traditional controller is used for a doublet plasma is the impossibility to independently control the two plasma currents. The ohmic coil, which represents the actuator of a single-axis plasma current control system, produces a uniform toroidal electric field inside the VV. Therefore, it is not possible to independently control the two plasma currents with a standard plasma control system.

The problem is even more complicated due to the unstable nature of the system. Since the plasma resistance decreases with the electron temperature, if one of the plasma columns has a slightly higher plasma current, the electron plasma temperature will probably be higher, leading to a smaller plasma resistance. As a consequence, since the toroidal electric field is the same for

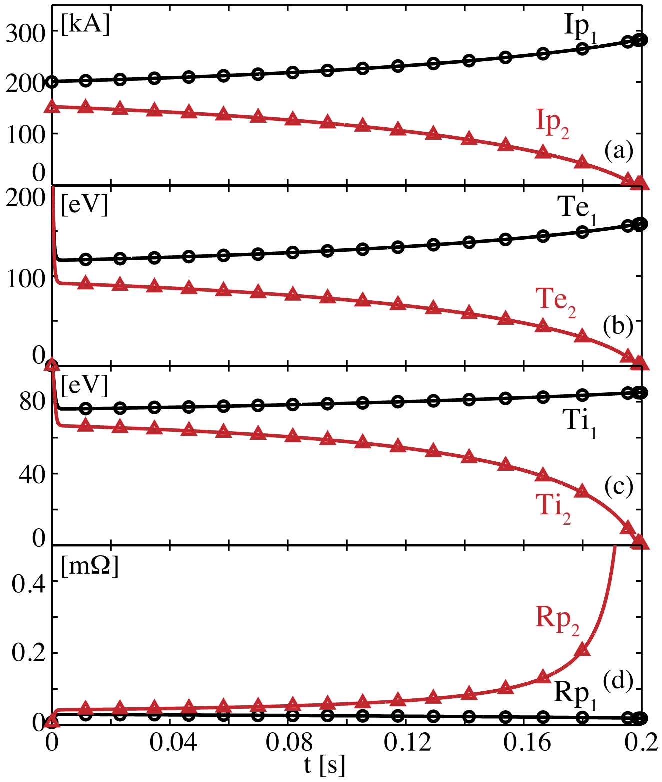

Figure 5.4.3: Temporal evolution of the (a) plasma current, (b) electron temperature, (c) ion temperature and (d) plasma resistance for the two doublet plasma columns.

the two plasma columns, the difference in plasma current will be even larger leading to unstable behavior of the system.

To better understand this behavior, a simple 0-D model of the two plasma columns is used to describe the system. Each of the two plasmas is considered as uniform and the effect of impurities is neglected. The plasma density, shape and position are constant and equal for the two plasmas. The following set of equations is solved for plasma column 1:

$$\frac{3}{2}\frac{\mathrm{d}}{\mathrm{d}t}(n_{e1}k_BT_{e1}) = P_{OH1} - P_{\mathrm{ion1}} - P_{\mathrm{rad1}} - P_{ei1} - P_{b1} - \frac{3}{2}\frac{n_{e1}k_BT_{e1}}{\tau_{E1}} \tag{5.4.15}$$

$$\frac{3}{2}\frac{\mathrm{d}}{\mathrm{d}t}(n_{e1}k_BT_{i1}) = P_{ei1} - P_{cx1} - \frac{3}{2}\frac{n_{e1}k_BT_{i1}}{\tau_{E1}} \tag{5.4.16}$$

$$L_{P1}\frac{\mathrm{d}I_{P1}}{\mathrm{d}t} = U - R_{P1}I_{P1} - M_{P1P2}\frac{\mathrm{d}I_{P2}}{\mathrm{d}t} \tag{5.4.17}$$

A similar set of equations can be written for plasma column 2. Each element in Eqs. 5.4.16-5.4.17 has already been described in Sec. 4.6. The plasma minor radius is assumed constant ($a_1 = 0.2$ m), together with the electron plasma density ($n_{e1} = 4 \times 10^{19}$ m^{-3}). The particle confinement time is assumed equal to the energy confinement time ($\tau_{p1} = \tau_{E1} = 1$ ms). The parameter M_{P1P2} in Eq. 5.4.17 is the mutual inductance between the two plasmas ($M_{P1P2} = 3.9 \times 10^{-7}$ H).

Figure 5.4.3 shows the evolution of some plasma quantities computed from this model. The two plasma columns have similar initial conditions ($T_{e1} = T_{e2} = 300$ eV, $T_{i1} = T_{i2} = 100$ eV). The only difference is the initial value of the plasma current, assumed smaller in plasma column 2 ($I_{P1} = 200$ kA, $I_{P2} = 150$ kA). The difference in the plasma current is responsible for the different evolution of the two plasma columns. The electron temperature of plasma column 2 decreases (Fig. 5.4.3(b)). As a consequence, the plasma resistance rises (Fig. 5.4.3(c)) and the

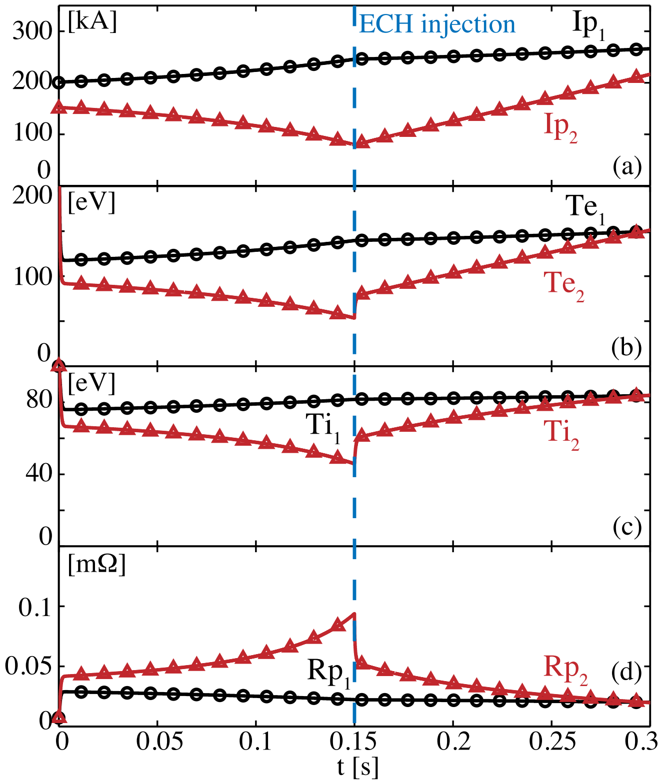

Figure 5.4.4: Temporal evolution of the (a) plasma current, (b) electron temperature, (c) ion temperature and (d) plasma resistance for the two doublet plasma columns. The dashed blue line represents the time instant of the step in the ECH power in the plasma column 2.

plasma current decreases still further. The timescale of this evolution is relatively slow, of the order of the plasma electric time constant ($\tau \sim \frac{L_P}{R_P}$).

Stressing the fact that acting on the ohmic coil current, as in a standard plasma control system, does not prevent this unstable behavior, a different actuator able to control the two plasmas independently must be used. The ECH system of TCV can be used to heat and drive current independently in the two plasma columns. Figure 5.4.4 shows the temporal evolution of the same plasma quantities represented in Fig. 5.4.3, but now with the addition of ECH power. The initial conditions are equal to those in Fig. 5.4.3. The temperature of plasma column 2 decreases, leading to an increase of the plasma resistance and a reduction of the plasma current. At $t = 0.15$ s, ECH power is injected into plasma column 2 ($P_{ECH} \sim 0.5 P_{OH2}$ - no current drive). This leads to a relatively fast increase of the plasma temperature and a reduction of the plasma resistance. As a consequence, the current in column 2 rises, preventing disruption.

5.4.2.1 Doublet plasma current observer

It seems clear that in a doublet configuration it is important to monitor the current in the two plasma columns. Instead of independently controlling the two plasmas, it is indeed easier to control the common mode (Q-mode), defined from the total plasma current ($I_P^Q = \frac{I_{P1}+I_{P2}}{2}$) and the differential mode (S-mode), defined from the difference between the two plasma currents ($I_P^S = \frac{I_{P1}-I_{P2}}{2}$).

The observer for the Q-mode is similar to the conventional single-axis plasma observer used on TCV. The absence of a Rogowski coil that can be used by the control system imposes a deduction of the plasma current from the pick-up coils mounted on the VV. From Ampere's law:

$$\mu_0 \mathbf{j} = \nabla \times \mathbf{B} \rightarrow I_P^Q = \frac{I_P}{2} = \frac{\sum_i b_i \Delta l_i}{2\mu_0} \tag{5.4.18}$$

where Δl_i is the distance between two adjacent pick-up coils. This signal is then compared with the reference plasma current, obtaining the Q-mode plasma current error sent to the controller. Concerning the S-mode, the two plasma currents are obtained from the Eq. 5.4.3:

$$I_P^S = \frac{I_{P1} - I_{P2}}{2} = \frac{\sum I_x^U - \sum I_x^L}{2} \tag{5.4.19}$$

These observers are a linear combination of the measured quantities and are therefore simple to implement even in the analog TCV hardware control system.

5.4.2.2 Doublet plasma current actuator

The actuator for the Q-mode plasma current control system is the ohmic coil. Since the Q-mode refers to the total plasma current, the ohmic coil produces a uniform electric field inside the VV and therefore is suitable for this purpose.

Concerning the S-mode, two ECH launchers can be used, one directed toward the upper plasma and the second one towards the lower plasma column. The ECH power should be proportional to the signal I_P^S in Eq. 5.4.19 according to the controller properties. For positive errors ($I_P^S > 0$), the lower launcher alone should be operational. Conversely, for negative errors ($I_P^S < 0$) only the upper launcher should be active.

5.5 Doublet plasma start-up

One of the most critical aspects of the doublet plasma scenario is the plasma start-up. The neutral gas inside the VV must be ionized in two regions close enough to the position of the two initial plasmas in the droplet configuration. Once the ionization phase ends, the two plasma channels must grow simultaneously until the flat-top is reached.

The evolution is associated with some complications. To obtain a double ionization, two poloidal magnetic nulls need to be present in the right position. The ionization must start simultaneously in the two null regions, otherwise the plasma current of the first ionized region will destroy the magnetic structure of the second null point. During the ramp-up phase, the two plasmas should follow a similar evolution. Their vertical position should be such that the vertical growth rate is minimized, especially in this early phase characterized by small plasma currents (see Fig. 5.3.4).

Several attempts to create an ohmic doublet plasma have been made on TCV. Nevertheless, without the assistance of the ECH system there is little chance of obtaining a reproducible scenario. Only on one occasion was an ohmic doublet shaped plasma obtained (Fig. 5.5.1) [64].

The doublet configuration was only maintained for a short time (∼ 10 ms). The current in the lowest plasma decreased until a single-axis plasma was obtained (Fig. 5.5.1(b)).

In 2009, a new experimental campaign started on TCV to create, control and study the doublet configuration. The magnetic field structure used at the time of breakdown is illustrated in Fig. 5.5.2(a).

Several poloidal field null points are present, with different magnetic properties. The null point having the longest connection length is the null point 1 (Fig. 5.5.2(b)). When a toroidal electric field is applied, the gas ionization is mainly localized in the null point 1 region (Fig. 5.5.3(a)).

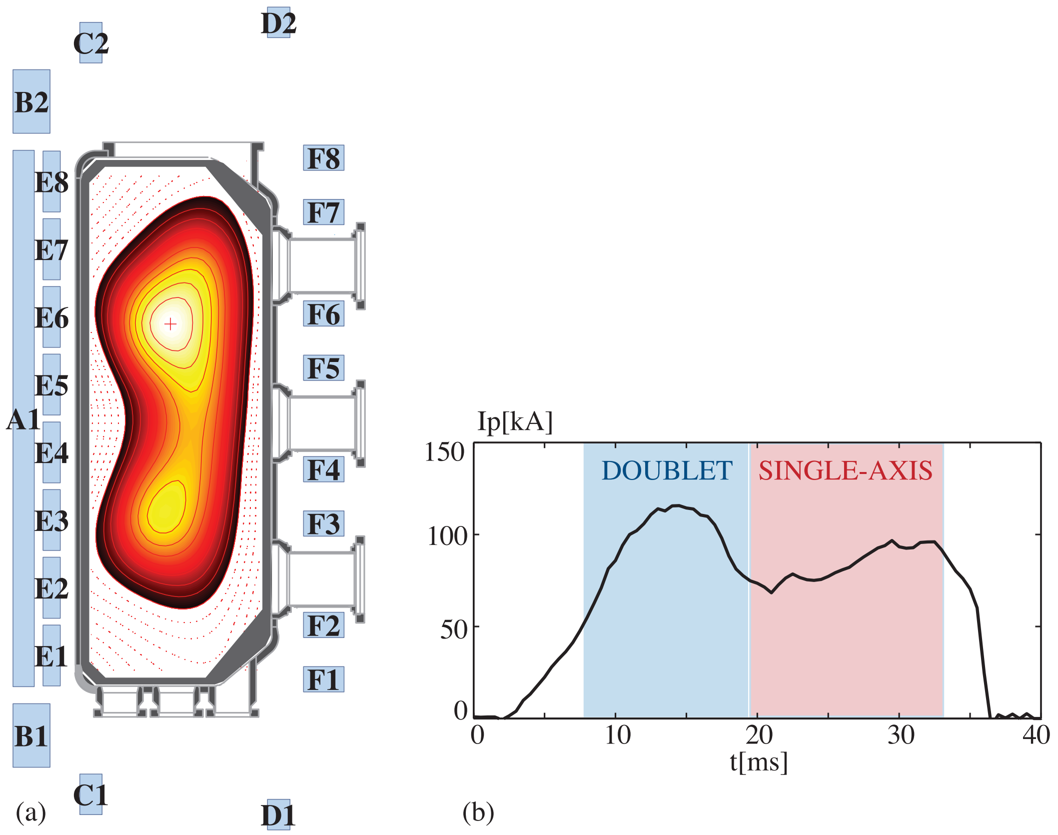

Figure 5.5.1: Doublet configuration obtained in TCV (shot #10159). (a) Magnetic field reconstruction ($t = 10$ ms, $I_P = 110$ kA, $\kappa = 2.6$); (b) Plasma current temporal evolution.

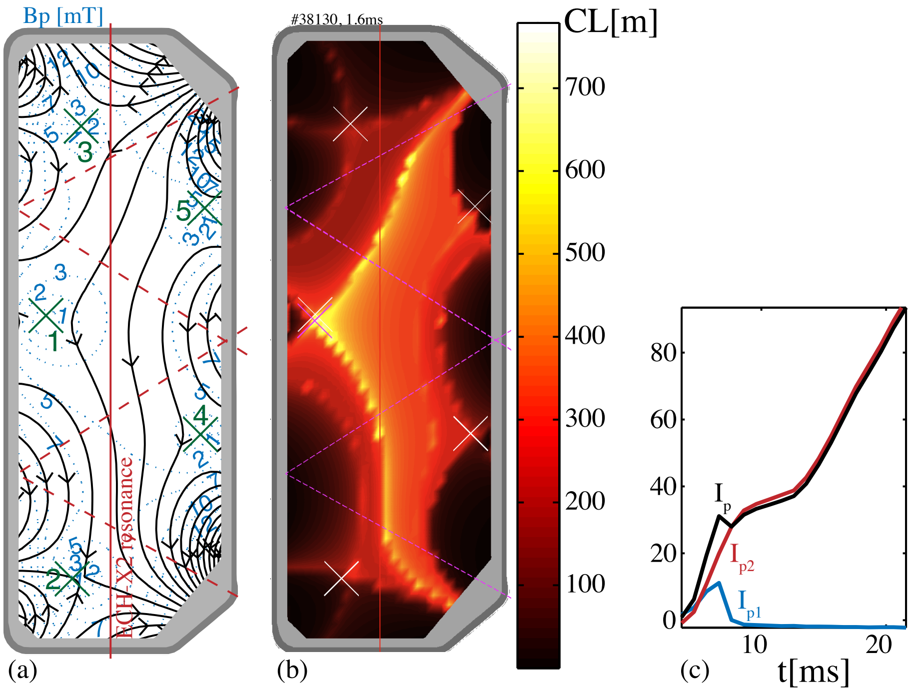

Figure 5.5.2: (a) Poloidal magnetic flux (black lines) and poloidal magnetic field at the breakdown time (shot #38130, 1.6 ms). The green crosses are the poloidal magnetic field null points. The solid red line represents the resonance position and the dashed red lines the trajectory of the injected ECH-X2 beams. (b) Spatial distribution of the connection length. (c) Evolution of the plasma current of the upper plasma (blue), lower plasma (red) and the total plasma current (black).

This is not surprising, considering the very high connection length of this null point compared to the other null points present inside the VV.

Clearly the magnetic field configuration at the time of breakdown could be improved to increase the quality of the null points 2 and 3 and remove the null point 1. Even achieving such a configuration (not a simple problem considering the challenge of imposing a given poloidal magnetic field inside the highly conductive TCV VV) the probabilities of succeeding in an ohmic double breakdown may remain small.

To obtain a double breakdown, the evolution of the connection length should be similar for the two null points. The connection length in the desired breakdown positions should be the longest, to avoid a earlier breakdown in a different region. Differences in the connection length between the two null point regions can lead to a delay of the ionization process of one of the two plasmas. In this case, the successful breakdown can deteriorate the already not optimal conditions of the other breakdown point. Two effects are responsible for this deterioration:

1. The growing plasma induces a negative voltage in the other breakdown region, reducing the effective loop voltage and therefore the probability of achieving a second successful breakdown. Assuming we have the two breakdown regions at the same radial position and a vertical separation of $\Delta z = 0.8$ m, the mutual inductance between two filaments placed at the breakdown positions is $M = 4 \times 10^{-7}$ H. The programmed plasma current derivatives have a maximum value of $\dot{I}_P = 2$ MA/s (see Sec. 4.2), but it can reach ~ 5 MA/s in the early ramp-up phase. Taking these values, the negative loop voltage induced in the other breakdown region can be estimated as follows:

$$v_{12} = M \cdot \dot{I}_P \sim 2 \text{ V} \tag{5.5.1}$$

   which is the 20% of the maximum ohmic loop voltage applicable on TCV (Sec. 4.2).

2. The magnetic field produced by the growing plasma destroys the magnetic field configuration of the second plasma. The magnetic field produced by a filamentary current in the second null point region can be computed from the Green's functions ($B_{12} = 1.4 \times 10^{-7}$ T/A). The minimum magnetic field necessary to have a significant perturbation of the null point region is $b \sim 1$ mT. The current in the growing filament will perturb the second breakdown region if:

$$I_{P2} > \frac{b}{B_{12}} \sim 7 \text{ kA} \tag{5.5.2}$$

   This condition is obtained if the delay between the two plasmas is:

$$\Delta t > \frac{I_{P2}}{\dot{I}_P} \sim 1.4 \text{ ms} \tag{5.5.3}$$

The ionization may also be completely compromised if the connection length in one of the two null regions is too small compared with the other. For a given toroidal electric field and neutral pressure, the ionization is possible only if the connection length is larger than a given threshold value (Figs. 4.4.2-4.4.3). It is clear that to succeed in a double ohmic breakdown, significant attention must be dedicated to the poloidal magnetic field configuration and the quality of the null points.

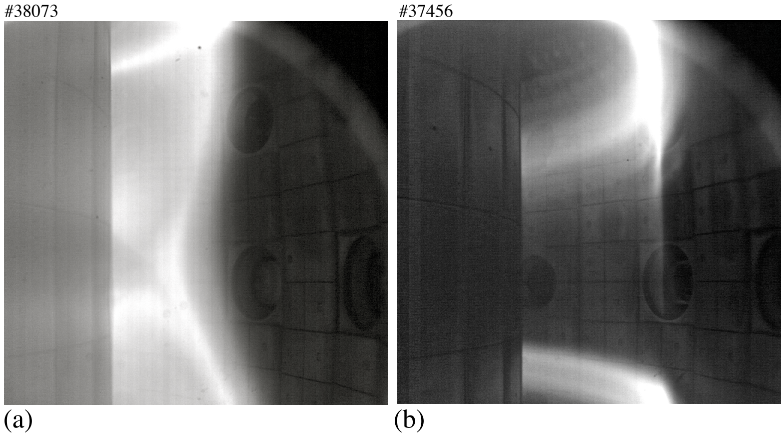

Figure 5.5.3: Images from the fast tangential visible camera at the breakdown time for a doublet ohmic breakdown (a) and a doublet assisted breakdown with ECRH (b).

To increase the parameters space allowing a successful double breakdown, ECH-X2 can be used to assist the double plasma start-up. Single plasma ECH assisted start-up experiments have been performed on TCV (see Sec. 4.10), showing that the ECH system does allow a more robust and reliable breakdown.

The ECH-X2 should therefore improve the probability to have a double breakdown, especially in a non optimal magnetic configuration. In TCV, two ECH-X2 beams were injected towards the two null point regions (Fig. 5.5.2(a)). The result is shown in Fig. 5.5.3(b), where the fast visible camera clearly shows two plasma channels created inside the VV. The location of the plasma channels corresponds to the position of the first-pass resonance of the injected beams (Fig. 5.5.2(a)). This evolution is robust and reproducible, even for different values of the ECH poloidal angles. Unfortunately, the success obtained is limited to the double ionization problem, since it was not possible to obtain two stable plasmas growing inside the VV (Fig. 5.5.2(c)).

This appears to be a burn-through problem rather than a vertical stability problem, since the two plasmas are probably too small and far away from each other to show a noticeable vertical instability (Fig. 5.3.4). The weakest plasma was always the top one, even when the ECH-X2 power on the bottom plasma was reduced and the power on the top plasma maximized. The low efficiency of the ECH-X2 in controlling the two plasma channels during the early ramp-up phase is mainly due to the low plasma temperature,leading to poor second harmonic absorption [82]. Moreover during the early ramp-up phase, the size of the two plasma channels is too small (Fig. 5.2.1(a)), and the ECH-X2 resonance (Fig. 5.5.2(a)) is only marginally intersected. The resonance could be shifted towards the plasma center reducing the toroidal magnetic field, bearing in mind that a resonance too close to the HFS may become problematic during the doublet flattop phase, since only the plasma edge will be heated. The toroidal magnetic field should therefore be optimized during the discharge to keep the ECH-X2 resonance close to the plasma axis.

5.6 Conclusions

This chapter reported on a theoretical study of the possibility to establish a doublet shaped plasma on TCV and presented a few initial experimental results.

A scenario based on merging of two droplet plasmas is identified as the most promising, due to its better stability. The problem of the doublet vertical stability is analyzed, showing that two doublet unstable vertical modes can be predicted by the KINX code and only partially with a rigid plasma displacement model. The reason for this discrepancy depends on the presence of surface currents, not described by the rigid model.

Several strategies to control the main doublet quantities have been illustrated, showing a possible solution to establish and control a doublet on TCV. Finally, the first experimental results have been presented, where two plasma channels were successfully created using the ECH-X2 system in a magnetic configuration with two null points. More experimental work would be necessary to control these two plasma channels through the ramp-up phase to create a doublet.

The next chapter reports about another extreme and unusual plasma shape: the “snowflake” divertor configuration.

Part II

The snowflake divertor

Chapter 6

Snowflake divertor

6.1 Introduction

In nuclear fusion facilities based on the tokamak concept, the plasma is confined within closed magnetic flux surfaces generated by a combination of fields due to currents flowing in external conductors and in the plasma. The LCFS defines the shape of the plasma cross-section and it is bounded either by the intersection of closed magnetic surfaces with a solid surface (limited plasma) or by the magnetic field itself (diverted plasma). In those magnetic confinement devices, power exhaust handling and plasma-wall interaction must be mastered to a level compatible with wall materials.

Nowadays, the divertor configuration has emerged as the preeminent solution to managing power and particle exhaust and core impurity content. In the presence of a magnetic X-point, where the poloidal field vanishes, energy and particle losses are channeled primarily into a divertor region that is separated from the confined plasma region. The drawback of this approach is the high power flux impinging on the divertor plates, which may consequently overheat and undergo destructive erosion. This is particularly true during edge localized modes (ELMs) [83,84,85,86,87] occurring in the high-confinement H-mode [70], which cause periodic, violent, and potentially highly damaging ejections of energy and particles onto the divertor surfaces [88,89]. While these instabilities can reduce core plasma impurity accumulation and permit quasi-steady operation, they also limit the lifetime of the plasma-facing components (PFCs). If their amplitude is not maintained below certain limits, the divertor PFC lifetime would be too short for a viable tokamak power plant. Heat flux management in the tokamak divertor and, in particular, the control of ELMs [90,91,92], remain therefore a primary goal of magnetic fusion research.

Different solutions have been proposed to reduce the plasma-wall interaction in the divertor region by acting on the magnetic field topology [23,93,94,95,96,97]. One of these solutions is the so-called snowflake divertor [23,94].

In this chapter, the snowflake divertor is described and the potential advantages of this configuration are exposed. The feasibility of this configuration was demonstrated for the first time [24,98,99] in the TCV tokamak. Dedicated experiments have been carried out to study the properties of this configuration in the H-mode regime [100,101,102,103,104]. A review of the experimental results obtained is given in this chapter.

6.2 The snowflake divertor concept

The basic concept of the snowflake divertor (SF) is illustrated in Fig. 6.2.2. In a conventional single null (SN) configuration (Fig. 6.2.1), the poloidal magnetic field vanishes at the X-point

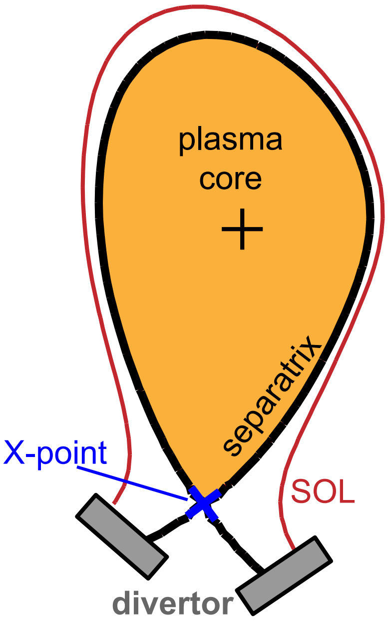

Figure 6.2.1: Plasma tokamak conventional single null divertor configuration.

(first-order null). A SF diverted configuration is characterized by a second-order null, i.e. the first derivatives of the magnetic field also vanish at the null point and the separatrix divides the poloidal plane into six sectors, Fig. 6.2.2(b). Perturbing the exact SF configuration by shifting the plasma column away from the null point or towards it, while keeping divertor currents I_{d1}, I_{d2} and plasma current I_P constant, produces the magnetic configurations which are respectively shown in Fig. 6.2.2(a) and Fig. 6.2.2(c). In these two configurations, the first derivatives of the poloidal magnetic field are small compared to those of a SN. Following Ref. [23, 94], we will refer to these two configurations as of snowflake-plus (SF^+) and snowflake-minus (SF^-) respectively. The two configurations have two contiguous X-points that, for the SF^- configuration, are both located at the separatrix. These configurations of course chart a continuum, which can be conveniently parametrized by the distance between X-points normalized to the plasma minor radius, which will be labeled σ.

The second-order null modifies the magnetic topology near the plasma boundary and is therefore expected to affect the edge plasma properties. In particular, the flux expansion around the null point is 2-3 times larger than in the SN configuration and the connection length in that region increases, reducing the local heat load to the divertor plates [23, 94, 105, 106]. Additionally, the magnetic shear in the edge where an H-mode pedestal would lie is modified, providing a possible way to influence ELM activity [107]. Squeezing the flux tubes near the null point may also decouple the turbulence in the divertor legs and in the SOL and affect any radial blob displacement [108,109]. Moreover, the large flux expansion around the null point should change the prompt losses of ions having turning points in the vicinity of the poloidal field null [110].

6.3 Snowflake feasibility on TCV

To assess the capability of TCV for creating an SF divertor, a limiter plasma equilibrium is modified to obtain a second-order null. The initial Grad-Shafranov equilibrium is created with FBTE/MGAMS [39, 38], the suite of software tools used routinely on TCV to determine the poloidal coil currents for a given plasma configuration. The poloidal coil currents required to create a SF from a limited plasma equilibrium are evaluated by imposing the following conditions:

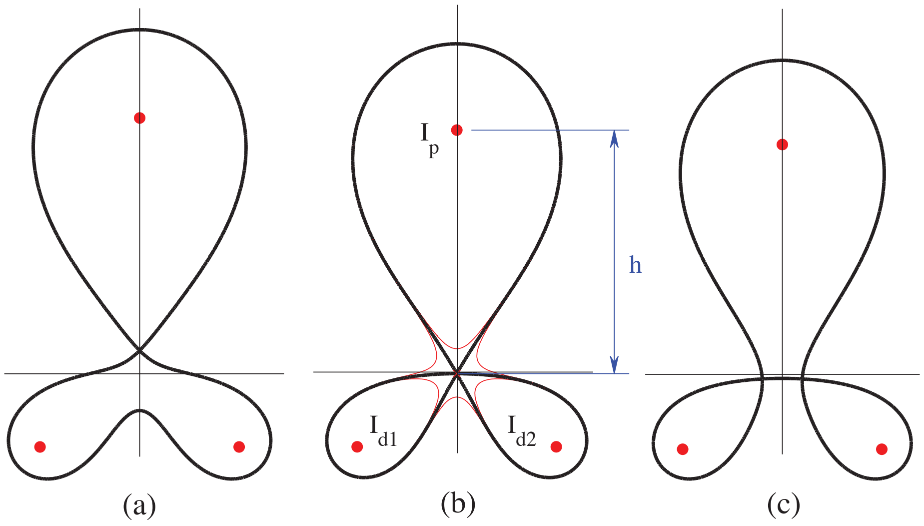

Figure 6.2.2: SF configurations using a straight tokamak model. The circles represent the current filaments (plasma, I_P, and divertor conductors, $I_{d1,2}$) and the bold black line is the separatrix. The SF$^+$ configuration in (a) and the SF$^-$ configuration in (c) have been obtained by shifting the plasma position of the SF configuration vertically by ±5%, while keeping I_P and $I_{d1,2}$ constant.

1. the magnetic field must vanish at the null point:

$$-\mathbf{B}_{n0} = \underline{\underline{\mathbf{B}}}_{nc} \cdot \delta\mathbf{I}_c \tag{6.3.1}$$

   where $\mathbf{B_{n0}}$ is the poloidal magnetic field vector at the desired null point for the initial limited configuration, $\underline{\underline{\mathbf{B}}}_{nc}$ is the matrix containing the Green's functions used to evaluate the magnetic field at the null point from the currents in the poloidal coils and $\delta\mathbf{I}_c$ is the vector with the corrections in the poloidal coil currents;

2. the derivatives of the magnetic field must also vanish at the null point:

$$-\mathbf{dB_{n0}} = \underline{\underline{\mathbf{dB}}}_{nc} \cdot \delta\mathbf{I}_c \tag{6.3.2}$$

   where $\mathbf{dB_{n0}}$ is a vector containing the all derivatives of the poloidal magnetic field at the null point before the correction and $\underline{\underline{\mathbf{dB}}}_{nc}$ is a matrix containing the spatial derivatives of the Green's functions used to evaluate the derivatives of the magnetic field in the R and z directions at the null point from the currents in the poloidal coils;

3. the poloidal flux perturbation in the main plasma region produced by the change in the coil currents is minimized:

$$\mathbf{0} = \underline{\underline{\mathbf{dM}}}_{nc} \cdot \delta\mathbf{I}_c \tag{6.3.3}$$

   where $\underline{\underline{\mathbf{dM}}}_{nc}$ is used to evaluate the flux variation on a certain number of points that belong to the same flux surface, Fig. 6.3.1(a). These points are chosen to be close to the LCFS but far from the null region. This supplementary condition preserves the plasma shape.

4. the solution with the minimum change of the poloidal coil currents is imposed:

$$\min\left(|\delta\mathbf{I}_c|^2\right). \tag{6.3.4}$$

A solution to equations (1-4) is determined using a least squared approach. This minimization process is applied to produce the calculated SF configuration shown in Fig. 6.3.1(a) together with

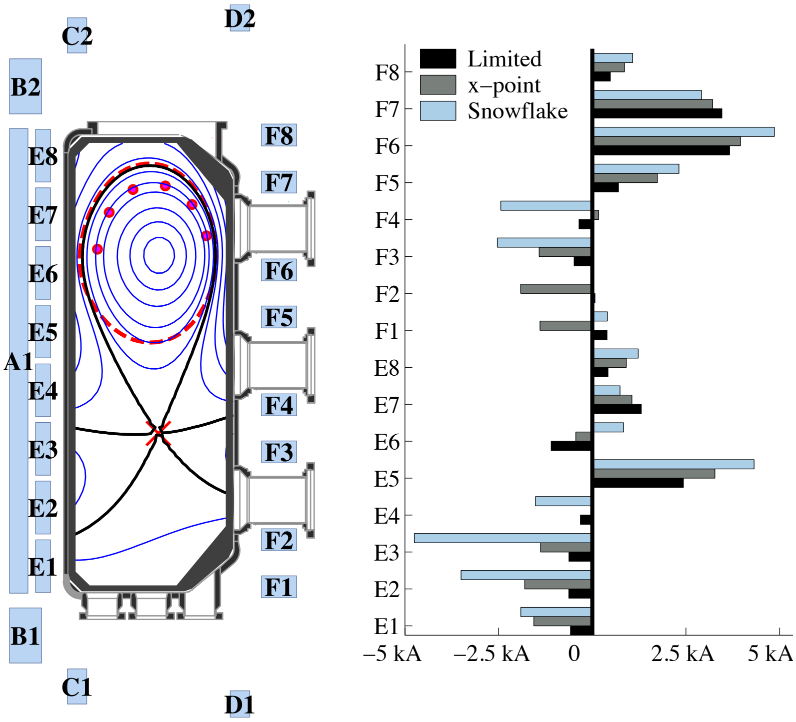

(a) (b)

Figure 6.3.1: (a) The result of the magnetic perturbed equilibrium approach are shown for a plasma current of 500 kA. The thin lines are the flux contours for the SF configuration and the bold lines trace its separatrix; the dashed line is the LCFS of the initial limited plasma, the cross localizes the null point and the solid circles are the control points where the same-flux condition is imposed. In (b), the currents in the poloidal coils for a limited plasma (black), a standard diverted plasma (grey) and a SF (light-grey) are plotted. The maximum permitted current in the TCV poloidal field coils is 7.7 kA.

the currents in each coil, Fig. 6.3.1(b), for $I_P = 500$ kA. In Fig. 6.3.1(b), the currents in the poloidal coils for the initial limited plasma (black), a standard diverted plasma (grey) and the SF (light-grey) are compared. The data show that the currents in the poloidal coils necessary to create an SF are larger compared to a SN due to the magnetic dipole fields required by the configuration (coils E3, E4, E5 and F3, F4, F5). Nevertheless, the currents are compatible with the current limits in the TCV poloidal coils (7.7 kA). Different SF configurations are possible within the coil current limits. We focus our attention on a configuration with positive triangularity (which is expected to have better MHD stability [111]) and with one divertor strike point on the LFS between the F3 and F4 coils, Fig. 6.3.1(a), to ensure that power is deposited on protection tiles. The discharge parameters necessary to experimentally produce the SF plasma are determined from the solution of the free boundary equilibrium problem, solved using the MGAMS/FBTE code suite. Since FBTE is not able to impose a second-order null condition directly, a configuration with two X-points (close to each other) is instead evaluated. The exact SF configuration is then achieved by moving the plasma position vertically during the discharge.

6.4 Snowflake scenario on TCV

Starting from a limited plasma, a SN configuration is created with both strike points on the central column. One of the strike points is subsequently moved to the LFS producing a SF$^+$ configuration. Using the LIUQE code [39, 112], the magnetic equilibria for the SN and the SF configurations are reconstructed from the magnetic measurements to constrain the Grad-Shafranov solution. The

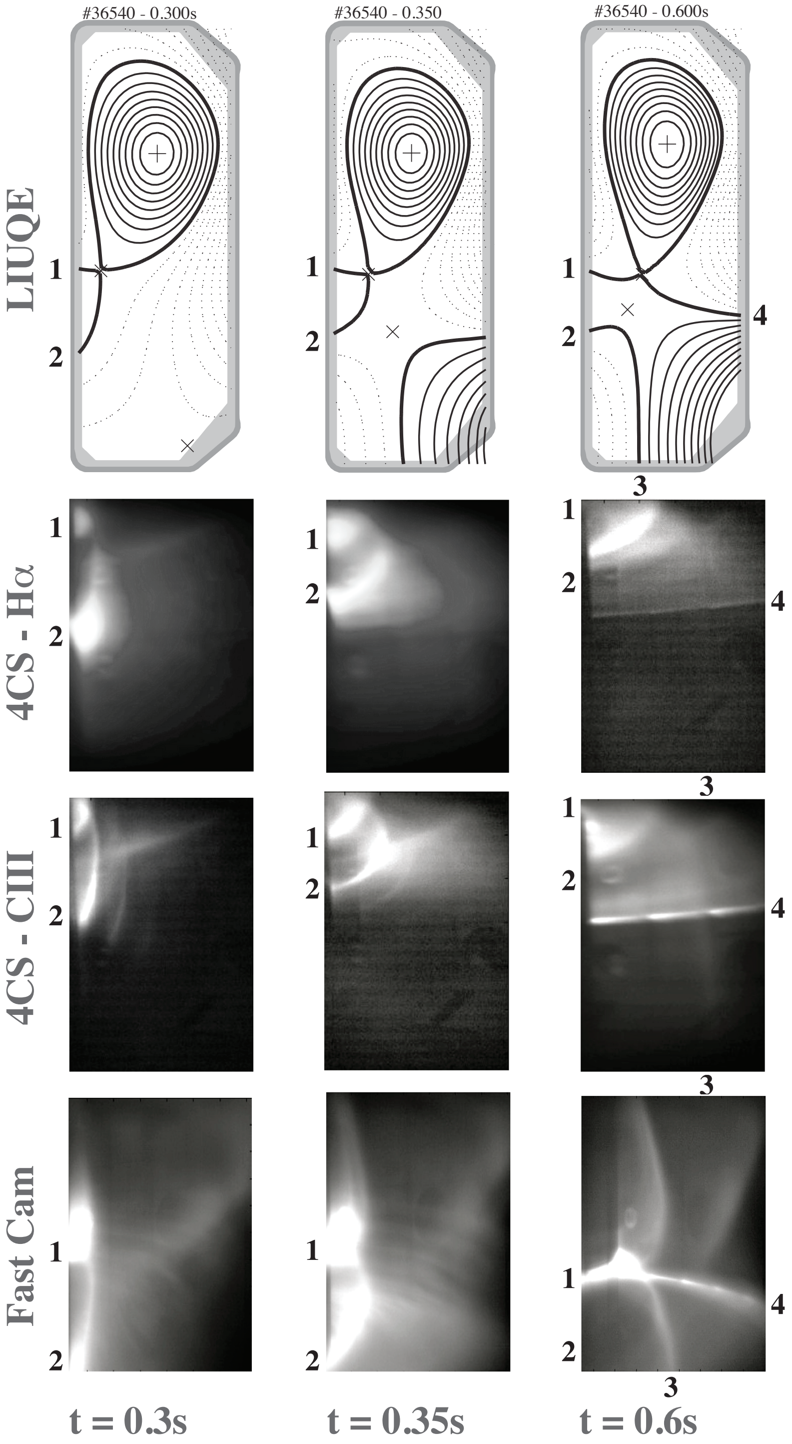

Figure 6.4.1: Evolution from SN configuration to SF$^+$ divertor. From top to bottom: LIUQE reconstructions, frames from MultiCam with H_α filter, frames from MultiCam with C^{III} filter, frames from the FastCam.

scenario that leads to a SF$^+$ creation from a SN plasma is illustrated in Fig. 6.4.1, where a sequence of LIUQE equilibria is illustrated together with the respective frames from the MultiCam with an H_α filter and with a C^{III} filter and from the FastCam (see Sec. 2.4.3.3).

Once the SF$^+$ is created, moving the plasma vertically, the SF and the SF$^-$ are also established during the same discharge. The reconstructed equilibria are shown in Fig. 6.4.2 together with visible light emission obtained with an unfiltered, tangentially viewing CCD camera. The visible emission qualitatively confirms the presence of the SF divertor. At the relatively low plasma

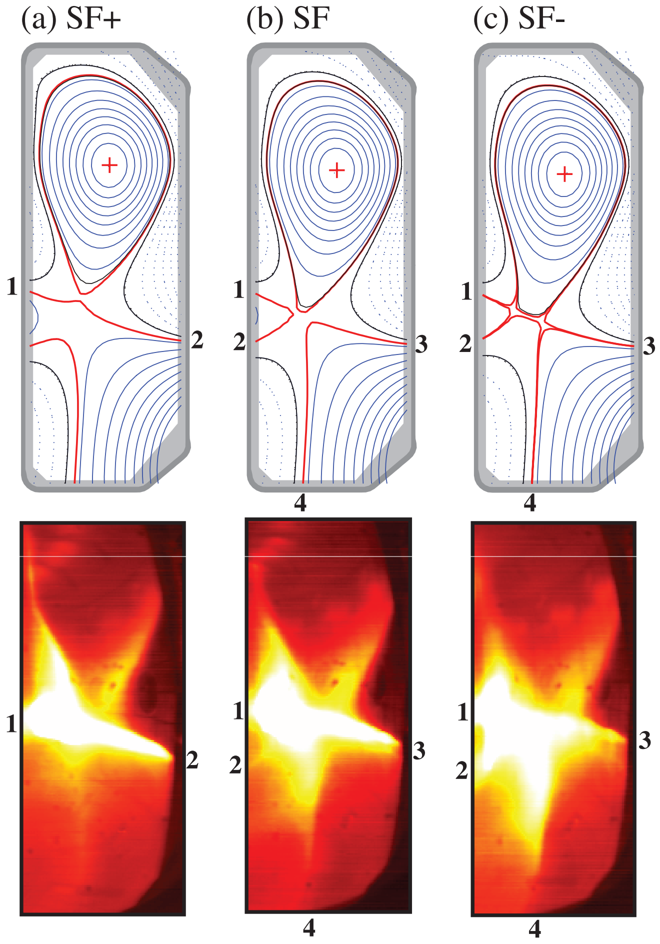

Figure 6.4.2: Equilibrium reconstructions and images from the tangential visible CCD camera for a SF$^+$ (a), a SF (b) and a SF$^-$ configuration (c), all obtained in the same discharge by vertical plasma movement. In each frame, numbers indicate the divertor strike point positions. Notice the different vertical plasma position for each SF configuration (shot #36151; SF$^+$ at 0.411 s, SF at 0.457 s, SF$^-$ at 0.504 s; $I_P = 230$ kA; $q_{95} = 3.5$; $k_{95} = 1.45$; $\delta_{95} = 0.15$; $n_{e0} = 7 \cdot 10^{19}\mathrm{m}^{-3}$).

current and high density of the discharge, the majority of the emission is concentrated in the cool X-point region and along the divertor legs. Here, the plasma temperature is such as to promote strong carbon radiation from impurities generated at the graphite first wall. These visible images also show clearly that radiation occurs in all four divertors only for the SF and SF$^-$ configurations and in particular for the SF$^-$ equilibrium. Here, this is likely due to the increased size of the region over which the core plasma has direct access to the null point, increasing the power channelled through the divertor volume and thus radiated in the four divertor legs.

Fig. 6.4.3 compiles tomographic inversions of total radiation emission from a poloidal array of AXUV diode pinhole cameras [113, 114]. The inversions are performed at the same time instants as those of the CCD images in Fig. 6.4.2. In all three SF configurations, the radiation is observed to peak in the null point vicinity, with the highest levels observed for the SF equilibrium. This is again a likely consequence of the increased radiating volume in the flux expanded null point region. In a carbon dominated machine, emission at the edge is most powerful in the UV spectral region, corresponding to plasma temperatures in the range 10-20 eV. Under the conditions of these experiments, this will correspond to the X-point region, as seen in the reconstructions. The low radiation levels in the vicinity of the strike points, together with strong visible emission along the divertor legs, is a qualitative indication of extremely low plasma temperatures there and thus of detached divertor states. This is unsurprising given the low plasma current ($I_P = 230$ kA) and

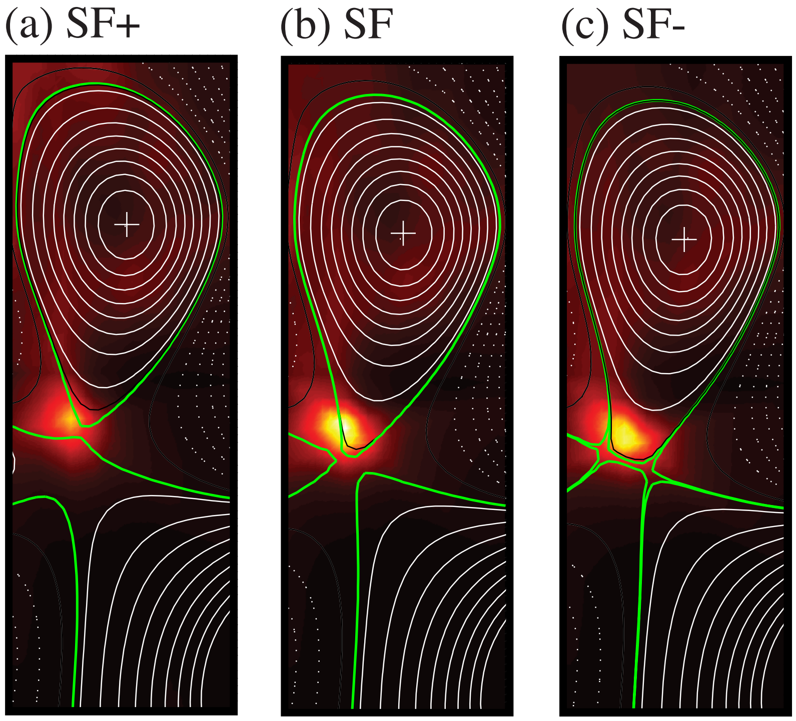

Figure 6.4.3: Tomographic reconstructions of total radiated power obtained from an array of AXUV diode pinhole cameras for the configurations in Fig. 6.4.2.

relatively high density ($n_{e0} = 7 \times 10^{19}$ m^{-3}) of these plasmas, particularly when the power sharing into several divertor branches is taken into account. The AXUV diodes have a non-linear spectral response [113, 114] and thus cannot be used to assess the absolute radiated power.
The flexibility of TCV allows to establish several SF configurations with different values of the σ parameter.
In Fig. 6.4.4, the LIUQE reconstruction of different SF$^+$, SF$^-$ and SF configurations is shown. For values of $\sigma < 20\%$, the configuration is considered as a perfect SF, since the magnetic properties are similar to those of a ideal SF configuration. Note that to define the magnetic properties of the SF$^-$ configurations, an additional parameter must be introduced: ΔR_S, defined as the distance at the outer midplane of the flux surfaces of the two X-points, gives an indication of the proximity to a perfect, ideal SF$^-$ configuration.

6.5 Magnetic properties of the snowflake

The magnetic properties of the SF configurations are compared with those of the SN configuration using the magnetic measurements from the equilibria in Fig. 6.4.2. The SF$^+$ and the SF$^-$ are characterized by $\sigma \sim 40\%$ and the SF in Fig. 6.4.2(b) has $\sigma \sim 15\%$.
For the SOL, an important parameter is the flux expansion. This quantity is related to the reduction of the poloidal magnetic field near the null point. The flux expansion influences the SOL thickness and the size of the radiating volume. Radial transport, and possibly formation of filaments in the edge/SOL region, may also be influenced by this flux expansion.
For a given flux surface, two geometrical parameters may be defined (see inset in Fig 6.5.1): Δ, the minimum distance between the null point and a flux surface in the LFS, and ξ, the distance between the same flux surface and the separatrix at the outer midplane. The flux expansion is now defined as the ratio Δ/ξ.
In Fig. 6.5.1, the flux expansion for the SF configurations and for the SN configuration are plotted

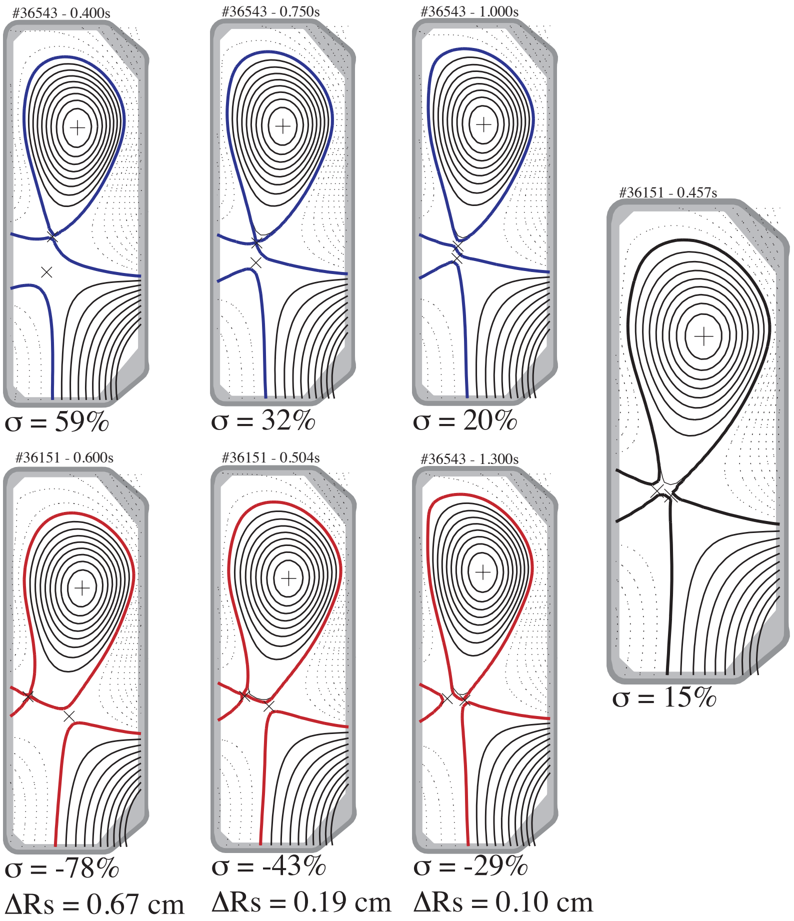

Figure 6.4.4: LIUQE reconstruction of several SF$^+$ (blue), SF$^-$ (red) and SF (black) configurations established on TCV.

as a function of the distance ξ from the separatrix. In the same figure, the connection length from the equatorial plane to the point closest to the null point (Lx) is shown as a function of ξ. The connection length determines the residence time of a particle in the SOL and therefore affects the radiative losses and the thermal power to the divertor surfaces. The thickness of the SOL at the outer midplane is typically ~ 2 cm. The SF configuration has a flux expansion near the separatrix (near SOL) and a connection length more than twice larger than that of the SN. The SF$^+$ and the SF$^-$ have similar values of flux expansion and connection length, with values that fall between the values computed for the SF configuration and the SN configuration.

The safety factor profile (q) and the magnetic shear ($s = \frac{\rho_{vol}}{q}\frac{dq}{d\rho_{vol}}$) are computed using the CHEASE code [115] and are shown in Fig. 6.5.2. The LCFS used to compute these quantities ($\rho_{vol} = 1$) is just inside the separatrix to avoid the singularity of q and s at the null point. The SF configuration has a larger magnetic shear than that for the SN configuration. This difference is important for $\rho_{vol} > 0.96$. The SF$^+$ and the SF$^-$ configurations also have a larger magnetic shear compared to the SN configuration. In the case of the SF$^-$ configuration, the presence of a double null in the separatrix results in a large volume where the poloidal magnetic field is small. This property emphasizes a dissimilarity in the magnetic shear profile compared with the SF$^+$ configuration. Note that the profiles of the SF$^-$ are very similar to the SF up to $\rho_{vol} \simeq 0.985$ but then become closer to the SF$^+$ and the SN. This might lead to differences in the MHD stability limits in between the SF$^+$ and SF$^-$.

Another interesting magnetic property is the geometry of the flux tubes in the SOL. The cross-section of the flux tubes and of the plasma blobs/filaments eventually present in the SOL, is not

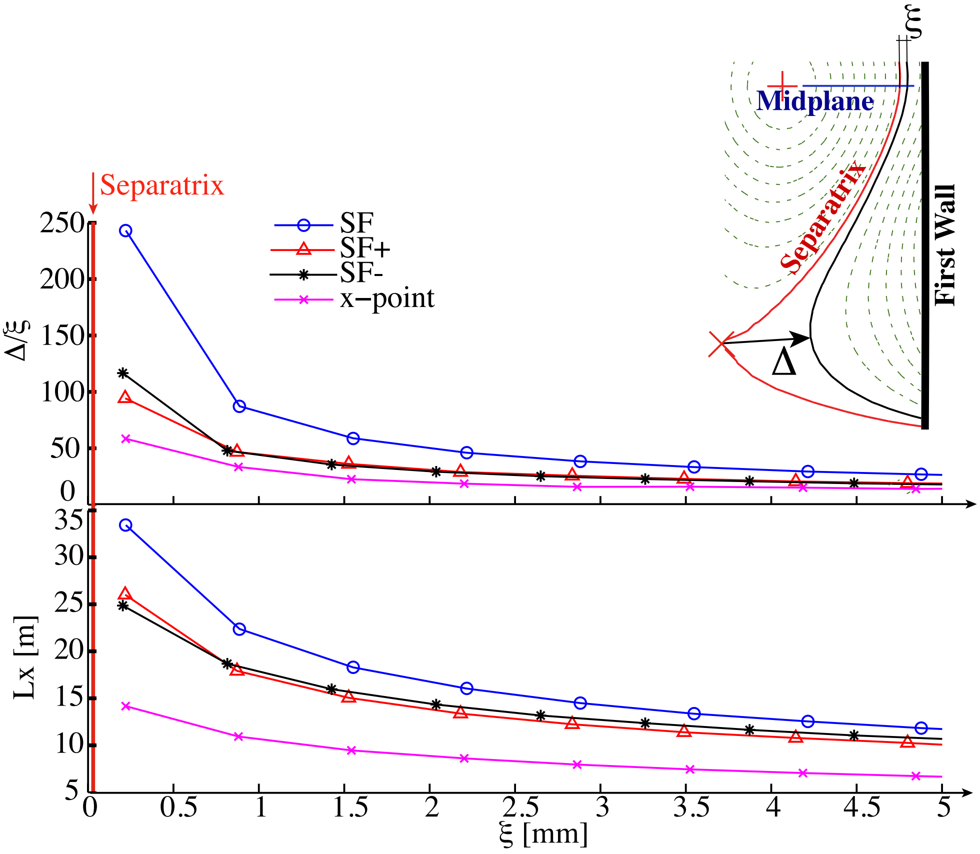

Figure 6.5.1: Flux expansion (Δ/ξ) and Connection Length (Lx) for a SF(circles), a SF$^+$(triangle), a SF$^-$ (points) and a SN (crosses). The typical SOL thickness at the equatorial plane is 2 cm. SF shot #36151 (SF$^+$ 0.411 s, SF 0.457 s, SF$^-$ 0.504 s), SN shot #35137, 0.6 s. In the same figure, the geometrical parameters Δ and ξ are also defined.

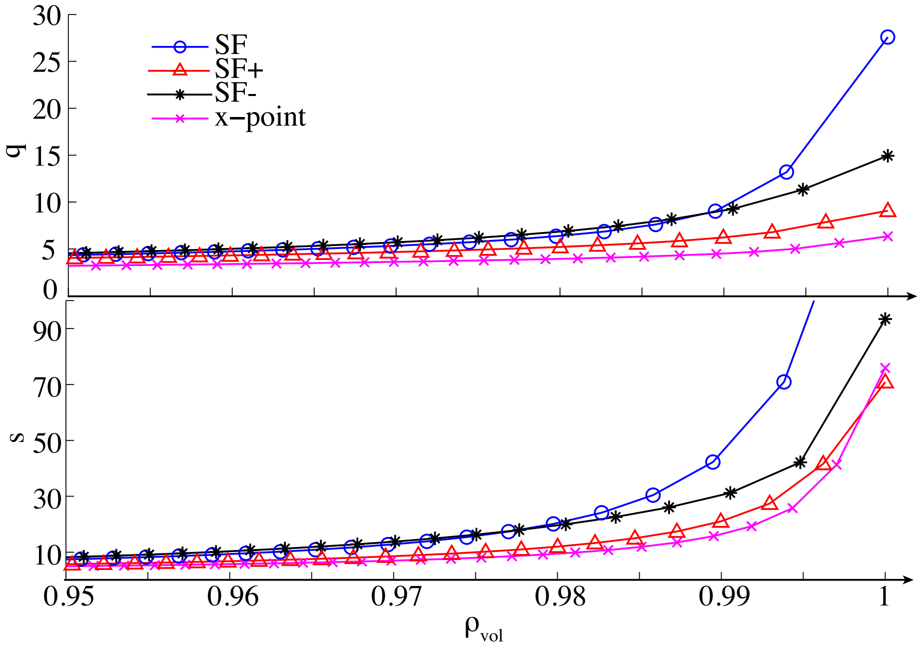

Figure 6.5.2: q-profile (q) and magnetic shear (s) for an SF (circles), a SF$^+$ (triangle), a SF$^-$ (points) and a SN (crosses) as a function of $\rho_{vol} = \sqrt{V/V_{edge}}$. SF shot #36151 (SF$^+$ at 0.411 s, SF at 0.457 s, SF$^-$ at 0.504 s), SN shot #35137 at 0.6 s.

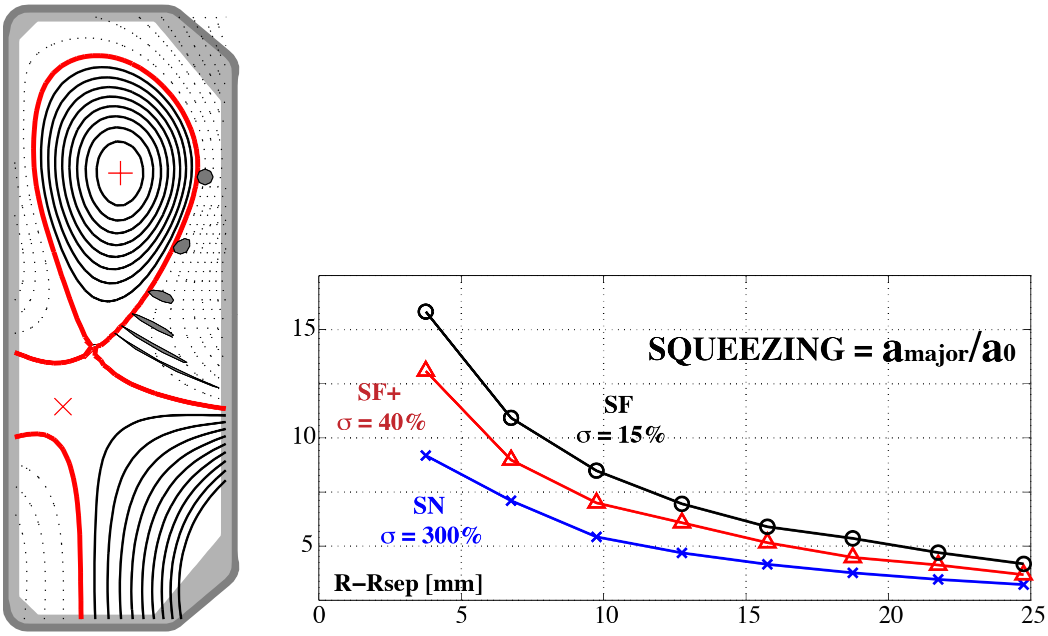

(a) (b)

Figure 6.5.3: (a) Flux tube geometry at the LFS of a SF$^+$ configuration; (b) squeezing of the flux tubes in a SF (black), SF$^+$ (red) and a SN (blue) configuration as a function of the distance from the separatrix evaluated at the outer plasma midplane.

constant along the field lines. This is due to the variation of the poloidal magnetic field which leads to a squeezing/stretching of the flux tubes [108, 109]. In the presence of an X-point, where the poloidal magnetic field vanishes, the effect is particularly strong and a perturbation of the blobs dynamics is expected. In the case of a SF divertor, the larger flux expansion amplifies this effect and, as a consequence, the blobs/filaments dynamics should be different compared to a SN configuration.

In Fig. 6.5.3(a) the flux tube geometry in the LFS SOL of a SF$^+$ configuration is represented. The circular cross-section of the flux tube at the outer midplane is squeezed near the null point region. To quantify this squeezing mechanism, the ratio between the longest semi-axis of the blob in the null point region and the initial radius of the blob at the outer midplane (3 mm) is represented in Fig. 6.5.3(b). This ratio is higher near the separatrix (small values of $R - R_{sep}$) and for small values of σ. As a consequence, in the SF configuration, the flux tubes in the SOL exhibit a remarkable deformation compared to the SN configuration.

6.6 H-mode snowflake plasma scenario

The improved confinement regime, known as the H-mode, is the most promising reference scenario for ITER due to its high energy confinement time. This regime is characterized by the onset of ELMs [83, 84] which cause periodic ejections of large fractions of the plasma energy through the SOL. These transient bursts of energy and particles produce high peak heat loads on the divertor PFCs that have important consequences on the economical viability of a fusion power plant. However, ELMs are beneficial in removing impurity and preventing the build-up of density, allowing a stationary H-mode operation. Although the H-mode regime and the ELM instabilities are extremely important for magnetic fusion research, the mechanisms that trigger an H-mode and the nature of the ELMs are still far from completely understood and are still a matter of debate.

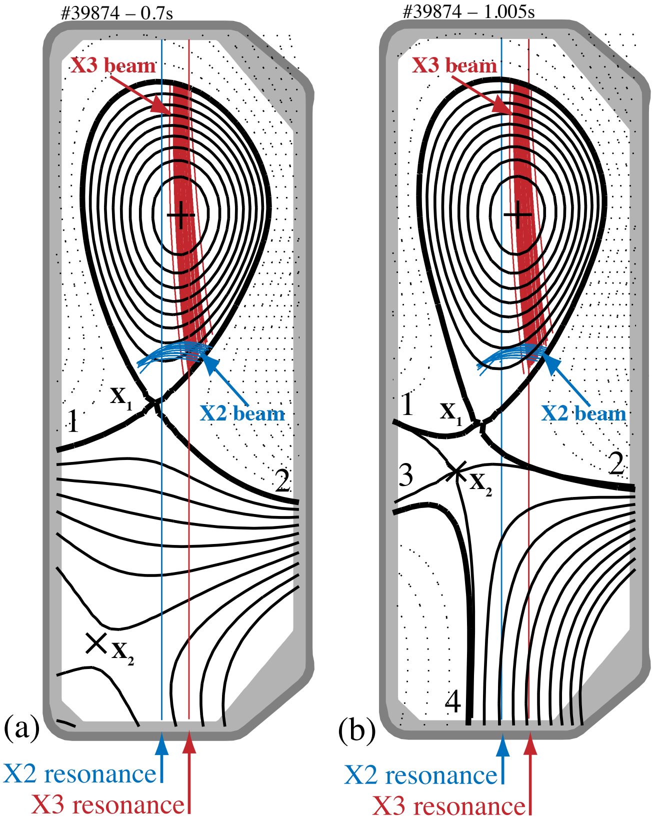

Figure 6.6.1: SN configuration (a) and SF$^+$ configuration (b). Red lines: ECH-X3 beam injected from the top of TCV. blue lines: ECH-X2 beam injected from the low-field side. The positions of the second and third harmonic shown are represented together with the strike point and null point positions.

Nowadays it is clear that the edge of a tokamak plasma plays a crucial role in determining the global properties of the system. As a matter of fact, it is well known that the direction of the $\mathbf{B} \times \nabla \mathbf{B}$ ion drift with respect to the X-point position in diverted configurations affects the L-H mode power threshold, that is even higher for limited plasmas [71]. In H-mode plasmas, the plasma edge influences the ELM dynamics. For highly shaped plasmas, the peeling-ballooning modes are more stable and a steeper pedestal is obtained [107].

This represents a strong motivation to study the properties of the H-mode regime in a SF divertor configuration. The SF divertor is the first truly new magnetic configuration to come along in tokamaks in some three decades. It is first important to verify that the configuration allows access to the H-mode regime. Having different edge magnetic properties, the properties of the H-mode in a SF and the associated ELMs may be different. The study of the H-mode SF is therefore important to discover possible advantages and disadvantages of this innovative configuration. Moreover, the obtained results may provide a contribution to clarification of existing models for the H-mode and the ELMs and improve our understanding of these phenomena.

In this section, the properties of the H-mode regime established in a SF$^+$ divertor for the first time are documented. In particular, the capability of the configuration to reach a stable H-mode is investigated, showing the differences compared to a SN configuration.

The SF$^+$ configuration used to study the H-mode properties is shown in Fig. 6.6.1(b). This configuration is characterized by $\sigma \sim 50\%$, a compromise between the enhancement of the plasma parameters due to the vicinity to the ideal SF configuration and the stable sustainment of the configuration by TCV's poloidal coil array and control system. The SN plasma used for the comparison is shown in Fig. 6.6.1(a). This is not the conventional TCV SN plasma shape, rather it is the result of a careful tuning process to match the shape and wall separations of the SF$^+$

configuration even though $\sigma \sim 300\%$. Differences between the two shapes are only significant in the null point region where the larger flux expansion of the SF$^+$ configuration results in a small modification of the plasma separatrix geometry. For comparison, the LCFS of the two moderately shaped configurations (triangularity $\delta = 0.2$ and elongation $\kappa = 1.75$) are shown in Fig. 6.6.2.

Figure 6.6.2: LCFS of the SN (black) and the SF$^+$ (red) configurations.

The magnetic properties of the SOL in the two configurations are summarized in Table 6.1. The connection length (L) and the flux expansion (Ψ_{ex}) are computed between 0.5 mm outside the LCFS on the plasma outer mid-plane and the strike points 1 and 2 in Fig. 6.6.1. The flux expansion for a given flux surface is defined as the ratio between its vertical distance along the machine wall from a specific strike point and its horizontal distance from the separatrix at the outer mid-plane.

Table 6.1: SOL magnetic properties of the SN and the SF$^+$ in Fig. 6.6.1.

	L_1 [m]	L_2 [m]	Ψ_{ex1}	Ψ_{ex2}
SN	17	13	2.8	1.4
SF$^+$	24	21	3.9	1.5

Note that the two configurations have similar values of flux expansion at the strike points in spite of the longer connection length of the SF$^+$ configuration. This is due to the long divertor legs which characterize the two configurations leading to a strong flux re-compression far from the null point region.

In these scenarios, the $\mathbf{B} \times \nabla \mathbf{B}$ ion-drift direction is towards the null point, the plasma current is 300 kA, limited by the maximum mechanical force on the F coils, and the toroidal magnetic field at the TCV major radius is 1.43 T.

6.7 L-H mode power threshold

The L-H mode threshold power for the two configurations is identified with a sequence of discharges with increasing heating power. Figure 6.7.1 shows the minimum heating power necessary to establish an H-mode as a function of the volume averaged plasma density n_{eV}. Above $n_{\mathrm{eV}} \sim 5 \times 10^{19}$ m^{-3} H-mode access is possible with ohmic heating power alone. For these plasmas, the minimum heating power was found increasing the plasma current. For lower plasma densities, access to the H-mode was possible only by adding ECH power at the second (X2) and third (X3)

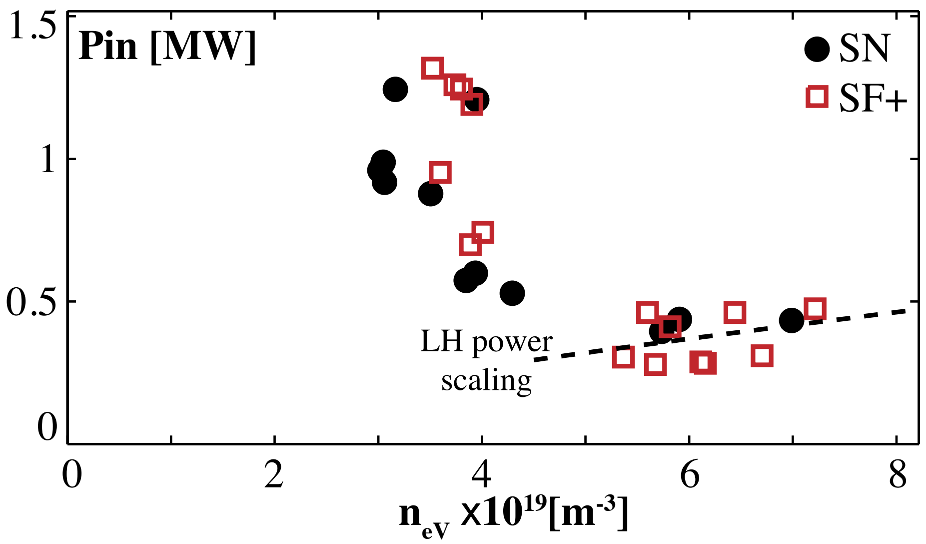

Figure 6.7.1: H-mode input power threshold vs volume averaged electron plasma density for the SN (black circles) and the SF$^+$ (red squares) configurations. The dashed line represents the L-H mode transition scaling from the international H-mode threshold database [3].

harmonics. In this case, the L-H transition power threshold was found ramping-up the ECH power until the H-mode transition. For plasma densities $< 3 \times 10^{19}$ m^{-3}, H-mode access was not obtained even at maximum injected ECH power.

Figure 6.7.1 shows that the power threshold is similar for the two configurations. The change in magnetic topology, i.e. the different magnetic shear at the plasma edge, does not thus appear to influence H-mode access. This is an important result since the main purpose of snowflake divertors is to open a new regime for ELMy H-modes.

6.8 The ohmic H-mode snowflake plasmas

An example of a typical H-mode SF plasma is given in Fig. 6.8.1. In this particular scenario, a SF$^+$ configuration is created from a limited plasma. At $t = 0.7$ s, the two X-points are moved to obtain a SF and a SF$^-$ at $t = 1$ s. Compared to the scenario already described in Sec. 6.4, the plasma density is lower (Fig. 6.8.1(a)) to reduce the L-H mode transition power threshold (see Fig. 6.7.1). The total ohmic input power is estimated to be $\sim$ 400 kW.

The H-mode regime is reached as soon as the SF$^+$ configuration is established. The H-mode is maintained during the whole SF$^+$ period. Later, during the transition SF$^+$ $\rightarrow$SF, the plasma returns to L-mode. During the H-mode phase, small ELMs are observed, presumably type III (Fig. 6.8.1).

Although considerable effort was dedicated to the improvement of this ohmic SF H-mode, a stable, regular EMLy phase was never obtained. The reason is that the ohmic input power was too low to sustain the H-mode regime. The low limit on the plasma current ($\max(I_P) = 300$ kA) imposed by the maximum vertical force on the F coils reduces the maximum ohmic power in these plasmas. For these reasons, the study of the ohmic SF H-mode was not pursued further.

6.9 The ECH H-mode snowflake plasmas

To increase the input power of the SF H-mode plasmas, 1 MW of ECH-X3 power is injected from the top of TCV (Fig. 6.6.1). The plasma density is reduced compared to the ohmic scenario to

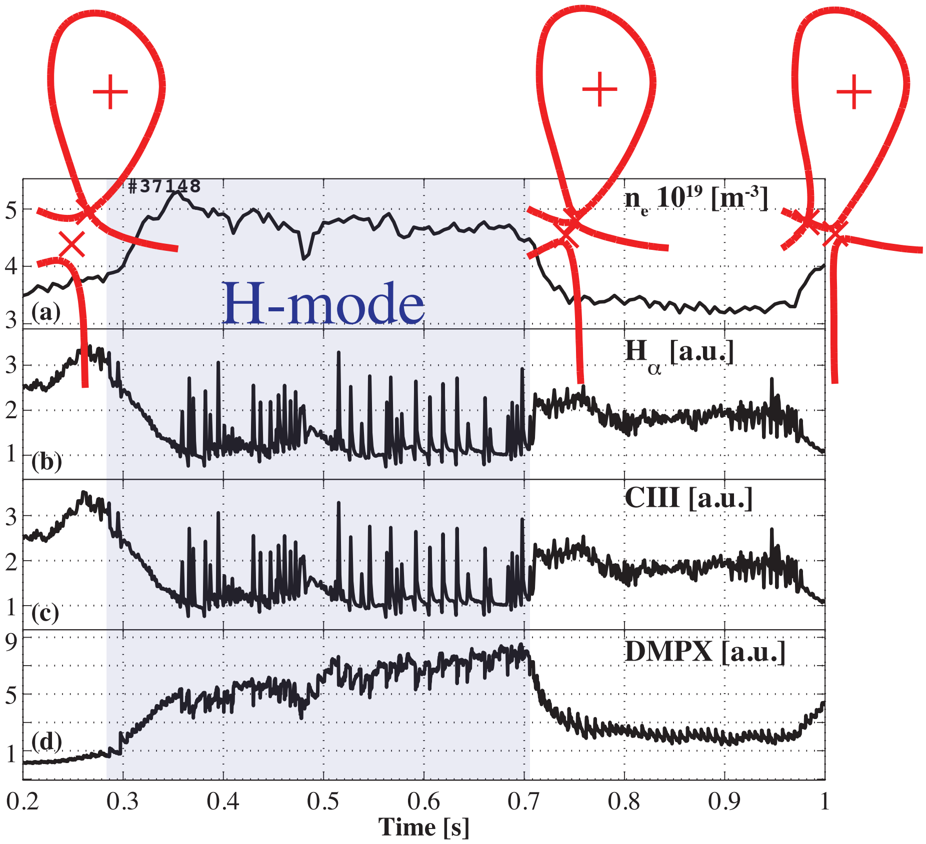

Figure 6.8.1: Ohmic H-mode SF plasma: (a) electron plasma density; (b) D_α and (c) CIII edge emission detected by a wide-angle filtered photodiode at the top of the vessel; (d) Duplex Multiwire Proportional X-ray counter (DMPX) signal from a central chord.

maximize the ECH absorption. The few experiments which have been performed at these ECH power levels exhibited a similar behavior to the ohmic SF H-mode. Several L-H mode transitions were present but it was difficult to stabilize a regular ELMy H-mode. The reason is that even if the input power was much higher, the L-H mode power threshold is considerably higher at lower plasma densities (Fig. 6.7.1). Moreover, the fraction of the ECH-X3 absorbed increases with the plasma temperature, which is relatively low before the transition to an H-mode.

To further increase the input power, $0.5 - 1$ MW of ECH-X2 power was injected from the LFS of TCV towards the plasma edge (Fig. 6.6.1). For these plasmas, the absorbed fraction computed by the ray tracing code TORAY-GA [116, 38] is 75% for the X3, primarily in the core region, and 100% for the X2, localized near the plasma edge.

Figure 6.9.1 shows plasma signals during an H-mode with a SN established between 0.28s and 0.7s, and a SF^+ stationary phase between 0.8s and 1.64s. At the transition, the X-point X_2 (Fig. 6.6.1) is moved towards the main X-point X_1 by the TCV control system. ECH is injected from 0.3s to 1.7s (Fig. 6.9.1(d)). This reproducible discharge, featuring both SN and SF^+ configurations within the same plasma pulse, is used to examine the differences and similarities in the H-mode and ELM behaviors. Operated at low plasma density to avoid the ECH cutoff ($\bar{n}_e \sim 0.16 n_{GW}$, with $\bar{n}_e$ the line averaged electron density and n_{GW} the Greenwald density), these plasmas are well below the ohmic H-mode TCV density power threshold and undergo a transition to H-mode only when the ECH power is applied, identified by the characteristic drop in D_α emission (Fig. 6.9.1(a)) and the development of an edge transport barrier in the pressure profile measured by Thomson scattering. The H-mode features steady ELMs, starting immediately after the transition. Figure 6.9.1(b,c) show the temporal evolution of the total plasma energy and $\bar{n}_e$. The plasma temperature increases

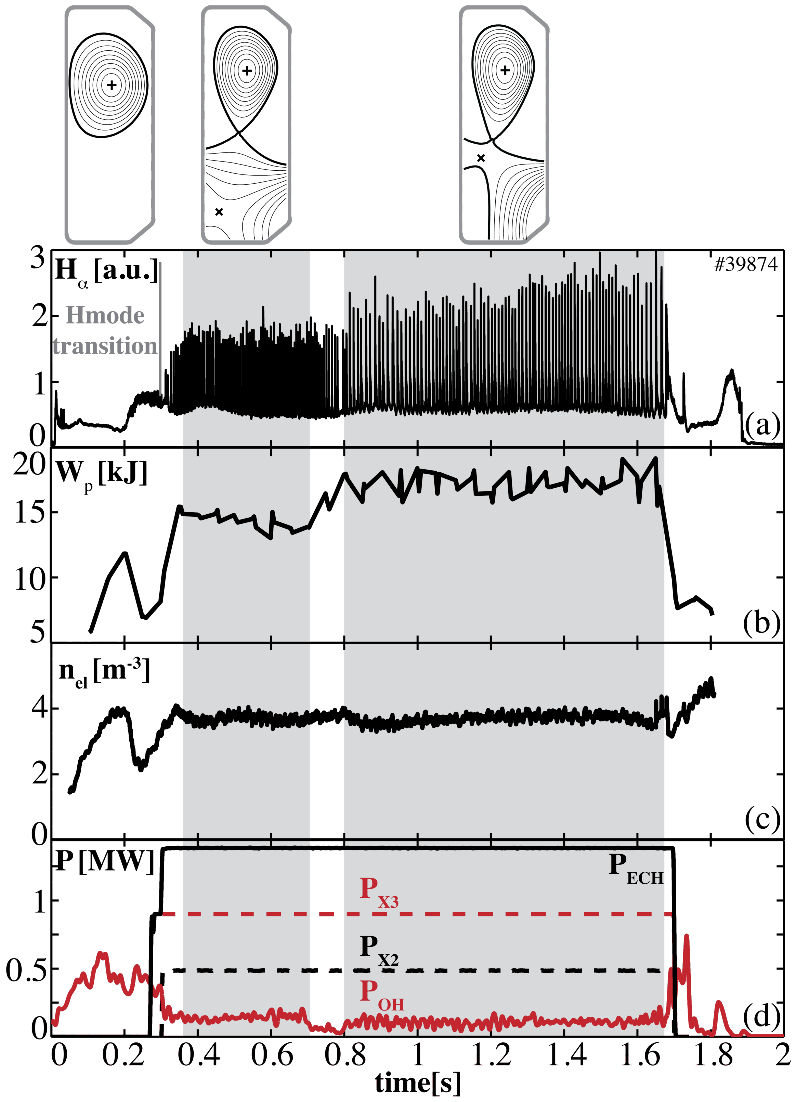

Figure 6.9.1: (a) D_α edge emission detected by a wide-angle filtered photodiode at the top of the vessel; (b) total plasma energy; (c) line averaged electron plasma density; (d) ohmic power (red solid line), ECH-X2 power (black dashed line), ECH-X3 power (red dashed line), and total ECH power (black solid line).

by $\sim$ 15% after the SN to SF$^+$ transition, increasing the total plasma energy, confinement time and H-factor by $\sim$ 15%.

The vertical D_α-filtered photodiode, Fig. 6.9.1(a), has a field of view that covers all the strike points. A clear change is observed at the SN-SF$^+$ transition with a reduction in the ELM frequency and an increase in the amplitude of the D_α peaks and their integrated intensity across the ELM by $\sim$ 30%. The ELMing phases are compared for a sequence of discharges with stepwise increase of the heating power.

Figure 6.9.2(a) shows the ELM frequency (ν_{ELM}) versus the input power (P_{in}) for both configurations with quantities averaged over a power step held for 200ms, i.e. long compared to the confinement time and to ensure regular ELM activity. The vertical error bars depict the scatter in the computed ELM period and the horizontal error bars are mainly due to 15% uncertainties in the absorbed fraction of the ECH-X3 power. The ELM frequency increases with heating power ($d\nu_{\mathrm{ELM}}/P_{\mathrm{in}} > 0$), a behavior typically associated with Type I ELM regimes [83]. The high input power compared with the L-H transition power threshold and the absence of detectable magnetic precursor oscillations also favor a Type I classification [83,117]. For both configurations, the aver-

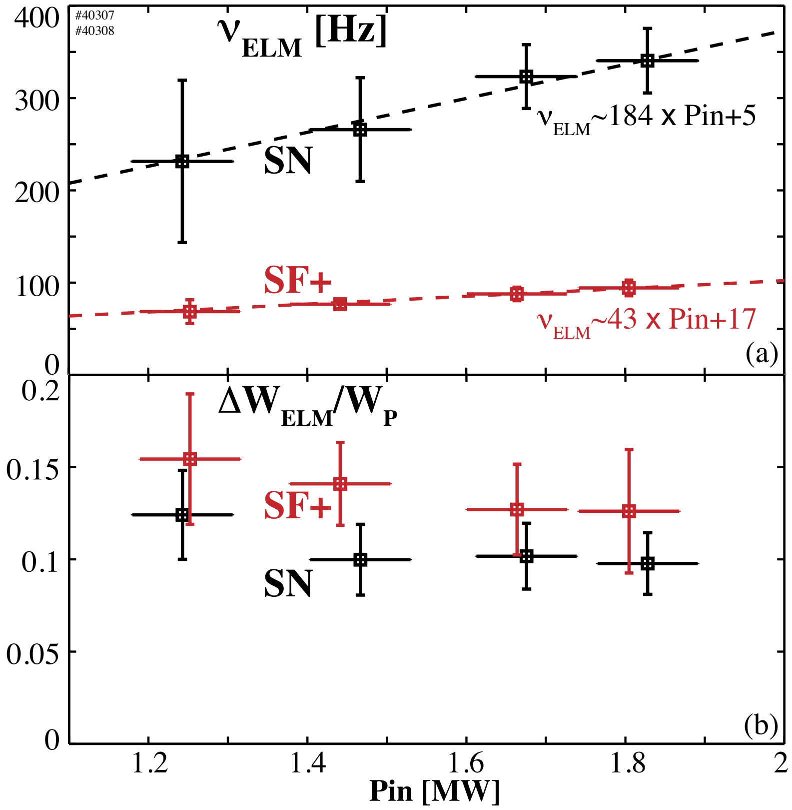

Figure 6.9.2: (a) ELM frequency variation and (b) ELM energy loss normalized to the plasma energy as a function of the total input power for the SN and the SF$^+$ configurations.

age energy drop at each ELM ($\Delta W_{\text{ELM}} > 1.6$ kJ, $\Delta W_{\text{ELM}}/W_p > 10\%$) is comparable to, or larger than, that of Type I ELMs in other devices [118]. The high edge temperature ($50-100$eV) and the low edge density ($\sim 1{\times}10^{19}\text{m}^{-3}$) lead to a low SOL collisionality parameter [119] $\nu_{SOL}* = L/\lambda \sim 2$, where λ is the self-collisionality length for electrons.

Strikingly, the ELM frequency for the SF$^+$ configuration is 2-3 times lower than for the SN configuration, whereas the normalized energy loss at each ELM increases by $20-30\%$. The ELM behavior is thus indeed strongly modified by the SF$^+$ configuration and results in improved plasma performance. The significant reduction of ν_{ELM} with a relatively smaller increase of ΔW_{ELM} causes a decrease of the normalized ELM power loss ($\nu_{\text{ELM}} \times \Delta W_{\text{ELM}}/P_{\text{in}}$), falling from 30% for the SN to $\sim$ 12% for the SF$^+$ configuration.

To verify that the change in the ELM frequency is only due to the different null point topology, the potential effects of the variation of the plasma elongation κ and of the ECH deposition location, within the uncertainty ranges, were investigated with a sequence of discharges (Fig. 6.9.3). These effects are seen to be small compared with the difference between the SN and SF$^+$ configurations.

6.10 Ideal MHD pedestal stability

An analysis of the stability of the plasma edge was undertaken to assess the nature of the ELMs for the two configurations. Figure 6.10.1(a,b) shows the temperature and density pedestal profiles for the SN and the SF$^+$ configurations, demonstrating no significant difference in the pedestal profiles, except for a slightly steeper temperature gradient for the SF$^+$ configuration just inside the pedestal region (leading to a 15% increase in T_{e0}). The magnetic shear ($s = \frac{\rho_{\text{v}}}{q}\frac{\text{d}q}{\text{d}\rho_{\text{v}}}$, where ρ_{v} is the square root of the normalized plasma volume) is computed for the two configurations using the

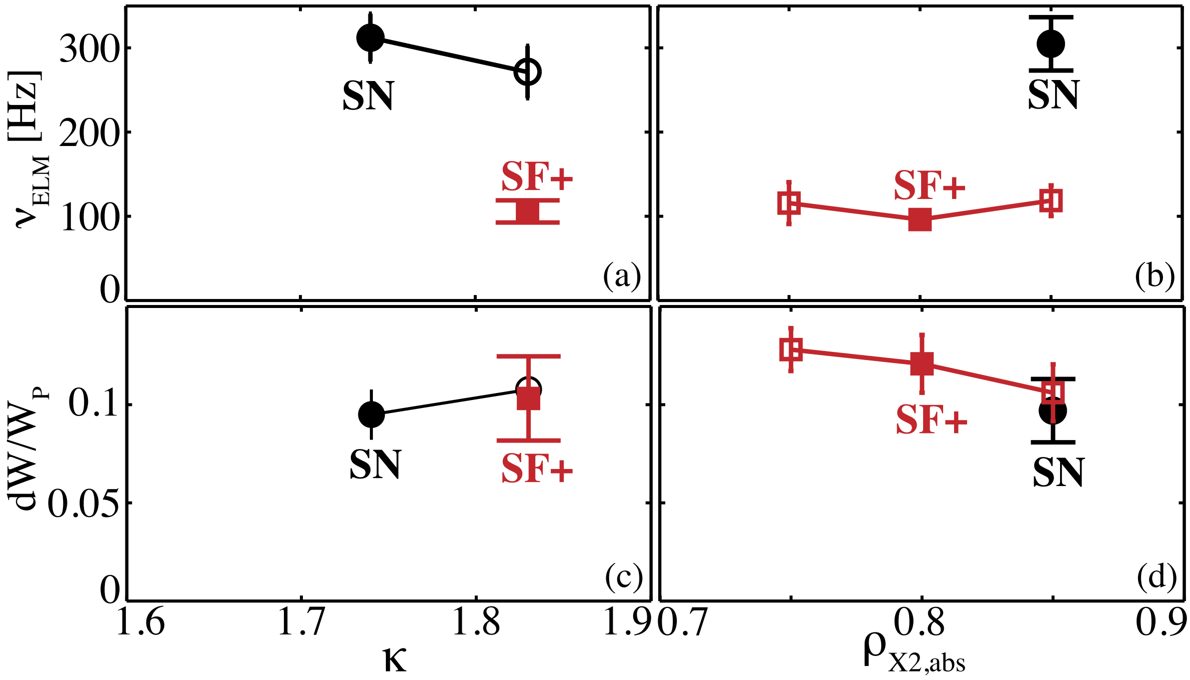

Figure 6.9.3: ELM frequency variation and normalized ELM power loss as a function of (a,c) the plasma elongation and (b,d) the position of the X2 absorption for the SN (black) and the SF$^+$ (red) configurations. The filled points represent the reference scenario.

CHEASE code [115] and is shown in Fig. 6.10.1(b). The edge bootstrap current, calculated from the electron temperature and density profiles [120], is fully taken into account in the computation. The SF$^+$ configuration has higher magnetic shear just inside the plasma separatrix and a slightly lower bootstrap current fraction.

Figure 6.10.1(c) shows the MHD stability space diagram of normalized parallel current density in the pedestal ($J_\parallel/<J>$) vs the normalized pressure gradient ($\alpha = \frac{\mu_0}{2\pi^2}\frac{\mathrm{d}p}{\mathrm{d}\psi}\frac{\mathrm{d}V}{\mathrm{d}\psi}\sqrt{\frac{V}{2\pi^2 R_0}}$ [121]) computed with the KINX code [73, 122]. The squares represent the experimental profiles derived from the Thomson scattering data in Fig. 6.10.1(a,b). The ion temperature is taken to be equal to the electron temperature, as indicated by Charge eXchange Recombination Spectroscopy (CXRS) measurements near the plasma edge. The experimental points for both configurations are close to the kink-ballooning stability boundary, as expected for Type I ELMy H-modes. The second stability region is slightly larger for the SF$^+$ configuration, i.e. coupled kink-ballooning modes at intermediate-high toroidal mode numbers are more stable. This is a general feature of SF configurations and is confirmed also when calculating the stability diagram with identical profiles.

6.11 Strike point properties

One of the main new attributes of the SF SOL is the presence of two additional divertor legs (strike points 3 and 4 in Fig. 6.6.1(b)). The properties of the strike point 4 of the SF$^+$ configuration are analyzed with the VIR camera monitoring the floor tiles (see Sec. 2.4.3.4). Figure 6.10.2(a) shows the coherently averaged ELM spatial profiles of the heat flux and temperature at the strike point 4. The peaks of the H_α signal are used as reference for the coherent averaging.

A considerable amount of power reaches this strike zone, even though this divertor leg is not directly connected to the main plasma SOL. Cross-field transport, which is important in the vicinity of the X-points, may explain this observation. The total energy deposited at strike point

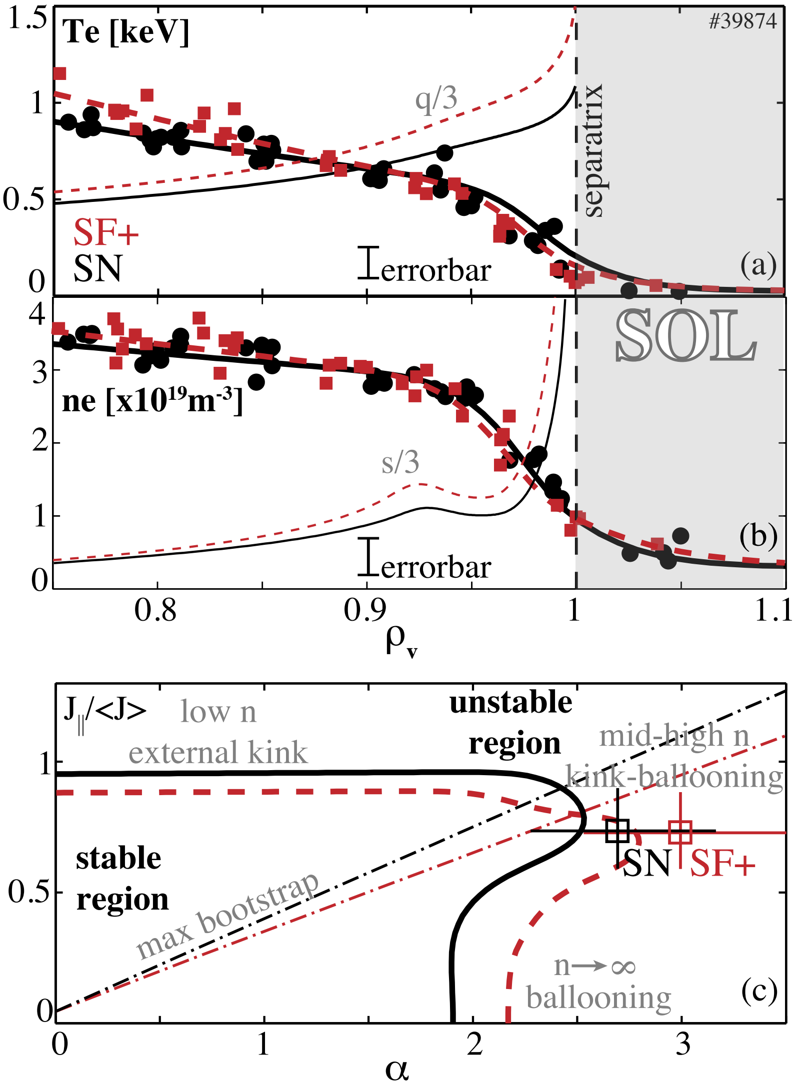

Figure 6.10.1: (a) Electron temperature and (b) density pedestal profiles for the SN (black solid line) and the SF$^+$ (red dashed line) configurations together with the Thomson scattering measurements (dots) as functions of ρ_v. Thin lines represent (a) the $q/3$ profile and (b) the magnetic shear $s/3$ (SN black solid line and SF$^+$ red dashed line). (c) Stability diagrams of the SN (black solid line) and the SF$^+$ (red dashed line) configurations. The collisionless bootstrap current is represented by dash-dot lines together with the experimental points for both configurations (squares).

4 is inferred by integrating the heat flux profile. On average, ∼ 15% of the total energy lost by the plasma at each ELM (measured with a Diamagnetic Loop) impinges on strike point 4, supported by independent calorimetry analysis based on thermocouples in the divertor tiles (see Sec. 2.4.3.4). No significant broadening of the profiles during the ELM is observed, in contrast with typical observations for the outer strike point of a SN plasma [123].

6.12 Conclusions

This chapter has described the strategy for the achievement of snowflake diverted plasmas in TCV. The three possible configurations (SF, SF$^+$ and SF$^-$) have been successfully created and controlled. The magnetic properties of the configurations have been analyzed, showing good agreement with the images from the tangential visible camera diagnostic and tomographically inverted total radiation emission measurements. The flux expansion, the connection length, the

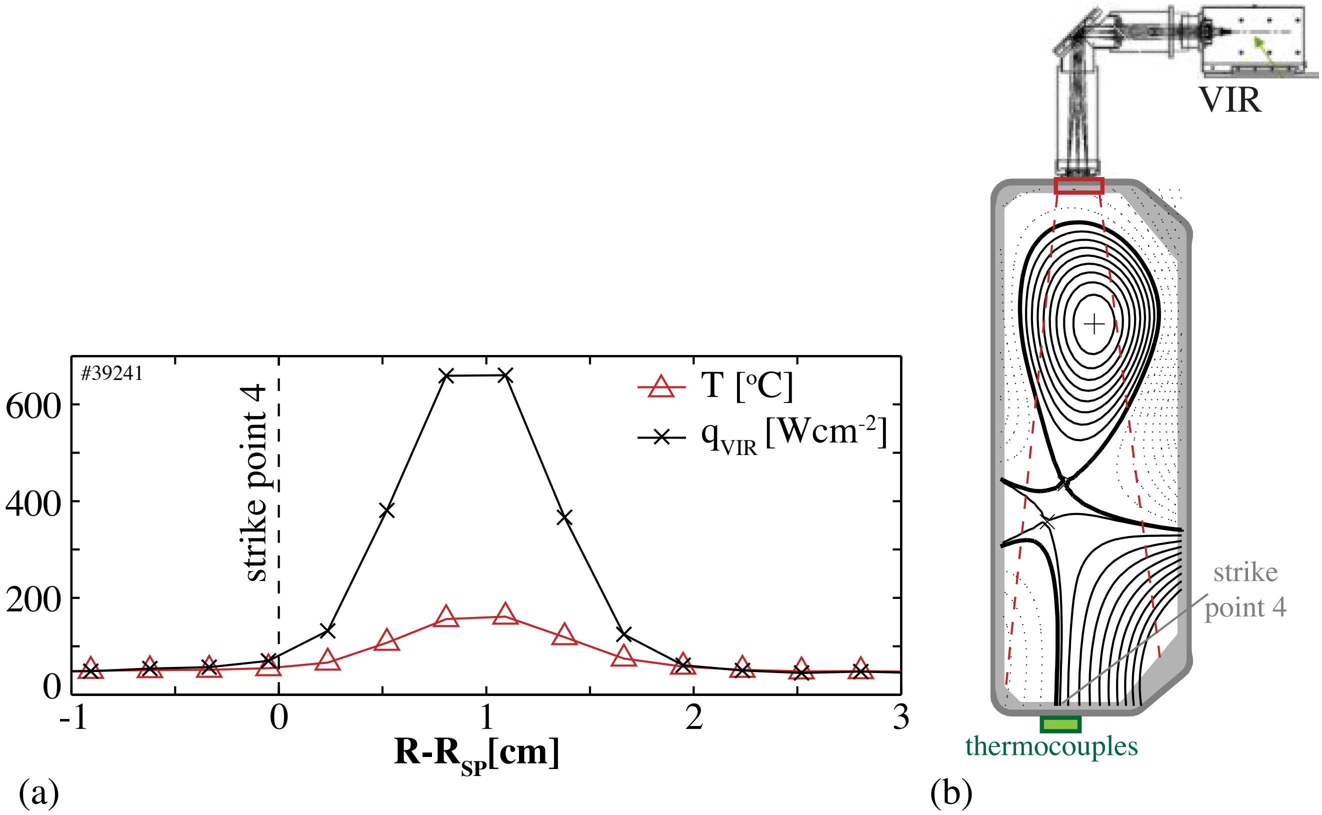

Figure 6.10.2: (a) Temperature T and heat flux q_{VIR} profiles at the strike point 4 vs the distance from the strike point at the time of the ELM H_α spike. The profiles are coherently averaged over 30 ELMs. (b) Vertical infra-red camera and thermocouples location on the TCV poloidal cross-section.

q-profile and the magnetic shear for the snowflake configurations have been compared with the standard X-point showing a strong variation of these parameters near the separatrix as a function of the null topology. The effects on the magnetic topology immediately inside the separatrix are not identical in between the SF^- and the SF^+ configurations.

A Type I ELMy H-mode regime has been achieved in a snowflake configuration and compared to an equivalent single-null discharge, especially with regard to the effect of the magnetic topology on ELMs. The two configurations have a similar H-mode power threshold, but the confinement is $\sim$ 15% higher in the SF^+ case. A non-negligible fraction of the energy expelled during an ELM, over 15%, reaches one of the additional strike points in the snowflake configuration. The most striking difference is in the ELM frequency, reduced by a factor 2-3 in the snowflake, while $\Delta W_{\mathrm{ELM}}/W_{\mathrm{P}}$ is only increased by $20-30\%$. Improved stability to kink-ballooning modes is consistent with this behavior, although the ELM frequency variation cannot be quantitatively explained at present.

Chapter 7

Conclusions and perspectives

This thesis reported on a study of plasma shaping in magnetic confinement tokamak reactors. The results presented were obtained at the *Centre de Recherches en Physique des Plasmas*, based on experiments performed on the TCV tokamak.
Two original and innovative plasma shapes were discussed in this manuscript: the doublet shaped plasma and the snowflake divertor.

Concerning the **doublet shaped plasma**, this thesis has presented a theoretical study of the possibility to create this configuration in TCV. Having introduced the possible advantages of this configuration, several strategies for its creation on TCV were analyzed. The scenario based on merging two droplet plasmas was identified as the most promising one. A necessary step to succeed through this scenario is the double plasma start-up, i.e. the creation of two plasmas inside the vacuum vessel. For this reason, the TCV plasma start-up has been subject of an extensive study. The general theory to describe the ionization phase and the ramp-up phase has been revised and applied to the TCV case. Both the theoretical model and the experimental results show that the neutral gas pressure, the toroidal electric field and the poloidal magnetic field influence the gas breakdown and the early ramp-up phase. Concerning the poloidal magnetic field in particular, a model was specifically developed to reconstruct the poloidal magnetic configuration during the plasma start-up.
To increase the precision of the computation, the whole TCV magnetic system was calibrated using an original technique. The error at the breakdown time given by the misalignment of the poloidal field coils was found to be of the order of 1 mT. Moreover, from the signal obtained by a set of saddle flux loops around the torus, the asymmetric error field was estimated to be smaller than 1 mT at the breakdown time.
The data obtained from the magnetic field reconstruction over $\sim$ 20000 start-ups were used as a base for a statistical analysis. The results showed the importance of having a long connection length in the ionization region at the breakdown time. Indeed, a long connection length can reduce the number of breakdown failures by half.
A dedicated experimental study of plasma start-up assisted by Electron Cyclotron Heating at the second harmonic (ECH-X2) was performed. Starting from a simple qualitative description of the ECH-X2 assisted plasma start-up, several TCV experiments were described in which some ECH parameters were varied systematically to study their influence on the ECH-X2 absorption efficiency. The results show an earlier breakdown and a faster burnthrough phase for high ECH injected power, perpendicular ECH injection and X-polarization. The results obtained represent the starting point for attacking the double breakdown problem. In this thesis, the first experiments of double breakdown with ECH-X2 were discussed, showing the successful creation of two plasma

channels.
The problem of the doublet vertical stability was also analyzed. The two doublet unstable vertical modes were predicted by the KINX code and only partially with a rigid plasma displacement model. This discrepancy is due to the perturbed surface currents, not described by the rigid model. Several strategies to control the main doublet quantities were illustrated, showing a possible solution to establish and control a doublet with the present TCV control system.

Concerning the **snowflake divertor**, this thesis described the strategy that led to the achievement, for the first time, of this configuration. The three possible configurations (snowflake, snowflake-plus and snowflake-minus) were successfully created and controlled. The magnetic properties of the configurations were analyzed, showing good agreement with the images from the tangential visible camera diagnostic and tomographically inverted total radiation emission measurements. The flux expansion, the connection length, the q-profile and the magnetic shear for the snowflake configurations were compared with the standard X-point configuration, showing a strong variation of these parameters near the separatrix (more than a factor 2) as a function of the null topology. The effects on the magnetic topology immediately inside the separatrix are not symmetric between the snowflake-minus and the snowflake-plus configurations. A type I ELMy H-mode regime was achieved in a snowflake configuration and compared to an equivalent single-null discharge, especially in regard to the effect of the magnetic topology on ELMs. The two configurations have a similar H-mode power threshold, but the confinement is $\sim 15\%$ higher in the snowflake-plus case. A non-negligible fraction of the energy expelled during an ELM, over 15%, reaches the additional strike points in the snowflake configuration. The most striking difference is in the ELM frequency, reduced by a factor 2-3 in the snowflake, while $\Delta W_{\mathrm{ELM}}/W_P$ is only increased by $20-30\%$. Improved stability to kink-ballooning modes is consistent with this behavior, although the ELM frequency variation cannot be quantitatively explained at present.

The point of view of the author is that most of the studies presented in this thesis should be pursued to better understand the observed phenomena and to complete the characterization of the new elements introduced by this thesis.
Concerning the magnetic calibration of TCV, a new set of diagnostics could be installed to measure the toroidal magnetic field around the vacuum vessel. This could allow an absolute identification of the $n = 1$ error field, expressed now in relative terms of the vacuum vessel position. A set of pick-up coils measuring the radial field could also be used to measure the $n > 1$ components of the error field.
The studies of the ohmic breakdown highlighted the dependence of the plasma start-up on several parameters. This study could be extended, investigating for example how the plasma breakdown depends on the polarization of the tungsten filament used to produce the free electrons. A measurement of the neutral gas flow and pressure is essential to validate the theoretical models used to describe the ohmic breakdown. Finally, since the poloidal magnetic configuration depends on the currents in the vacuum vessel and on the ohmic coils, a control system based on a Kalman filter to observe the eddy currents could help in imposing a given magnetic configuration at the breakdown time. Concerning the plasma start-up assisted with Electron Cyclotron Heating at the second harmonic, it would be interesting to study the role of the poloidal magnetic field (connection length, magnetic field in the resonance region, location of the null points, ...).
As for the doublet shaped plasma, the main challenge is to reach the ramp-up phase from the double ionization. Different experiments can be done to verify the possibility to affect independently the ramp-up of the two plasma channels by controlling the Electron Cyclotron Heating deposition

location and power as well as the poloidal and toroidal magnetic field. Once the ramp-up phase starts, the feedback control system can be switched on to control the two plasmas.
Finally, the snowflake experiments should also be continued to better investigate the properties of this configuration. To verify the potential ability of the configuration to reduce the plasma-wall interaction, several quantities at the strike points should be measured. The Langmuir probes, the vertical infrared camera and the bolometers are useful for this purpose. Another interesting aspect concerns the influence of the distance between the two X-points on the plasma properties. A scan of this distance during an H-mode snowflake-plus could for example give important information about the link between the edge magnetic shear and the pedestal stability. This may also be studied establishing an H-mode snowflake-minus configuration that, having a different magnetic shear profile, could influence in a different way the pedestal stability.

Appendix A

TCV sign conventions

The following sign conventions are used in the article. The z axis points towards the top of the tokamak and the $z = 0$ plane coincides with the equatorial midplane; the R axis points towards the outside; the toroidal angle φ is positive in the counterclockwise direction, the $\varphi = 0$ plane is chosen at the position of sector 16. The X axis corresponds to the toroidal angle $\varphi = 0$ and the Y axis is located at sector 4 ($\varphi = 90^o$). The conventions are summarized in Fig. 1.

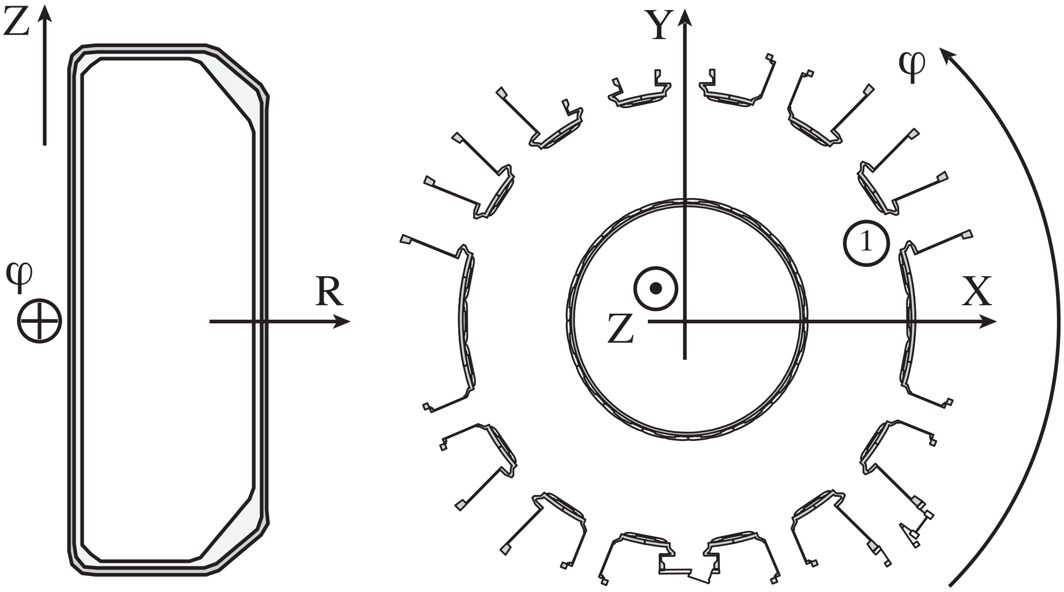

Figure 1: Sign convention.

Appendix B

The ITER vacuum vessel model

The ITER VV is a large torus with a double-wall structure. The inner and the outer shells are both 60 mm plates with a total combined toroidal resistance (vessel and blanket) of about 10 $\mu\Omega$.

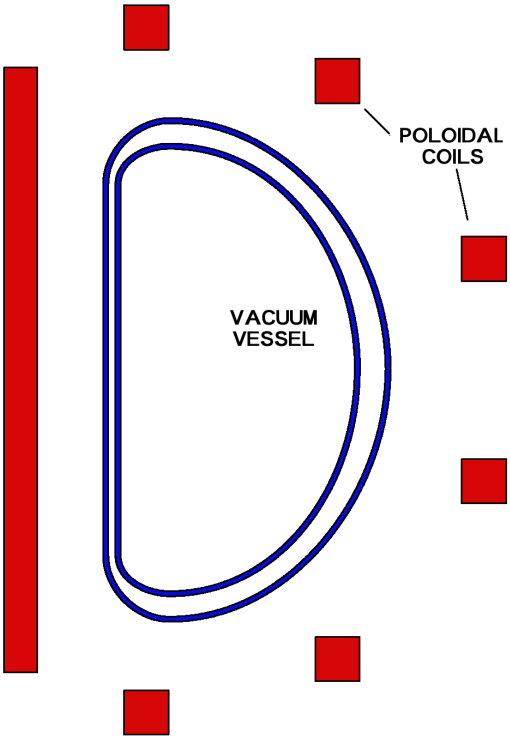

Figure 1: Simplified ITER vessel geometry.

To avoid the considerable work necessary to import the VV geometry from CAD models, and subsequently to simplify this to a level usable for an electromagnetic simulation, a fictive description of the geometry is used (Fig. 1). In this simplified model, the axisymmetric part of the VV is built from circular and straight segments. In the model the PF coils are considered as magnetic flux sources.

B.0.1 Filament model

In the axisymmetric case, the system is modeled using current filaments. The double-wall vessel is divided in two layers and for each of them a certain number of filaments is defined (Fig. 2). The PF coils are also divided in filaments, in order to improve the accuracy of the model. With this

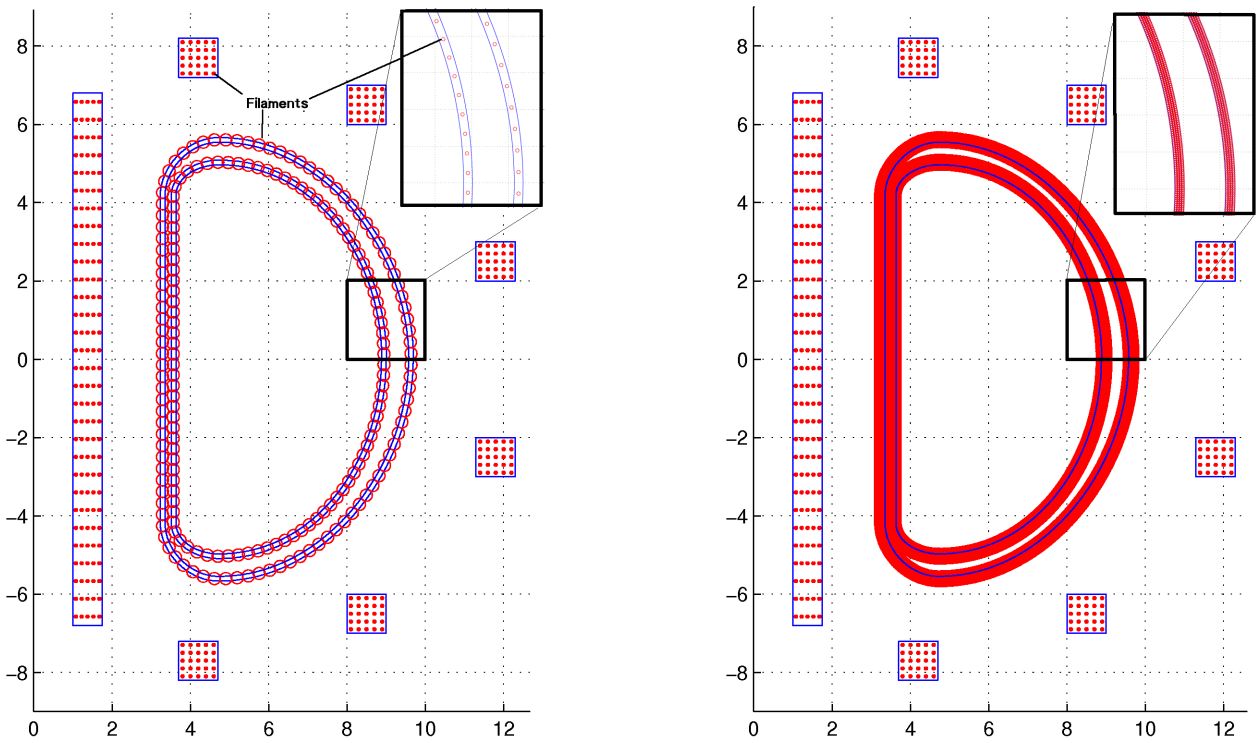

(a) 1 Layer, 100 filaments in each layer (b) 4 layers, 1000 filaments in each layer

Figure 2: ITER VV and poloidal coils divided in layers and filaments

assumption the model is cast in a circuit equation whose components are analytically calculated. The set of differential equations describing the vessel filaments is:

$$0 = \underline{\underline{R_{vv}}}\mathbf{I_v} + \dot{\psi}_{\mathbf{v}} = \underline{\underline{R_{vv}}}\mathbf{I_v} + \dot{\psi}_{\mathbf{vv}} + \dot{\psi}_{\mathbf{va}} \tag{B.0.1}$$

In this equation, $\underline{\underline{R_{vv}}}$ is a diagonal matrix containing the VV filament resistances, $\dot{\psi}_{\mathbf{v}}$ is the total flux variation in the vessel filaments produced by the PF coils ($\dot{\psi}_{\mathbf{va}}$) and the coupling between the VV filaments ($\dot{\psi}_{\mathbf{vv}}$).
Computing the mutual inductances between filaments and coils, Eq. B.0.1 become:

$$0 = \underline{\underline{R_{vv}}}\mathbf{I_v} + \underline{\underline{M_{vv}}}\dot{\mathbf{I}}_{\mathbf{v}} + \underline{\underline{M_{va}}}\dot{\mathbf{I}}_{\mathbf{a}} \tag{B.0.2}$$

where:

$\underline{\underline{M_{vv}}}$ = Matrix of mutual inductances between VV filaments
$\underline{\underline{M_{va}}}$ = Matrix of mutual inductances between VV and PF coils filaments

The last equation is used to compute the time evolution of the system, that can include harmonic response, step response and eigenmode representation.
An important aspect concerns the optimum number of layers and filaments that must be used to describe the ITER VV. A large number of filaments can clearly represent all the important

electromagnetic phenomena, but may result in a too complex model with not simple computational solutions.
Using a state-space representation, a set of standard diagnostics is defined to compare models with different number of layers and filaments.

B.0.2 The skin effect

In a solid cylindrical conductor, exited by an alternating current, the current density near the surface of the conductor is greater than that at its core. This is known as the "skin effect" and has been extensively studied by many researchers. The skin effect manifests itself as a variation of the resistance and the internal inductance of the conductor when the frequency is increased.
In a simple geometry, the skin effect can be quantified in an exact manner [124, 125]:

$$\frac{R(\omega)}{R_{DC}} = \frac{r}{\delta\sqrt{2}} \left[\frac{b_r b_i' u^2 - b_i b_r' u^2}{(b_r' u)^2 + (b_i' u)^2} \right] \tag{B.0.3}$$

$$\frac{L(\omega)}{L_{DC}} = \frac{4}{\sqrt{2}} \frac{\delta}{r} \left[\frac{b_r b_i' u^2 - b_i b_r' u^2}{(b_r' u)^2 + (b_i' u)^2} \right] \tag{B.0.4}$$

where $R(\omega)$ and $L(\omega)$ are the effective resistance and inductance and R_{DC} and L_{DC} are the respective values when $\omega = 0$. The functions b_r, b_r' and b_i, b_i' are Bessel functions, r is the conductor radius, σ is the conductivity, μ is the permeability and u is defined as follows:

$$u = \frac{r\sqrt{2}}{\delta} \tag{B.0.5}$$

where:

$$\delta = \left(\frac{1}{\pi f \mu \sigma} \right) \qquad \text{skin depth} \tag{B.0.6}$$

Increasing the frequency, the effective resistance ($R(\omega)$) increases and the effective inductance ($L(\omega)$) decreases starting from the DC value [126].

B.0.3 Results and discussion

The optimum number of layers and filaments to be used in the model has been evaluated comparing the total vessel current induced from a sinusoidal current flowing in one coil. Other diagnostics can be easily implemented for more detailed analysis (eg. magnetic field distribution, magnetic flux variation).
Figure 3(a) shows a comparison between models with the same number of filaments in each layer but with a different number of layers. Increasing the number of layers increases the total vessel current. This is due to the reduction of the effective inductance when the frequency increases (skin effect), and is better modeled by increasing the number of layers.
From the Fig. 3(a) it is clear that the optimum number of layers increases with the frequency. This result is in accordance with the formulation in Sec. B.0.2, where the skin depth decreases with the frequency. Taking for example a frequency of 10^3 rad/s, good results can be obtained using 4 layers (a greater number of layers does not improve the estimation of the induced vessel

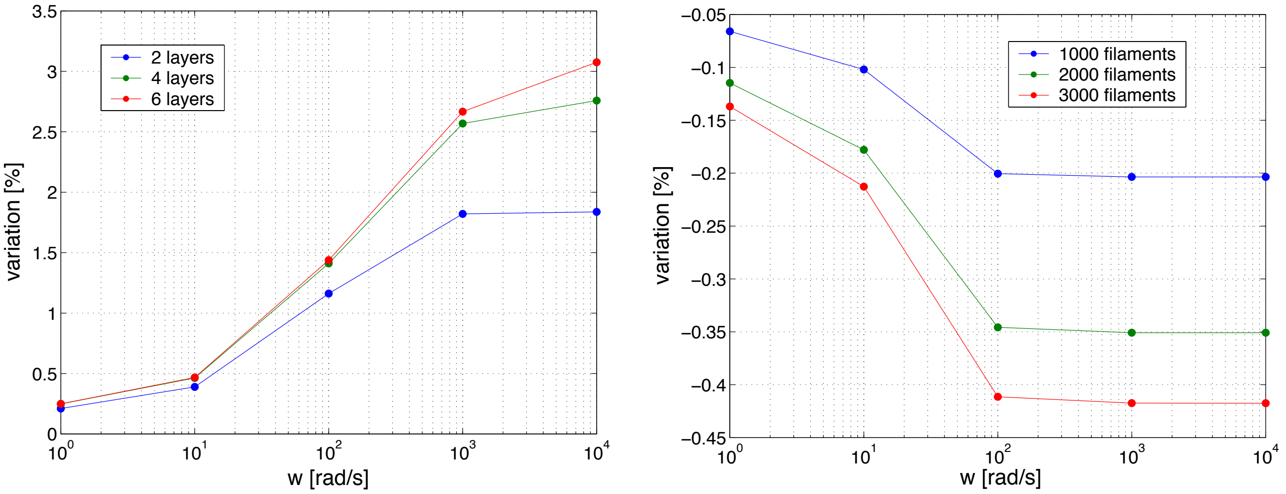

(a) Comparison between the case with 500 filamentsand 1 layer and the cases with 500 filaments and 2, 4 and 6 layers

(b) Comparison between the case with 1 layer and 500 filaments and the cases with 1 layer and 1000, 2000 and 3000 filaments

Figure 3: Comparison of the total vessel current induced using different models with a vessel resistivity of 10^{-7} Ωm

current). At this frequency, the skin depth is about 13 mm, comparable with the thickness of the layer.

The total vessel current variation increases with the frequency and saturate approximately around 10^3 rad/s for the case with 2 layers. Increasing the number of layers, the saturation frequency is higher, because we are able to describe phenomena with a smaller skin depth.

Figure 3(b) shows a comparison between models with one layer but different number of filaments. The total vessel current is not strongly influenced by the number of filaments. Different diagnostic should be defined to better estimate the optimum total number of filaments.

Appendix C

MGAMS PF coils current computation

The system of Eqs. 4.3.1-4.3.2 at the time step $t(k)$ can be rewritten as follows:

$$\begin{aligned} 0 &= \underline{\underline{R}}_{vv}\mathbf{I_v}(k)\Delta t + \underline{\underline{M}}_{vv}(\mathbf{I_v}(k) - \mathbf{I_v}(k-1)) && \text{(C.0.1)} \\ &+ \underline{\underline{M}}_{va}(\mathbf{I_a}(k) - \mathbf{I_a}(k-1)) + \underline{\underline{M}}_{vP}(k)I_P(k) - \underline{\underline{M}}_{vP}(k-1)I_P(k-1) \\ \mathbf{b}_p^{R,Z}(k) - \underline{\underline{\alpha_{pT}}}b_T &= \underline{\underline{B_{pa}}}\mathbf{I_a}(k) + \underline{\underline{B_{pv}}}\mathbf{I_v}(k) && \text{(C.0.2)} \end{aligned}$$

where Δt is the time step length and $\mathbf{I_a} = [\mathbf{I_a^p}, \mathbf{I_a^s}]$ is the vector of the current in the PF coils. $\mathbf{I_a^s}$ represents the current in the subset of the PF coils used to impose the magnetic field configuration and $\mathbf{I_a^p}$ the current vector in the other coils.
The solution of the system at time step $t(k)$ is $\mathbf{x}(k) = [\mathbf{I_v}(k), \mathbf{I_a^s}(k)]$. The result is found solving the following equation, in the least square sense:

$$\mathbf{y}(k) = \underline{\underline{A}}(k)\mathbf{x}(k) \tag{C.0.3}$$

where the following quantities have been defined:

$$\mathbf{y} = \begin{pmatrix} \underline{\underline{M}}_{vv}\mathbf{I_v}(k-1) - \underline{\underline{M}}_{vP}(k)I_P(k) + \underline{\underline{M}}_{vP}(k-1)I_P(k-1) - \underline{\underline{M}}^p_{va}\mathbf{I_a^p}(k) + \underline{\underline{M}}_{va}\mathbf{I_a}(k-1) \\ \mathbf{b_p^{R,Z}}(k) - \underline{\underline{\alpha_{pT}}}b_T - \underline{\underline{B_{pa}}}^p\mathbf{I_a^p}(k) \end{pmatrix} \tag{C.0.4}$$

$$\underline{\underline{A}} = \begin{pmatrix} \underline{\underline{R}}_{vv}\Delta t & \underline{\underline{M}}^s_{va} \\ \underline{\underline{B_{pv}}} & \underline{\underline{B_{pa}}}^s \end{pmatrix} \tag{C.0.5}$$

$\underline{\underline{M}}^s_{va}$, $\underline{\underline{B_{pa}}}^s$ being matrices of the Green's functions of the selected subset of controlled PF coils and $\underline{\underline{M}}^p_{va}$, $\underline{\underline{B_{pa}}}^p$ the matrices of the Green's functions for the pre-programmed PF coil currents.

Appendix D

Vacuum vessel current distribution estimation

The system of Eqs. 2.4.1 and 4.7.1 can be written as follow:

$$\begin{pmatrix} \mathbf{F_f} \\ \mathbf{B_m} \\ \mathbf{I_a} \\ \mathbf{U_f} \\ \mathbf{0} \\ \dot{\mathbf{I}}_\mathbf{a} \\ \dot{\mathbf{I}}_\mathbf{v} \end{pmatrix}(k) = \begin{pmatrix} \underline{\underline{M}}_{fa} & \underline{\underline{M}}_{fv} & \underline{\underline{0}} & \underline{\underline{0}} \\ \underline{\underline{B}}_{ma} & \underline{\underline{B}}_{mv} & \underline{\underline{0}} & \underline{\underline{0}} \\ \underline{\underline{1}} & \underline{\underline{0}} & \underline{\underline{0}} & \underline{\underline{0}} \\ \underline{\underline{0}} & \underline{\underline{0}} & \underline{\underline{M}}_{fa} & \underline{\underline{M}}_{fv} \\ \underline{\underline{0}} & \underline{\underline{R}}_{vv} & \underline{\underline{M}}_{va} & \underline{\underline{M}}_{vv} \\ \underline{\underline{0}} & \underline{\underline{0}} & \underline{\underline{1}} & \underline{\underline{0}} \\ \underline{\underline{0}} & \underline{\underline{0}} & \underline{\underline{0}} & \underline{\underline{1}} \end{pmatrix} \begin{pmatrix} \hat{\mathbf{I}}_\mathbf{a} \\ \hat{\mathbf{I}}_\mathbf{v} \\ \dot{\hat{\mathbf{I}}}_\mathbf{a} \\ \dot{\hat{\mathbf{I}}}_\mathbf{v} \end{pmatrix}(k) \tag{D.0.1}$$

where on the left side there is the vector of the measured quantities $\mathbf{y}$ and on the right side the coupling matrix $\underline{\underline{M}}$ and the vector of the fitted quantities $\mathbf{x}$. The vector of measured quantities contains the flux measurement $\mathbf{F_f}$, the magnetic field measurements $\mathbf{B_m}$, the current in the PF coils $\mathbf{I_a}$, the time derivatives of the flux $\mathbf{U_f}$ and the time derivatives of the current in the external conductors $\dot{\mathbf{I}}_\mathbf{a}$ and $\dot{\mathbf{I}}_\mathbf{v}$. This system is solved at each time step k such that $t(k)$ is smaller than the breakdown time. The first four rows of the $\mathbf{y}$ vector are measured quantities. The fifth row represents the vessel Eq. 2.4.1. The last two terms are computed from Eq. 4.7.2, using the fitted currents computed at the previous iteration.

Note that at the first iteration, only the following subsystem is solved:

$$\begin{pmatrix} \mathbf{F_f} \\ \mathbf{B_m} \\ \mathbf{I_a} \end{pmatrix}(k) = \begin{pmatrix} \underline{\underline{M}}_{fa} & \underline{\underline{M}}_{fv} \\ \underline{\underline{B}}_{ma} & \underline{\underline{B}}_{mv} \\ \underline{\underline{1}} & \underline{\underline{0}} \end{pmatrix} \begin{pmatrix} \mathbf{I_a} \\ \mathbf{I_v} \end{pmatrix}(k) \tag{D.0.2}$$

The current derivatives are then computed:

$$\dot{\mathbf{I}}_\mathbf{a,v} = \frac{\mathrm{d}\mathbf{I}_\mathbf{a,v}}{\mathrm{d}t} \tag{D.0.3}$$

and introduced in the full system of Eqs. D.0.2.

Bibliography

[1] BP Company, ***Statistical Review of World Energy***. `www.bp.com`, 2010.

[2] David JC MacKay, ***Sustainable Energy - without the hot air***. UIT Cambridge Ltd., 2009.

[3] Y.R.Martin and T.Takizuka, "**Power requirement for accessing the H-mode in ITER**," *J. Phys.: Conf. Ser.*, vol. 123, p. 012033, 2008.

[4] M.G.Haines, "**Fifty years of controlled fusion research**," *Plasma Phys. Control. Fusion*, vol. 38, p. 643, 1996.

[5] M.Keilhacker, A.Gibson, C.Gormezano, P.J.Lomas, P.R.Thomas, M.L.Watkins, P.Andrew, B.Balet, D.Borba, C.D.Challis, I.Coffey, G.A.Cottrell, H.P.L.DeEsch, N.Deliyanakis, A.Fasoli, C.W.Gowers, H.Y.Guo, G.T.A.Huysmans, T.T.C.Jones, W.Kerner, R.W.T.Kőnig, M.J.Loughlin, A.Maas, F.B.Marcus, M.F.F.Nave, F.G.Rimini, G.J.Sadler, S.E.Sharapov, G.Sips, P.Smeulders, F.X.Söldner, A.Taroni, B.J.D.Tubbing, M.G.vonHellermann and D.J.Ward, "**High fusion performance from deuterium-tritium plasmas in JET**," *Nucl. Fusion*, vol. 39, p. 209, 1999.

[6] F.Troyon, R.Gruber, H.Saurenmann, S.Semenzato and S.Succi, "**MHD-Limits to Plasma Confinement**," *Plasma Phys. Control. Fusion*, vol. 26, p. 209, 1984.

[7] F.Troyon, R.Gruber, "**A semi-empirical scaling law for the β limit in tokamaks.**" *Phys. Letters*, vol. 110A, p. 29, 1985.

[8] J.-M.Moret, S.Franke, H.Weisen, M.Anton, R.Behn, B.P.Duval, F.Hofmann, B.Joye, Y.Martin, C.Nieswand, Z.A.Pietrzyk and W.V.Toledo, "**Influence of Plasma Shape on Transport in the TCV Tokamak**," *Phys. Rev. Lett.*, vol. 79, p. 2057, 1997.

[9] T.H.Osborne, J.R.Ferron, R.J.Groebner, L.L.Lao, A.W.Leonard, M.A.Mahdavi, R.Maingi, R.L.Miller, A.D.Turnbull, M.Wade and J.Watkins, "**The effect of plasma shape on H-mode pedestal characteristics on DIII-D**," *Plasma Phys. Control. Fusion*, vol. 42, p. A175, 2000.

[10] F.Hofmann, J.B.Lister, M.Anton, S.Barry, R.Behn, S.Bernel, G.Besson, F.Bühlmann, R.Chavan, M.Corboz, M.J.Dutch, B.P.Duval, D.Fasel, A.Favre, S.Franke, A.Heym, A.Hirt, Ch.Hollenstein, P.Isoz, B.Joye, X.Llobet, J.C.Magnin, B.Marletaz, Ph.Marmillod, Y.Martin, J.M.Moret, Ch.Nieswand, P.J.Paris, A.Perez, Z.A.Pietrzyk, R.A.Pitts, A.Pochelon, R.Rage, O.Sauter, G.Tonetti, M.Q.Tran, F.Troyon, D.J.Ward and H.Weisen, "**Creation and Control of Variably Shaped Plasmas in TCV**," *Plasma Phys. Control. Fusion*, vol. 36, p. B277, 1994.

[11] D.Fasel, G.Depreville, A.Favre, J.-D.Pahud, A.Perez and F.Puchar, **“19 Rectifiers to Supply the Coils of the TCV tokamak**,” *Proc.* 16th *Symp. Fusion Technology*, 1990.

[12] A.Perez, I.M.Canay, J.-J.Morf, J.-D.Pahud, R.Seysen and J.-J.Simond, **“A 220 MVA Turbo-Alternator for the TCV Tokamak Power SUpplies**,” *Proc.* 15th *Symp. Fusion Technology*, 1988.

[13] A.Favre, A.Elkjaer, D.Fasel, J.-M.Moret, A.Perez and E.Steinmann, **“Fast Power Supply for Vertical Stabilization of TCV Tokamak Plasmas**,” *Proc. Conf. Electrical Power Technology in European Physics Research*, 1995.

[14] J.B.Lister, F.Hofmann, J.-M.Moret, F.Bühlmann, M.J.Dutch, D.Fasel, A.Favre, P.-F.Isoz, B.Marletaz, P.Marmillod, Y.Martin and A.Perez, **“The control of tokamak configuration variable plasmas**,” *Fusion Sci. Technol.*, vol. 32, p. 321, 1997.

[15] R.A.Pitts, R.Chavan and J.-M.Moret, **“The design of central column protection tiles for the TCV tokamak**,” *Nucl. Fusion*, vol. 39, p. 1433, 1999.

[16] J.-M.Moret, F.Hofmann, B.P.Duval and J.B.Lister, **“Breakdown in a continuous low resistivity vessel in TCV**,” 23rd *EPS Conference, Kiev*, vol. I, p. 1, 1996.

[17] J.-M.Moret, F.Buhlmann, D.Fasel, F.Hofmann and G.Tonetti, **“Magnetic measurements on the TCV Tokamak**,” *Rev. Sci. Instrum.*, vol. 69, p. 2333, 1998.

[18] H.Weisen, Y.Martin and J.-M.Moret, **“On the dependence of energy confinement on elongation in single null plasmas**,” *Nucl. Fusion*, vol. 42, p. L5, 2002.

[19] H.Weisen, J.-M.Moret, S.Franke, I.Furno, Y.Martin, M.Anton, R.Behn, M.J.Dutch, B.P.Duval, F.Hofmann, B.Joye, C.Nieswand, Z.A.Pietrzyk and W.V.Toledo, **“Effect of plasma shape on confinement and MHD behaviour in the TCV tokamak**,” *Nucl. Fusion*, vol. 37, p. 1741, 1997.

[20] R.A.Pitts, C.Nieswand, H.Weisen, M.Anton, R.Behn, R.F.Chavan, M.J.Dutch, B.P.Duval, S.Franke, F.Hofmann, B.Joye, J.B.Lister, X.Llobet, Y.Martin, J.-M.Moret, J.Petzilla, Z.A.Pitrzyk, V.Piffl, P.Reinke and M.E.Rensink, **“Divertor target profiles and recycling studies in TCV single null lower standard discharges**,” *J. Nucl. Mater.*, vol. 241, p. 867, 1997.

[21] R.A.Pitts, B.P.Duval, A.Loarte, J.-M.Moret, J.A.Boedo, D.Coster, I.Furno, J.Horacek, A.S.Kukushkin, D.Reiter and J.Rommers, **“Divertor geometry effect on detachment in TCV**,” *J. Nucl. Mater.*, vol. 290, p. 940, 2001.

[22] T.P.Goodman, S.Alberti, M.A.Henderson, A.Pochelon and M.Q.Tran, **“Design and installation of the electron cyclotron wave system for the TCV tokamak**,” *Proceedings of the mathrm19th Symposium on Fusion Technology*, vol. 1, p. 565, 1997.

[23] D.D.Ryutov, **“Geometrical properties of a “snowflake” divertor**,” *Phys. Plasmas*, vol. 14, p. 064502, 2007.

[24] F.Piras, S.Coda, I.Furno, J.-M.Moret, R.A.Pitts, O.Sauter, B.Tal, G.Turri, A.Bencze, B.P.Duval, F.Felici, A.Pochelon and C.Zucca, **“Snowflake divertor plasmas on TCV**,” *Plasma Phys. Control. Fusion*, vol. 51, p. 055009, 2009.

[25] R.J.Crossland, **“-**,” *Symposium on Fusion Technology (SOFT), London*, 1990.

[26] R.J.La Haye and J.T.Scoville, **"A method to measure poloidal field coil irregularities in toroidal plasma devices**," *Rev. Sci. Instrum.*, vol. 62, p. 2146, 1991.

[27] J.L.Luxon, M.J.Schaffer, G.L.Jackson, J.A.Leuer, A.Nagy, J.T.Scoville and E.J.Strait, **"Anomalies in the applied magnetic fields in DIII-D and their implications for the understanding of stability experiments**," *Nucl. Fusion*, vol. 43, p. 1813, 2003.

[28] T.C.Hender, R.Fitzpatrick, A.W.Morris, P.G.Carolan, R.D.Durst, T.Edlington, J.Ferreira, S.J.Fielding, P.S.Haynes, J.Hugill, I.J.Jenkins, R.J.LaHaye, B.J.Parham, D.C.Robinson, T.N.Todd, M.Valovič and G.Vayakis, **"Effect of resonant mangetic perturbation on COMPASS-C tokamak discharges**," *Nucl. Fusion*, vol. 32, p. 2091, 1992.

[29] A.W.Morris, P.G.Carolan, R.Fitzpatrick, T.C.Hender and T.N.Todd, **"Driven magnetic reconnection in the COMPASS-C tokamak**," *Phys. Fluids B*, vol. 4, p. 413, 1992.

[30] J.T.Scoville, R.J.LaHaye, A.G.Kellman, T.H.Osborne, R.D.Stambaugh, E.J.Strait and T.S.Taylor, **"Locked modes in DIII-D and a method for prevention of the low density mode**," *Nucl. Fusion*, vol. 31, p. 875, 1991.

[31] R.J.La Haye, R.Fitzpatrick, T.C.Hender, A.W.Morris, J.T.Scoville and T.N.Todd, **"Critical error for locked mode instability in tokamaks**," *Phys. Fluids B*, vol. 7, p. 2098, 1992.

[32] G.M.Fishpool and P.S.Haynes, **"Field error instabilities in JET**," *Nucl. Fusion*, vol. 34, p. 109, 1994.

[33] J.T.Scoville and R.J.LaHaye, **"Multi-mode error field correction on the DIII-D tokamak**," *Nucl. Fusion*, vol. 43, p. 250, 2003.

[34] F.Piras, J.-M.Moret and J.X.Rossel, **"Measurement of the magnetic field errors on TCV**," *Fusion Eng. Des.*, vol. 85, p. 739, 2010.

[35] J.X.Rossel, J.-M.Moret and Y.Martin, **"A 3D multi-mode geometry-independent RMP optimization method and its application to TCV**," *Plasma Phys. Control. Fusion*, vol. 52, p. 035006, 2010.

[36] D.R.Whaley, T.P.Goodman, A.Pochelon, R.Behn, A.Cardinali, B.P.Duval, B.Joye and M.Q.Tran, **"X- and O-mode electron cyclotron heating breakdown and start-up in TCA**," *Nucl. Fusion*, vol. 32, p. 757, 1992.

[37] I.H.Hutchinson, **"Principles of Plasma Diagnostics**," *Cambridge University Press*, 1992.

[38] F.Hofmann, M.J.Dutch and J.-M.Moret, **"Plasma Shape Control in TCV using MGAMS**," 22rd *EPS Conference, Bournemouth*, vol. 19C, pp. II–101, 1995.

[39] F.Hofmann, **"FBT - a free-boundary tokamak equilibrium code for highly elongated and shaped plasmas**," *Comput. Phys. Comm.*, vol. 48, p. 207, 1988.

[40] J.S.Townsend, "–," *Phil. Mag.*, vol. 1, p. 198, 1901.

[41] D.J.Rose, **"Townsend Ionization Coefficient for Hydrogen and Deuterium**," *Phys. Rev.*, vol. 104, p. 273, 1956.

[42] S.C.Brown, **"Basic Data of Plasma Physics**," *The M.I.T. Press Cambridge, Massachusetts*, 1959.

[43] R.B.Brode, **“The Quantitative Study of the Collisions of Electrons with Atoms**,” *Rev. Mod. Phys.*, vol. 5, p. 257, 1933.

[44] N.E.Bradbury and R.A.Nielsen, **“Absolute Values of the Electron Mobility in Hydrogen**,” *Phys. Rev.*, vol. 49, p. 388, 1936.

[45] B.I.H.Hall, **“–**,” *Australian J. Phys.*, vol. 8, p. 468, 1955.

[46] R.Papoular, **“The genesis of toroidal discharges**,” *Nucl. Fusion*, vol. 16, p. 37, 1976.

[47] B.Lloyd, G.L.Jackson, T.S.Taylor, E.A.Lazarus, T.C.Luce, R.Prater, **“Low voltage ohmic and electron cyclotron heating asssited startup in DIII-D**,” *Nucl. Fusion*, vol. 31, p. 2031, 1991.

[48] J.A.Nelder and R.Mead, **“A simplex method for function minimization**,” *Comput. J.*, vol. 7, p. 308, 1965.

[49] T.Ocho, S.Kubo, M.Ikeda, T.Saito, Y.Terumichi, Y.Hamada and S.Tanaka, **“Microwave preionization of the tokamak discharge at the electron cyclotron resonance**.”

[50] A.G.Kulchar, O.C.Eldridge, A.C.England, C.E.Bush, P.H.Edmonds, G.G.Kelley, C.M.Loring, Y.-K.M.Peng, J.B.Wilgen and S.K.Borowski, **“Preionization and start-up in the ISX-B tokamak using electron cyclotron heating at 28 GHz**,” *Phys. Fluids*, vol. 27, p. 1869, 1984.

[51] K.Hoshino, T.Yamamoto, A.Funahashi, N.Suzuki, T.Matoba, T.Yamauchi, H.Matsumoto, T.Kawakami, H.Kimura, S.Konoshima, M.Maeno, T.Matsuda, Y.Matsuzaki, K.Odashima, K.Ohasa, S.Sengoku, T.Shoji, T.Sugie, S.Yamamoto, Y.Tanaka, C.P.Moeller, R.J.Lahaye and R.Prater, **“Electron Cyclotron Heating and Pre-Ionization in the JFT-2 Tokamak**,” *J. Phys. Soc. Japan*, vol. 54, p. 2503, 1985.

[52] V.Erckmann and U.Gasparino, **“Electron cyclotron resonance heating and current drive in toroidal fusion plasmas**,” *Plasma Phys. Control. Fusion*, vol. 36, p. 1869, 1994.

[53] S.Tanaka, K.Hanada, T.Minami, S.Ide, M.Iida, H.Tanaka, T.Maekawa and Y.Terumichi, **“Initiation of plasma current with the assistance of electron cyclotron waves in the WT-3 tokamak**,” *Nucl. Fusion*, vol. 33, p. 505, 1993.

[54] K.Kajiwara, Y.Ikeda, M.Seki, S.Moriyama, T.Oikawa and T.Fujii, **“Electron cyclotron heating assisted startup in JT-60U**,” *Nucl. Fusion*, vol. 45, p. 694, 2005.

[55] G.L.Jackson, J.S.deGrassie, C.P.Moeller and R.Prater, **“Second harmonic electron cyclotron pre-ionization in the DIII-D tokamak**,” *Nucl. Fusion*, vol. 47, p. 257, 2007.

[56] G.L.Jackson, P.A.Politzer, D.A.Humphreys, T.A.Casper, A.W.Hyatt, J.A.Leuer, J.Lohr, T.C.Luce, M.A.VanZeeland and J.H.Yu, **“Understanding and predicting the dynamics of tokamak discharges during startup and rampdown**,” *Phys. Plasmas*, vol. 17, p. 056116, 2010.

[57] T.Ohkawa and H.G.Voorhies, **“Plasma-current multipole experiments**,” *Phys. Rev. Lett.*, vol. 22, p. 1275, 1969.

[58] T.Ohkawa, C.C.Baker, N.H.Brooks, Ming Sheng Chu, J.C.DeBOO, R.K.Fisher, R.L.Freeman, Chung Lih Hsieh, T.H.Jensen, M.A.Mahdavi, K.Matsuda, A.A.Schupp, T.Tamano, V.Vanek and J.C.Wesley, **"Studies of noncircular cross-section toroida in the doublet II and IIA device**," 5th *IAEA Conference, Tokyo*, vol. 1, p. 281, 1974.

[59] J.C.Wesley, T.Angel, C.J.Armentrout, D.R.Baker, F.P.Blau, G.Bramson, N.H.Brooks, R.W.Callis, R.P.Chase, J.C.Deboo, J.S.Degrassie, S.E.Ejima, R.K.Fisher, E.S.Fairbanks, R.J.Groebner, C.L.Hsieh, G.L.Jackson, G.L.Jahns, A.J.Lieber, J.M.Lohr, J.L.Luxon, M.A.Mahdavi, F.B.MArcus, C.H.Meyer, T.Ohkawa, P.I.Petersen, W.W.Pfeiffer, T.W.Petrie, P.J.Rock, M.T.Saito, R.P.Seraydarian, A.M.Sleeper, J.N.Smith, J.R.Smith, R.T.Snider, R.D.Stambaugh, R.Stav, T.Tamano, T.Taylor, D.F.Vaslow, T.S.Wang and S.S.Wojtowicz, **"Shaping and characteristics of ohmically heated non-circular plasmas in Doublet III**," 8th *IAEA Conference, Brussels*, vol. 1, p. 35, 1980.

[60] J.E.Miller, **"Unique design of Doublet and Big Dee vacuum vessels**," *J. Vac. Sci. Technol.*, vol. 20, p. 1168, 1981.

[61] T.Ohkawa and T.H.Jensen, **"Parameter studies for tokamaks and doublets**," *Plasma Physics*, vol. 12, p. 789, 1970.

[62] T.H.Jensen, R.K.Fisher, C.L.Hsieh, M.A.Mahdavi, V.Vanek and T.Ohkawa, **"Confinement of Plasma in the Doublet-II Device**," *Phys. Rev. Lett.*, vol. 34, p. 257, 1975.

[63] L.Degtyarev, A.Martynov, S.Yu.Medvedev, F.Troyon and L.Villard, **"Studies of noncircular cross-section toroida in the doublet II and IIA device**," 5th *IAEA Conference, Tokyo*, vol. 1, p. 281, 1974.

[64] F.Hofmann, M.J.Dutch, J.B.Lister, Y.Martin and J.-M.Moret, **"On the Possibility of Creating Doublet-Shaped Plasmas in TCV**," 23rd *EPS Conference, Kiev*, vol. 1, p. 127, 1996.

[65] S.H.Batha, F.M.Levinton, M.C.Zarnstorff and G.L.Schmidt, **"supershot Performance with Reverse Magnetic Shear in TFTR**," 22th *EPS Conference, Bournemouth*, vol. 19C, p. 113, 1995.

[66] J.Wesson, **"Tokamaks**," *Oxford: Oxford University Press*, vol. 2nd edition, p. 186, 1997.

[67] L.Degtyarev, A.Martynov, S.Yu.Medvedev, F.Troyon and L.Villard, **"External kink stability of tokamaks with finite edge current density in plasma outside separatrix**," 23rd *EPS Conference, Kiev*, vol. IV, p. 1191, 1996.

[68] L.Degtyarev, A.Martynov, S.Yu.Medvedev and L.Villard, **"Beta Limits Against External Kink Modes in Tokamaks Taking into Account Plasma Outside Separatrix**," 24th *EPS Conference, Berchtesgaden*, vol. II, p. 845, 1997.

[69] S.Yu.Medvedev, T.C.Hender, O.Sauter and L.Villard, **"Theoretical MHD limits in tokamaks with a separatrix**," 28th *EPS Conference, Funchal*, vol. 25A, p. 21, 2001.

[70] F.Wagner, G.Becker, K.Behringer, D.Campbell, A.Eberhagen, W.Engelhardt, G.Fussmann, O.Gehre, J.Gernhardt, G.v.Gierke, G.Haas, M.Huang, F.Karger, M.Keilhacker, O.Klüber, M.Kornherr, K.Lackner, G.Lisitano, G.G.Lister, H.M.Mayer, D.Meisel, E.R.Müller, H.Murmann, H.Niedermeyer, W.Poschenrieder, H.Rapp, H.Röhr, F.Schneider, G.Siller, E.Speth, A.Stäbler, K.H.Steuer, G.Venus, O.Vollmer and Z.Yü, **"Regime of Improved**

Confinement and High Beta in Neutral-Beam-Heated Divertor Discharges of the ASDEX Tokamak," *Phys. Rev. Lett.*, vol. 49, p. 1408, 1982.

[71] F.Wagner, "**A quarter-century of H-mode studies**," *Plasma Phys. Control. Fusion*, vol. 49, p. B1, 2007.

[72] S.Yu.Medvedev, L.Villard, L.M.Degtyarev, A.Martynov, R.Gruber and F.Troyon, "**MHD Equiibrium and Stability of Doublet Configurations**," 20th *EPS Conference, Lisbon*, vol. IV, p. 1279, 1993.

[73] L.Degtyarev, A.Martynov, S.Yu.Medvedev, F.Troyon, L.Villard and R.Gruber, "**The KINX ideal MHD stability code for axisymmetric plasmas with separatrix**," *Comput. Phys. Comm.*, vol. 103, p. 10, 1997.

[74] E.A.Lazarus, J.B.Lister and G.H.Neilson, "**Control of the vertical stability in tokamaks**," *Nucl. Fusion*, vol. 30, p. 111, 1990.

[75] J.B.Lister, Y.Martin and J.-M.Moret, "**On locating the poloidal field coils for tokamak vertical position control**," *Nucl. Fusion*, vol. 36, p. 1547, 1996.

[76] F.Hofmann, M.J.Dutch, D.J.Ward, M.Anton, I.Furno, J.B.Lister and J.-M.Moret, "**Vertical instability in TCV: comparison of experimental and theoretical growth rates**," *Nucl. Fusion*, vol. 37, p. 681, 1997.

[77] R.Gruber, S.Semenzato, F.Troyon, T.Tsunematsu, W.Kerner, P.Merkel and W.Schneider, "**Hera and other extensions of Erato**," *Comput. Phys. Comm.*, vol. 24, pp. 363–376, 1981.

[78] S.Yu.Medvedev, A.A.Martynov and L.Villard, "**MHD_NX code: kink mode stability with islands on unstructured grids**," 37th *EPS Conference, Dublin*, vol. IV, p. P4.144, 2010.

[79] A.A.Martynov, S.Yu.Medvedev and L.Villard, "**Axisymmetric Mode Stability in Tokamaks with Reversed Current Density**," 33th *EPS Conference, Rome*, vol. 30I, pp. P–1.167, 2006.

[80] ——, "**Tokamaks with Reversed Current Density: Current Holes, AC Operation and Axisymmetric Stabilty**," 34th *EPS Conference, Warsaw*, vol. 31F, pp. P–4.087, 2007.

[81] J.I.Paley, J.Berrino, S.Coda, N.Cruz, B.P.Duval, F.Felici, T.P.Goodman, Y.Martin, J.-M.Moret, F.Piras, A.P.Rodriques, B.Santos, and C.A.F.Varandas, "**Real time control of plasmas and ECRH systems on TCV**," *Nucl. Fusion*, vol. 49, p. 085017, 2009.

[82] R.Prater, "**Heating and current drive by electron cyclotron waves**," *Phys. Plasmas*, vol. 11, p. 2349, 2004.

[83] H.Zohm, "**Edge localized modes (ELMs)**," *Plasma Phys. Control. Fusion*, vol. 38, p. 105, 1996.

[84] J.W.Connor, "**A review of models for ELMs**," *Plasma Phys. Control. Fusion*, vol. 40, p. 191, 1998.

[85] H.Takahashi, E.D.Fredrickson and M.J.Schaffer, "**Scrape-Off-Layer Current Model for Filament Structure Observed during Edge-Localized Modes in the DIII-D Tokamak**," *Phys. Rev. Lett.*, vol. 100, p. 205001, 2008.

[86] L.J.Zheng, H.Takahashi and E.D.Fredrickson, "**Edge-Localized Modes Explained as the Amplification of Scrape-Off-Layer Current Coupling**," *Phys. Rev. Lett.*, vol. 100, p. 115001, 2008.

[87] A.Wingen, T.E.Evans, C.J.Lasnier and K.H.Spatschek, "**Numerical Modeling of Edge-Localized-Mode Filaments on Divertor Plates BAsed on Thermoelectric Currents**," *Phys. Rev. Lett.*, vol. 104, p. 175001, 2010.

[88] T.Eich, A.Herrmann and J.Neuhauser, "**Nonaxisymmetric Energy Deposition Pattern on ASDEX Upgrade Divertor Target Plates during Type-I Edge-Localized Modes**," *Phys. Rev. Lett.*, vol. 91, p. 195003, 2003.

[89] A.Kirk, B.Koch, R.Scannell, H.R.Wilson, G.Counsell, J.Dowling, A.Hermann, R.Martin and M.Walsh, "**Evolution of Filament Structures during Edge-Localized Modes in the MAST Tokamak**," *Phys. Rev. Lett.*, vol. 96, p. 185001, 2006.

[90] T.E.Evans, R.A.Moyer, P.R.Thomas, J.G.Watkins, T.H.Osborne, J.A.Boedo, E.J.Doyle, M.E.Fenstermacher, K.H.Finken, R.J.Groebner, M.Groth, J.H.Harris, R.J.LaHaye, C.J.Lasnier, S.Masuzaki, N.Ohyabu, D.G.Pretty, T.L.Rhodes, H.Reimerdes, D.L.Rudakov, M.J.Schaffer, G.Wang and L.Zeng, "**Suppression of Large Edge-Localized Modes in High-Confinement DIII-D Plasmas with a Stochastic Magnetic Boundary**," *Phys. Rev. Lett.*, vol. 92, p. 235003, 2004.

[91] T.E.Evans, R.A.Moyer, K.H.Burrell, M.E.Fenstermacher, I.Joseph, A.W.Leonard, T.H.Osborne, G.D.Porter, M.J.Schaffer, P.B.Snyder, P.R.Thomas, J.G.Watkins and W.P.Wesr, "**Edge stability and transport control with resonant magnetic perturbations in collisionless tokamak plasmas**," *Nature Phys.*, vol. 2, p. 419, 2006.

[92] Y.Liang, H.R.Koslowski, P.R.Thomas, E.Nardon, B.Alper, P.Andrew, Y.Andrew, G.Arnoux, Y.Baranov, M.Bécoulet, M.Beurskens, T.Biewer, M.Bigi, K.Crombe, E.DeLaLuna, P.deVries, W.Fundamenski, S.Gerasimov, C.Giroud, M.P.Gryaznevich, N.Hawkes, S.Hotchin, D.Howell, S.Jachmich, V.Kiptily, L.Moreira, V.Parail, S.D.Pinches, E.Rachlew and O.Zimmermann, "**Active Control of Type-I Edge-Localized Modes with n=1 Perturbation Field in the JET Tokamak**," *Phys. Rev. Lett.*, vol. 98, p. 265004, 2007.

[93] D.D.Ryutov, "**ERRATUM:Geometrical properties of a "snowflake" divertor**," *Phys. Plasmas*, vol. 15, p. 069901, 2008.

[94] D.D.Ryutov, R.H.Cohen, T.D.Rognlien and M.V.Umansky, "**The magnetic field structure of a snowflake divertor**," *Phys. Plasmas*, vol. 15, p. 092501, 2008.

[95] A.S.Kukushkin, H.D.Pacher, V.Kotov, D.Reiter and G.W.Pacher, "**Effect of neutral transport on ITER divertor performance**," *Nucl. Fusion*, vol. 45, p. 608, 2005.

[96] M.A.Mahdavi, J.C.DeBoo, C.L.Hsieh, N.Ohyabu, R.D.Stambaugh and J.C.Wesley, "**Particle Exhaust from Plasma Discharges with an Expanded-Boundary Divertor**," *Phys. Rev. Lett.*, vol. 47, p. 1602, 1981.

[97] P.M.Valanju, M.Kotschenreuther, S.M.Mahajan and J.Canik, **"Super-X divertors and high power density fusion devices**," *Phys. Plasmas*, vol. 16, p. 056110, 2009.

[98] F.Piras, A.Bencze, S.Coda, B.P.Duval, I.Furno, J.-M.Moret, R.A.Pitts, O.Sauter, B.Tal, D.Wágner, F.Felici, B.Labit, J.Marki, Y.Martin, S.Yu.Medvedev, A.Pitzschke, A.Pochelon, G.Turri, G.Veres, L.Villard and C.Zucca, **"Snowflake Divertor Plasmas on TCV**," *TTF Workshop, San Diego*, vol. 1, p. 1, 2009.

[99] F.Piras, A.Bencze, S.Coda, B.P.Duval, I.Furno, J.-M.Moret, R.A.Pitts, O.Sauter, B.Tal, D.Wágner, F.Felici, B.Labit, J.Marki, Y.Martin, S.Yu.Medvedev, A.Pitzschke, A.Pochelon, G.Turri and C.Zucca, **"Snowflake Divertor Plasmas on TCV**," *36th EPS Conference, Sofia*, vol. P2, p. 141, 2009.

[100] F.Piras, S.Coda, B.P.Duval, B.Labit, J.Marki, S.Yu.Medvedev, J.-M.Moret, A.Pitzschke and O.Sauter, **""Snowflake" H-mode in a tokamak plasma**," *Phys. Rev. Lett.*, vol. 105, p. 155003, 2010.

[101] ——, **""Snowflake" Divertor Experiments on TCV**," *Plasma Phys. Control. Fusion*, vol. 52, p. 124010, 2010.

[102] ——, **""Snowflake" Divertor Experiments on TCV**," *37th EPS Conference, Dublin*, vol. I5, p. 115, 2010.

[103] ——, **"H-mode Snowflake Divertor Plasmas on TCV**," *52nd APS Conference, Chicago*, vol. PP9, p. 00136, 2010.

[104] ——, **""Snowflake" H-mode in Tokamak Plasmas**," *15td Workshop on MHD Stability and Control, Madison*, vol. 1, p. 1, 2010.

[105] M.V.Umansky, T.D.Rognlien, D.D.Ryutov and P.B.Snyder, **"Edge Plasma in Snowflake Divertor**," *Contrib. Plasma Phys.*, vol. 50, p. 350, 2010.

[106] M.V.Umansky, R.H.Bulmer, R.H.Cohen, T.D.Rognlien and D.D.Ryutov, **"Analysis of geometric variation in high-power tokamak divertors**," *Nucl. Fusion*, vol. 49, p. 075005, 2009.

[107] P.B.Snyder, H.R.Wilson, J.R.Ferron, L.L.Lao, A.W.Leonard, T.H.Osborne, A.D.Turnbull, D.Mossessian, M.Murakami and X.Q.Xu, **"Edge localized modes and the pedestal: A model based on coupled peeling-ballooning modes**," *Phys. Plasmas*, vol. 9, p. 2037, 2002.

[108] D.Farina, R.Pozzoli and D.D.Ryutov, **"Effect of the magnetic field geometry on the flute-like perturbations near the divertor X point**," *Nucl. Fusion*, vol. 33, p. 1315, 1993.

[109] R.H.Cohen and D.D.Ryutov, **"Dynamics of an Isolated Blob in the Presence of the X-point**," *Contrib. Plasma Phys.*, vol. 46, p. 678, 2006.

[110] D.D.Ryutov and M.V.Umansky, **"Ion drifts in a snowflake divertor**," *Phys. Plasmas*, vol. 17, p. 014501, 2010.

[111] A.Scarabosio, A.Pochelon and Y.Martin, **"Plasma shape stabilization of current rise MHD instabilities in TCV**," *Plasma Phys. Control. Fusion*, vol. 49, p. 1041, 2007.

[112] F.Hofmann and G.Tonetti, **"Tokamak equilibrium reconstruction using faraday rotation measurements**," *Nucl. Fusion*, vol. 28, p. 1871, 1988.

[113] A.W.Degelingm H.Weisen, A.Zabolotsky, B.P.Duval, R.A.Pitts, M.Wischmeier, P.Lavanchy, Ph.Marmillod and G.Pochon, **"AXUV bolometer and Lyman-α camera system on the TCV tokamak**," *Rev. Sci. Instrum.*, vol. 75, p. 4139, 2004.

[114] I.Furno, H.Weisen, J.Mlynar, R.A.Pitts, X.Llobet, Ph.Marmillod and G.P.Pochon, **"Fast bolometric measurements on the TCV tokamak**," *Rev. Sci. Instrum.*, vol. 70, p. 4552, 1999.

[115] H.Lddotutjens, A.Bondeson and O.Sauter, **"The CHEASE code for toroidal MHD equilibria**," *Comput. Phys. Comm.*, vol. 97, p. 219, 1996.

[116] K.Matsuda, **"Ray tracing study of the electron cyclotron current drive in DIII-D using 60 GHz**," *IEEE Trans. Plasma Sci.*, vol. 17, p. 6, 1989.

[117] W.Suttrop, **"The physics of large and small edge localized modes**," *Plasma Phys. Control. Fusion*, vol. 42, p. A1, 2000.

[118] A.Loarte, M.Becoulet, G.Saibene, R.Sartori, D.J.Campbell, T.Eich, A.Herrmann, M.Laux, W.Suttrop, B.Alper, P.J.Lomas, G.Matthews, S.Jachmich, J.Ongena and P.Innocente, **"Characteristics and scaling of energy and particle losses during Type I ELMs in JET H-modes**," *Plasma Phys. Control. Fusion*, vol. 44, p. 1815, 2002.

[119] B.LaBombard, R.L.Boivin, M.Greenwald, J.Hughes, B.Lipschultz, D.Mossessian, C.S.Pitcher, J.L.Terry and S.J.Zweben, **"Particle transport in the scrape-off layer and its relationship to discharge density limit in Alcator C-Mod**," *Phys. Plasmas*, vol. 8, p. 2107, 2001.

[120] O.Sauter, C.Angioni and Y.R.Lin-Liu, **"Neoclassical conductivity and bootstrap current formulas for general axisymmetric equilibria and arbitrary collisionality regime**," *Phys. Plasmas*, vol. 6, p. 2834, 1999.

[121] R.J.Groebner and T.H.Osborne, **"Scaling studies of the high mode pedestal**," *Phys. Plasmas*, vol. 5, p. 1800, 1998.

[122] S.Yu.Medvedev, A.A.Ivanov, A.A.Martynov, Yu.Yu.Poshekhonov, R.Behn, Y.R.Martin, J.-M.Moret, F.Piras, A.Pitzschke, A.Pochelon, O.Sauter and L.Villard, **"Edge Stability and Pedestal Profile Sensitivity of Snowflake Diverted Equilibria in the TCV Tokamak**," *Contrib. Plasma Phys.*, vol. 50, p. 324, 2010.

[123] J.Marki, R.A.Pitts, J.Horacek and D.Tskhakaya, **"ELM induced divertor heat loads on TCV**," *J. Nucl. Mater.*, vol. 390-391, p. 801, 2009.

[124] R.E.Matick, ***Transmission lines for digital and communication networks***. MaGraw Hill, New York, 1969.

[125] R.E.Chipman, ***Theory and problems of transmission lines***. MaGraw Hill, New York, 1968.

[126] O.M.O.Gatous and J.Pissolato, **"Frequency-dependent skin-effect formulation for resistance and internal inductance of a solid cylindrical conductor**," *IEEE Proc. Microw. Antennas Propag.*, vol. 151, 2004.

Glossary

AXUV	Absolute eXtreme UltraViolet bolometer cameras
BOLO	Foil bolometers diagnostic
CRPP	Centre de Recherches en Physique des Plasmas
CXRS	Charge eXchange Recombination Spectroscopy
D	Deuterium
DEMO	DEMOnstration Power PLant
DMPX	Duplex Multiwire Proportional soft X-ray counter
ECE	Electron Cyclotron Emission diagnostic
ECH	Electron Cyclotron Heating
ECH-X1	Electron Cyclotron Heating - first harmonic
ECH-X2	Electron Cyclotron Heating - second harmonic
ECH-X3	Electron Cyclotron Heating - third harmonic
ELM	Elm Localized Mode
Eq.	Equation
FastCam	Fast tangential visible Camera
Fig.	Figure
FIR	Far InfraRed laser diagnostic
GA	General Atomics
HFS	High Field Side
H-mode	High confinement mode
ITER	International Thermonuclear Experimental Reactor
LCFS	Last Closed Flux Surface
LFS	High Field Side
L-mode	Low confinement mode
MFTF-B	Mirror Fusion Test Facility-B
MultiCam	Multi-Camera ssytem
NIF	National Ignition Facility
OH	Ohmic
PD	PhotoDiodes
PF	Poloidal Field
PFC	Plasma Facing Component
Sec.	Section
SF	Snowflake
SF^+	Snowflake-plus
SF^-	Snowflake-minus

SL	Saddle Loop
T	Tritium
TC	ThermoCouple
TCV	Tokamak à Configuration Variable
TF	Toroidal Field
TS	Thomson Scattering
VIR	Vertical InfraRed camera
VV	Vacuum Vessel
XTOMO	Soft X-ray tomographic system

Acknowledgements

Les résultats exposés dans cette thèse ont été possible grâce aux nombreuses personnes qui m'ont soutenu.
Je dois les résultats les plus importants à S.Coda, B.Duval et O.Sauter, que j'aimerais remercier particulièrement. Ils ont su me donner toute l'aide nécessaire, surtout pendant les moments difficiles de mon doctorat. Ils restent aujourd'hui une référence scientifique et amicale importante.
J'aimerais également remercier J.-M.Moret, pour avoir accepté de suivre mon travail comme directeur de thèse et surtout pour son apport dans le domaine de l'analyse magnétique, essentielle pour ma thèse.
Merci à S.Alberti, T.Goodman et L.Porte, les grands maîtres du chauffage ECH! Sans qui ce travail n'aurait été possible.
Beaucoup de personnes m'ont aidé et m'ont fait confiance, surtout quand le sort du "snowflake" paraissait incertain: A.Bortolon, I.Furno, D.Ryutov, G.Turri et L.Villard. Merci.
J'ai rencontré, pendant ces quatre années, des personnes brillantes qui ont été fondamentales pour mon développement professionnel: M.Albergante, Y.Camenen, F.Felici, C.Schlatter et C.Theiler. Les résultats de ma thèse sont également le fruit de votre capacité à regarder plus loin que vous m'avez transmis.
Faire une thèse expérimentale sur une machine complexe comme un tokamak signifie avant tout résoudre des problèmes techniques, des solutions sans lesquelles nous ne pourrions pas avancer dans la recherche de ce domaine. J'ai eu la chance d'avoir le support d'une équipe de techniciens et ingénieurs dont les capacités et l'expérience ont été indispensable à la réussite de mon travail. Merci à S.Antonioni, P.Conti, P.Lavanchy, X.Llobet, B.Marletaz, P.Marmillod et C.Raggi.
Merci aussi à E.Gruter et tout le personnel administratif du CRPP pour la leur disponibilité et gentillesse.
Mon remerciement va également à la commission examinatrice composé de Y.Martin, J.-M.Moret, R.Pitts, D.Ryutov, R.Schaller et L.Villard.

Tout au long de mon doctorat, j'ai eu le plaisir de passer des moments très agréable avec mes collègues. Je n'oublierai jamais les adventures de ski avec Andreas, Christian, Joaquim, Miguel et Theo, les sorties en vélo avec Ambrogio, David, Ivo, Kees, Stefano et Ugo, les longues (pour moi) séances de natation avec Jean-Philippe et Stefan, les journées de voile avec James et Yanis et les soirées avec Andres et David.
Un merci spécial à Helena, Christian et Paula pour les beaux moments qu'on partage ensemble, en particulier les délicieux repas, enrichit par votre passion pour la cuisine.
Merci à Reto, mon colloque, guide et ami suisse.
Je remercie profondément ma famille qui m'a soutenue moralement et n'a pas arrêté un seul instant de croire on moi.
Pour finir je remercie le CRPP, l'EPFL et la Suisse, qui m'ont offert l'opportunité de vivre cette expérience unique et inoubliable. Merci.

Curriculum Vitae

Francesco Piras
Ecole Polytechnique Fédérale de Lausanne
Centre de Recherches en Physique des Plasmas
Station 13, PPB 310
CH-1015 Lausanne, SWITZERLAND

Phone: +41 (0)21 693 6548
Fax: +41 (0)21 693 5176
email: `francesco.piras@epfl.ch`

Education/Honors and Awards

2010	EPFL Prize for demonstrating a high level of dedication and enthusiasm.
2010	Special notice from the Itoh Project Prize Committee during the 2010 EPS Conference in Dublin.
2006-2010	PhD in Plasma Physics (Ecole Polytechnique Fédérale de Lausanne).
2006	Prize for the best curriculum in the Faculty of Electrical Engineering.
2006	Master Degree in Electrical Engineering, Politecnico di Torino (110 cum laude/110).
2006	Certificate for merit by the Industrial Union of Turin.
2004	Bachelor Degree in Electrical Engineering, Politecnico di Torino (110 cum laude/110).
2001	Diploma in Electrotechnology for the Industrial Automation, ITIS Oristano.

Professional Experience/Internships

2006-2010 - CRPP/EPFL experimental physicist and diagnostic responsible
Conception, design and analysis of a complex multi-diagnostic tokamak experiment. This resulted in several peer-reviewed scientific publications and invited oral presentations in conferences.
Support teaching activity (General Physics, Plasma Physics).
Responsible for the tokamak magnetic system and bolometers.
Conception, realization and maintenance of the internal website.

2006 - RFX Consortium Padova (Padova - IT)
Optimization of the real-time control system of a nuclear fusion facility to control the plasma position. The new control system achieved a new record for the plasma current.

2006 - Politecnico di Torino (Torino - IT)
Drafting course notes, teaching activity.

2004 - Tuttonormel s.r.l. (Torino - IT)
Drafting articles for the Tuttonormel Journal concerning electrical installation regulations.

2004 - I.E.N. "Galileo Ferraris" (Torino - IT)
Design of a new contact-less system to monitor the temperature in a vacuum pump.

The design constraints of robustness, simplicity were achieved minimizing the product cost. A prototype was realized based on the suggested design.

2003 - Company (Arborea - IT)

Statistical analysis of the milk production line of the 3A Company to identify the least reliable components.

Competences

Social Skills

Communicative and adapting easily to different conditions, developed presenting my scientific results in several conferences abroad.

Motivated to solve new and challenging problems with attention to the technical and management details.

Organizational Skills

Analytical, innovative, with a global view and problem solving oriented, developed during my academic research experience.

Capable in organizing and co-ordinating work in a team, developed by leading a team of scientists.

Engineering Skills

Control systems, electronics, electromagnetic devices, electricity market, energy production and transmission.

Experimental Physics Skills

Electromagnetism, electromagnetic simulations, plasma physics and applications, plasma measurements.

IT Skills

Operating systems (Windows, UNIX/LINUX, OSX, VMS).
Languages (Fortran, PHP, MySQL, HTML).
Graphics tools (Autocad, Adobe Illustrator).
Analysis tools (PSpice, Matlab).
Office suites (Microsoft Office, iWork, Latex).

Languages

Italian	Mother tongue.
English	Fluent reading (B2) and writing (B2).
French	Fluent reading (B2) and writing (B2).
Spanish	Basic understanding (A2).
German	Beginner (A1).

Extra-curricular Activities

Competitive sports (sailing, biking, swimming, running, triathlon, ...).

Personal Information

28, single, italian citizen, exempt from military service.

References

Prof. Ambrogio Fasoli, Director of CRPP, EPFL, +41 2169 33492, `ambrogio.fasoli@epfl.ch`
Dr. Stefano Coda, Responsible for TCV operations, EPFL, +41 2169 33463, `stefano.coda@epfl.ch`
Dr. Dmitry D. Ryutov, Scientist, LLNL, +1 925 422 9832, `ryutov1@llnl.gov`
Dr. Adriano Luchetta, Scientist, RFX, +39 049 829 5043, `adriano.luchetta@igi.pd.cnr.it`
Dr. Piero Martin, Scientist, RFX, +39 049 829 5997, `piero.martin@igi.cnr.it`

List of Publications

F.Piras et al, **"On the Possibility to Create and Control a Doublet Shaped Plasma on TCV"**, *Plasma Phys. Control. Fusion*, to be published.

F.Piras et al, **"Plasma Start-up on TCV"**, *Plasma Phys. Control. Fusion*, to be published.

F.Piras, S.Coda, B.P.Duval, B.Labit, J.Marki, S.Yu.Medvedev, J.-M.Moret, A.Pitzschke and O.Sauter, **"Snowflake Divertor Experiments on TCV"**, *Plasma Phys. Control. Fusion*, vol. 52, p. 124010 (2010).

Y.Camenen, A.Bortolon, B.P.Duval, L.Federspiel, A.G.Peeters, F.J.Casson, W.A.Hornsby, A.N.Karpushov, F.Piras, O.Sauter, A.P.Snodin and G.Szepesi **"Experimental demonstration of an up-down asymmetry effect on intrinsic rotation in the TCV tokamak"**, *Plasma Phys. Control. Fusion*, vol. 52, p. 124037 (2010).

Y.Camenen, A.Bortolon, B.P.Duval, L.Federspiel, A.G.Peeters, F.J.Casson, W.A.Hornsby, A.N.Karpushov, F.Piras, O.Sauter, A.P.Snodin and G.Szepesi , **Experimental Evidence of Momentum Transport Induced by an Up-Down Asymmetric Magnetic Equilibrium in Toroidal Plasmas**, *Phys. Rev. Lett.*, vol. 105, p. 135003 (2010).

F.Piras, S.Coda, B.P.Duval, B.Labit, J.Marki, S.Yu.Medvedev, J.-M.Moret, A.Pitzschke and O.Sauter, **"Snowflake H-mode in a tokamak plasma"**, *Phys. Rev. Lett.*, vol. 105, p. 155003 (2010).

S.Yu.Medvedev, A.A.Ivanov, A.A.Martynov, Yu.Yu.Poshekhonov, R.Behn, Y.R.Martin, J.- M.Moret, F.Piras, A.Pitzschke, A.Pochelon, O.Sauter and L.Villard, **Edge Stability and Pedestal Profile Sensitivity of Snowflake Diverted Equilibria in the TCV Tokamak**, *Contrib. Plasma Phys.*, vol. 50, p. 324 (2010).

F.Piras, J.-M.Moret and J.X.Rossel, **Measurement of the magnetic field errors on TCV**, *Fusion Eng. Des.*, vol. 85, p. 739 (2010).

J.I.Paley, J.Berrino, S.Coda, N.Cruz, B.P.Duval, F.Felici, T.P.Goodman, Y.Martin, J.M.Moret, F.Piras, A.P.Rodriques, B.Santos and C.A.F.Varandas, **Real time control of plasmas and ECRH systems on TCV**, *Nucl. Fusion*, vol. 49, p. 085017 (2009).

J.I.Paley, F.Felici, S.Coda, T.P.Goodman and F.Piras, **Real time control of the sawtooth period using EC launchers**, *Plasma Phys. Control. Fusion*, vol. 51, p. 055010 (2009).

F.Piras, S.Coda, I.Furno, J.-M.Moret, R.A.Pitts, O.Sauter, B.Tal, G.Turri, A.Bencze, B.P.Duval, F.Felici, A.Pochelon and C.Zucca, **Snowflake divertor plasmas on TCV**, *Plasma Phys. Control. Fusion*, vol. 51, p. 055009 (2009).

List of Conferences

F.Piras, S.Coda, B.P.Duval, B.Labit, J.Marki, S.Yu.Medvedev, J.-M.Moret, A.Pitzschke and O.Sauter, **Snowflake H-mode in Tokamak Plasmas**, *15th Workshop on MHD and Stability, Madison, USA*, 2010

F.Piras, S.Coda, B.P.Duval, B.Labit, J.Marki, S.Yu.Medvedev, J.-M.Moret, A.Pitzschke and O.Sauter, **H-mode Snowflake Divertor Plasmas on TCV**, *52nd Annual Meeting of the APS Division of Plasma Physics, Chicago, USA*, 2010

B.P.Duval, A.Bortolon, L.Federspiel, F.Felici, I.Furno, A.Karpushov, J.Paley and F.Piras, **Momentum Transport in TCV Across Sawteeth Events**, *23rd IAEA Fusion Energy Conference in Daejon, KOREA*, 2010

B.Labit, A.Pochelon, M. Rancic, F.Piras, A.Bencze, A.Bottino, S.Brunner, Y.Camenen, P.K.Chattopadhyay, S.Coda, E.Fable, T.P.Goodman, S.Jolliet, A.Marinoni, L.Porte, B.F.McMillan, S.Yu.Medvede O.Sauter, V.S.Udintsev and L.Villard, **Transport and Turbulence with Innovative Plasma Shapes in the TCV Tokamak**, *23rd IAEA Fusion Energy Conference in Daejon, KOREA*, 2010

F.Piras, T.Goodman, J.-M.Moret, A.Bencze, B.P.Duval, J. X.Rossel and D.Wágner, **Plasma start-up in the TCV tokamak**, *17th EPS Conference on Plasma Physics, Dublin, IRELAND*, 2010

S.Yu.Medvedev, A.A.Ivanov, A.A.Martynov, Yu.Yu.Poshekhonov, Y.R.Martin, J.-M.Moret, F.Piras, A.Pitzschke, A.Pochelon, O.Sauter and L.Villard, **Free-Boundary Equilibrium and Stability of Snowflake Diverted and Negative Triangularity Plasmas in the TCV Tokamak**, *17th EPS Conference on Plasma Physics, Dublin, IRELAND*, 2010

Y.Camenen, A.Bortolon, B.P.Duval, L.Federspiel, A.G.Peeters, F.J.Casson, W.A.Hornsby, F.Piras, A.Karpushov, O.Sauter, A.P.Snodin and G.Szepesi, **Experimental demonstration of an up-down asymmetry effect on intrinsic rotation in the TCV tokamak**, *17th EPS Conference on Plasma Physics, Dublin, IRELAND*, 2010 - INVITED TALK

F.Piras, S.Alberti, R.Behn, A.Bencze, S.Coda, B.P.Duval, T.Goodman, B.Labit, J.Marki, J.-M.Moret, A.Pitzschke, L.Porte, O.Sauter and D.Wágner, **Snowflake Divertor Experiments on TCV**, *17th EPS Conference on Plasma Physics, Dublin, IRELAND*, 2010 - INVITED TALK

N.Cruz, J.-M.Moret, S.Coda, J.Paley, A.P.Rodrigues, F.Piras, F.Felici and C.A.F.Varandas, **Using APCS for Plasma Vertical Control at TCV**, *17th Real Time Conference, Lisbona, PORTUGAL*, 2010

A.Bencze, D.Wágner, B.P.Duval, Y.Andrebe, F.Piras and G.Veres, **Visible video diagnostic systems on TCV**, *5th German-Polish Conference on Plasma Diagnostics for Fusion and Applications, Pont-à-Mousson, FRANCE*, 2010

A.Pitzschke, F.Piras, R.Behn and S.Yu.Medvedev, **MHD stability calculations for H-mode plasmas with snowflake divertor configuration**, *Réunion Annuelle de la Société Suisse de Physique, Innsbruck, AUSTRIA*, 2009

S.Yu.Medvedev, A.A.Ivanov, A.A.Martynov, Yu.Yu.Poshekhonov, Y.R.Martin, J.-M.Moret, F.Piras, A.Pitzschke, A.Pochelon, O.Sauter and L.Villard, **Stability of Snowflake Diverted and Negative Triangularity Plasmas in the TCV Tokamak**, *36th European Physical Society Conference on Plasma Physics, Sofia, BULGARIA*, 2009

F.Piras, A.Bencze, S.Coda, B.P.Duval, I.Furno, J.-M.Moret, R.A.Pitts, O.Sauter, B.Tal, D.Wagner, F.Felici, B.Labit, J.Marki, Y.Martin, S.Medvedev, A.Pitzschke, A.Pochelon, G.Turri and C.Zucca, **Snowflake Divertor Plasmas on TCV**, *36th European Physical Society Conference on Plasma Physics, Sofia, BULGARIA*, 2009

F.Piras, S.Coda, I.Furno, S.Yu.Medvedev, J.-M.Moret, R.A.Pitts, A.Pitzschke, O.Sauter, B.Tal, G.Turri, A.Bencze, B.P.Duval, F.Felici, A.Pochelon and C.Zucca, **Snowflake Divertor Plasmas on TCV**, *TTF-2009, US-EU Transport Task Force meeting, San Diego, USA*, 2009

A.Pochelon, Y.Camenen, A.Marinoni, S.Brunner, S.Coda, I.Furno, J.Graves, An.Martynov, S.Medvedev, F.Piras, H.Reimerdes, O.Sauter and A.Scarabosio, **Physics Insight and Performance Benefit from Plasma Shaping Experiments in MHD and Energy Transport in the TCV Tokamak**, *IAEA FEC, 22nd IAEA Fusion Energy Conf., Geneva, SWITZERLAND*, 2008

J.I.Paley, F.Felici, J.Berrino, S.Coda, N.Cruz, B.P.Duval, T.P.Goodman, Y.Martin, J.M.Moret, F.Piras and A.P.Rodriques, **Real Time Control of Plasmas and ECRH Systems on TC**, *IAEA FEC, 22nd IAEA Fusion Energy Conf., Geneva, SWITZERLAND*, 2008

F.Felici, E.Asp, S.Coda, E.Fable, T.Goodman, J.Graves, M.Henderson, J.Paley, F.Piras, O.Sauter, G.Turri, V.Udintsev and C.Zucca, **Recent results of ECRH/ECCD experiments on TCV**, *18th International Toki Conference (ITC18), Toki Gifu, JAPAN*, 2008

J.I.Paley, F.Felici, S.Coda, T.P.Goodman and F.Piras, **Real time feedback control of the sawtooth period using ECRH launchers**, *50th APS Division of Plasma Physics Meeting in Dallas, USA*, 2008